

Dario Narducci · Peter Bermel
Bruno Lorenzi · Ning Wang
Kazuaki Yazawa

Hybrid and Fully Thermoelectric Solar Harvesting

Springer Series in Materials Science

Volume 268

Series editors

Robert Hull, Troy, USA

Chennupati Jagadish, Canberra, Australia

Yoshiyuki Kawazoe, Sendai, Japan

Richard M. Osgood, New York, USA

Jürgen Parisi, Oldenburg, Germany

Udo W. Pohl, Berlin, Germany

Tae-Yeon Seong, Seoul, Republic of Korea (South Korea)

Shin-ichi Uchida, Tokyo, Japan

Zhiming M. Wang, Chengdu, China

The Springer Series in Materials Science covers the complete spectrum of materials physics, including fundamental principles, physical properties, materials theory and design. Recognizing the increasing importance of materials science in future device technologies, the book titles in this series reflect the state-of-the-art in understanding and controlling the structure and properties of all important classes of materials.

More information about this series at <http://www.springer.com/series/856>

Dario Narducci · Peter Bermel
Bruno Lorenzi · Ning Wang
Kazuaki Yazawa

Hybrid and Fully Thermoelectric Solar Harvesting



Springer

Dario Narducci
Department of Materials Science
University of Milano-Bicocca
Milan
Italy

Peter Bermel
Birck Nanotechnology Center
Purdue University
West Lafayette, IN
USA

Bruno Lorenzi
University of Milano-Bicocca
Milan
Italy

Ning Wang
Chinese Academy of Sciences
Institute of Soil and Water Conservation
Yangling
China

Kazuaki Yazawa
Birck Nanotechnology Center
Purdue University
West Lafayette, IN
USA

ISSN 0933-033X ISSN 2196-2812 (electronic)
Springer Series in Materials Science
ISBN 978-3-319-76426-9 ISBN 978-3-319-76427-6 (eBook)
<https://doi.org/10.1007/978-3-319-76427-6>

Library of Congress Control Number: 2018935848

© Springer International Publishing AG, part of Springer Nature 2018
This work is subject to copyright. All rights are reserved by the Publisher, whether the whole or part
of the material is concerned, specifically the rights of translation, reprinting, reuse of illustrations,
recitation, broadcasting, reproduction on microfilms or in any other physical way, and transmission
or information storage and retrieval, electronic adaptation, computer software, or by similar or dissimilar
methodology now known or hereafter developed.

The use of general descriptive names, registered names, trademarks, service marks, etc. in this
publication does not imply, even in the absence of a specific statement, that such names are exempt from
the relevant protective laws and regulations and therefore free for general use.

The publisher, the authors and the editors are safe to assume that the advice and information in this
book are believed to be true and accurate at the date of publication. Neither the publisher nor the
authors or the editors give a warranty, express or implied, with respect to the material contained herein or
for any errors or omissions that may have been made. The publisher remains neutral with regard to
jurisdictional claims in published maps and institutional affiliations.

Printed on acid-free paper

This Springer imprint is published by the registered company Springer International Publishing AG
part of Springer Nature
The registered company address is: Gewerbestrasse 11, 6330 Cham, Switzerland

Preface

Thermoelectricity is, on many counts, a solution in search of a problem.

Thermoelectricity as a physical phenomenon was discovered in the nineteenth century, and its very first application was provided by Peltier who built a portable cooler just a few years after the discovery of the thermoelectric effect that was named after him. Applications of the Seebeck effect to convert heat into electric power began instead over the first part of the twentieth century, especially in the Soviet Union, but found a major opportunity with deep-space exploration, wherever sunlight is too weak for solar panels to power spacecrafts. Plutonium oxide radioactive decay was used in Radioisotope Thermoelectric Generators (RTGs) by NASA in many missions including Apollo (along with photovoltaic panels), Pioneer, Viking, Voyager, Galileo, and Cassini—and, quite recently, to power the Curiosity rover on Mars. Although inefficient, RTGs were preferred over alternate technological solutions because of their remarkable reliability and lifetime due to the absence of moving parts.

For terrestrial applications, instead, thermoelectric converters still struggle to find their path. As known, efficiency progress of thermoelectric materials and generators have been delayed by the need of separately controlling electron and phonon transport in solids, keeping phonon mean free paths as small as possible while increasing the corresponding quantity for charge carriers—a result partly achieved just over the last decade by the introduction of nanotechnology. Despite their limited efficiency, also for non-space applications, thermoelectric generators have been considered to harvest heat when lack of moving parts and small sizes were at a premium. Deployment of thermoelectric generators to recover heat from car mufflers prompted quite a bit of basic and applied research, stimulating the search for novel low-cost, geo-abundant materials. The automotive industry, which was looking for ways to contain CO₂ emissions in the wake of the Paris Agreement, reported, however, severe problems concerning the economic sustainability of thermoelectric converters. Although paying back their cost over the average car lifetime, they required an extra capital cost for customers that made thermoelectric harvesters a viable solution only for the high-end automotive segment. Furthermore, the volatility of the environmental policies (both in Europe and in the

USA) along with the advancements (achieved and/or announced) in the making of electric cars turned out to cool down the initial enthusiasm toward thermoelectric harvesters.

Thermoelectric generators (either miniaturized or fully integrated) are also considered an interesting supporting technology for the so-called Internet of Things (IoT), namely networks of interconnected, distributed devices embedding electronics, software, sensors, and actuators. Although IoT devices are not necessarily wireless, physical autonomy is a key aspect of a large subset of such networks. Thus, unplugged devices would ideally pair with their being wireless as of data exchanges. Batteries may be once again a viable and ready solution. However, especially when device maintenance is inconvenient or impossible, harvesters may either complement or replace batteries, targeting the making of deploy-and-forget network nodes. Development of suitable thermoelectric harvesters has advanced over the last years. In this case, economical aspects are a rather marginal limitation, the hurdle to be overcome being essentially that of the power density available over small (sometimes very small) temperature differences. Body heat harvesters are a good example of this issue.

If the IoT might provide a good driver to move thermoelectric generators from niche to bulk application for microharvesting (i.e., power outputs in the order of some milliwatts), use of thermoelectricity to complement the dominating renewable energy source, i.e., photovoltaics, might play a similar role for macroharvesting. In 1954, when Mária Telkes published her pioneering work on thermoelectric sun power converters, the efficiency of thermoelectric generators (3–4%) was comparable to that of the first photovoltaic cells (4–6%). As known, in the following years, efficiency of photovoltaics skyrocketed to two-digit figures, while thermoelectrics could not break the 10% efficiency threshold till relatively recent times, therefore leaving the race for solar harvesting. It could re-enter it now, however, as a partner more than as a competitor. Currently, the photovoltaic market is dominated by silicon panels, with efficiencies now leveled off to about 20%. Use of multiple junctions, capable of efficiencies already exceeding 40% is limited by capital costs. Also, power costs, albeit heavily doped by taxation and incentives by public authorities, have also reached a plateau since more than 5 years. This implies that, unless radically new fabrication technologies are conceived, capital and power costs for silicon-based photovoltaics may not be expected to decrease substantially over the next decades. Novel photovoltaic materials have surfaced, instead, currently with lower efficiencies but also with promising lower costs, should they be fully promoted to production. Perovskites are only the most recent example. Differently from silicon, such materials would take significant advantages from being paired to a thermoelectric stage, remarkably increasing the total electric power output of the solar harvester. Furthermore, preliminary economic estimates show that their power costs, payback periods, and capital investments per electric watt would be sustainable.

It is therefore not surprising that both fundamental and applied research on hybrid (photovoltaic–thermoelectric) solar harvesters have lately gained a great momentum. The number of papers covering this topic has increased, exceeding 500

articles published in the year 2017 (Data source: Scopus). With a publication rate still increasing linearly at the noteworthy rate of 46 papers/year² since 2006, the field is clearly still under accelerated expansion. This is one of the main motivations behind this book—namely providing a self-consistent yet thorough and in-depth introduction to hybrid harvesters to the newcomers. This book is primarily thought as a primer to experienced scientists willing to enter this lively field of research. It is meant both for scientists working on thermoelectrics and willing to catch the basic physics of photovoltaics; and for professionals working on photovoltaic science and technology who are curious to consider the application of thermoelectric harvesters to enhance the total efficiency of solar converters. Therefore, further to core chapters on full and hybrid thermoelectric solar harvesters, introductory chapters on thermoelectricity and photovoltaics are provided. This turns out to make the book also suitable for Ph.D. students and post-docs, who will use the first chapters to have an introduction to both harvesters before moving to their joined applications to solar converters. But we also hope that this book may be of some interest to entrepreneurs and public decision-makers looking for an insight into the opportunities (and the limits, too) of hybrid solar harvesters. Although all authors of this book are actively engaged in this research field, we did our very best to uncover also what hybridization cannot afford to do. However, as will be shown, premises look as good as promises for this technology, and it seems fair to suggest more attention to the opportunities it might deliver in the short- and mid-terms.

Taking a picture of a quickly moving subject is not simple at all, and some blurring is unavoidable. This book is no exception, and it inescapably reflects the views and the sentiments of its authors. We are fully aware that we could not catch all possible approaches to modern hybrid solar harvesters. We then apologize for any promising approach we did not mention or that we insufficiently covered. We did not aim at being exhaustive in a field showing such a rapid growth simply because a catalog of ideas, hints, and strategies would have suffered a too rapid obsolescence, becoming outdated over the time needed just to publish it. Our aim was instead to write a self-contained, agile introduction to the topic, which was yet missing—as an invitation to senior and junior colleagues to join the effort. This said, any suggestion, criticism, and comment from readers on how to update and complete our picture will be highly appreciated, and might be used for forthcoming editions of this book.

Milan, Italy
West Lafayette, USA
Cambridge, USA
Yangling, China
West Lafayette, USA

Dario Narducci
Peter Bermel
Bruno Lorenzi
Ning Wang
Kazuaki Yazawa

Acknowledgements

Bruno Lorenzi has received funding from the European Union’s Horizon 2020 research and innovation programme under the Marie Skłodowska-Curie grant agreement No. 745304.

Contents

1	Introduction	1
1.1	Solar Harvesting: Photovoltaics and Beyond	1
1.1.1	The Emergence of Renewable Energy Sources	1
1.1.2	Photovoltaics: A Technological Success History	3
1.2	Aims of This Book	7
References		8
2	A Primer on Thermoelectric Generators	11
2.1	Introduction	11
2.2	Fundamentals of Thermodynamics of Thermoelectricity	12
2.2.1	Thermoelectricity in Linear Thermodynamics	12
2.2.2	Thomson Effect	17
2.3	Thermoelectric Efficiency in the Constant-Property Limit	17
2.3.1	Dirichlet Boundary Conditions	18
2.3.2	Neumann Boundary Conditions	25
2.4	Thermoelectric Efficiency in the Presence of Large Temperature Differences	30
2.4.1	Thermoelectric Potential	32
2.4.2	Comparison to CPL Efficiency	33
2.4.3	Compatibility and Efficiency	33
2.4.4	Engineering Figure of Merit	34
2.5	Finite-Rate Thermoelectric Efficiency	36
2.5.1	Efficiency of Finite-Rate Thermal Engines	36
2.5.2	Application to Thermoelectric Generators	39
2.6	Thermoelectric Efficiency Under Non-steady State Conditions	40
2.7	Summary and Conclusions	41
References		42

3 Solar Thermoelectric Generators	45
3.1 System Description and State of the Art	45
3.1.1 Optical Collector	47
3.1.2 Opto-Thermal Converter	47
3.1.3 Thermal Collector	50
3.1.4 Thermoelectric Converter	51
3.1.5 Heat Dissipater	52
3.2 Efficiency of STEGs	52
3.3 TEG Design	55
3.4 Materials Characteristics	57
References	59
4 A Primer on Photovoltaic Generators	63
4.1 Background and Theory	63
4.1.1 Introduction	63
4.1.2 Solar Spectrum	64
4.1.3 Solar Cell I-V Characteristics	65
4.1.4 Solar Cell Efficiency	68
4.1.5 Solar Cell Applications	69
4.2 Review of Photovoltaic Technologies: Types and Classifications	70
4.2.1 Overview	70
4.2.2 The First-Generation Cells	71
4.2.3 The Second Generation Cells	73
4.2.4 The Third Generation Cells	77
4.3 Solar Cell Device Physics	81
4.3.1 The Prevalent Photovoltaic Physical Process	81
4.3.2 Silicon Solar Cells	81
4.3.3 Dye Sensitized Solar Cells	83
4.3.4 Quantum Dot Sensitized Solar Cells	84
4.3.5 Conjugated Polymer-Based Solar Cells	85
4.3.6 Perovskite Solar Cells	86
4.4 Summary	88
References	89
5 Hybrid Photovoltaic–Thermoelectric Generators: Theory of Operation	91
5.1 System Description	91
5.2 Solar Cells as Efficient Opto-Thermal Converters	92
5.3 Efficiency of HTEPV	95
5.4 PV Temperature Sensitivity	97
5.5 Fully Hybridized Solar Cells	98
5.6 Summary and Conclusions	100
References	101

6 Hybrid Photovoltaic–Thermoelectric Generators: Materials	
Issues	103
6.1 Introduction	103
6.2 Organic Photovoltaic Materials	104
6.2.1 Dye-Sensitized Solar Cells	105
6.2.2 Polymer-Based Solar Cells	107
6.2.3 Photothermally Activated Pyroelectrics	109
6.2.4 Perovskite Solar Cells	110
6.3 Inorganic Photovoltaic Materials	111
6.3.1 First Investigations: Polysilicon Solar Cells	111
6.3.2 Multi-junction Concentrated Solar Cells	113
6.3.3 Non-silicon-Based Solar Cells	113
6.4 Summary and Conclusions	114
References	115
7 Photovoltaic–Thermoelectric–Thermodynamic Co-Generation	117
7.1 Photovoltaic–Thermoelectric–Thermodynamic Co-Generation	117
7.1.1 Introduction to Triple Cogeneration	117
7.1.2 Component Technologies	120
7.1.3 Tandem Solar Cells with Optical Concentration	123
7.1.4 High Temperature Thermoelectrics	123
7.1.5 High Temperature Thermal Storage	126
7.1.6 Thermodynamic Mechanical Heat Engines	127
7.2 Efficiency of Triple Co-Generation System	127
7.2.1 Modeling of Spectrum Integrated System and Trade-Off	128
7.2.2 Efficiency and Concentration	129
7.2.3 System Scaling Impact	132
7.3 Solar Photovoltaic/Thermophotovoltaic/Thermal Triple Cogeneration	132
7.3.1 TPV Integrated System	132
7.3.2 Practical Considerations	133
7.4 Summary	135
References	135
8 Hybrid Solar Harvesters: Technological Challenges, Economic Issues, and Perspectives	137
8.1 Introduction	137
8.2 Photovoltaic and Thermoelectric Materials	138
8.3 Technological Challenges	139
8.4 Economical Sustainability	140
8.4.1 Thermoelectric Generators	140
8.4.2 Photovoltaic Cells and Modules	143

8.4.3 Hybrid Solar Harvesters	143
8.4.4 Pay-Back Period	149
8.5 Conclusive Remarks	149
References	150
Index	153

Acronyms

BOS	Balance of System
CIGS	Copper Indium Gallium Selenide ($\text{CuIn}_x\text{Ga}(1-x)\text{Se}_2$)
CPL	Constant-property Limit
CPV	Concentrating Photovoltaic
CZTS	Copper Zinc Tin Sulfide
DCPL	Dirichlet Constant-Property Limit
DSSC	Dye-Sensitized Solar Cell
EHP	Electron–Hole Pair
ERE	External Radiative Efficiency
FF	Fill Factor
FTP	Fluorine-doped Tin Oxide
HCPV	High Concentrating Photovoltaic
HM	Heat Mirror
HOMO	Highest Occupied Molecular Orbital
HTEPG	Hybrid Thermoelectric–Photovoltaic Generator
HTEPV	Hybrid Thermoelectric–Photovoltaic
HTM	Hole Transport Material
IQE	Internal Quantum Efficiency
ITEPV	Inorganic Thermoelectric–Photovoltaic
ITO	Indium Tin Oxide
LCOE	Levelized Cost of Energy
LUMO	Lowest Unoccupied Molecular Orbital
MJ	Multi-junction
NCPL	Neumann Constant-Property Limit
ORC	Organic Rankine Cycle
OTEPV	Organic Thermoelectric–Photovoltaic
PBP	Payback Period
PCM	Phase-Change Material
PV	Photovoltaic
QD	Quantum Dot

QDSSC	Quantum Dot Sensitized Solar Cells
RHS	Right-Hand Side
SHR	Shockley-Read-Hall
SJ	Single-junction
SSAR	Selective Solar Absorber and Reactor
SSA	Selective Solar Absorber
STEG	Solar Thermoelectric Generator
TEG	Thermoelectric Generator
TES	Thermal Energy Storage
TE	Thermoelectric
TPV	Thermophotovoltaic
USD	United States Dollar

Chapter 1

Introduction



Abstract The main topics covered in this book will be introduced. An overview of the historical trend of energy consumption over the last one hundred years will show the crucial need for renewable sources progressively replacing fossil and nuclear power supply. Among renewables, solar harvesting is surely the most promising technology, already playing a significant role in the global power landscape. Demand for higher efficiencies and lower power costs may open yet partially unexplored paths where PV modules are paired to ancillary harvesters to improve the usability of solar power, which will be the main focus of this book.

1.1 Solar Harvesting: Photovoltaics and Beyond

1.1.1 *The Emergence of Renewable Energy Sources*

The use of energy by Mankind has seen a continual increase over the Centuries. It was estimated that power needs from the beginning of civilization up to the Middle Age was in the order of 580 W per capita (mostly food and heating), modestly raising to 1.3 kW per capita around 1400 A.D. Figures showed a major jump only with the Industrial Revolution (XIXth Century), getting to about 3.4 kW per capita [1]. Continued expansion of fossil fuel consumption further raised power requests, that quite diversified at the beginning of the XXth Century. As noted by Jorgenson [2], between 1920 and 1955 electric power requests expanded by a factor of more than ten, while consumption of all other forms of energy just doubled. This was mostly the result of the enhancement of thermal efficiency in the conversion of fuels into electricity (almost tripled over less than three decades) but also of the advantages of electric power distribution over traditional energy vectors. Currently, power consumption in First and Second World countries is in the order of 11 kW per capita, about ten times larger than at the end of the Middle Age. World power needs further scale when reported as global figures, namely accounting for the increase of population. World power needs are seen to jump from 2×10^{10} W at the beginning of Renaissance to 10^{12} W in the age of the Industrial Revolution, currently exceeding 10^{13} W.

It may be interesting to observe that the tenfold increase of power needs over the last 150 years almost scales as the World population, which raised from about 1 billion to 7 billion—quite a surprising fact considering that power per capita itself had more than tripled. Figures possibly find a rationale if one considers that over the last 150 years Europe reported a demographic increase of only $2.7\times$, properly combining with the $3\times$ increase of per capita power demand. If this is correct, one may then conclude that the projected global power demand, were access to energy uniform worldwide, should be larger than 30 TW.

Use of fossil sources has dominated energy production till very recent years, the only relevant source of renewable energy before 1950 having been wind and waterflow used by mills; and waterfalls for electric energy generation. Around the middle of the XXth Century it became clear that use of non-renewable resources was reaching unsustainable rates, not only from the viewpoint of its impact on the ecosystem but also from that of economical affordability of fossil resources [3]. Access to deep oil basins would have required an investment in terms of funds and of energy to extract petrol that would have made the whole operation inconvenient. Furthermore, geopolitical factors rang an alarm bell, showing how the distribution of fossil energy resources was setting the agenda of industrial growth, with fossil sources acting as the leverage of the economic development at a global level.

For about two decades nuclear (fission) energy seemed to have the potential to reset the energy clock, and many countries in the First and Second World focused a significant technological effort to develop safe, economically convenient nuclear plants. However, three issues soon shut down the enthusiasms for the new nuclear Eldorado. On one side, the cost of nuclear energy was aggravated by the unsolvable issue of safely disposing of the exhausted nuclear fuel. A lifecycle analysis (LCA) of nuclear plants, including plant decommissioning and safety issues, provided evidence that fossil nuclear energy would have been far less competitive than initially expected [4]. Furthermore, safety concerns raised a rather widespread societal refusal for nuclear plants, that either led to their shutdown or that further increased energy production costs related to the political requests of extended safety measures. Finally, the development of nuclear know-how raised the possibly legitimate concern that nuclear technology might have been reused for military applications—or might have led to an anyway uncontrolled availability of fissile material. All these factors added up to the limited and uneven availability of uranium worldwide, critically favoring China, former Soviet block countries, and Australia [5, 6]. As a matter of fact, the rate of construction of new civilian fission-electric reactors essentially halted in 1984 [7], although the increased capacity of the existing reactors has led to a continuing increase of their electrical energy production up to 2006, declining afterward [8] (Fig. 1.1).

While fusion reactors remain a tomorrow technology, the increasing demand for evenly distributed, affordable, and green energy sources has motivated over the last three decades not only a research effort but also an accelerated diffusion of plants converting fully renewable energy sources into electric energy. Tides, wind, and sun, along with a more efficient use of waterfalls in hydroelectric plants, began complementing oil and gas for electricity production. Among them, solar energy

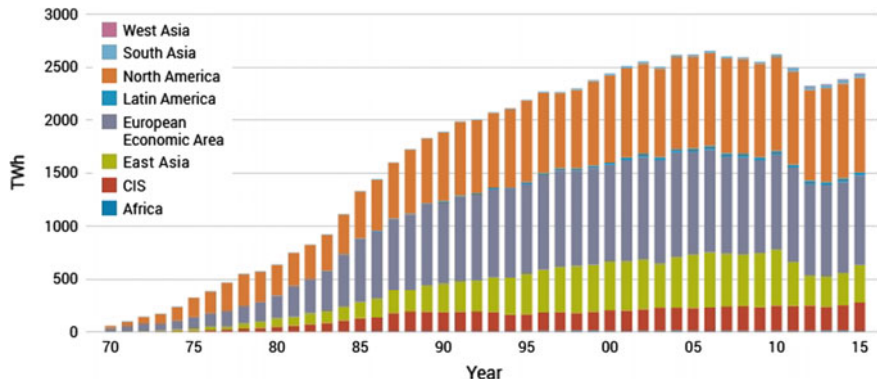


Fig. 1.1 Historical trend of worldwide electric power generated by nuclear plants. *Source IEA [9]*

conversion displayed the most spectacular increase of conversion efficiency that, along with its scalability and wide usability, made it the reference renewable energy source.

1.1.2 *Photovoltaics: A Technological Success History*

This subsection briefly reviews the history of photovoltaic cells, discussing both their technological advancements and their deployment in large and distributed solar plants in view of the interplay among materials research, technological ingenuity, and economical leverages and constraints. A more technical discussion on photovoltaics is postponed to Chap. 4.

It is well known that the first evidence of the possibility to convert sun light into electricity was provided by Bequerel in 1839 [10]. The first modern PV cell was however built in 1954 at Bell labs by Chapin, Fuller and Pearson [11]. Based on single-crystalline silicon, it had a 6% efficiency. Silicon technology allowed however to rapidly escalate such a conversion rate, that in a few year reached a value of about 10%. The advantage of using a well-established and mature manufacturing technology was actually a key issue to make silicon the reference material for PV solar cells. High-perfection single crystals obtained by Czochralski (CZ) growth enabled to achieve efficiency rates in excess to 20% [12], with a very moderate degradation upon use (<10%).

Degradation of performance is nonetheless a relevant issue in photovoltaics. In single-crystalline silicon it is known to be mostly due to the formation of $[B_1O_1]$ complexes [13], altering the doping profile of the material. A way to avoid the phenomenon would be in principle that of using float-zone, oxygen-free Si single crystals, but production costs make the approach unrealistic, save for high-end applications.

Use of magnetic CZ (MCZ) showed instead to be more feasible. Efficiencies as high as 24.5% were reported [14], with almost no degradation over time. As an alternative, boron could be replaced by gallium with excellent results, so that a record efficiency of 20.2% was reported [15].

Use of bulk single crystals, while granting large efficiencies, negatively affects PV cell installation costs. This led in the Seventies to the parallel development of PV cells based upon the so-called multicrystalline silicon, namely polycrystalline silicon with grain sizes ranging from some millimeters to some centimeters. Grain boundaries along with a larger impurity content (due to diffusion from the crucible during ingot growth) impart the material a lower carrier lifetime—and therefore a lower efficiency, compared to single crystals. However, cast techniques allowed to obtain squared (instead of round) wafers that could be more easily accommodated into PV modules. Therefore, the larger active area in modules compensated for the lower intrinsic efficiency, making low-cost cells capable of output power densities fully comparable to those achieved by high-cost monocrystalline silicon. Efficiency could be further enhanced by wise passivation of deep-traps, e.g. using hydrogen [16, 17].

As an alternative to single-and multi-crystalline silicon, amorphous silicon (a-Si) was considered after the late Sixties. PV technology based upon a-Si surfaced to the market in 1981, although full understanding and control of a-Si could not be reached before the late Nineties. PV cells based upon a-Si showed not only low efficiencies compared to their crystalline cousins but also a remarkable degradation over short periods of time due to the so-called Staebler-Wronski effect [18]. Currently, a-Si cells may be stabilized at an efficiency of 13%, and module efficiencies ranging from 6 to 8% are reported.

More recently, other materials have been proposed to challenge silicon. Multinary alloys of general formula $\text{Cu}(\text{In}, \text{Ga})(\text{S}, \text{Se})_2$ (referred to as CIGS) [19] and $\text{Cu}_2\text{ZnSnS}_4$ (CZTS) [20] along with CdTe have been scrutinized.

Among them, cadmium telluride has a rather long history as candidate material for photovoltaic applications. Heterojunctions of CdTe/CdS may be obtained by growing CdS thin layers on top of SnO_2 transparent contacts deposited onto a glass substrate. CdTe is then deposited, and the PV structure is completed by the deposition of a suitable metallic contact. The cell is then exposed to light from the glass side. CdTe-based PV cells are reported with efficiencies of about 16%, that downgrade to 10% for large-area modules [21]. In spite of its almost ideal bandgap and its ease of deposition as thin film, this class of PV cell pays the high price of being based on a toxic metal as cadmium and on a rare chemical as tellurium.

Figure 1.2 summarizes the state of the art of PV technologies and their advancements over the last forty years. Note that efficiencies refer to laboratory-level cells. Module efficiencies are usually smaller by 30–50%.

Although PV materials technology plays a naturally dominant role in the improving performances of PV cells and modules, other materials issues concur to set the overall efficiency of a photovoltaics, especially at the module level. As an example, materials reflectivity may hinder the conversion rate of a cell. This is especially relevant with silicon cells, due to the large surface reflectivity of the semiconductor.

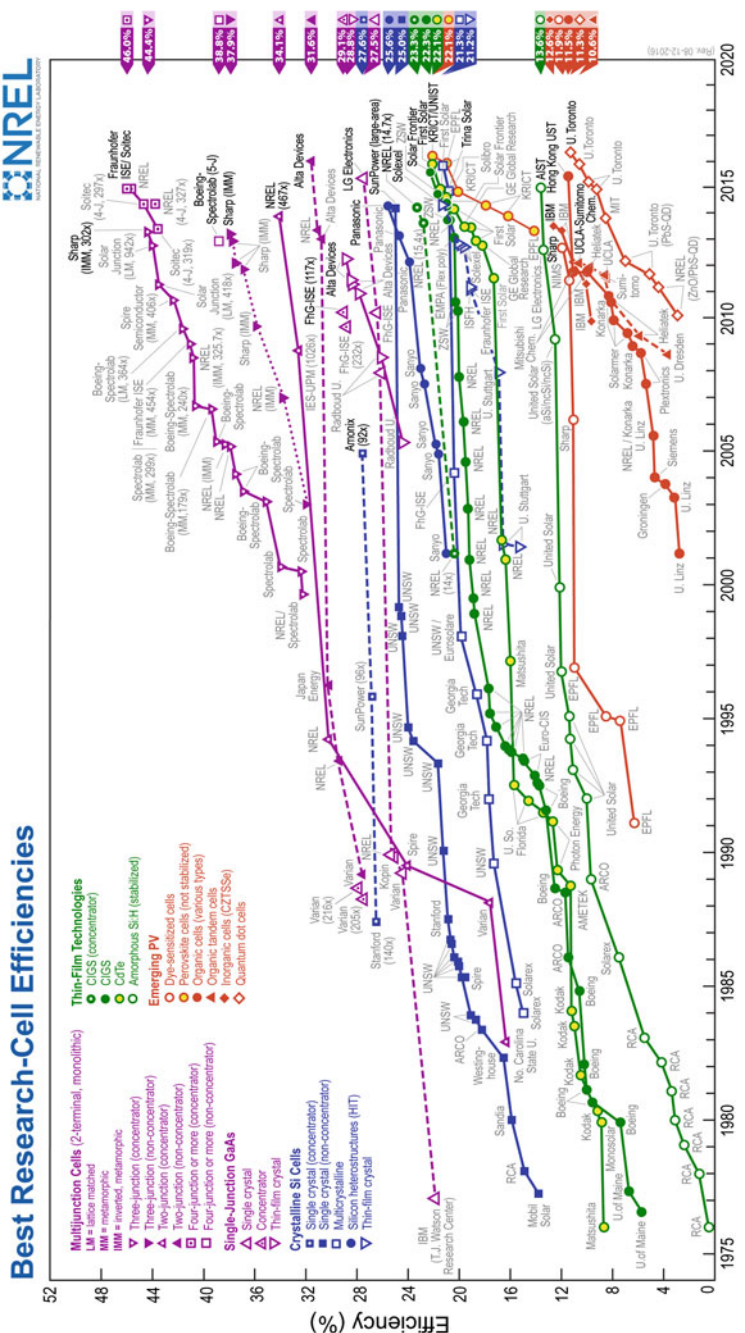


Fig. 1.2 Advancements of PV cell efficiencies over the last forty years. Figures refer to cell efficiencies at the laboratory level. Data from NREL [22].

Technological solutions had then to be devised to minimize the radiation loss at the PV top surface. Anti-reflective coatings or surface texturization [23] are common examples, often coupled to back-reflectors that further help light trapping. Carrier recombination at the outer surfaces also decreases the light conversion rate. Thus, a thin SiO₂ layer is often deposited or anyway grown on the front side, while a thin heavily-doped Si layer is introduced on the cell back surface to generate an electric field that prevents charge carriers from recombination at the back side. Other instances of this class of problems will be discussed in Chap. 4. Suffice here to note that the road to efficiency is paved by an increasing technological complexity, that translates into an increasing number of manufacturing steps needed to build cells and modules. Thus, a compromise has often to be found among PV conversion rates, installation costs and costs of ownership—a trade-off that sets up the sustainability of photovoltaics and their competitiveness to other conventional and renewable energy sources.

With the wider diffusion of PV cells, additional constraints are setting the agenda of photovoltaics. On one side, installation costs compete with the cost of ownership. While PV cells pay back through the electric power they generate, low-cost module with too low efficiencies are anyway inconvenient because of the area fixed costs. Solar cells have actually to be hermetically sealed in modules, mechanically supported, and require electric wiring—all factors that grow up with the cell area and that add up to the final cost of PV electricity [12]. Therefore, a minimum conversion efficiency of 10% is needed for any PV module (12% at cell level), independently of its cost per unit area.

Another qualifying issue of current PV technology relies upon material availability and costs. Both for grid-connected and standalone systems, materials choice depends not only on the efficiency they may grant for solar power conversion but also on the amount of material needed to achieve optimal yields. Comparing a direct-gap semiconductor as GaAs with silicon (indirect-gap) one immediately verifies that only 1 μm of the former is needed to absorb 90% of photons with energy exceeding the energy gap, while about 100 μm of Si are needed to the same aim. Further to set very high purity and crystallinity standards for silicon (as carriers have to travel a relatively long distance to reach the collector), this also imposes a minimum materials thickness that is two orders of magnitude larger than that requested by direct-gap semiconductors [12].

On the other hand, in bulk cells the effective use of materials is way above that set by radiation absorption. A number of strategies have then been pursued to reduce the cost of the inactive material. For Si-based cells, use of low-quality silicon or foreign substrates (i.e. glass, ceramics or graphite) has been considered. Although solving one problem, non-silicon substrates generate another technological challenge. Since the cell manufacture requires some high-temperature steps, harmful diffusion of impurities may occur from the substrate into active silicon. Thus, diffusion barriers have to be introduced, increasing the fabrication complexity. In addition, growth of thin or thick films may often lead to fine-grained active PV layers. Since grain boundaries largely contribute to carrier recombination, PV efficiency degrades. Additional

regrowth steps have then to be introduced, leading to large-grained polycrystalline films.

Overall, this motivates scientific and technological efforts to increase solar conversion efficiency, either by improving PV efficiency or by pairing PV cells with other harvesting technologies—including thermoelectric generation.

1.2 Aims of This Book

Aim of this book is to explore strategies to enhance solar power harvesting by pairing PV modules to thermoelectric generators or to other power converting devices.

The book will cover an empty niche in solar conversion and thermoelectrics. In spite of the growing number of papers dealing with the use of thermoelectrics in solar power conversion, no book exists today that might be used either by a PV specialist or a thermoelectricity expert to enter this field. The book is then intended as a primer for scientists and engineers willing to complement their expertise in one of the two fields, and to get an updated, critical review of the state of the art in thermoelectric solar harvesting.

Chapter 2 will be a dedicated primer to the physics of thermoelectric power conversion. Ample room will be given to issues that impact on module efficiency and reliability. Solar thermoelectric generators will be the subject of Chap. 3. The chapter will report an analysis of the full-thermal approach to solar-to-electricity conversion along its historical development, showing advantages and technical problems solved and yet to be solved to achieve competitive efficiencies.

Readers interested in an introduction to photovoltaic generators will find a self-contained introduction to PV cell physics in Chap. 4. The chapter will focus on single-junction cells but will also provide essential information on multi-junction cells, dye-sensitized solar cells, and recent developments in the field of photovoltaics.

The book will then move to its core subject. Hybrid photovoltaic-thermoelectric generators will be discussed in Chaps. 5 and 6, which will be dedicated to the fundamentals of hybrid photovoltaic–thermoelectric harvesters and to materials issues and current applications of the hybrid technology. The two chapters will review and compare the strategies being considered to couple PV solar cells and thermoelectric generators to enhance the conversion rate of solar plants, discussing the contrasting requirements of PV and thermoelectric sections of hybrid harvesters. Triple co-generation, using photovoltaic and thermoelectric stages to generate electric power along with a thermodynamic third stage for hot water production will be the topic of Chap. 7. Triple co-generation solutions that have been developed and implemented will be described along with the advantages to electric power generation resulting from the enhanced heat dissipation provided by the thermodynamic stage.

Chapter 8 will summarize the topics covered by the book and will expand the topics drafted in this *Introduction* concerning the competitiveness of all solar harvesters *in se* and in comparison to renewable and non-renewable power sources. The

economic and technical benchmarks that have been introduced in this Chapter will be used to outline a preliminary discussion of the non-technological hurdles still to be overcome to bring hybrid harvesters to the market. This will be done by reviewing cost factors (scalability of initial costs, current and potential market size, initial costs of production facilities, etc.) along with foreseeable technology improvements, both for the PV-only cells and for full thermoelectric cells, hybrid generators, and photovoltaic-thermoelectric-thermodynamic co-generators. An outlook at the role that solar power generation will play over the next years will end the volume. It will also be the occasion to discuss the opportunities that the expected evolution of the energy market will open to all harvesters, and the demands they generate to materials science.

References

1. C.S. Mattick, E. Williams, B.R. Allenby, IEEE Tech. Soc. Mag. **29**(3), 22 (2010)
2. D.W. Jorgenson, Energy J. **5**(3), 11 (1984). <http://www.jstor.org/stable/41321692>
3. R.L. Hirsch, R. Bezdek, R. Wendling, Peaking of world oil production: Impacts, mitigation, and risk management. Technical Report, (U.S. Department of Energy, Washington D.C., 2005)
4. International Energy Agency, www.iea.org/statistics
5. J. Graham, J. Malone, The global nuclear fuel market: Supply and demand 2007–2030. Technical Report (World Nuclear Association, London, 2007), p. 112
6. OECD, Nuclear Energy Agency and the International Atomic Energy Agency, Uranium 2009: Resources, production and demand. Technical Report (OECD Nuclear Energy Agency and the International Atomic Energy Agency, 2010)
7. U.S. Energy Information Administration, www.eia.gov/beta/international/data/browser
8. International Atomic Energy Agency, www.iaea.org/PRIS/WorldStatistics/WorldTrendinElectricalProduction.aspx
9. International Energy Agency, Key world energy statistics 2015. Technical Report (International Energy Agency, 2015)
10. A.E. Becquerel, Compte Rend. Acad. Sci. **9**, 561 (1839)
11. D.M. Chapin, C.S. Fuller, G.L. Pearson, J. Appl. Phys. **25**(5), 676 (1954)
12. A. Goetzberger, C. Hebling, H.W. Schock, Mater. Sci. Eng. R Rep. **40**(1), 1 (2003)
13. T. Saitoh, A. Rohatgi, I. Yamasaki, T. Nunoi, H. Sawai, H. Ohtsuka, Y. Yazawa, T. Warabisako, J. Zhao, M. Green, X. Wang, H. Hashigami, T. Abe, T. Igarashi, S. Glunz, W. Wetling, A. Ebong, B. Damiani, in *Technical Digest of the 11th International Photovoltaic Science and Engineering Conference*, (1999), pp. 553–556
14. J. Zhao, A. Wang, M. Green, Prog. Photovolt. Res. Appl. **7**(6), 471 (1999)
15. S. Glunz, J. Lee, S. Rein, in *Conference Record of the IEEE Photovoltaic Specialists Conference* (2000), pp. 201–204
16. B. Sopori, X. Deng, J. Benner, A. Rohatgi, P. Sana, S. Estreicher, Y. Park, M. Roberson, Sol. Energy Mater. Sol. Cells **41–42**, 159 (1996)
17. S. Pizzini, M. Acciarri, S. Binetti, D. Cavalcoli, A. Cavallini, D. Chrastina, L. Colombo, E. Grilli, G. Isella, M. Lancin, A. Le Donne, A. Mattoni, K. Peter, B. Pichaud, E. Poliani, M. Rossi, S. Sanguinetti, M. Texier, H. von Kaenel, Mater. Sci. Eng. B Solid-State Mater. Adv. Tech. **134**(2–3), 118 (2006)
18. D. Staebler, C. Wronski, Appl. Phys. Lett. **31**(4), 292 (1977)
19. R. Miles, G. Zoppi, I. Forbes, Mater. Today **10**(11), 20 (2007). [https://doi.org/10.1016/S1369-7021\(07\)70275-4](https://doi.org/10.1016/S1369-7021(07)70275-4). <https://www.scopus.com/inward/record.uri?eid=2-s2.0-35148818407&doi=10.1016%2fS1369-7021%2807%2970275-4&partnerID=40&md5=8bdd892698518564e17dbe40fc82f6a>

20. M. Suryawanshi, G. Agawane, S. Bhosale, S. Shin, P. Patil, J. Kim, A. Moholkar, Mater. Tech. **28**(1–2), 98 (2013). <https://doi.org/10.1179/1753555712Y.0000000038>. <https://www.scopus.com/inward/record.uri?eid=2-s2.0-84868089322&doi=10.1179%2f1753555712Y.0000000038&partnerID=40&md5=37b04f4069456de3da4d2937e76777bf>
21. P. Meyers, S. Albright, Prog. Photovolt. Res. Appl. **8**(1), 161 (2000)
22. National Renewable Energy Laboratory, <http://www.nrel.gov/pv/>
23. C.H. Sun, P. Jiang, B. Jiang, Appl. Phys. Lett. **92**(6) (2008)

Chapter 2

A Primer on Thermoelectric Generators



Abstract This chapter is devoted to an analysis of the physics behind the conversion efficiency of thermoelectric generators. After recalling the basic theory of linear irreversible thermodynamics of thermoelectricity, we will focus on the materials and device factors ruling the conversion efficiency of thermoelectric generators. Moving from the well-known Ioffe–Altenkirch formula, the efficiency in the constant-property limit will be comparatively analyzed under Dirichlet and Neumann boundary conditions. Efficiency will be then reconsidered when large temperature differences are applied, using both Snyder’s concept of compatibility and Ren’s engineering figure of merit. Perfect thermoelectric generators as instances of exo- and endo-reversible engines will also be briefly reviewed along with the yet widely unsolved problem of thermoelectric efficiency under transient conditions.

2.1 Introduction

Thermoelectric effects are an age-old set of physical phenomena correlating heat flows (thermal current densities) and electrical current densities to temperature and electric fields. It is nowadays quite well assessed that the first observation of the insurgence of voltages due to temperature differences across a metal was reported by Alessandro Volta (1745–1827) in 1794. The same phenomenon was rediscovered independently by Thomas Johann Seebeck (1770–1831) in 1821, who observed the magnetic effect of a current circulating through a metal chain when its ends were kept at different temperatures. Seebeck suggested however to explain the phenomenon as resulting from a magnetothermal effect. It was Hans Christian Ørsted (1777–1851) who in 1825 provided the correct interpretation of the observed current, relating it to a charge flow in the conductor induced by the temperature gradient. The reverse effect, namely the induction of a thermal current flowing through a conductor from its cold to its hot side as a result of the application of an electrical current, was instead fully assessed by Jean Charles Athanase Peltier (1785–1845) in 1834.

Further to their phenomenology, thermoelectric effects are more properly described as a subset of a larger group of physical phenomena occurring under steady-state conditions in thermodynamic systems kept out of equilibrium by a

suitable thermodynamic force. Framing thermoelectricity within non-equilibrium thermodynamics not only enables a more consistent description of the phenomena but also enables a more complete description of the correlation between Seebeck and Peltier effects, along with other thermoelectric effects (Thomson and Bridgman effects)—both in the linear and non-linear regimes.

This chapter will provide a primer on thermoelectricity. We will closely follow a thermodynamic approach, limiting our analysis to the linear regime. Since a number of excellent books [1–5] and reviews [6–13] are available on the physics of thermoelectricity, this chapter will not give a general analysis of thermoelectric materials and phenomena but will be mostly focused on the specific issue of the efficiency of thermoelectric devices, acting either as thermal engines (Seebeck generators partially converting heat currents into electric power) or as refrigerators (Peltier coolers). After a general introduction to thermoelectric phenomena seen from the viewpoint of non-equilibrium thermodynamics (Sect. 2.2), non-equilibrium thermodynamics will be used to compute the efficiency of a thermoelectric engine. Section 2.3 will lead to the evaluation of the thermodynamic efficiency in the so-called constant-property model, both under Dirichlet and Neumann boundary conditions. This will lead to the introduction of a key parameter for the evaluation of a material and device efficiency, namely the *thermoelectric figure of merit*. The constant-property approximation will be relaxed in Sect. 2.4, where the concept of *compatibility* will be introduced.

As for any endoreversible engine, also thermoelectric engines optimize the conversion efficiency in the zero-power limit. Extension to estimate the finite-time efficiency will be discussed in Sect. 2.5, while a discussion of the non-steady state efficiency will be reported in Sect. 2.6. A summary of the main conclusions reached in the chapter will be provided in Sect. 2.7.

2.2 Fundamentals of Thermodynamics of Thermoelectricity

This Section aims at recalling a few fundamental topics in the thermodynamic analysis of thermoelectric phenomena. For a far more complete account on this subject the reader may refer to the classical review paper by Domenicali [6].

2.2.1 Thermoelectricity in Linear Thermodynamics

The modern theory of thermoelectricity is strongly indebted to the theory of thermodynamic phenomena out of equilibrium as developed mostly by Lars Onsager (1903–1976) and Sybren Ruurds De Groot (1916–1994). In non-equilibrium thermodynamics two thermodynamic field variables are introduced, namely *thermodynamic forces*, acting as the driving force of a non-equilibrium process, and *thermodynamic*

fluxes, which are the system response to the acting driving forces. Both forces and fluxes are in general function of the position in the system.

Let us consider an open system, i.e. a thermodynamic system capable of exchanging particles and energy with the ambient. This implies that both a particle and an energy flux may occur through the system and at system boundaries. Let \mathbf{j}_q be the heat current density (W/m^2) flowing through the system boundaries, while let \mathbf{j}_N be the corresponding particle flux ($\text{m}^{-2}\text{s}^{-1}$). Note that the two fluxes are independent of each other. An entropy current density may be also defined as

$$\mathbf{j}_S \equiv \frac{\mathbf{j}_q}{T} \quad (2.1)$$

while, assuming that only electrons (holes) may flow through the system, the overall energy current density reads

$$\mathbf{j}_E = \mathbf{j}_q + \tilde{\mu}_e \mathbf{j}_N \quad (2.2)$$

where $\tilde{\mu}_e$ is the electron electrochemical potential. Extension to other charged particles (e.g. ions) is trivial but will not be considered here for the sake of conciseness. As expected, the energy flux encompasses both the energy transported by particles and the heat exchange with the ambient.

In the presence of a temperature gradient and/or of an electrochemical potential gradient, two thermodynamic forces are therefore active, namely

$$\mathbf{F}_N = \nabla \left(-\frac{\tilde{\mu}_e}{T} \right) \quad (2.3)$$

and

$$\mathbf{F}_E = \nabla \left(\frac{1}{T} \right) \quad (2.4)$$

Thus, in the linear limit it follows that

$$\begin{bmatrix} \mathbf{j}_N \\ \mathbf{j}_E \end{bmatrix} = \mathcal{L}' \begin{bmatrix} \nabla \left(-\frac{\tilde{\mu}_e}{T} \right) \\ \nabla \left(\frac{1}{T} \right) \end{bmatrix} \quad (2.5)$$

that may be rewritten in view of (2.2) as

$$\begin{bmatrix} \mathbf{j}_N \\ \mathbf{j}_q \end{bmatrix} = \mathcal{L} \begin{bmatrix} -\frac{1}{T} \nabla \tilde{\mu}_e \\ \nabla \left(\frac{1}{T} \right) \end{bmatrix} \quad (2.6)$$

Both \mathbf{L}' and \mathbf{L} are 2×2 matrices encompassing the so-called *phenomenological coefficients* linearly correlating forces and fluxes. Limiting to isotropic systems, each element of \mathbf{L}' and \mathbf{L} is a scalar. Extension to anisotropic systems is formally simple, leading to tensorial matrix elements [14].

Insights in the physical meaning of \mathbf{L} elements may be achieved by decoupling forces and fluxes.

In an isothermal system ($\nabla(1/T) \equiv \mathbf{0}$) (2.6) reads

$$\mathbf{j} = e\mathbf{j}_N = -\frac{e\mathbf{L}_{11}}{T}\nabla\tilde{\mu}_e \quad (2.7)$$

where \mathbf{j} is the charge current density. Since $\tilde{\mu}_e = \mu_e + e\mathcal{V}$ (where \mathcal{V} potential), then $-(\nabla\tilde{\mu}_e)/e = -\nabla\mathcal{V} = \mathcal{E}$, where \mathcal{E} is the electric field. Thus, one easily gets that

$$\mathbf{j} = \sigma_T \mathcal{E} \quad (2.8)$$

with the isothermal electric conductivity $\sigma_T = e^2\mathbf{L}_{11}/T$. Therefore,

$$\mathbf{L}_{11} = \frac{\sigma_T T}{e^2}. \quad (2.9)$$

Equation (2.6) may be alternately solved when no electric current may flow, namely $\mathbf{j} = \mathbf{j}_N = \mathbf{0}$. In such an (electric) open-circuit (oc) scenario, it is immediate to write

$$\mathbf{j}_{q\text{ oc}} = \frac{1}{T^2} \left(\frac{\mathbf{L}_{21}\mathbf{L}_{12} - \mathbf{L}_{11}\mathbf{L}_{22}}{\mathbf{L}_{11}} \right) \nabla T \quad (2.10)$$

so that, in view of Fourier law, the open-circuit thermal conductivity κ_{oc} reads

$$\kappa_{\text{oc}} = \frac{1}{T^2} \left(\frac{\mathbf{L}_{21}\mathbf{L}_{12} - \mathbf{L}_{11}\mathbf{L}_{22}}{\mathbf{L}_{11}} \right) \quad (2.11)$$

Should instead the electric circuit be closed (cc), a heat current sets up under the alternate constraint $\nabla\tilde{\mu} = \mathbf{0}$ (namely, no electric field may be sustained through the system). The heat current reads then

$$\mathbf{j}_{q\text{ cc}} = \frac{\mathbf{L}_{22}}{T^2} \nabla T \quad (2.12)$$

that leads to the closed-circuit thermal conductivity κ_{cc} :

$$\kappa_{\text{cc}} = \frac{\mathbf{L}_{22}}{T^2} \quad (2.13)$$

Moving to coupled fluxes and forces, let us consider once again an open-circuit configuration (namely $\mathbf{j} \equiv \mathbf{0}$). Thus, (2.6) reads

$$-\mathsf{L}_{11} \frac{\nabla \tilde{\mu}_e}{T} + \mathsf{L}_{12} \nabla \left(\frac{1}{T} \right) = \mathbf{0} \quad (2.14)$$

Thus one may define the Seebeck coefficient α as

$$-\frac{1}{e} \nabla \tilde{\mu}_e \equiv \alpha \nabla T \quad (2.15)$$

or, equivalently, as

$$\alpha \nabla T = \mathcal{E}_{oc} \quad (2.16)$$

Thus

$$\alpha = \frac{1}{eT} \frac{\mathsf{L}_{12}}{\mathsf{L}_{11}} \quad (2.17)$$

so that

$$\mathsf{L}_{12} = \frac{\alpha \sigma_T T^2}{e} \quad (2.18)$$

Instead, closing the circuit but setting isothermal conditions one may write

$$\mathbf{j} = \frac{e \mathsf{L}_{11}}{T} \nabla \tilde{\mu}_e \quad (2.19)$$

and

$$\mathbf{j}_q = -\frac{\mathsf{L}_{21}}{T} \nabla \tilde{\mu}_e \quad (2.20)$$

so that

$$\mathbf{j}_q = \frac{\mathsf{L}_{12}}{e \mathsf{L}_{11}} \mathbf{j} \quad (2.21)$$

This returns the Peltier coefficient Π , defined as $\mathbf{j}_q \equiv \Pi \mathbf{j}$:

$$\Pi = \frac{\mathsf{L}_{12}}{e \mathsf{L}_{11}} \quad (2.22)$$

Note that as a direct consequence of Onsager's relations, in view of (2.15)

$$\Pi = \alpha T \quad (2.23)$$

Therefore, in summary

$$\mathbf{j} = e\mathbf{j}_N = \sigma_T \mathcal{E} - \alpha \sigma_T \nabla T \quad (2.24)$$

$$\mathbf{j}_q = \alpha \sigma_T T \mathcal{E} - \kappa_{cc} \nabla T \quad (2.25)$$

The Seebeck coefficient admits a remarkably strong physical interpretation. Using (2.1) and (2.6) one may write the entropy current as

$$\mathbf{j}_s = \frac{\mathbf{L}_{21}}{eT\mathbf{L}_{11}} \mathbf{j} + \frac{\mathbf{L}_{22}}{T} \nabla \left(\frac{1}{T} \right) \quad (2.26)$$

The equation shows how the entropy current is made of two terms: while the second term is the standard thermal component of \mathbf{j}_s , the first one accounts instead for the entropy current associated to the particle flux. More explicitly, the particle-borne entropy current $\mathbf{L}_{21}/(T\mathbf{L}_{11})\mathbf{j}_N$ leads to compute an entropy contribution per particle of $\mathbf{L}_{21}/(T\mathbf{L}_{11}) = \alpha$. Thus,

$$\mathbf{j}_s = \alpha \mathbf{j} - \frac{\kappa_{cc} \nabla T}{T} \quad (2.27)$$

Therefore, the Seebeck coefficient may be interpreted as the (average) contribution of carriers to the entropy current.

As an additional result of our analysis, closed- and open-circuit thermal conductivities (2.11) and (2.13) may be correlated to each other through α and σ_T as

$$\kappa_{cc} - \kappa_{oc} = T \alpha^2 \sigma_T \quad (2.28)$$

Note that if the overall thermal conductivity of a medium is set also by non-charged energy carriers (NCC – e.g. phonons) and since for such particles both α and σ_T are obviously zero, the same relationship holds true when replacing each thermal conductivity with the relevant total thermal conductivity $\kappa_{oc|cc}^{\text{tot}} = \kappa_{oc|cc} + \kappa_{NCC}$.

A first glance at the conditions that have to be fulfilled to optimize the conversion rate in a thermoelectric generator may be now attained. If one considers a thermoelectric generator as a thermal engine, it is intuitive that the largest conversion rate will be achieved when the heat flowing from the hot to the cold sink is maximized, while the temperature difference across the engine is kept as large as possible. These two seemingly contrasting requirements implies that κ_{cc} , ruling the heat flow, should be as large as possible while κ_{oc} should be minimized. Therefore, κ_{cc}/κ_{oc} should be maximized. Comparing (2.11) and (2.13) one gets that

$$\frac{\kappa_{cc}}{\kappa_{oc}} = 1 + \frac{\alpha^2 \sigma_T}{\kappa_{oc}} T \quad (2.29)$$

This introduces quite naturally the so-called *thermoelectric figure of merit* zT , where

$$z \equiv \frac{\alpha^2 \sigma_T}{\kappa_{oc}} \quad (2.30)$$

Note that the thermal conductivity appearing in the denominator is the open-circuit ($\mathbf{j} = \mathbf{0}$) thermal conductivity.

2.2.2 Thomson Effect

A rigorous application of linear thermodynamics deals with phenomenological coefficients as constant quantities. Nonetheless, both the electrical conductivity, the Seebeck coefficient, and the Peltier coefficient depend on the temperature. Specifically, for the Seebeck coefficient one defines for its temperature coefficient a quantity named Thomson coefficient τ [6]:

$$\tau = T \frac{d\alpha}{dT} \quad (2.31)$$

Manifestly enough, the Thomson coefficient is also temperature dependent.

The Thomson coefficient may be alternately (and equivalently) introduced considering the heat exchanged when an electric current passes through a circuit composed of a single material that has a temperature difference along its length. In addition to the Joule heat, a Peltier heat is exchanged as a result of the non-zero Seebeck coefficient of the materials itself (Thomson effect).

Thomson effect and τ will be relevant in the analysis of thermoelectric generation in the presence of large temperature differences.

2.3 Thermoelectric Efficiency in the Constant-Property Limit

The first evaluation of efficiency of a thermoelectric generator (TEG) under Dirichlet boundary conditions (fixed heat sink temperatures) is due to Altenkirch [15] although it was restated and rewritten in a more rigorous and general way by Ioffe in his famous book *Semiconductor Thermoelements and Thermoelectric Cooling* [16]. In this Section we will demonstrate this formula using two different paths, namely that originally purported by Altenkirch and Ioffe and one avoiding any assumption on the actual geometry of the TEG. Finally, the thermoelectric efficiency will be computed in a differential form.

Also, the corresponding formula under Neumann boundary conditions (fixed heat flow) will be obtained.

Under both kinds of boundary conditions, in this Section it will be assumed that all transport coefficients are constant, namely that materials are homogeneous phases and that thermal and electric conductivities as well as the Seebeck coefficient are independent of the temperature. Manifestly enough, this makes all conclusions rigorously valid only when the temperature difference across the thermoelectric materials are vanishingly small. Actual application of the formula is therefore sensitive upon the actual temperature difference experienced by the active parts of the TEG. We will refer to this set of assumptions as constant-property limit (CPL).

2.3.1 Dirichlet Boundary Conditions

In general terms, a TEG is often (although not necessarily) made of pairs of *p* and *n*-type semiconductors connected to form a series electric circuit while being set in a thermal parallel circuit with respect to the two heat sinks (Fig. 2.1). For obvious reasons it is commonplace to refer to this configuration as a Π -configuration. Since each element nominally senses the same temperature difference $\Delta T_{\text{TEG}} \equiv T_{\text{H}} - T_{\text{C}}$, where T_{H} and T_{C} are the temperatures of the two heat sinks (with $T_{\text{H}} \geq T_{\text{C}}$), the thermovoltage developed by each element (often referred to as *leg*) sum to each other, leading to a total thermovoltage $\mathcal{V}_{\text{tot}} = N(|\alpha_n| + |\alpha_p|)\Delta T_{\text{TEG}}$ where N is the number of leg pairs.

The most widely used formula to assess the thermoelectric efficiency of a TEG assumes that the TEG operates between two heat sources with fixed temperatures. It is further assumed that the temperature of each sink equals the temperature of the relevant end of each leg. This implicitly assumes that no thermal contact resistance occurs at the sink-TEG interface and that any temperature drop due to electrically insulating but thermally conductive layers interposed between the sinks and the legs may be neglected. It is rather obvious that such assumptions are a strong oversimplification of the actual thermal chain, and more realistic analyses are needed even when the Dirichlet CPL (DCPL) model is a legitimate approximation. The reader may refer to the technical literature for more realistic DCPLs [1].

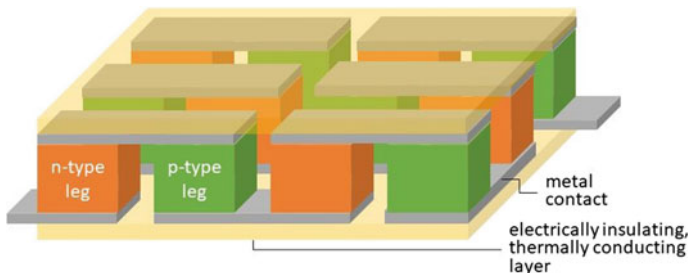


Fig. 2.1 Standard Π -type layout of a thermoelectric generator, setting a series *p-n* electric circuit in a parallel connection with the two heat sinks

2.3.1.1 Altenkirch–Ioffe Argument

Following Ioffe's argument [16], let us consider a two-leg circuit made of thermoelectric materials of length d and sections A_1 and A_2 (Fig. 2.2) operating between two heat sinks at T_H and T_C , with $T_H > T_C$: Let i be the circulating current, r_1 and r_2 the electrical resistances of the legs, k_1 and k_2 their thermal conductances, and R_L the load resistance. The heat balance at the hot and cold junctions accounts for a number of terms:

1. the heat current flowing through the legs by thermal conduction:

$$\dot{q}_c = (k_1 + k_2)\Delta T_{\text{TEG}} \quad (2.32)$$

2. the Peltier heating (cooling) due to the current flowing through the circuit

$$\begin{aligned} \dot{q}_H &= i\Pi_H = \alpha_H T_H i \\ \dot{q}_C &= i\Pi_C = \alpha_C T_C i \end{aligned} \quad (2.33)$$

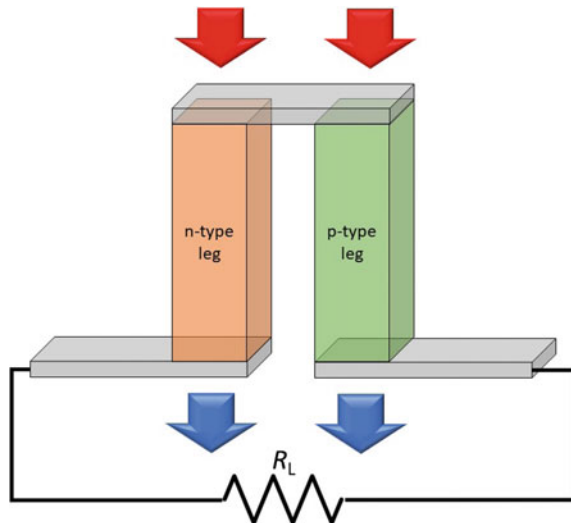
where the subscripts refer to the interface where Peltier heating (cooling) occurs;

3. the heat current generated by Joule effect:

$$\dot{q}_J = i^2(r_1 + r_2) \quad (2.34)$$

In the CPL $\alpha_1(T_C) = \alpha_1(T_H), \alpha_2(T_C) = \alpha_2(T_H)$. The electric power W generated by a single-pair circuit is simply given by $W = i^2 R_L$, where the current flowing through the circuit is controlled by the thermoelectric voltage $\mathcal{V}_{\text{tot}} = (|\alpha_1| + |\alpha_2|)\Delta T_{\text{TEG}}$.

Fig. 2.2 Schematics of a thermoelectric generator partially converting heat into electrical energy



Thus, defining $\alpha \equiv |\alpha_1| + |\alpha_2|$, $k \equiv k_1 + k_2$ and $r \equiv r_1 + r_2$, one may write $i = \mathcal{V}_{\text{tot}}/(R_L + r)$ so that

$$W = \left(\frac{\alpha \Delta T_{\text{TEG}}}{R_L + r} \right)^2 R_L \quad (2.35)$$

Thus

$$\phi \equiv \frac{W}{\dot{q}_H + \dot{q}_C - \frac{1}{2}\dot{q}_J} = \frac{T_H - T_C}{T_H} \frac{m/(m+1)}{1 + \frac{kr}{\alpha^2} \frac{m+1}{T_H} - \frac{1}{2} \frac{\Delta T}{T_H(m+1)}} \quad (2.36)$$

where $m \equiv R_L/r$. Note that the Joule heating has been taken as equally partitioned as two heat flows directed toward the two heat sinks. Note also that the input thermal current encompasses the Peltier heat generated by the circulating current through the thermoelectric material. Such a heat generates at the hot side of the thermoelement and it therefore adds up to the heat current density provided by the heat sink.

For ϕ to be an actual thermodynamic conversion efficiency it has to be optimized twice—so as to minimize the heat flow dissipated by direct thermal conduction and to maximize the electrical output. In the first respect, ϕ may be maximized by minimizing kr , that in turn implies an optimization over the leg cross-sections. Actually, writing kr in terms of material electrical resistivities ρ_1 , ρ_2 and thermal conductivities κ_1 , κ_2 , we get

$$\begin{aligned} kr &= (\kappa_1 A_1/d + \kappa_2 A_2/d)(\rho_1 d/A_1 + \rho_2 d/A_2) \\ &= (\kappa_1 \rho_1 + \kappa_2 \rho_2) + \kappa_1 \rho_2 (A_1/A_2) + \kappa_2 \rho_1 (A_2/A_1) \end{aligned} \quad (2.37)$$

Setting to zero its derivative with respect to A_1/A_2 one obtains

$$(A_1/A_2)^2 = (\rho_1/\kappa_1)/(\rho_2/\kappa_2) \quad (2.38)$$

so that

$$kr = \left(\sqrt{\kappa_1 \rho_1} + \sqrt{\kappa_2 \rho_2} \right)^2 \quad (2.39)$$

Inserting (2.39) into (2.36) one readily finds that

$$\tilde{\phi} = \eta_{\text{Carnot}} \frac{m/(m+1)}{1 + \frac{m+1}{Z T_H} - \frac{1}{2} \frac{\Delta T}{T_H(m+1)}} \quad (2.40)$$

where $\eta_{\text{Carnot}} = (T_H - T_C)/T_H$ and the figure of merit of the paired legs Z_{12} is defined as

$$Z_{12} \equiv \frac{\alpha^2}{kr} = \frac{\alpha^2}{\left(\sqrt{\kappa_1 \rho_1} + \sqrt{\kappa_2 \rho_2} \right)^2} \quad (2.41)$$

Note that (2.40) no longer depends on the device geometry, all parameters referring only to material properties. It is also customary to define a power factor PF:

$$\text{PF} \equiv \frac{\alpha^2}{\rho} \quad (2.42)$$

If $|\alpha_1| = |\alpha_2|$, $\rho_1 = \rho_2$, and $\kappa_1 = \kappa_2$, then Z_{12} equals the single-material figure of merit $z_i \equiv \alpha_i^2/(\rho_i \kappa_i)$ [cf. (2.30)], namely $Z_{12} = z_1 = z_2$. Otherwise no close form exists expressing Z_{12} as a function of z_1 and z_2 . Note also that this scheme of analysis does not allow to clearly set which thermal conductivity (either κ_{oc} or κ_{cc}) sets the figure of merit. A more general analysis will be required to this aim [cf. Sect. 2.3.1.2].

A second optimization of $\tilde{\phi}$ (over m) is needed to obtain the actual TE efficiency. As for any circuit, also in the case of a TEG the maximum output power is delivered when the load is matched to the generator, i.e. for $m = 1$. In the present case this leads to

$$\eta_w^{\text{DCPL}} = \eta_{\text{Carnot}} \frac{1/2}{1 + \frac{2}{Z_{12} T_H} - \frac{\Delta T_{\text{TEG}}}{4 T_H}} \quad (2.43)$$

Instead, by maximizing $\tilde{\phi}(m)$ one gets the largest possible conversion efficiency. It is straightforward to compute that $d\tilde{\phi}(m)/dm = 0$ leads to $m = \sqrt{1 + Z_{12}\bar{T}}$ (where $\bar{T} = (T_H + T_C)/2$) so that

$$\eta_{\text{eff}}^{\text{DCPL}} = \eta_{\text{Carnot}} \frac{\sqrt{1 + Z_{12}\bar{T}} - 1}{\sqrt{1 + Z_{12}\bar{T}} + T_C/T_H} \quad (2.44)$$

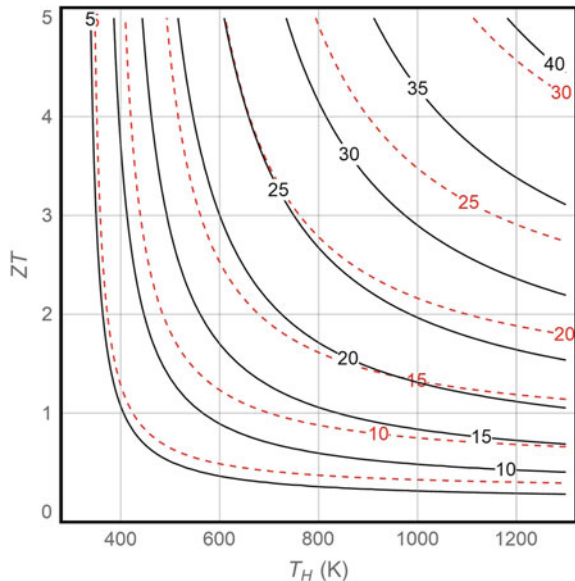
It is worthwhile to remark once again that the highest power output for a given TEG is obtained when $r = R$ with an efficiency $\eta_w^{\text{DCPL}} < \eta_{\text{eff}}^{\text{DCPL}}$ while the best conversion efficiency $\eta_{\text{eff}}^{\text{DCPL}}$ for a given heat current is reached for a load $R_L = r\sqrt{1 + Z_{12}\bar{T}}$. Figure 2.3 shows both DCPL efficiencies for a device operating between $T_C = 300$ K as a function of T_H for different Z values. As well known, $\eta_{\text{eff}}^{\text{DCPL}} \rightarrow \eta_{\text{Carnot}}$ for $Z_{12} \rightarrow \infty$. Also note that η_w^{DCPL} and $\eta_{\text{eff}}^{\text{DCPL}}$ significantly differ from each other only at high temperatures and for large Z_{12} values.

2.3.1.2 A More General Demonstration

The Altenkirch–Ioffe argument relies upon a number of assumptions on the geometry of the TEG. More substantially, thermal and electrical conductivities are not exactly identified to any of the transport coefficients (σ_T , κ_{oc} and κ_{cc}) introduced in Sect. 2.2. Thus, it may be convenient to demonstrate (2.43) and (2.44) also in a more general (and possibly rigorous) way [17, 18].

To this aim, we have to rearrange first (2.24) and (2.25). Replacing \mathcal{E} from (2.24) into (2.25) we obtain

Fig. 2.3 Thermoelectric efficiencies (%) computed at maximum conversion yield ((2.44), black solid lines) and at maximum power output ((2.43), red dashed lines) for devices operating between $T_C = 300\text{ K}$ and T_H for different ZT



$$\mathbf{j}_q = \alpha T \mathbf{j} + (\alpha^2 \sigma_T T - \kappa_{cc}) \nabla T \quad (2.45)$$

that, in view of (2.28), reads

$$\mathbf{j}_q = \alpha T \mathbf{j} - \kappa_{oc} \nabla T \quad (2.46)$$

Let us now consider (without loss of generality) a single leg of a thermoelectric phase. Using (2.1) and (2.46), the total energy current density (2.2) reads

$$\mathbf{j}_E = \mathbf{j}_q + \tilde{\mu}_e \frac{\mathbf{j}}{e} = (\alpha T \mathbf{j} - \kappa_{oc} \nabla T) + \tilde{\mu}_e \frac{\mathbf{j}}{e} \quad (2.47)$$

Taking the divergence, energy conservation imposes $\nabla \cdot \mathbf{j}_E = 0$ so that

$$\mathbf{j} \cdot (\alpha \nabla T + T \nabla \alpha) - \nabla(\kappa_{oc} \nabla T) + \frac{\mathbf{j}}{e} \nabla \tilde{\mu}_e = 0 \quad (2.48)$$

Thus, in view of (2.6), (2.9) and (2.18) one may write

$$\mathbf{j}_N = -\frac{\sigma}{e^2} \nabla \tilde{\mu}_e - \frac{\alpha \sigma_T}{e} \nabla T \quad (2.49)$$

that returns

$$\nabla \tilde{\mu}_e = -\frac{e}{\sigma} \mathbf{j} - \alpha e \nabla T \quad (2.50)$$

Replacing it into (2.48) and simplifying, one gets

$$T \mathbf{j} \cdot \nabla \alpha - \nabla(\kappa_{oc} \nabla T) - \frac{\mathbf{j} \cdot \mathbf{j}}{\sigma_T} = 0 \quad (2.51)$$

which is the stationary form of the Domenicali equation [17].

In the CPL $\nabla \alpha = \nabla \kappa_{oc} = \mathbf{0}$ so that

$$\frac{\mathbf{j} \cdot \mathbf{j}}{\sigma_T} = -\kappa_{oc} \nabla^2 T \quad (2.52)$$

In a one-dimensional conductor aligned along the x -axis it reduces to

$$T''(x) = -\frac{j^2}{\sigma_T \kappa_{oc}} \quad (2.53)$$

Since all terms but T are independent of x , it is immediate to compute that

$$T(x) = -\frac{1}{2} \frac{j^2 \ell^2}{\sigma_T \kappa_{oc}} \left(\frac{x^2}{\ell^2} - \frac{x}{\ell} \right) - \Delta T_{TEG} \frac{x}{\ell} + T_H \quad (2.54)$$

where ℓ is the length of the conductor and the hot and cold heat sinks are at $x = 0$ and $x = \ell$, respectively.

The electric power flow j_w generated by the thermoelectric element computes to

$$j_w = - \int_0^\ell j \mathcal{E}(x) dx \quad (2.55)$$

where the electric field follows from (2.24):

$$\mathcal{E}(x) = \frac{j}{\sigma_T} + \alpha T'(x) \quad (2.56)$$

Thus, the electric power density reads

$$j_w = -\frac{j^2}{\sigma_T} \ell + j \alpha \Delta T_{TEG} \quad (2.57)$$

Correspondingly, (2.46) provides the heat current density. In one dimension

$$j_q(x) = -\kappa_{oc} T'(x) + \alpha j T(x) \quad (2.58)$$

The heat injected at the hot side is then

$$j_q|_{x=0} = \kappa_{oc} \frac{\Delta T_{TEG}}{\ell} - \frac{1}{2} \frac{j^2 \ell}{\sigma_T} + \alpha j T_H \quad (2.59)$$

The efficiency may be then immediately written as a function of the charge current density:

$$\phi_{DCPL}(j) = \frac{j_w}{j_q(j)|_{x=0}} = \frac{j \alpha \Delta T_{TEG} - (j^2 \ell / \sigma_T)}{(\kappa_{oc} \Delta T_{TEG} / \ell) - \frac{1}{2} (j^2 \ell / \sigma_T) + \alpha j T_H} \quad (2.60)$$

It is interesting to compare (2.60)–(2.36). The comparison helps recognize that also in (2.60) three terms show up in the expression of the adsorbed heat, namely the heat transmitted by thermal conduction ($\kappa_{oc} \Delta T_{TEG} / \ell$), the Peltier heat current at the hot side ($\alpha j T_H$) and half of the Joule heat generated by the circulating charge current ($j^2 \ell / \sigma_T$). The electric power flow at the numerator shows instead that the non-zero circulating current leads to a reduction of the available output power density with respect to the thermoelectric power density $j(\alpha \Delta T_{TEG})$ by the Joule effect $j^2 \ell / \sigma_T$.

One may proceed to optimize either the efficiency $\phi_{DCPL}(j)$ or the power flow $j_w(j)$ with respect to j . In the former case, setting $d j_w(j) / d j = 0$, the current computes to

$$j_{\max w} = \frac{\alpha^2 \sigma_T \Delta T_{TEG}^2}{4\ell} \quad (2.61)$$

and

$$\eta_w^{DCPL} \equiv \phi(j_{\max w}) = \frac{2z \Delta T_{TEG}}{8 + z(4T_H - \Delta T_{TEG})} \quad (2.62)$$

(where $z = \sigma_T \alpha^2 / \kappa_{oc}$) that, with a little of algebra, returns

$$\eta_w^{DCPL} = \eta_{Carnot} \frac{1/2}{1 + \frac{2}{z T_H} - \frac{\Delta T_{TEG}}{4 T_H}} \quad (2.63)$$

Instead, optimization of the efficiency $\phi(j)$ leads to a current density

$$j_{\max \eta} = \frac{\sigma_T \alpha \Delta T_{TEG}}{\ell z \bar{T}} (\sqrt{1 + z \bar{T}} - 1) \quad (2.64)$$

while the maximum efficiency computes to

$$\eta_{\max}^{DCPL} = \frac{\Delta T_{TEG}}{T_H} \frac{\sqrt{1 + z \bar{T}} - 1}{\sqrt{1 + z \bar{T}} + T_C / T_H} \quad (2.65)$$

Note that both optimal efficiencies are defined with reference to the open-circuit thermal conductivity and to the isothermal electrical conductivity. Furthermore, properly matched electric loads R_L have to be obtained by invoking the maximum power transfer theorem [19].

2.3.1.3 Differential Efficiency

While the constant property hypothesis is clearly an approximation over a finite temperature difference, (2.65) and (2.62) are *exact* for $\Delta T_{\text{TEG}} \rightarrow 0$. Infinitesimal (local) efficiencies are obtained, namely

$$\delta\eta_w^{\text{DCPL}} = \frac{z dT}{4 + 2zT} \quad (2.66)$$

and

$$\delta\eta_{\max}^{\text{DCPL}} = \frac{dT}{T} \frac{\sqrt{1+zT} - 1}{\sqrt{1+zT} + 1} \quad (2.67)$$

This result will be of use when considering TEGs operating over large temperature differences (Sect. 2.4).

2.3.2 Neumann Boundary Conditions

Quite often thermoelectric generators do not operate between two heat sinks at fixed temperature. Instead, a thermostat injects heat while a heat exchanger sets the heat flow released at the cold side—so that Neumann boundary conditions are to be used to model the TEG.

2.3.2.1 Castro–Happ Argument

TEGs operating under constant heat flow absorbed at the hot sink have received much less attention in the literature. Possibly the first paper targeting the analysis of such a configuration was that by Castro and Happ [20]. They analyzed the efficiency under Neumann conditions using a scheme strongly reminiscent of that adopted by Altenkirch and Ioffe for TEGs operating under Dirichlet boundary conditions. Taking a standard Π -type layout (Fig. 2.1), the thermal power (heat current) injected at the hot junction Φ_{tot} is written as in the Altenkirch-Ioffe analysis as $\Phi_{\text{tot}} = \Phi_c + \Phi_H - \Phi_J/2$, namely

$$\Phi_{\text{tot}} = \left(\frac{\kappa_1 A_1}{\ell} + \frac{\kappa_1 A_1}{\ell} \right) \Delta T_{\text{TEG}} + i\alpha T_H - \frac{1}{2} i^2 r \quad (2.68)$$

where i is the electric current and all other terms are as defined in (2.32), (2.33) and (2.34). The electric power output is then $w = i^2 R_L$ with $i = \alpha \Delta T_{\text{TEG}} / (R_L + r)$. Thus, replacing for i in (2.32)–(2.34) one obtains

$$\Phi_{\text{tot}} = w \frac{2m+1}{2m} + (w/R_L)^{1/2} \left(\frac{\alpha(1+m)}{\tilde{z}} + \alpha T_H \right) \quad (2.69)$$

where m is still r/R_L and

$$\tilde{z} = \frac{\alpha^2}{r(\kappa_1 A_1/d + \kappa_2 A_2/d)} \quad (2.70)$$

Equation (2.69) provides the input thermal power density as a function of the output electric power density w and then may be directly used to maximize the conversion ratio W/Φ_{tot} .

For any given set of values of Φ_{tot} and of transport parameters, Φ_{tot} is clearly minimized by maximizing \tilde{z} over the device geometry by setting $d\tilde{z}/d(A_1/A_2) = 0$. This leads to $A_1/A_2 = \sqrt{(\kappa_2 \sigma_2)/(\kappa_1 \sigma_1)}$ and thus to $\tilde{z} = Z_{12}$. In the maximum of \tilde{z} the minimum input heat current is then

$$\Phi_{\text{tot}} = w \frac{2m+1}{2m} + \frac{\alpha}{Z_{12}} (w/R_L)^{1/2} (m + ZT_C + 1) \quad (2.71)$$

One may now optimize the electric power output by setting $dw/dR_L = 0$. Since only m and w depend on R_L , the optimum m is the root of

$$m^{3/2} - (Z_{12}T_C + 1)m^{1/2} - \frac{Z_{12}}{\alpha}(Wr)^{1/2} = 0 \quad (2.72)$$

Since however w is usually unknown, it may be more convenient to recast the previous equation by replacing w from (2.71), obtaining

$$(m - Z_{12}T_C - 1)(2m^2 + (1 - 2Z_{12}T_C)m + (Z_{12}T_C + 1)) - \frac{2Z_{12}^2}{\alpha^2}(\Phi_{\text{tot}}r) = 0 \quad (2.73)$$

The maximum efficiency follows immediately:

$$\eta_{\text{NCPL}} = \max \frac{w}{\dot{q}_{\text{tot}}} = \frac{2\bar{M}(\bar{M} - Z_{12}T_H - 1)}{2\bar{M}^2 + (1 - 2Z_{12}T_H)\bar{M} + (1 + Z_{12}T_H)} \quad (2.74)$$

where \bar{M} is the root of (2.73). The electric matching load is obviously $R_L = r\bar{M}$. Note that, differently from the Dirichlet case, here the maximum efficiency coincides with the efficiency at maximum power output, so that only one optimum efficiency needs to be computed.

Equation (2.74) may be rewritten as a function of the hot side temperature. Since

$$Z_{12}\Delta T_{\text{TEG}} = (\bar{M} + 1)(\bar{M} - Z_{12}T_{\text{C}} - 1) \quad (2.75)$$

solving (2.73) for T_{C} and replacing it in (2.75) one obtains

$$T_{\text{H}} = \frac{1 - 3\bar{M} + \bar{M}\sqrt{4\bar{M}^2 + (2\bar{M} - 1)YZ_{12}}}{Z_{12}(2\bar{M} - 1)} \quad (2.76)$$

where we introduced $Y \equiv 2\frac{\Phi_{\text{tot}}\ell}{\kappa}$ (in K). Its solution provides $\bar{M} = \bar{M}(T_{\text{H}}, Y, Z_{12})$. Efficiency finally reads

$$\eta_{\text{NCPL}} = \frac{2\bar{M}YZ_{12}}{8\bar{M}^2 + (2\bar{M} - 1)YZ_{12} + 4\bar{M}\sqrt{4\bar{M}^2 + (2\bar{M} - 1)YZ_{12}}} \quad (2.77)$$

As will be discussed in more details in Sect. 2.5, the Castro–Happ engine at maximum efficiency operates as an exoreversible engine, wherein irreversibility arises only within the engine due to the finite thermal resistance of the engine itself. No contact thermal resistance is considered. This makes the analysis less general and, possibly, more idealized than it could be, since thermal contact resistances, further to be unavoidable, play a significant role to set TEG efficiency. Nonetheless, Castro–Happ model reports that the power output depends (through \bar{M} – and through η_{NCPL} thereof) not only on the physical boundary conditions of the problem (hot side temperature and input thermal power Φ_{tot}) and on Z_{12} but also, *and independently*, on Y , namely on κ and ℓ . While ℓ is often constrained by practical reasons, κ provides an additional handle that may be used to maximize the efficiency in a Neumann problem – a handle apparently unavailable in its Dirichlet analog. Figure 2.4 displays the efficiency as a function of the hot source temperature and of Y for different values of Z_{12} . It is remarkable, and possibly somewhat overlooked, how the same efficiency may be reached for any given T_{H} by increasing either Z_{12} or Y values.

2.3.2.2 Yazawa–Shakouri Argument

The full complexity of the Neumann problem, namely that of optimizing the efficiency of a TEG operating with thermal contact resistances and with inner non-zero electrical and thermal resistances, was more recently analyzed by Yazawa and Shakouri [21]. The analysis was carried out considering a single-leg thermoelectric element of length ℓ and figure of merit Z in a double (thermal and electrical) paired equivalent circuit (Fig. 2.5). Power output density is easily found to be

$$w = \frac{m\sigma\alpha^2}{(1+m)^2\ell}(T_{\text{H}} - T_{\text{C}})^2 \quad (2.78)$$

Fig. 2.4 Contour plot of Castro–Happ efficiency (%) as a function of the hot source temperature and of $Y \equiv 2\Phi_{\text{tot}}\ell/\kappa$. Black, blue, and red lines refer to $Z_{12}\bar{T} = 0.5, 1$, and 2 for $\bar{T} = 300\text{ K}$

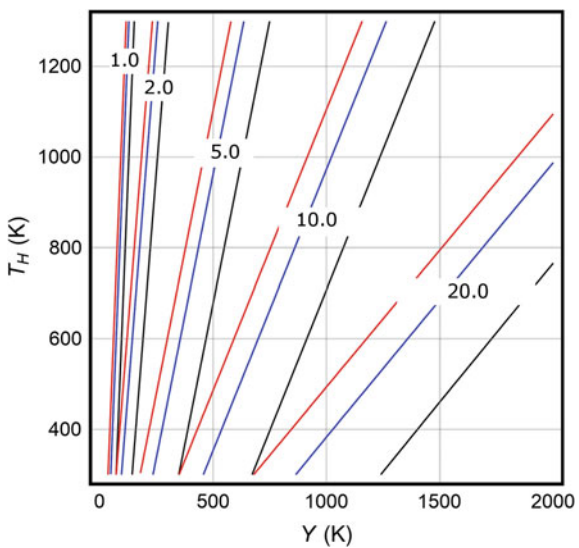
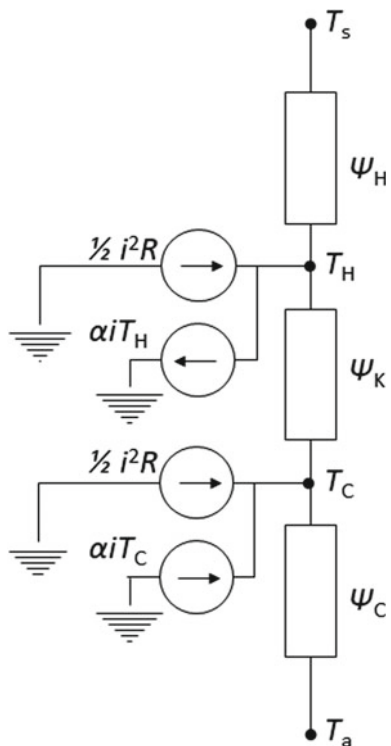


Fig. 2.5 Equivalent circuit modeling a one-leg thermoelectric element converting heat into electrical power. Note that both internal and external thermal resistances are accounted for. Adapted from [21]



where all symbols are as previously defined and T_H and T_h refer to the end leg temperatures, namely $T_a < T_c < T_H < T_s$ where T_a and T_s are respectively the cold and hot sink temperatures. Temperatures relate to each other as

$$\frac{T_H - T_C}{T_s - T_a} = \frac{\ell}{\ell + \kappa(\Psi_X + \Psi_Y)} \quad (2.79)$$

where

$$\begin{aligned} \frac{\Psi_X}{\Psi_H} &= 1 + \frac{Z}{2(1+m)^2} ((2m+1)T_H + T_C) \\ \frac{\Psi_Y}{\Psi_C} &= 1 + \frac{Z}{2(1+m)^2} ((2m+1)T_C + T_H) \end{aligned} \quad (2.80)$$

and Ψ_H and Ψ_C are the contact thermal resistances at the hot and cold sides, respectively. Using energy balance, T_H and T_C may be obtained in view of the relations

$$\begin{aligned} \frac{\kappa}{\ell} \Psi_X (T_H - T_C) - (T_s - T_H) &= 0 \\ \frac{\kappa}{\ell} \Psi_Y (T_H - T_C) - (T_C - T_a) &= 0 \end{aligned} \quad (2.81)$$

Equations do not admit an analytically closed solution so that maximization was pursued by using the Lagrange multiplier method and numerical techniques. An optimal leg length $\bar{\ell}$ was shown to exist that for $\Psi_H = \Psi_C$ reads:

$$\frac{\bar{\ell}}{\kappa} = 2m\Psi_H \quad (2.82)$$

Since optimal m computes to $\bar{m} = \sqrt{1 + Z(T_H + T_C)/2}$, then one obtains that

$$\frac{T_H - T_C}{T_s - T_a} = \frac{1}{2} \quad (2.83)$$

leading to a maximum efficiency

$$\eta_{\max} = \frac{(\bar{m} - 1)(T_H - T_C)}{\bar{m}T_H - T_C} \quad (2.84)$$

Although the result is only formally in a closed form, it provides a general solution to the Neumann problem in the constant-property limit.

2.4 Thermoelectric Efficiency in the Presence of Large Temperature Differences

Whenever the temperature difference over which a TEG operates is large or it is anyway inconvenient to neglect the temperature dependency of transport parameters, the analysis carried out in the previous Section is almost unavoidably bound to set only an upper limit to the actual TEG efficiency.

Taking full account of the temperature dependence of σ_T , α , and κ_{oc} may be carried out often only by numerical methods [22, 23]. Nonetheless, the concept of *thermoelectric compatibility* (hereafter more simply referred to as *compatibility*) may be of support to devise limits and possibility of real materials to be used in TEGs.

The concept of compatibility was introduced by Snyder in 2003 [24, 25] and refers to the reduced electric current flowing through a thermoelectric element that leads to the TEG maximum efficiency. In a one-dimensional system aligned along the x axis, in view of (2.56) and (2.58) one may write that

$$\begin{aligned}\mathcal{E} &= \alpha T'(x) - \rho_T j \\ j_q &= \alpha T(x)j + \kappa_{oc}T'(x)\end{aligned}\tag{2.85}$$

where $\rho_T = 1/\sigma_T$ and signs were reverted so that the energy balance is referred to the system. Therefore, the electric power consumed by the TEG (e.g. by Joule effect) is hereafter negative.

Energy conservation obviously sets that the electric power flow j_w must equals the net heat flow j_q so that, if $w = \mathcal{E}j$ is the specific electric power (power per volume of thermoelectric material), then $dj_q/dx = w$. Thus, in view of (2.85) one may conclude that charge build-up is disallowed, namely $dj/dx = 0$. Note that such a result is different from simply stating that $\nabla \mathbf{j} = \mathbf{0}$ since in the present case $j = j(T(x))$.

One of the key points of this analysis relies on the observation that temperature may be used as the space metrics since the temperature monotonically drops from the hot to the cold side of the thermoelectric element. Thus, $T(x)$ is invertible, namely $x = x(T)$ is a single-valued function. Therefore, under steady-state conditions

$$\frac{d}{dx} (\kappa_{oc}T'(x)) = -T(x) \frac{d\alpha}{dT} j T'(x) - \rho_T j^2\tag{2.86}$$

so that

$$\frac{d(\alpha T)}{dx} = T \frac{d\alpha}{dT} T'(x) + \alpha T'(x)\tag{2.87}$$

where $\alpha = \alpha(x(T), T)$ and $d\alpha/dT$ is the total derivative of α with respect to T .

One may now define a reduced current density

$$u \equiv \frac{j}{\kappa_{oc}T'(x)}\tag{2.88}$$

Thus, replacing \mathcal{E} from the first of (2.85) in w one gets

$$w = \alpha j T' - \rho_T j^2 = \kappa_{oc}(T')^2 u (\alpha - u \rho_T \kappa_{oc}) \quad (2.89)$$

while the second of (2.85) reads

$$j_q = \kappa_{oc} T' (\alpha u T + 1) \quad (2.90)$$

Finally, (2.86) may be recast as

$$\frac{du}{dT} = u^2 T \frac{d\alpha}{dT} + u^3 \rho_T \kappa_{oc} \quad (2.91)$$

An infinitesimal efficiency may be immediately written as a measure of power $w dx$ produced over an infinitesimal distance dx :

$$\delta\eta = \frac{wdx}{j_q} = \frac{dT}{T} \frac{u(\alpha - u \rho_T \kappa_{oc})}{u\alpha + \frac{1}{T}} \quad (2.92)$$

that may be rearranged as $\delta\eta \equiv \delta\eta_C \times \eta_r$ where $\delta\eta_C$ is the infinitesimal Carnot efficiency while

$$\eta_r = \frac{u(\alpha - u \rho_T \kappa_{oc})}{u\alpha + \frac{1}{T}} = \frac{1 - u \frac{\alpha}{z}}{1 + \frac{1}{u\alpha T}} \quad (2.93)$$

where the last equality holds true if both u (j) and α are non-zero.

Manifestly enough, η_r has a maximum over u . This maximum must depend on T as all terms in (2.93) depend on T . One easily obtains that such a maximum occurs for $u = s$ where

$$s = \frac{\sqrt{1+zT} - 1}{\alpha T} \approx \frac{z}{2\alpha} \quad (2.94)$$

is named (*thermoelectric*) compatibility. The maximum relative efficiency computes to

$$\max_u \eta_r = \frac{\sqrt{1+zT} - 1}{\sqrt{1+zT} + 1} \quad (2.95)$$

It may be worth comparing (2.95) to the infinitesimal efficiency (2.67) computed in the CPL. The relative efficiency at maximum u clearly coincides with the efficiency that would be reached over an infinitesimal temperature difference, where trivially $u = s$ always.

It should be remarked that u may be adjusted to s (by changing the electric load, typically) only for a given temperature as u is set by (2.90). Thus, one has to reach the conclusion that no thermoelectric device may operate optimizing its local efficiency

$\delta\eta$ at each point. However, electric currents in TEGs are usually small so that actual local efficiency may be kept to within $\approx 20\%$ of its maximum value [25]. Much more relevant is the issue in Peltier cooler, where electric currents are much larger.

2.4.1 Thermoelectric Potential

It is convenient to further recast the previous equations by introducing a *thermoelectric potential* Φ . Setting $\Phi = \alpha T + u^{-1}$ [25] it is easy to show that

$$\Phi = \alpha T + \frac{\kappa_{oc} T'}{j} \quad (2.96)$$

while $j_q = j\Phi$ and $\mathcal{E} = \Phi'(x)$. Therefore, the efficiency of a finite-length thermoelectric element may be written as

$$\int_{T_C}^{T_H} \eta_r \frac{dT}{T} = \int_{T_C}^{T_H} \frac{w dx}{j_q} = \int_{T_C}^{T_H} \frac{j \Phi'(x) dx}{j \Phi} = \int_{T_C}^{T_H} \frac{d\Phi}{\Phi} = \ln\left(\frac{\Phi(T_H)}{\Phi(T_C)}\right) \quad (2.97)$$

In an alternate view, one may use instead (2.93) to compute the actual efficiency considering the leg as a series of infinitesimal thermoelectric elements. Thus

$$1 - \eta_{\text{series}} = \prod_i (1 - \eta_{r,i}) \quad (2.98)$$

With a little of algebra one obtains

$$\eta_{\text{series}} = 1 - \exp\left(-\int \frac{\eta_r}{T} dT\right) \quad (2.99)$$

where the approximation $\ln(1 - \eta_r) \approx -\eta_r$ was used.

Comparing now (2.97) and (2.99) one immediately obtains that

$$\eta_{\text{series}} = 1 - \frac{\Phi(T_C)}{\Phi(T_H)} \quad (2.100)$$

or, using the definition of Φ ,

$$\eta_{\text{series}} = 1 - \frac{\alpha(T_C)T_C + 1/u(T_C)}{\alpha(T_H)T_H + 1/u(T_H)} \quad (2.101)$$

2.4.2 Comparison to CPL Efficiency

One expects (2.95) to reduce to (2.65) in the CPL. If all transport coefficients are independent of the temperature, (2.86) may be analytically solved for u to give

$$u(T)^{-2} = u(T_C)^{-2} - 2(T - T_C)\kappa_{oc}\rho_T \quad (2.102)$$

Setting $T = T_H$ in the previous equation, efficiency from (2.101) may be maximized using T_H as a free parameter. One obtains

$$u(T)^{-2} = s(\bar{T})^{-2} + (\bar{T} - T)^2\kappa_{oc}\rho_T + \left(\frac{\Delta T_{TEG}}{2}\kappa_{oc}\rho_T s(\bar{T})\right)^2 \quad (2.103)$$

where may be worth noting that both u and s remain dependent on the temperature even when the transport parameters are not. Thus

$$\begin{aligned} u(T_C)^{-1} &= s(\bar{T})^{-1} + \frac{\Delta T_{TEG}}{2}\kappa_{oc}\rho_T s(\bar{T}) \\ u(T_H)^{-1} &= s(\bar{T})^{-1} - \frac{\Delta T_{TEG}}{2}\kappa_{oc}\rho_T s(\bar{T}) \end{aligned} \quad (2.104)$$

so that the efficiency recovers the known CPL result (2.101), namely

$$\eta_{\text{series}}^{\text{CPL}} = \frac{\Delta T_{TEG}}{T_H} \frac{\sqrt{1 + z\bar{T}} - 1}{\sqrt{1 + z\bar{T}} + T_C/T_H} \quad (2.105)$$

2.4.3 Compatibility and Efficiency

From the previous analysis it should be apparent that, since s depends upon T while u is independently set by (2.86), it will be uncommon to have that all parts of a thermoelectric generator operating over a large temperature difference may work with its highest efficiency. Even in the CPL, could each section of the series operate at optimal efficiency (i.e. could a leg be made of an infinitesimally graded material fulfilling at each point the condition $u = s$ while keeping z constant throughout) one would obtain from (2.99)

$$\begin{aligned} \eta_{\text{series}}^* &= 1 - \exp\left(-\int_{T_C}^{T_H} \frac{\sqrt{1 + zT} - 1}{\sqrt{1 + zT} + 1} \frac{dT}{T}\right) \\ &= 1 - \left(\frac{1 + \sqrt{1 + zT_C}}{1 + \sqrt{1 + zT_H}}\right)^2 \exp\left[\frac{2(\sqrt{1 + zT_H} - \sqrt{1 + zT_C})}{(1 + \sqrt{1 + zT_C})(1 + \sqrt{1 + zT_H})}\right] \end{aligned} \quad (2.106)$$

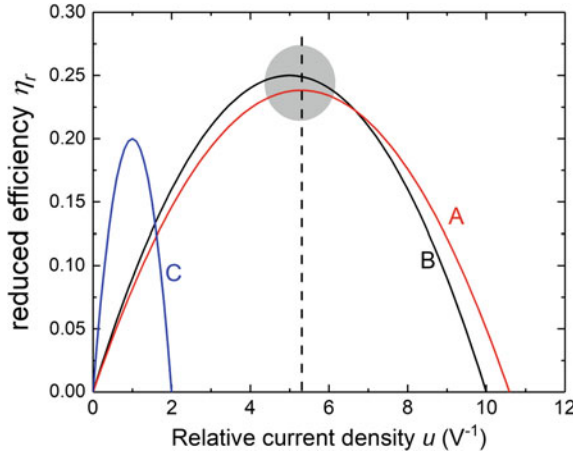


Fig. 2.6 Compared reduced efficiencies of three hypothetical thermoelectric materials versus their reduced current density. Note how A and B materials are *compatible* to each other, i.e. a u value may be set that keep both material efficiencies close to their maximum. Instead, no u enables A and C (or B and C) to operate in series (same u) efficiently. Therefore, the overall leg would provide conversion yields lower than those achievable in a single-segment leg

As a way of example, for $z = 3 \times 10^{-3} \text{ K}^{-1}$, $T_C = 300 \text{ K}$, and $T_H = 1000 \text{ K}$ one would obtain $\eta_{\text{series}}^{\text{CPL}} = 24.90\%$ versus $\eta_{\text{series}}^* = 25.18\%$.

In a real situation, segmented legs may approximate such a situation. Two or more materials are used in a thermal series, where each segment is chosen so as to provide the largest efficiency in the range of temperatures it operates. However, the simple criterion of choosing the material based on its thermoelectric figure of merit may not be the best. Instead, materials should be selected so that each may work at u values as close as possible to their relevant s . Figure 2.6 displays η_r for three hypothetical thermoelectric materials. It shows that while a good compromise on u may be obtained to achieve high efficiencies from A and B, combining A and C (or B and C) would lead to largely sub-optimal η_r values for one the two segments. Therefore, the series efficiency would be severely affected. In principle, being s temperature-dependent, also a single-material leg may run into compatibility issues, meaning that no u value may be set that is sufficiently close to $s(T)$ over the whole range of temperatures spanned by the leg. Such a *self-compatibility* problem is however uncommon in homogeneous thermoelectric materials, while it may show up in graded thermoelectrics.

2.4.4 Engineering Figure of Merit

A different approach to the analysis of the efficiency over large temperature differences introduced the concepts of engineering figure of merit and power factor [26].

Relaxing the assumption that transport coefficients are independent of the temperature, the (non-optimized) efficiency of a homogeneous thermoelectric leg reads [cf. (2.36)]

$$\phi = \frac{V_{\text{oc}}^2}{R} \frac{m/(1+m)^2}{(A/d) \int_{T_C}^{T_H} \kappa(T) dT + i T_H \alpha(T_H) - i^2 R/2} \quad (2.107)$$

where the leg resistance accounts to $R = (d/A) \Delta T_{\text{TEG}}^{-1} \int_{T_C}^{T_H} \rho(T) dT$ while $V_{\text{oc}} = \int_{T_C}^{T_H} \alpha(T) dT$. Optimizing over m leads to

$$m_{\text{opt}} = \sqrt{1 + (ZT)_{\text{eng}} \left(\frac{\hat{\alpha}}{\eta_{\text{Carnot}}} - \frac{1}{2} \right)} \quad (2.108)$$

where $\hat{\alpha}$ is a dimensionless intensity factor of the Thomson effect:

$$\hat{\alpha} = \frac{\alpha(T_H) \Delta T_{\text{TEG}}}{\int_{T_C}^{T_H} \alpha(T) dT} \quad (2.109)$$

and an *engineering figure of merit* is introduced:

$$(ZT)_{\text{eng}} \equiv Z_{\text{eng}} \Delta T = \frac{\left(\int_{T_C}^{T_H} \alpha(T) dT \right)^2}{\left(\int_{T_C}^{T_H} \kappa(T) dT \right) \left(\int_{T_C}^{T_H} \rho(T) dT \right)} \Delta T \quad (2.110)$$

Optimization over the efficiency leads to

$$\eta_{\text{max}} = \eta_{\text{Carnot}} \frac{\sqrt{1 + (ZT)_{\text{eng}} \left(\frac{\hat{\alpha}}{\eta_{\text{Carnot}}} - \frac{1}{2} \right)} - 1}{\hat{\alpha} \left(\sqrt{1 + (ZT)_{\text{eng}} \left(\frac{\hat{\alpha}}{\eta_{\text{Carnot}}} - \frac{1}{2} \right)} + 1 \right) - \eta_{\text{Carnot}}} \quad (2.111)$$

while the efficiency at maximum power output reads

$$\eta_{\text{W}} = \eta_{\text{Carnot}} \frac{1}{\frac{4\eta_{\text{Carnot}}}{(ZT)_{\text{eng}}} + 2\hat{\alpha} - \frac{1}{2}\eta_{\text{Carnot}}} \quad (2.112)$$

Note that both efficiencies reduce to their CPL for $Z_{\text{eng}} = Z$ and $\hat{\alpha} = 1$.

Equations (2.111) and (2.112) enable a realistic yet simple evaluation of the actual efficiency of thermoelectric materials operating over large temperature differences,

saving the burden of lengthy numerical computations. However, having neglected the Thomson term in (2.107) may still cause slight overestimates of the actual efficiency. More accurate expressions, also accounting for the Thomson heat $\tau(T)$, may be obtained, although at the price of some additional algebraic complexity. It could be shown that the maximum efficiency computes to

$$\eta_{\max} = \eta_{\text{Carnot}} \frac{\sqrt{1 + (ZT)_{\text{eng}} \alpha_1 \eta_{\text{Carnot}}^{-1}} - 1}{\alpha_0 \sqrt{1 + (ZT)_{\text{eng}} \alpha_1 \eta_{\text{Carnot}}^{-1} + \alpha_2}} \quad (2.113)$$

with

$$\alpha_i = \hat{\alpha} - \frac{\int_{T_C}^{T_H} \tau(T) dT}{\int_{T_C}^{T_H} \alpha(T) dT} W_T \eta_{\text{Carnot}} - i W_J \eta_{\text{Carnot}} \quad (2.114)$$

where

$$W_J = \frac{\int_{T_C}^{T_H} \left(\int_T^{T_H} \rho(T') dT' \right) dT}{\Delta T_{\text{TEG}} \int_{T_C}^{T_H} \rho(T) dT} \quad (2.115)$$

and

$$W_T = \frac{\int_{T_C}^{T_H} \left(\int_T^{T_H} \tau(T') dT' \right) dT}{\Delta T_{\text{TEG}} \int_{T_C}^{T_H} \tau(T) dT} \quad (2.116)$$

2.5 Finite–Rate Thermoelectric Efficiency

2.5.1 Efficiency of Finite–Rate Thermal Engines

Thermoelectric generators are thermal engines, and it may be interesting to consider their efficiency limit. In the CPL, the Dirichlet problem has a well known upper bound for $Z \rightarrow \infty$, returning $\eta_{\text{DCPL}} = \eta_C$. This simply confirms that the limiting efficiency of a Dirichlet TEG equals that of a Carnot engine, which is the thermal engine with the largest possible efficiency. As a fully reversible engine, however, Carnot engine requires an infinite time to complete a cycle, so that it converts heat into useful work at zero power.

A more challenging issue in heat conversion is that of computing the largest possible efficiency at maximum power. Finite power implies that heat is converted in a partially irreversible cycle, operating at finite rate.

The problem of computing efficiency maximizing the power output has a rather long tradition. Possibly the first attempt to compute maximum efficiency at finite rate is due to Novikov [27] who considered the problem in view of the maximization of the power output in nuclear power stations. Larger visibility had instead a paper by Curzon and Ahlborn [28] who independently recomputed the same upper bound more than fifteen years later. The so-called Curzon–Ahlborn efficiency η_{CA} reads

$$\eta_{CA} = 1 - \sqrt{\frac{T_C}{T_H}} \quad (2.117)$$

where, as in the whole Section, T_C and T_H are the temperature of the two thermostats.

Equation (2.117), beyond its proof, did not end up the analysis of finite-rate efficiency. Actually, both Novikov and Curzon–Ahlborn arguments only partially cover the whole set of possible finite-rate thermal engines. As recently pointed out by Apertet et al. [29], irreversibility in engines operating between two thermostats may arise *externally*, due to the temperature difference between the thermostats and the engine itself; or *internally*, namely due to the occurrence of irreversible adiabatic transformations within the engine. In the former case the engine is named *endoreversible* and irreversibility is set by its finite (non-zero) contact thermal conductance. In the latter instance, instead, the engine is named *exoreversible*, with its irreversibility being set by internal friction over the adiabatic steps. In both cases, irreversibility guarantees non-zero power input – and therefore non-zero power output. Figure 2.7 displays the entropy–temperature plot of both engines along with Carnot engine and the most general case (fully irreversible engine).

Of the four classes of engines, Curzon–Ahlborn efficiency describes the endoreversible case only, so that (2.117) cannot be considered (as sometimes is) a general form for the ideal engine operating at maximum power output.

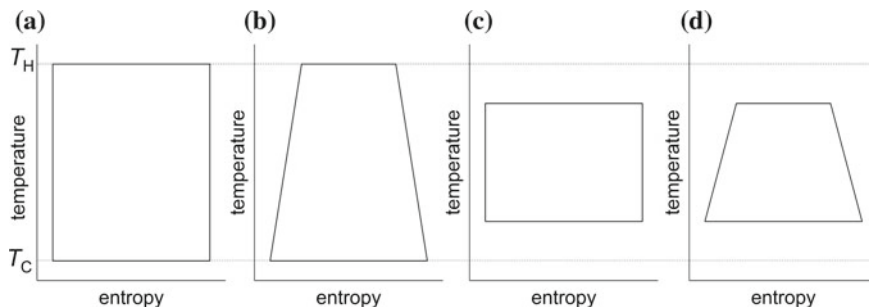


Fig. 2.7 Entropy–temperature plots of **a** reversible, **b** exoreversible, **c** endoreversible, and **d** irreversible thermal engines

A more general argumentation for thermoelectric generators was provided by Van den Broeck [30] who made use of the concept of degree of coupling λ among phenomenological coefficients L_{ij} (cf. Sect. 2.2.1) originally proposed by Kedem and Caplan [31]:

$$\lambda = \frac{L_{12}}{\sqrt{L_{11}L_{22}}} \quad -1 \leq \lambda \leq +1 \quad (2.118)$$

where L refers to two linear coupled flows driven by any thermodynamic force $F_1 = \mathcal{F}/T$ where \mathcal{F} is any external force (electrical, mechanical, or chemical); and by a temperature difference, namely $F_2 = T_C^{-1} - T_H^{-1}$. It was demonstrated that the upper bound for efficiency reads

$$\eta'_B = \frac{1}{2} \eta_C \frac{\lambda^2}{2 - \lambda^2} \quad (2.119)$$

Generalizing to a cascade of heat engines, which allows to extend the formula to non-vanishingly small temperature differences, it could be shown that

$$\eta_B = 1 - \left(\frac{T_C}{T_H} \right)^{p/2}, \quad p = \frac{\lambda^2}{2 - \lambda^2} \quad (2.120)$$

It returns the Curzon–Ahlborn limit for $\lambda^2 \rightarrow 1$, namely in the strong coupling limit, but may take lower values for lower $|\lambda|$.

Along a different route, studying cyclic Brownian heat engines within the frame of linear thermodynamics, Schmiedl and Seiffert [32] obtained a rather different equation for the efficiency at finite rate, namely

$$\eta_{SS} = \frac{\eta_C}{2 - \beta \eta_C} \quad (2.121)$$

where β eventually depends on the temperature of the thermostats. It is noteworthy to observe that while $\eta_{SS} = \eta_{CA}$ for $\beta = 1/(1 + \sqrt{T_C/T_H})$, η_{SS} may exceed η_{CA} . Such a result finds an explanation considering that, as mentioned, η_{CA} sets an upper bound for endoreversible engines. Within exoreversible engines (and in engines where both internal and external irreversibilities are allowed), friction converts work back into heat, possibly (but not necessarily) reducing the net amount of heat that is input into the engine. Therefore, efficiency may exceed the Curzon–Ahlborn limit because of the lower input instead of the larger output [29].

In summary, engines operating at finite rate are expected to reach an efficiency at maximum output significantly lower than the Carnot efficiency. For a generator operating between room temperature and 600 K, Carnot efficiency computes to 50% while $\eta_{CA} = 29\%$. Indeed, TEGs are typically fully irreversible engines, as they operate with non-zero contact and internal thermal resistances, so that Schmiedl–Seiffert efficiency, not Carnot efficiency, should be considered as the upper limit for their efficiency.

2.5.2 Application to Thermoelectric Generators

Although thermoelectric phenomena have always served as reference points for theories in irreversible thermodynamics, yet a complete analytical model for the efficiency of thermoelectric generators operating at finite rate is not available yet.

Castro–Happ efficiency models an exoreversible TEG as it fully neglects any contact thermal resistance. It is interesting to note, however, that its limiting efficiency (for $Z \rightarrow \infty$) tends to η_{CA} . With a little of algebra one shows that the asymptotic expansion on Z of η_{NCPL} computes to

$$\eta_{NCPL} \sim 2\alpha \sqrt{\frac{T_C}{Z\Phi_{tot}r}} \quad (2.122)$$

while

$$T_H \sim \frac{\sqrt{ZT_C\Phi_{tot}r}}{\alpha} \quad (2.123)$$

Thus

$$\eta_{NCPL} \sim 1 - \frac{1}{2} \frac{T_C}{T_H} \quad (2.124)$$

that approximates η_{CA} at the lowest order in $(T_H - T_C)/T_H$. Note that such a result is not necessarily expected, as the Curzon–Ahlborn limit is attained by exoreversible engines only for specific β values.

Instead, Curzon–Ahlborn upper bound is consistently reached for TEGs exchanging heat across thermal contact resistances K_H and K_C at the TEG hot and cold sides. In a model of an endoreversible TEG one verifies that, neglecting the internal (leg) thermal resistance, power output reads [33]

$$W = \frac{K_C K_H T_H \eta (\eta_C - \eta)}{(K_C + K_H)(1 - \eta)} \quad (2.125)$$

Thus, maximizing W with respect to η , one easily obtains that $\eta = \eta_{CA}$.

Quite interestingly, the same limiting efficiency is obtained by the Yazawa–Shakouri argument. As seen, the model accounts for both contact and internal thermal resistances, thereby qualifying as the closest attempt to analyze the efficiency a TEG where finite rates arise from both internal friction and limited thermal contact conductances. Also in this case, efficiency is found to tend to $1 - \sqrt{T_C/T_H}$ for $Z \rightarrow \infty$, supporting the view that η_{CA} has to be considered an upper bound for *any* TEG operating at non-zero power [21].

2.6 Thermoelectric Efficiency Under Non-steady State Conditions

In most real situations, TEGs operate under non-steady state conditions, namely the temperature of the hot and cold heat sinks and/or the heat flow change with time. Under quasi-static conditions this adds little new physics to the conversion rate issue. However, it is intuitive that some threshold frequency must exist above which rapid changes of boundary condition may affect the TEG efficiency.

For common this issue may be, no complete theory of time-dependent thermoelectric conversion is available yet [34]. Under non stationary conditions heat equation reads

$$\delta c \frac{\partial T}{\partial t} + \nabla \cdot \mathbf{j}_q = \mathcal{E} \cdot \mathbf{j} \quad (2.126)$$

where δ is the mass density, and c is the specific heat per mass unit. Thus, in view of (2.56), (2.58) and (2.31) one obtains

$$c\delta \frac{\partial T}{\partial t} = \nabla \cdot (\kappa_{oc} \nabla T) + \frac{\mathbf{j} \cdot \mathbf{j}}{\sigma_T} - \tau \mathbf{j} \cdot \nabla T - T \mathbf{j} \cdot (\nabla \alpha)_T \quad (2.127)$$

where $(\nabla \alpha)_T$ is the gradient of the Seebeck coefficient under isothermal conditions.

Comparing (2.127)–(2.51) shows how in the time-dependent problem an additional dependence of the efficiency on the heat capacity $c\delta$ is expected, which reports about the possible accumulation of heat within the thermoelectric leg in non-stationary conditions. Also, one should observe that \mathbf{j} can no longer be treated as an independent variable as it depends in turn on the junction temperatures. Therefore, (2.127) becomes a non-linear partial differential equation.

The first attempt to analyze the non-stationary problem is probably due to Gray [35] who analyzed the small-signal dynamic behavior of a TEG under time-dependent Dirichlet conditions. Linearization led to anyway very complicated expressions, which slightly simplify when neglecting the Thomson effect and assuming that leg thermal conductivities are equal to each other. Singularities for the device natural frequencies were computed, showing that they set the dynamic behavior of the device. Specifically, proper adjustments of the thermoelectric legs and of the transport properties of the materials may control the response time of the device, more closely meeting its static efficiency and power output.

More recently, the problem was reconsidered by several authors. Among them, Apostol and Nedelcu considered the advantages of operating TEGs by using heat and charge pulses. It could be shown that in a cyclic, nonstationary, transient regime the effects of thermal diffusion are lessened. The electric power output is found to be higher than for stationary transport. This is mostly due to the fact that pulsed mode concentrates the charge carriers on pulses of small spatial extent. Also, material requirements are slightly modified, making low thermal conductivity less critical [36].

Over more recent years, while progress has been reported for thermoelectric (Peltier) coolers [37, 38], theoretical analysis of TEGs operated under non-stationary conditions lagged behind. This has encouraged a mixed approach, using numerical simulations and direct experiments to verify the impact of pulsed or any-way time-dependent heat currents on the TEG efficiency. Among the most notable examples, Stockholm et al. reported a finite-time thermodynamics approach to the description of TEGs delivering power to an active (adaptive) electric load [39], in excellent agreement with experiments of impedance spectroscopy carried out by García-Cañadas and Min [40]. Measurements on TEG modules converting heat current packets obtained by introducing duty cycles of different durations in place of a continual heat flow. An increase of efficiency of more than 300% was reported, that was qualitatively explained with the increase of the time-averaged ΔT_{TEG} [41]. Numerical simulations also confirmed the possibility that efficiency (and average power output) should increase upon application of periodic temperature profiles, although smaller improvements, of the order of $\approx 10\%$, were expected. Interestingly, numerical analyses suggested a dependence of such an increase also on the phase shift between $T_{\text{H}}(\omega)$ and $T_{\text{C}}(\omega)$ [42].

It should be remarked that a second, different problem is often filed under the name of non-steady state thermoelectricity, referring to the frequency-dependence of the Seebeck coefficient itself. On this topic, dynamic theories of thermoelectricity were elaborated, leading to a nowadays well-assessed framework [43]. This is however quite a different issue, since it refers to the microscopic dynamics of condensed phases, namely to electronic response to traveling temperature waves and/or alternate electric fields. Typical response times fall at much higher frequencies, which may be hardly reached by randomly fluctuating macroscopic heat sinks.

2.7 Summary and Conclusions

In this chapter we have reviewed the physics ruling the conversion efficiency of thermoelectric generators. Focus was placed both on the material properties and on the thermal scenario in which the device is operated. While the Ioffe–Altenkirch formula is often used as a benchmark for material assessment and for device simulation, it has been shown how, even in the constant–property limit (i.e. when a TEG operates over a small temperature difference), its conversion efficiency significantly depends upon operational conditions. TEGs working between heat sources working as thermostats (Dirichlet conditions) require optimization that quite differs from that applying to TEGs wherein the cold side temperature is not set (Neumann boundary conditions). This is specifically important to properly design and to estimate the performances of hybrid solar converters.

Thermoelectric efficiency is further to be reconsidered for thermal harvesters working over large temperature differences. Thermoelectric compatibility and the engineering figure of merit provide accurate tools to realistically design TEGs and to compute realistic efficiencies. Although temperature differences in standard hybrid

thermoelectric–photovoltaic solar converters are small enough to make CPL a reasonable approximation, recent proposed use of optical and/or thermal concentrators in this class of systems was shown to set temperature drops over the TEG largely exceeding 100 K [44], thereby making non-CPL analysis highly recommendable.

References

1. D. Rowe, *CRC Handbook of Thermoelectrics* (CRC Press, Boca Raton, 1995)
2. H. Goldsmid, *Introduction to Thermoelectricity*, Springer Series in Materials Science (Springer, Berlin, 2009)
3. V. Zlatić, R. Monnier, *Modern Theory of Thermoelectricity* (Oxford University Press, Oxford, 2014)
4. K. Behnia, *Fundamentals of Thermoelectricity* (Oxford University Press, Oxford, 2015)
5. C. Goupil, *Continuum Theory and Modeling of Thermoelectric Elements* (Wiley, Weinheim, 2016)
6. C.A. Domenicali, Rev. Mod. Phys. **26**, 237 (1954)
7. G.J. Snyder, E.S. Toberer, Nat. Mater. **7**(2), 105 (2008)
8. A.J. Minnich, M.S. Dresselhaus, Z.F. Ren, G. Chen, Energy Environ. Sci. **2**, 466 (2009)
9. M.G. Kanatzidis, Chem. Mater. **22**(3), 648 (2010)
10. A. Shakouri, Annu. Rev. Mater. Res. **41**, 399 (2011)
11. L.D. Zhao, V.P. Dravid, M.G. Kanatzidis, Energy Environ. Sci. **7**, 251 (2014)
12. G. Tan, L.D. Zhao, M.G. Kanatzidis, Chem. Rev. **116**(19), 12123 (2016)
13. W.G. Zeier, A. Zevalkink, Z.M. Gibbs, G. Hautier, M.G. Kanatzidis, G.J. Snyder, Angewandte Chemie - International Edition **55**(24), 6826 (2016)
14. K. Zabrocki, C. Goupil, H. Ouerdane, Y. Apertet, W. Seifert, E. Müller, in *Continuum Theory and Modeling of Thermoelectric Elements*, ed. by C. Goupil (Wiley, Weinheim, 2016), pp. 75–156. Chap. 2
15. E. Altenkirch, Phys. Z. **10**, 560 (1909)
16. A. Ioffe, *Semiconductor Thermoelements and Thermoelectric Cooling* (Infosearch Ltd., London, 1957)
17. C.A. Domenicali, Phys. Rev. **92**, 877 (1953)
18. C.A. Domenicali, J. Appl. Phys. **25**(10), 1310 (1954)
19. H. Jackson, D. Temple, B. Kelly, *Introduction to Electric Circuits* (Oxford University Press, Oxford, 2015)
20. P.S. Castro, W.W. Happ, J. Appl. Phys. **31**(8), 1314 (1960)
21. K. Yazawa, A. Shakouri, J. Appl. Phys. **111**(2), 024509 (2012)
22. B. Sherman, R.R. Heikes, R.W. Ure Jr., J. Appl. Phys. **31**(1), 1 (1960)
23. M.S. El-Genk, H.H. Saber, Energy Convers. Manag. **44**(7), 1069 (2003)
24. G.J. Snyder, T.S. Ursell, Phys. Rev. Lett. **91**(14), 148301 (2003)
25. G.J. Snyder, in *Thermoelectrics Handbook: Macro to Nano*, ed. by D.M. Rowe (CRC Press, 2005), pp. 9–26
26. H.S. Kim, W. Liu, G. Chen, C.W. Chu, Z. Ren, Proc. Natl. Acad. Sci. **112**(27), 8205 (2015)
27. I. Novikov, J. Nuclear Energy (1954) **7**(1-2), 125 (1958)
28. F.L. Curzon, B. Ahlborn, Am. J. Phys. **43**(1), 22 (1975)
29. Y. Apertet, H. Ouerdane, C. Goupil, P. Lecoer, Phys. Rev. E **85**, 041144 (2012)
30. C. Van den Broeck, Phys. Rev. Lett. **95**, 190602 (2005)
31. O. Kedem, S.R. Caplan, Trans. Faraday Soc. **61**, 1897 (1965)
32. T. Schmiedl, U. Seifert, EPL (Europhysics Letters) **81**(2), 20003 (2008)
33. D. Agrawal, V. Menon, J. Phys. D Appl. Phys. **30**(3), 357 (1997)
34. W. Seifert, K. Zabrocki, S. Achilles, S. Trumper, in *Continuum Theory and Modeling of Thermoelectric Elements*, ed. by C. Goupil (Wiley, Weinheim, 2016), pp. 177–226

35. P. Gray, *The Dynamic Behavior of Thermoelectric Devices*. Technology Press research monographs, 6 (The Technology Press of the Massachusetts Institute of Technology, 1960)
36. M. Apostol, M. Nedelcu, J. Appl. Phys. **108**(2), 023702 (2010)
37. A. Snarskii, I. Bezsdudnov, Energy Convers. Manag. **94**, 103 (2015)
38. G.D. Aloysio, G. D'Alessandro, F. de Monte, Int. J. Heat Mass Transf. **95**, 972 (2016)
39. J.G. Stockholm, C. Goupil, P. Maussion, H. Ouerdane, J. Electron. Mater. **44**(6), 1768 (2015)
40. J. García-Cañadas, G. Min, AIP Adv. **6**(3), 035008 (2016)
41. L. Chen, J. Lee, Energy Convers. Manag. **119**, 75 (2016)
42. W.H. Chen, P.H. Wu, X.D. Wang, Y.L. Lin, Energy Convers. Manag. **127**, 404 (2016)
43. I. Volovichev, Physica B **492**, 70 (2016)
44. G. Contento, B. Lorenzi, A. Rizzo, D. Narducci, Energy **131**, 230 (2017)

Chapter 3

Solar Thermoelectric Generators



Abstract In this chapter we will present the full-thermal approach to thermoelectric solar harvesting. Analysing the state of the art of this field we will report on its historical development, showing its advantages. Technical and technological issues solved and yet to be solved will be addressed as well. Starting from a description of the main system components we will analyse the literature and the strategies reported so far. Then we will discuss how a solar thermoelectric generator (STEG) may be modeled, quantitatively predicting their final efficiency. This analysis will show which are the main parameters influencing STEG performances, suggesting which are the best solutions to achieve efficiencies competitive with other solar strategies.

3.1 System Description and State of the Art

A solar thermoelectric generator (STEG) is a system intended to harvest solar power by converting it into electricity by means of a thermoelectric generator (TEG). From an energetic point of view, in STEGs solar power is thus firstly converted into heat, then into electricity.

In general terms the system is made of five main elements (Fig. 3.1):

- an optical collector, which collects photons coming from the Sun;
- an opto-thermal converter, which converts photons into heat;
- a thermal collector, which drives the heat towards the thermoelectric converter;
- a thermoelectric converter, which converts heat into electricity; and
- a thermal dissipation system, which dissipate heat at the TEG cold side.

As will be shown with greater detail in Sect. 3.2, the scheme of Fig. 3.1 implies that the overall STEG conversion efficiency is the product of all the component efficiencies in collecting, converting, and dissipating energy. The technological solutions and the layouts implemented for these components define the various possible approaches to STEG.

The history of STEG development reports the first attempt to harnessing power from the Sun by a STEG system in 1922 by Coblentz [1]. The efficiency of his system, which was made of copper-constantan thermocouples soldered to a black painted copper foil, exhibited a very low efficiency of less than 0.01%. A major

progress was achieved by Telkes in 1954 [2], who demonstrated an efficiency of 0.63%, and 3.35% respectively at $1\times$ and $50\times$ optical concentrations. At that time such an efficiency was extremely competitive with other solar harvesting technology [3]. The main reason of the efficiency enhancement in Telkes' setup was the availability of more efficient thermoelectric elements made of BiSb/ZnSb alloys [4]. Starting from Telkes' seminal work, along the following twenty years the efforts to develop effective STEGs systems were mainly focused on space applications [5–9], with no significant improvements for terrestrial uses. The interest for non-space applications rejuvenated starting in the Eighties and it has been rather intermittent without significant progresses until the last five-six years, when main improvements were achieved (Fig. 3.2). Also in this case, recent improvements are mostly due to progresses in the thermoelectric material figure of merit (ZT) occurred over the last decade [10], which

Fig. 3.1 Scheme of the main components of a STEG system

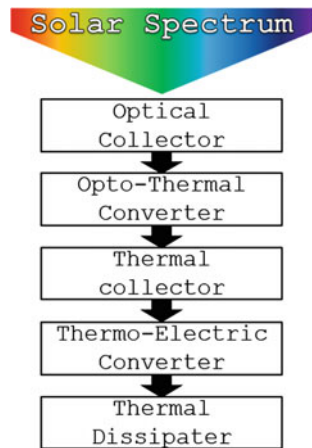
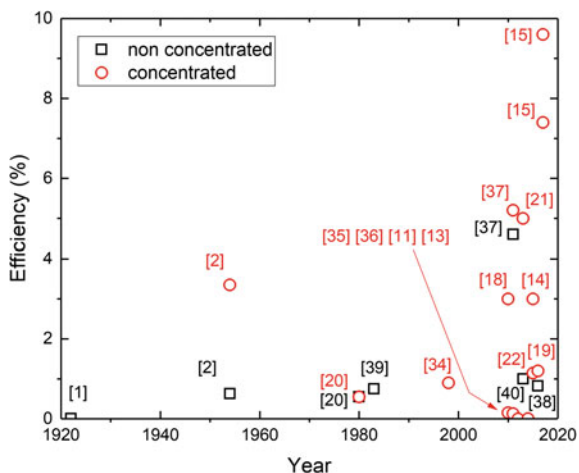


Fig. 3.2 Historical view of STEGs efficiencies for the main experimental work reported in the open literature. Red circles and black squares refer respectively to optically concentrated and non concentrated systems



led to higher thermoelectric conversion efficiencies that in turn stimulated increasing attention around the possible of TEGs as viable solar harvesters. Table 3.1 displays a summary of the main experimental approaches.

3.1.1 Optical Collector

From a system point of view, a first classification of the approaches reported in literature can be made based on the kind of optical collectors used, either an optical concentration system or not. Optical concentration collectors can be based on cylindrical lenses [2, 11–17], Fresnel lenses [18, 19], parabolic mirrors [20–29], dish mirrors [18, 30–33], or compound parabolic concentrators [34–36] (Fig. 3.3). Non-concentrated solution are instead limited to evacuated [37, 38] and non-evacuated [1, 2, 20] flat plane collectors, and to evacuated tubes [39, 40].

The kind of optical collector sets the amount of power reaching the opto-thermal converter, and thus contributes to set the temperature difference on the TEG. Since the thermoelectric efficiency increases upon increasing such a temperature difference at the TEG sides, it follows that the incoming optical power should be maximized. Concentrations up to $600\times$ were tested [36]. However, the additional costs and the footprint area have to be taken into account when evaluating the practical effectiveness of concentrated systems. In addition, it should be stressed that the final efficiency of the systems is not only dependent on the input power, since it is influenced by several other parameters including heat loss management and the temperature dependence of the TEG performances.

3.1.2 Opto-Thermal Converter

The opto-thermal converter in STEGs consists in most cases in a proper Solar Selective Absorber (SSA) deposited on a metallic substrate. Exceptions are early works in which authors used black painted metallic foils [1, 2] or carbon thin films [11, 36].

In general terms, the ideal opto-thermal converter should exhibit absorbance equal to one in the whole solar spectral range, and emissivity equal to zero for the spectral range corresponding to a black body with temperature equal to the device temperature. Such a converter would clearly maximize the input power while minimizing radiative thermal losses. This characteristics can be achieved with materials exhibiting high absorbance in the ultraviolet-visible range up to a certain cutoff wavelength, and high reflectance for higher wavelengths. Depending on the device temperature, the possible spectral overlap between the solar and black body spectrum (especially for high working temperatures) sets a trade off between maximum absorbance and minimum emissivity, setting therefore an optimal cutoff wavelength. Thus, important requirements for SSAs are temperature stability, and the possibility of easily tuning their cutoff wavelength.

Table 3.1 Performances and main characteristics of experimental works on STEGs. FP = Flat Plane, Par = parabolic, EV = evacuated, Fres = Fresnel, BP = black painted, comm = commercial, Graph = graphite, TF = thin film, ML = multi-layer, SC = single couple, Sku = skutterudites, El = electric

Author	References	Year	Efficiency	C	Opt collect	Opt-Th conv	Th collect	TE conv	ZT	ΔT (K)	Heat dissipater
Coblentz	[1]	1922	0.01	1	FP	BP Cu	Cu	Cu/Const	–	17	Air/Water
Telkes	[2]	1954	0.63	1	FP	BP Cu	Cu	BiSb/ZnSb	0.40	70	Heat sink
Telkes	[2]	1954	3.35	50	Lens	BP Cu	Cu	BiSb/ZnSb	0.40	270	Heat sink
Goldsmid	[20]	1980	0.55	1	FP	BP Al	Al	Comm BiTe	0.70	57	Heat sink
Goldsmid	[20]	1980	0.55	3	Par Mir	BP Al	Al	BiTe SC	0.70	120	Fix T
Durst	[39]	1983	0.75	1	EV tube	–	Oil	Comm BiTe	–	100	Water
Omer	[34]	1998	0.90	20	CPC	BP Teg	Al ₂ O ₃	Comm BiTe	–	100	Heat sink
Mgbemene	[35]	2010	0.15	6	CPC	Cu	Cu	Comm BiTe	–	10	El Fan
Amatya	[18]	2010	3.00	66	Par Dish+Fres	Si poly	–	Comm BiTe	0.40	150	Heat sink
Kraemer	[37]	2011	4.60	1	EV FP	Comm ML SSA on Cu	Cu	nano-BiTe SC	1.03	200	Fix T
Kraemer	[37]	2011	5.20	2	Lens	Comm ML SSA on Cu	Cu	nano-BiTe SC	1.03	–	Fix T
Suter	[36]	2011	0.13	600	CPC	Graph on Al ₂ O ₃	Cavity	Oxides	0.05	620	Water

(continued)

Table 3.1 (continued)

Author	References	Year	Efficiency	C	Opt collect	Opt-Th conv	Th collect	TE conv	ZT	ΔT (K)	Heat dissipater
Mizoshiri	[11]	2012	8.8 10^{-4}	13	Lens	Carbon TF	Carbon TF	TF BiTe	–	40	Cu bulk
Zhang	[40]	2013	1.00	1	EV tube	SSA on tubes	Heat pipe	Conn BiTe	0.59	70	Water
Urbiola	[21]	2013	5.00	52	Par Mir	Hot plate	–	Conn BiTe	0.70	150	Water
Deleon	[13]	2014	2 10^{-3}	17	Lens	p-silicon	SOI	1,15 10^{-4}	18	Substrate	
Miao	[22]	2015	1.14	40	Par Mir	TF SSA on Al	Al	Conn BiTe	0.64	152	Water
Pereira	[14]	2015	3.00	107	Lens	TiAlN/SiO2 on AlN	AlN	SiGe	0.60	400	Heat sink
Sudharshan	[38]	2016	0.82	1	Lens	SSA on steel	Steel	Conn BiTe	0.40	120	Heat sink
Kraemer	[19]	2016	7.40	38	Lens	ML double-cermet	Steel	BiTeSku Segm	1.02	400	Fix T
Candadai	[15]	2016	1.20	62	Fres	SSA on steel	Steel	Conn BiTe	0.40	215	Heat sink
Kraemer	[15]	2016	9.60	211	Lens	ML double-cermet	Steel	BiTeSku Segm	1.02	550	Fix T

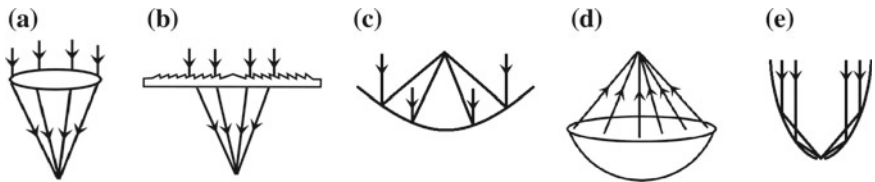


Fig. 3.3 Scheme of the optical concentration strategies for the optical collectors. **a** cylindrical lens, **b** Fresnel lens, **c** parabolic mirror, **d** dish mirror, **e** compound parabolic concentrator

Several kinds of SSA were reported. The main strategies are based on multilayer dielectric/metal stacks, or metal dielectric composites. An example of the former approach is provided by Candadai et al. [19] who reported on a multilayer stack of W/TiAlN/TiAlSiN/TiAlSiON/TiAlSiO deposited by magnetron sputtering on a stainless-steel substrate. The authors reported an absorbance of 0.95 with an emittance of 0.07 at 82 °C with material stability up to 600 °C in vacuum. The latter approach is instead reported for example by Cao et al. [41] who developed an SSA based on a WNiAl_2O_3 double layer cermet, covered by two different anti-reflective coatings. In this case, a stable absorptance of 0.90, with an emittance of 0.15 at 500 °C was reported.

Less frequently, SSA implemented in STEGs are based on intrinsic selective materials such as boron-doped silicon [13], or metals with textured surfaces. Recently, new solutions based on photonic crystals grown on metals substrates [42, 43] have promised to increase the efficiency of SSA with a better control of their selectivity.

3.1.3 Thermal Collector

The thermal collector is the part of the system intended to direct the heat converted by the opto-thermal section to the hot side of the TEG. The main requirement for this device component is the minimization of thermal losses upon heat transfer, i.e. a high thermal conductivity and, possibly, a low emittance. Most of the research on thermal collectors has focused on systems based on flat plane collectors. Normally, a SSA metallic substrate is used to this scope since it naturally exhibits a high thermal conductivity. In addition, an evacuated encapsulation can reduce thermal convective losses avoiding decreases in the system performances.

In few cases heat pipes wherein water [40] or oil [39] is used as heat vectors are also considered.

Another viable solution consists in the use of cavities in which the solar power is focused through a small aperture on an absorbing surface within the cavity [36]. The advantage of this approach consists in the fact that the heat re-emitted by the absorbing surface is reflected back to it by the other sides of the cavity, strongly reducing heat losses to the environment. Such systems were demonstrated to lead to very large differences of temperature at the TEG sides (up to 600 °C), promising

highly competitive performances [44, 45]. However experimental demonstrations of high conversion efficiencies in cavity based STEGs are still missing, especially for the lack of efficient thermoelectric materials and TEGs able to work over large differences of temperature.

Recently, also phase change materials (PCMs) have been proposed as thermal collectors [46, 47]. The main advantages of this approach are the stability of the working temperature, and the possibility of energy storage. Such advantages however are obtained at the expense of a more modest system efficiency [48].

3.1.4 Thermoelectric Converter

The thermoelectric convert is the part of the STEG system which converts the thermal input into electrical power. Two main approaches has been reported so far in literature, the first based on commercial TEGs, and the second on user-made thermoelectric converters. Commercial TEGs were in all the cases made of Bi_2Te_3 alloys doped with antimony and selenium. TEG figures of merit (ZT) varied from 0.4 [18] to 0.7 [20], depending especially on the system working temperature.

User-made TEGs were instead based on different materials such as silicon-germanium (SiGe) alloys [14], $\text{LaSrCuO}/\text{CaMnNbO}$ pairs [36] (both designed to work over wide differences of temperature), or nanostructured Bi_2Te_3 [37] working on a maximum of 150–200 °C of temperature difference. In these cases ZT values were reported to be 0.5–0.6 for SiGe alloys working between 500 and 700 °C, 0.005 for $\text{LaSrCuO}/\text{CaMnNbO}$, and 1.02 for nanostructured Bi_2Te_3 [49, 50].

Also thin film based TEGs were object of several computational works [51–55] showing that theoretically their efficiencies could be comparable with those of bulk STEGs systems. However the experimental attempts reported by Mizoshiri et al. [11] and de Leon et al. [13], based respectively on Bi_2Te_3 and on silicon-on-insulator (SOI) structures showed very low efficiency values (less than 0.002%).

Finally, also segmented legs were studied from a theoretical point of view, showing the advantage in the case of large temperature gradients [56–60]. Only in one case were these kinds of thermoelectric legs implemented experimentally, obtaining the highest efficiency ever reported on STEGs [15] where thermal concentration by means of a very low filling factor (FF—defined as the ratio between the thermoelectric active area and the whole TEG area) was deployed as well. Low FF values joined with a proper encapsulation actually lead to an increase of STEGs working temperatures and, consequently, of their efficiencies [12, 34, 37, 59].

3.1.5 Heat Dissipater

The heat dissipater is the part of the STEG system intended to eject heat from the TEG cold side. Its operation is very important to guarantee the maximum difference of temperature at the TEG edges.

Heat dissipation systems are either passive or active. In both cases the heat dissipater performances can be identified by its heat exchange coefficient (normally expressed in W/m²K) defined by the ratio between the heat flux flowing through the dissipater and the difference of temperature at its edges.

Passive cooling strategies are normally based on metallic fins and are infrequently met in the literature, especially in the case of optical/thermal concentration. Actually, most of the papers reporting passive cooling are either early works [1, 2, 20] or recent works mostly aimed at exploiting the feasibility of natural convection approaches [18, 19]. Unavoidably, passive dissipaters lead to a considerable increase of the cold side temperature, and therefore to a decrease of the STEG output power. Active cooling, normally using air or water as dissipative fluids, quite obviously presents higher heat exchange coefficients. However, they need a circulation system has to be added to the heat dissipater section, and its energetic cost has to be properly taken into account. Thus, the overall STEGs power is the difference between the power produced by the TEG and the power consumption due to fluid circulation.

3.2 Efficiency of STEGs

As mentioned, the efficiency of STEGs can be calculated as the product of the efficiencies of all the components reported in Fig. 3.1 as all parts are in series with each other. One may therefore define the efficiency of the optical collector in transmitting the input power $CP_{in}A_{opt}$ through the opto-thermal converter as

$$\eta_{opt} = \frac{CP_{in}A_{opt}\tau_{opt}}{CP_{in}A_{opt}} = \tau_{opt} \quad (3.1)$$

In the previous Equation C is the optical concentration, P_{in} the solar power density, A_{opt} the optical collector aperture area, and τ_{opt} is either the optical collector transmittance or reflectivity, depending on the selected optical component (a lens or a mirror). Since τ_{opt} is expected to be high (0.9 or more), a good approximation is to consider that the optical collector does not absorb power, and thus it does not heat up. Therefore η_{opt} can be considered as temperature independent.

The efficiency of the opto-thermal converter can be written instead by considering the opto-thermal absorbance along with the heat lost towards the ambient:

$$\eta_{\text{otconv}} = \frac{CP_{\text{in}} \tau_{\text{opt}} A_{\text{opt}} \alpha_{\text{otconv}} \tau_{\text{enc}} - \left[\varepsilon_{\text{otconv}} \sigma A_{\text{abs}} (T_h^4 - T_a^4) + A_{\text{abs}} \frac{T_h - T_a}{R_{\text{conv}}} \right]}{CP_{\text{in}} \tau_{\text{opt}} A_{\text{opt}}} = \frac{\alpha_{\text{otconv}} \tau_{\text{enc}} - \frac{\varepsilon_{\text{otconv}} \sigma A_{\text{abs}} (T_h^4 - T_a^4) + A_{\text{abs}} \frac{T_h - T_a}{R_{\text{conv}}}}{CP_{\text{in}} \tau_{\text{opt}} A_{\text{opt}}}}{\alpha_{\text{otconv}} \tau_{\text{enc}}} \quad (3.2)$$

where α_{otconv} , and $\varepsilon_{\text{otconv}}$ are the opto-thermal convert absorbance and emittance, and τ_{enc} is the transmittance of the possible encapsulation. The first and the second therm in square brackets account respectively for the radiative and convective heat losses between the opto-thermal converter (at temperature T_h) and the ambient (at temperature T_a), with A_{abs} being the opto-thermal converter area. Since the opto-thermal converter is supposed to be directly deposited onto the thermal collector top surface, in (3.2) the convective and radiative losses are considered to occur only at the opto-thermal top surface. In addition it should be stressed that differently from η_{opt} , η_{otconv} is strongly dependent on the temperature.

Analysing the thermal collector operation one may assume that heat is lost by conduction only when it is transferred to the thermal collector and to the TEG, while it is dissipated by convection and radiation from the part of the top surface not covered by the opto-thermal converter, and from the bottom surface as well. Summing all these contributions, the thermal collector efficiency reads

$$\eta_{\text{thcol}} = 1 - \frac{\varepsilon_{\text{thcol}'} \sigma A_{\text{thcol}} [(T_{\text{thcol}}^4 - T_a^4) + (T_{\text{thcol}}^4 - T_c^4)]}{\eta_{\text{otconv}}} - \frac{(2A_{\text{thcol}} - A_{\text{otconv}}) \frac{T_{\text{thcol}} - T_a}{R'_{\text{conv}}}}{\eta_{\text{otconv}}} - \frac{A_{\text{otconv}} \frac{T_{\text{otconv}} - T_{\text{thcol}}}{R'_{\text{cond}}}}{\eta_{\text{otconv}}} \quad (3.3)$$

where A_{thcol} , and T_{thcol} are respectively the area and the temperature of the thermal collector. Instead, R'_{conv} and R'_{cond} are the convective resistance between the thermal collector and the environment, and the conductive thermal resistance between the opto-thermal converter and the thermal collector.

In the second therm of the radiative heat exchange one supposes that the bottom of the thermal collector acts also as the TEG hot plate, and then it faces the TEG cold side. Thus, $\varepsilon_{\text{thcol}'}$ is the resultant emittance of the TEG parallel surfaces, one at temperature T_{thcol} with emittance $\varepsilon_{\text{thcol}}$, and the second with temperature T_c and emittance ε_c , computed as [61]

$$\varepsilon_{\text{thcol}'} = \frac{1}{\frac{1}{\varepsilon_{\text{thcol}}} + \frac{1}{\varepsilon_c} - 1} \quad (3.4)$$

Equations (3.2) and (3.3) can be usefully grouped, as suggested by Chen [62], by defining an opto-thermal efficiency η_{ot} that is the system efficiency in converting the optical solar power into heat flowing through the TEG.

For the sake of simplicity, we assume here that the opto-thermal converter and the thermal collector have the same area, and that they work within an evacuated envi-

ronment, as in most of the works reported in the literature. Under such assumptions the opto-thermal efficiency can be written as

$$\eta_{\text{ot}} = \alpha_{\text{otconv}} \tau_{\text{enc}} - \frac{\sigma A_{\text{abs}} [\varepsilon_{\text{otconv}} (T_h^4 - T_a^4) + \varepsilon_{\text{thcol'}} (T_h^4 - T_c^4)]}{CP_{\text{in}} \tau_{\text{opt}} A_{\text{opt}}} \quad (3.5)$$

where the conductive heat loss was disregarded in view of the small thermal resistance between the opto-thermal converter and the thermal collector. Therefore, $T_{\text{thcol}} = T_h$.

It is useful to note that η_{ot} can be also be obtained as the ratio between the heat flowing through the TEG and the incoming power as

$$\eta_{\text{ot}} = \frac{Q_{\text{teg}}}{CP_{\text{in}} \tau_{\text{opt}} A_{\text{opt}}} \quad (3.6)$$

where the heat flowing through the TEG can be written as

$$Q_{\text{teg}} = S_{\text{teg}} T_h I + \frac{(T_h - T_c)}{R_{\text{tmp}}} - \frac{I^2 R_{\text{inp}}}{2} \quad (3.7)$$

with S_{teg} the TEG Seebeck coefficient, I the current flowing through the TEG legs, and R_{tmp} and R_{inp} respectively the TEG thermal and electrical resistances.

From (3.5), (3.6), and (3.7) one can then obtain the following energy balance equation:

$$CP_{\text{in}} \tau_{\text{opt}} A_{\text{opt}} \alpha_{\text{otconv}} \tau_{\text{enc}} = \sigma A_{\text{abs}} [\varepsilon_{\text{otconv}} (T_h^4 - T_a^4) + \varepsilon_{\text{thcol'}} (T_h^4 - T_c^4)] + S_{\text{pn}} T_h I + \frac{(T_h - T_c)}{R_{\text{tmp}}} - \frac{I^2 R_{\text{inp}}}{2} \quad (3.8)$$

which links the incoming power to the heat losses and to the heat flowing through the TEG.

Concerning the STEG thermoelectric converter, its efficiency follows from (2.44).

Finally, thermal dissipater efficiency has to be evaluated taking into account the electrical power needed to circulate the cooling fluid (P_{diss}). Thus

$$\eta_{\text{diss}} = 1 - \frac{P_{\text{diss}}}{P_{\text{steg}}^{\text{out}}} \quad (3.9)$$

where $P_{\text{steg}}^{\text{out}}$ is the STEG electrical output power.

It is clear that for passive dissipation $\eta_{\text{diss}} = 1$ while for active dissipation one has to consider the details of the heat dissipater geometry. A useful example of this evaluation is reported by Yazawa and Shakouri [63] who accounted for a heat dissipater made of parallel tubes dimensioned following a heat impedance matching condition between the heat leaving the TEG cold side and that carried away from the

dissipater [64]. The authors showed that even if power needed for heat dissipation varies depending on the system dimensions and the working temperature, P_{diss} is expected not to impact significantly on the STEG output power for systems with optical concentration smaller than 200.

In conclusion, the overall STEG efficiency reads

$$\eta_{\text{steg}} = \eta_{\text{opt}} \eta_{\text{ot}} \eta_{\text{teg}} \eta_{\text{diss}} \quad (3.10)$$

Apart from η_{diss} that, as mentioned, has to be evaluated case by case, and from η_{opt} , which is independent of the temperature, the main factor influencing η_{steg} is the product $\eta_{\text{ot}} \eta_{\text{teg}}$.

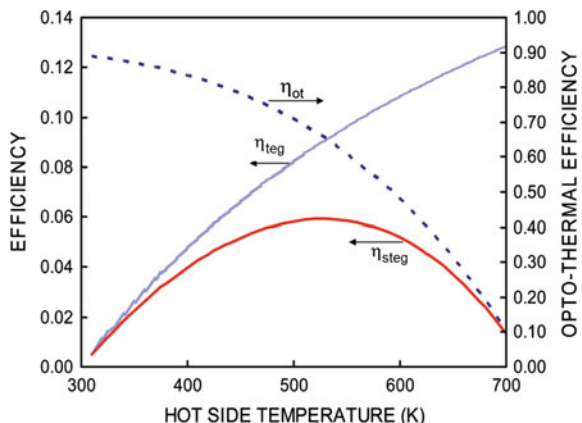
Actually, η_{ot} and η_{teg} are both strongly temperature-dependent, but with opposite trends (Fig. 3.4). This leads to the conclusion that there is an optimal operation temperature T_h maximizing the STEG efficiency that depends on the system characteristics. In 2011 Chen [62], followed in 2012 by Kreamer [12], demonstrated that the optimal T_h does not depend on the thermal TEG leg geometrical characteristics (e.g. the number of legs, their footprint area, or their length) but only on the system optical characteristics (C , τ_{opt} , $\varepsilon_{\text{otconv}}$, $\varepsilon_{\text{thcol'}}$) and on $Z\bar{T}$. Therefore once the optical properties and $Z\bar{T}$ are given, it is possible to design the TEG so as to make the system working at its optimal T_h .

This sets useful indications and some constrains for the thermoelectric material properties, and for the TEG design as will be shown in the next Section.

3.3 TEG Design

From Fig. 3.4 (which is taken here as case study) it is possible to note that the optimal temperature is expected to fall within a range of temperatures between 500 and

Fig. 3.4 η_{ot} and η_{teg} , and the resultant η_{steg} as function of the TEG hot side temperature T_h . In the graph $Z\bar{T}$ is set to 1, $T_c=T_a = 300$ K, and $\varepsilon_{\text{otconv}} + \varepsilon_{\text{thcol'}} = 0.006$. η_{opt} and η_{diss} are instead set to 1. Reproduced with permission from [62]



550 K. However, it is straightforward to calculate that without optical concentration (namely taking $P_{\text{in}} = 1000 \text{ W/m}^2$), and considering the typical thermal conductivities of current thermoelectric materials (i.e. $\kappa = 1 \text{ W/mK}$) the temperature drop across a thermoelectric leg of length 1–5 mm will be only 1–5 °C. It follows that concentration of the incoming power is mandatory. One possible solution is the use of optical concentration, as outlined in the previous paragraphs. An alternate solution is instead the implementation of thermal concentration, namely the use of thermoelectric elements having a smaller footprint area than the opto-thermal converter. Thermal concentration is defined as

$$C_{\text{th}} = \frac{A_{\text{abs}}}{A_{\text{legs}}} \quad (3.11)$$

where A_{legs} is the thermoelectric element area:

$$A_{\text{legs}} = N_{\text{couples}}(A_n + A_p) \quad (3.12)$$

with N_{couples} the number of thermoelectric pairs, and where A_n, A_p are respectively the n and p thermoelectric material areas.

Stated differently, the principle of thermal concentration implies the use of TEGs with reduced filling factors, defined as the ratio between the thermoelectric leg area and the total TEG area:

$$FF_{\text{teg}} = \frac{A_{\text{legs}}}{A_{\text{teg}}} \quad (3.13)$$

Thermal concentration is reported as a solution to increase the working temperature of STEGs in several works appeared in the literature, both theoretical and experimental [12, 34, 37, 59]. However, the implementation of such an approach requires a very effective heat loss management that implies encapsulation or other kinds of evacuated enclosings.

Thermal concentration along with the thermoelectric material conductivity and the leg length define the thermoelectric generator thermal resistance:

$$R_{\text{teg}}^{\text{th}} = N_{\text{couples}} \left(\frac{L_p}{\kappa_p A_p} + \frac{L_n}{\kappa_n A_n} \right) = \frac{C_{\text{th}}(A_n + A_p)}{A_{\text{abs}}} \left(\frac{L_p}{\kappa_p A_p} + \frac{L_n}{\kappa_n A_n} \right) \quad (3.14)$$

Since an optimal operation temperature exists (as displayed in Fig. 3.4), also an optimal TEG thermal resistance can be defined accordingly. Therefore, for any given set of thermoelectric properties an optimal layout exists that sets an optimal working temperature. In this sense, also the ratio between n and p leg sizes plays a role. It can be shown that the maximum efficiency corresponds to a ratio [62].

$$\gamma_{np} = \frac{A_n}{A_p} = \sqrt{\frac{\rho_n \kappa_p}{\rho_p \kappa_n}} \quad (3.15)$$

3.4 Materials Characteristics

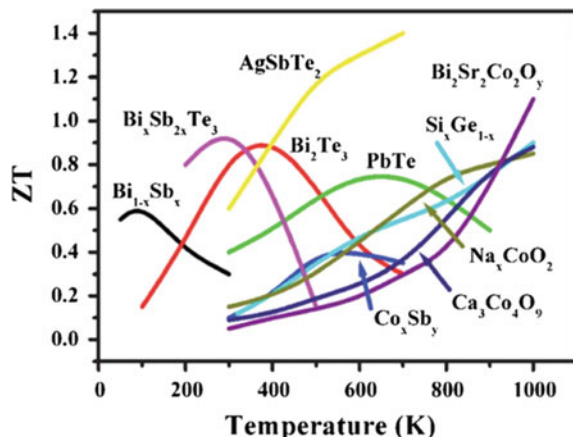
It is clear that, since an optimal working temperature for STEGs exists, the thermoelectric material has to be chosen accordingly, bearing in mind that the thermoelectric figure of merit (and then the efficiency) is strongly dependent on the temperature (Fig. 3.5). The thermoelectric materials of interest for STEGs mainly belong to four classes: bismuth telluride (Bi_2Te_3) alloys, lead telluride (PbTe) alloys, skutterudites, and silicon germanium (SiGe) alloys.

BiTe alloys are the most established and known class of materials for thermoelectric applications, and can be easily prepared as p or n type semiconductor when it is doped respectively with Sb or Se. These materials were reported to achieve peak ZT values of 1.8 at 43 °C for Sb doped [67], and 1.04 at 125 °C for Se doped alloys [66]. Both results were achieved using preparation techniques such as high-energy ball milling or spark plasma sintering able to form nanocomposites with a distribution of grain sizes ranging from a few hundreds of nanometers up to one micron, suppressing phonon transport without harm to their power factor.

Despite these very interesting values, the main drawback of BiTe alloys is the fact that their are efficient only over small temperatures (near room temperature) (Fig. 3.5), therefore limiting the final efficiency of STEGs.

An option to solve the limitation on the working temperature of BiTe comes from PbTe alloys. These materials and their composites made with Ag and Sb, often classified with the acronym LAST, are reported to exhibit ZT values higher than one at temperature above 300 °C. A maximum ZT of 2.2 around 650 °C was reported recently for a p type PbTe alloy doped with sodium (Na) in the presence of SrTe precipitates [68]. Regarding instead n type alloys, another record value of 2.2 at temperatures around 500 °C was reported for a PbTe alloy by Hsu et al. [69]. In this material Ag and Sb nano-precipitates were demonstrated to lead to a strong decrease of the thermal conductivity.

Fig. 3.5 Thermoelectric figure of merit of various materials as a function of temperature. Reproduced with permission from [65]



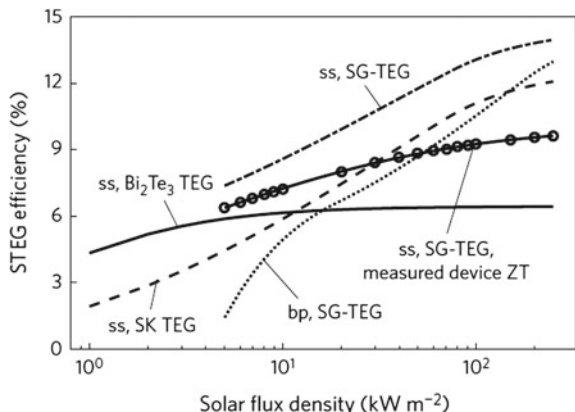
Another solution to operate at mid-high working temperature comes from skutterudites. In this materials a so-called rattling effect of small ions hosted within a crystal cage structure made of large voids is reported to scatter phonons. This effect, in addition to the high geo-abundance of the elements constituting this class of materials, makes skutterudites one the most promising thermoelectric material for mass production. A peak ZT of 1.3 at 527 °C was reported by Rogl et al. [70] for a CoSb p type alloy, while a record figure of merit of 1.34 at 580 °C was found by Zhao et al. [71] for a n type alloy.

In the case of very high working temperatures in STEGs such as in cavities [36], high-temperature thermoelectric materials are needed. SiGe alloys have been shown to have high figure of merits along with good stability. Nanocomposites developed with ball milling and pressing were reported to have ZT values of 0.95 at 950 °C [72], and 1.30 at 900 °C [73], respectively for p and n type alloys.

As already mentioned, due to the remarkable temperature variability of ZT , in the case of large difference of temperature across the TEG sides a single material cannot be efficient in the whole temperature range. In such cases segmented TEGs using different materials along the length of TEG legs are needed, as shown by several theoretical studies [56–58]. Another possible solution, albeit less considered, is the utilization of inhomogeneous doping along the leg length [60].

Finally, an example of the effect of the implementation of segmented legs to STEGs was reported recently by Kraemer et al. [15] (Fig. 3.6). The authors reported the results obtained by a flat plane optical concentrated STEG system implementing a segmented BiTe-skutterudites TEG. In the graph of Fig. 3.6 the authors compare these results with calculations for single-material TEGs. The comparison is made as a function of the solar flux input, showing how the segmented TEG is the best solution in this case.

Fig. 3.6 Efficiency of the STEG system reported by Kraemer et al. [15]. Note the effect of using a segmented TEG instead of single-material legs. In the graph ‘ss’ stands for spectrally selective solar absorber, ‘bp’ for black painted, and ‘SG’ for segmented. All the lines represent calculations, while circles report experimental data. Reported with permission from [15]



References

1. W.W. Coblenz, Sci. Am. **127**, 324 (1922)
2. M. Telkes, J. Appl. Phys. **25**(6), 765 (1954)
3. D.M. Chapin, C.S. Fuller, G.L. Pearson, J. Appl. Phys. **25**, 676 (1954)
4. M. Telkes, J. Appl. Phys. **18**(10), 1116 (1947). <https://doi.org/10.1063/1.362507>. <http://dx.doi.org/10.1063/1.1697593>
5. G.W. Glassburn, IEEE Trans. Aerosp. **1**(2), 1396 (1963). <https://doi.org/10.1109/TA.1963.4319515>
6. N. Fuschillo, R. Gibson, F.K. Eggleston, J. Epstein, IEEE Trans. Aerosp. **AS-3**(2), 652 (1965). <https://doi.org/10.1109/TA.1965.4319865>
7. F.K. Eggleston, N. Fuschillo, IEEE Trans. Aerosp. **AS-3**(2), 674 (1965). <https://doi.org/10.1109/TA.1965.4319867>
8. N. Fuschillo, R. Gibson, F. Eggleston, J. Epstein, Advanced Energy Conversion **6**(2), 103 (1966). [https://doi.org/10.1016/0365-1789\(66\)90004-X](https://doi.org/10.1016/0365-1789(66)90004-X)
9. M. Swerdlng, V. Raag, J. Energy **3**(5), 291 (1979). <https://doi.org/10.2514/3.62438>
10. J.P. Heremans, M.S. Dresselhaus, L.E. Bell, D.T. Morelli, Nat. Nanotechnol. **8**(July), 471 (2013)
11. M. Mizoshiri, M. Mikami, K. Ozaki, K. Kobayashi, J. Electron. Mater. **41**(6), 1713 (2012)
12. D. Kraemer, K. McEnaney, M. Chiesa, G. Chen, Sol. Energy **86**(5), 1338 (2012)
13. M.T. de Leon, H. Chong, M. Kraft, J. Micromechanics Microengineering **24**(8), 085011 (2014)
14. A. Pereira, T. Caroff, G. Lorin, T. Baffie, K. Romanek, S. Vesin, K. Kusiak, H. Duchemin, V. Salvador, N. Miloud-Ali, L. Aixala, J. Simon, Energy **84**, 485 (2015)
15. D. Kraemer, Q. Jie, K. McEnaney, F. Cao, W. Liu, L.A. Weinstein, J. Loomis, Z. Ren, G. Chen, Nat. Energy **1**, 16153 (2016). September
16. Y. Cai, J. Xiao, W. Zhao, X. Tang, Q. Zhang, J. Electron. Mater. **40**(5), 1238 (2011)
17. D. Kossyvakis, C. Vossou, C. Provatidis, E. Hristoforou, Renew. Energy **81**, 150 (2015)
18. R. Amatya, R.J. Ram, J. Electron. Mater. **39**(9), 1735 (2010)
19. A.A. Candadai, V.P. Kumar, H.C. Barshilia, Solar Energy Mater. Solar Cells **145**, 333 (2016)
20. H. Goldsmid, J. Giutronich, M. Kaila, Solar Energy **24**(5), 435 (1980). [https://doi.org/10.1016/0038-092X\(80\)90311-4](https://doi.org/10.1016/0038-092X(80)90311-4), <http://linkinghub.elsevier.com/retrieve/pii/0038092X80903114>
21. E.A. Chávez Uribiola, Y. Vorobiev, Int. J. Photoenergy **2013**(4) (2013). <https://doi.org/10.1155/2013/704087>
22. L. Miao, Y.P. Kang, C. Li, S. Tanemura, C.L. Wan, Y. Iwamoto, Y. Shen, H. Lin, J. Electron. Mater. **44**(6), 1972 (2015). <https://doi.org/10.1007/s11664-015-3626-7>
23. W. He, Y. Su, S. Riffat, J. Hou, J. Ji, Appl. Energy **88**(12), 5083 (2011)
24. C. Li, M. Zhang, L. Miao, J. Zhou, Y.P. Kang, C. Fisher, K. Ohno, Y. Shen, H. Lin, Energy Convers. Manag. **86**, 944 (2014)
25. A.E. Özdemir, Y. Köysal, E. Özba, T. Atalay, Energy Convers. Manag. **98**, 127 (2015)
26. N. Rehman, M.A. Siddiqui, J. Electron. Mater. **45**(10), 5285 (2016)
27. S. Manikandan, S. Kaushik, Sol. Energy **135**, 569 (2016)
28. G. Li, G. Zhang, W. He, J. Ji, S. Lv, X. Chen, H. Chen, Energy Convers. Manag. **112**, 191 (2016)
29. Y.J. Dai, H.M. Hu, T.S. Ge, R.Z. Wang, P. Kjellsen, Renew. Energy **92**, 83 (2016)
30. R. De Luca, S. Ganci, P. Zozzaro, B.G.D, R.F. De Luca R,Z,P, C.A, S.R.J, Y.H.D. F.W. Sears, M.W. Zemansky, Eur. J. Phys.**29**(6), 1295 (2008)
31. G. Muthu, S. Shanmugam, A. Veerappan, Energy Proc. **54**, 2 (2014)
32. N. Zhu, T. Matsuura, R. Suzuki, T. Tsuchiya, Energy Proc. **52**, 651 (2014)
33. G. Muthu, S. Shanmugam, A. Veerappan, J. Electron. Mater. **44**(8), 2631 (2015)
34. S. Omer, Solar Energy Mater. Solar Cells **53**(1–2), 67 (1998)
35. C.A. Mgbemene, J. Duffy, H. Sun, S.O. Onyegegbu, J. Solar Energy Eng. **132**, 031015 (2010)
36. C. Suter, P. Tomeš, A. Weidenkaff, A. Steinfeld, Sol. Energy **85**(7), 1511 (2011)
37. D. Kraemer, B. Poudel, H.P. Feng, J.C. Taylor, B. Yu, X. Yan, Y. Ma, X. Wang, D. Wang, A. Muto, K. McEnaney, M. Chiesa, Z. Ren, G. Chen, Nat. Mater. **10**(7), 422 (2011)

38. K. Sudharshan, V.P. Kumar, H.C. Barshilia, Solar Energy Mater. Solar Cells **157**, 93 (2016)
39. T. Durst, L.B. Harris, H.J. Goldsmid, Solar Energy **31**(4), 421 (1983). [https://doi.org/10.1016/0038-092X\(83\)90143-3](https://doi.org/10.1016/0038-092X(83)90143-3)
40. M. Zhang, L. Miao, Y.P. Kang, S. Tanemura, C.A.J. Fisher, G. Xu, C.X. Li, G.Z. Fan, Appl. Energy **109**, 51 (2013). <https://doi.org/10.1016/j.apenergy.2013.03.008>
41. F. Cao, D. Kraemer, T. Sun, Y. Lan, G. Chen, Z. Ren, Adv. Energy Mater. **5**(2), 1 (2015). <https://doi.org/10.1002/aenm.201401042>
42. Y. Da, Y. Xuan, Sci. China Technol. Sci. **58**(1), 19 (2015)
43. Z. Fang, C. Lu, D. Gao, Y. Lu, C. Guo, Y. Ni, Z. Xu, P. Li, J. Eur. Ceram. Soc. **35**(4), 1343 (2015)
44. L.L. Baranowski, E.L. Warren, E.S. Toberer, J. Electron. Mater. **43**(6), 2348 (2014)
45. M. Olsen, E. Warren, P. Parilla, E. Toberer, C. Kennedy, G. Snyder, S. Firdosy, B. Nesmith, A. Zakutayev, A. Goodrich, C. Turchi, J. Nettet, M. Gray, P. Ndione, R. Tirawat, L. Baranowski, A. Gray, D. Ginley, Energy Proc. **49**, 1460 (2014)
46. A. Agbossou, Q. Zhang, Z. Feng, M. Cosnier, Sens. Actuators A Phys. **163**(1), 277 (2010)
47. M.L. Olsen, J. Rea, G.C. Glatzmaier, C. Hardin, C. Oshman, J. Vaughn, T. Roark, J.W. Raade, R.W. Bradshaw, J. Sharp, A.D. Avery, D. Bobela, R. Bonner, R. Weigand, D. Campo, P.A. Parilla, N.P. Siegel, E.S. Toberer, D.S. Ginley, AIP Conference Proceedings AIP **0500351**(10) (2016). <https://doi.org/10.1063/1.4949121>, <http://dx.doi.org/10.1063/1.4949133>
48. Q. Zhang, A. Agbossou, Z. Feng, M. Cosnier, Sens. Actuators A Phys. **163**(1), 277 (2010). <https://doi.org/10.1016/j.sna.2010.06.026>, <http://dx.doi.org/10.1016/j.sna.2010.06.027>
49. Y. Ma, Q. Hao, B. Poudel, Y. Lan, B. Yu, D. Wang, G. Chen, Z. Ren, Nano Lett. **8**(1) (2008)
50. X. Yan, B. Poudel, Y. Ma, W.S. Liu, G. Joshi, H. Wang, Y. Lan, D. Wang, G. Chen, Z.F. Ren, Nano Lett. **10**, 3373 (2010). <https://doi.org/10.1021/nl101156v>
51. M.T.D. Leon, H. Chong, M. Kraft, Proc. Eng. **47**, 76 (2012)
52. L.A. Weinstein, K. McEnaney, G. Chen, J. Appl. Phys. **113**(16), 164504 (2013)
53. L. Tayebi, Z. Zamanipour, D. Vashaee, Renew. Energy **69**, 166 (2014)
54. W. Zhu, Y. Deng, M. Gao, Y. Wang, Energy Convers. Manag. **106**, 1192 (2015)
55. W. Zhu, Y. Deng, M. Gao, Y. Wang, J. Cui, H. Gao, Energy **89**, 106 (2015)
56. K. McEnaney, D. Kraemer, Z. Ren, G. Chen, J. Appl. Phys. **110**(7) (2011)
57. T. Yang, J. Xiao, P. Li, P. Zhai, Q. Zhang, J. Electron. Mater. **40**(5), 967 (2011)
58. J. Xiao, T. Yang, P. Li, P. Zhai, Q. Zhang, Appl. Energy **93**, 33 (2012)
59. W.H. Chen, C.C. Wang, C.I. Hung, C.C. Yang, R.C. Juang, Energy **64**, 287 (2014)
60. S. Su, J. Chen, IEEE Trans. Ind. Electron. **62**(6), 3569 (2015)
61. R. Siegel, J.R. Howell, M.P. Menguc, *Thermal Radiation Heat Transfer*, 5th edn. (Taylor & Francis, NY, 2002). <https://www.crcpress.com/Thermal-Radiation-Heat-Transfer-5th-Edition/Howell-Menguc-Siegel/p/book/9781439866689>
62. G. Chen, J. Appl. Phys. **109**(10) (2011)
63. K. Yazawa, A. Shakouri, in *Thermal Issues in Emerging Technologies, ThETA 3, Cairo Egypt, Dec 19–22nd 2010* (2010), pp. 283–290
64. K. Yazawa, G.L. Solbrekken, A. Bar-Cohen, in *2003 International Electronic Packaging Technical Conference and Exhibition*, vol. 2, (ASME, 2003), pp. 509–516. <https://doi.org/10.1115/IPACK2003-35242>, <http://proceedings.asmedigitalcollection.asme.org/proceeding.aspx?doi=10.1115/IPACK2003-35242>
65. Y. Qi, Z. Wang, M. Zhang, F. Yang, X. Wang, H. Lu, Y. Yang, F. Qiu, C. Trautmann, A. Bertsch, N.M. White, A.S. Paulo, A. Shakouri, L. Fonseca, K. Kim, J. Mater. Chem. A **1**(20), 6110 (2013). <https://doi.org/10.1039/c3ta01594g>, <http://xlink.rsc.org/?DOI=c3ta01594g>
66. X. Yan, B. Poudel, Y. Ma, W.S. Liu, G. Joshi, H. Wang, Y. Lan, D. Wang, G. Chen, Z.F. Ren, Nano Lett. **10**(9), 3373 (2010). <https://doi.org/10.1021/nl101156v>
67. S. Fan, J. Zhao, J. Guo, Q. Yan, J. Ma, H.H. Hng, Appl. Phys. Lett. **96**(18), 182104 (2010). <https://doi.org/10.1063/1.3427427>, <http://aip.scitation.org/doi/10.1063/1.3427427>
68. K. Biswas, J. He, I.D. Blum, Chun-IWu, T.P. Hogan, D.N. Seidman, V.P. Dravid, M.G. Kanatzidis, Nature **490**(7421), 570 (2012). <https://doi.org/10.1038/nature11645>

69. K.F. Hsu, S. Loo, F. Guo, W. Chen, J.S. Dyck, C. Uher, T. Hogan, E.K. Polychroniadis, M.G. Kanatzidis, *Science* **303**(5659) (2004). <http://science.sciencemag.org/content/303/5659/818>
70. G. Rogl, A. Grytsiv, P. Rogl, E. Bauer, M. Kerber, M. Zehetbauer, S. Puchegger, *Intermetallics* **18**(12), 2435 (2010). <https://doi.org/10.1016/j.intermet.2010.08.041>, <http://linkinghub.elsevier.com/retrieve/pii/S0966979510003821>
71. W. Zhao, P. Wei, Q. Zhang, C. Dong, L. Liu, X. Tang, *J. Am. Chem. Soc.* **131**(10), 3713 (2009). <https://doi.org/10.1021/ja8089334>, <http://pubs.acs.org/doi/abs/10.1021/ja8089334>
72. G. Joshi, H. Lee, Y. Lan, X. Wang, G. Zhu, D. Wang, R.W. Gould, D.C. Cuff, M.Y. Tang, M.S. Dresselhaus, G. Chen, Z. Ren, *Nano Lett.* **8**(12), 4670 (2008). <https://doi.org/10.1021/nl8026795>
73. X.W. Wang, H. Lee, Y.C. Lan, G.H. Zhu, G. Joshi, D.Z. Wang, J. Yang, A.J. Muto, M.Y. Tang, J. Klatsky, S. Song, M.S. Dresselhaus, G. Chen, Z.F. Ren, *Appl. Phys. Lett.* **93**(19), 193121 (2008). <https://doi.org/10.1063/1.3027060>

Chapter 4

A Primer on Photovoltaic Generators



Abstract The most common and efficient way to convert solar power into useful work is by photovoltaic generation. Photovoltaic cells are devices that convert radiative energy into electric energy. This chapter outlines the mechanism of photovoltaic conversion. The physical principles are introduced and described, and their implementation in real devices (cells and modules) is discussed with reference to the so called three solar cell generations, namely bulk cells, thin film cells, and cells based on dye sensitization. The role played by materials in each cell generation is also examined.

4.1 Background and Theory

4.1.1 Introduction

Earth receives an incredible supply of solar energy. The sun, an average star, is a fusion reactor that has been burning for over 4 billion years. Since the solar radiation received on earth is of $\approx 162,000$ TW, it provides enough energy in one minute to supply the world's energy needs for one year. In one day, it provides more energy than our current population would consume in 27 years. In fact, the amount of solar radiation striking the earth over a three-day period is equivalent to the energy stored in all fossil energy sources. It was estimated that the global electricity production in 2014 exceeded 24,000 TWh. Of them, only a small fraction (7%) was produced by using sun and wind. Increasing this fraction by 1% would lead to a reduction of CO₂ emission of roughly 1.32×10^8 tons.

Although solar energy is a free, inexhaustible resource, yet harnessing it is a relatively new idea. Solar cells are devices that convert a radiative input into an electric current. A photovoltaic (PV) cell is an electrical device that converts the energy of light directly into electricity by the PV effect, which was discovered by Alexander-Edmond Becquerel in 1839. The first PV device was built, using a Si pn junction, by Russell Ohl in 1939, but the biggest jumps in efficiency came with the advent of the transistor and accompanying semiconductor technology.

There are several advantages of photovoltaic solar power that makes it one of the most promising renewable energy sources in the world. It is non-polluting, has no moving parts that could break down, requires little maintenance and no supervision, and has a lifetime of 20–30 years with low running costs. It is especially unique because no large-scale installation is required. Remote areas can easily produce their own supply of electricity by constructing as small or as large of a system as needed. PV generators are simply distributed to homes, schools, or businesses, where their assembly requires no extra development or land area and their function is safe and quiet. Solar energy is most sought today in developing countries, the fastest growing segment of the PV market. Governments are finding its modular, decentralized character ideal for filling the electric needs of the thousands of remote villages in their countries. It is much more practical than the extension of expensive power lines into remote areas, where people do not have the possibility to pay for conventional electricity. There are only two limitations in using solar power, related to the real amount of sunlight available and the installation costs of PV modules. Manifestly enough, the amount of sunlight a location receives varies greatly depending on geographical location, time of day, season, and clouds—not necessarily in a proper synchronicity with the request of electric power. Instead, installation costs (and, consequently, also energy costs) are among the drivers of research for novel PV materials and module engineering.

4.1.2 *Solar Spectrum*

The solar spectrum typically extends from the IR to the UV region, wavelengths ranging from 4 to 0.2 μm . But the intensity is not uniform. A typical solar spectrum, as a plot of spectral irradiance versus wavelength, is shown in Fig. 4.1. The solar spectrum can be approximated by a blackbody radiation curve at temperature of approximately 5250 °C. There is also a difference in the spectra measured at the top of the atmosphere and at the surface, due to atmospheric scattering and absorption. The path length of the light in the atmosphere depends on the angle, which will vary with the time of day. This is given by the air mass number (AM), which is the secant of the angle between the sun and the zenith.

In Fig. 4.1a, the AM0 spectrum is based on ASTM standard E 490 and is used for satellite applications [1]. The AM1.5G spectrum, based on ASTM standard G173, is for terrestrial applications and includes direct and diffuse light. It integrates to 1000 W/m^2 . The AM1.5D spectrum, also based on G173, is for terrestrial applications but includes direct light only. It integrates to 888 W/m^2 [2]. The spectrum in Fig. 4.1b has been obtained from the AM1.5G spectrum of Fig. 4.1a by converting power to photons per second per m^2 . Photon spectra $\Phi^0(\lambda)$, exemplified in Fig. 4.1b, are more convenient for solar cell assessments.

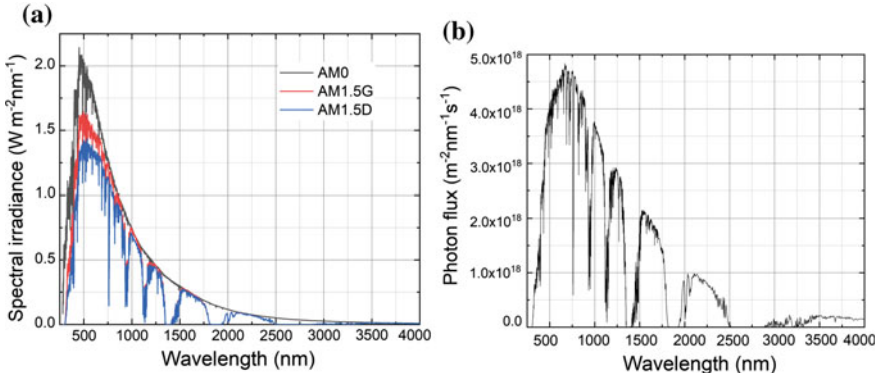


Fig. 4.1 Solar energy spectra. **a** Data expressed in watts per m^2 per 1 nm bandwidth for AM0 [1] and for AM1.5G and AM1.5D spectra [2]. **b** The AM1.5G data expressed in terms of impinging photons per second per m^2 per nm [3]

Standard spectra are needed in solar cell research, development, and marketing because the actual spectrum impinging on a cell in operation can vary due to weather, season, time of day, and location. Having standard spectra allows the experimental solar cell performance of one device to be compared to that of other devices and to be judged fairly, since the cells can be exposed to the same agreed-upon spectrum. The comparisons can be done even in the laboratory since standard distributions can be duplicated using solar simulators.

4.1.3 Solar Cell I-V Characteristics

It is possible to calculate the *I-V* characteristics of the solar cell by considering its equivalent circuit. The *I-V* characteristics depend on the intensity of the incident radiation and also on the operating point (external load) of the cell. Consider a pn junction solar cell under illumination, as shown in Fig. 4.2. If the external circuit is a short circuit (external load resistance is zero) then the only current is due to the generated electron hole pairs (EHPs) by the incident light. This is called the photocurrent, denoted by I_{ph} . Another name for this is the short circuit current, I_{sc} . By definition of current, this is opposite to the photocurrent and is related to the intensity of the incident radiation, I_{op} , by

$$I_{\text{sc}} = -I_{\text{ph}} = -k I_{\text{op}} \quad (4.1)$$

where k is a constant that depends on the particular device. It is equivalent to an efficiency metric that measures the conversion of light into EHPs.

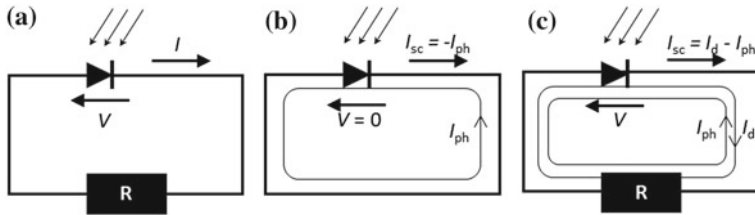


Fig. 4.2 **a** pn junction solar cell under illumination with an external load. The equivalent circuit **b** without and **c** with an external load. The illumination causes a photocurrent to flow through the external circuit. When an external load is applied the potential drop across it creates a forward bias current, that opposes the photocurrent

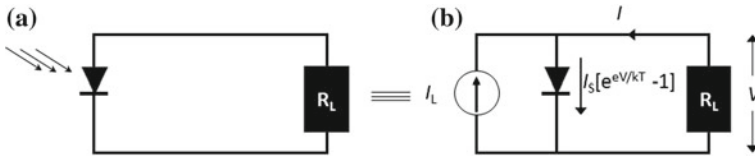


Fig. 4.3 **a** A solar cell connected to an external load. **b** Equivalent circuit, with a constant current source, a forward biased pn junction and the external load. The current from the forward biased pn junction opposes the constant current source

Consider instead the case when there is an external load R (Fig. 4.2). The equivalent circuit for this case is shown in Fig. 4.3. There is a voltage across the external load, given by $V = IR$. This voltage opposes the built-in potential and reduces the barrier for carrier injection across the junction. This is similar to a pn junction in forward bias, where the external bias causes injection of minority carriers and increased current. This forward bias current opposes the photocurrent generated within the device due to the solar radiation. This is because I_{ph} is generated due to electrons going to the n side and holes to the p side due to the electric field within the device (drift current) while the forward bias current is due to diffusion current caused by the injection of minority carriers. Thus, the net current can be written as

$$I = -I_{ph} + I_d \quad (4.2)$$

$$I_d = I_{s0} \left[\exp \left(\frac{eV}{k_B T} \right) - 1 \right] \quad (4.3)$$

$$I = -I_{ph} + I_{s0} \left[\exp \left(\frac{eV}{k_B T} \right) - 1 \right] \quad (4.4)$$

where k_B is the Boltzmann constant, I_d is the forward bias current that can be written in terms of the reverse saturation current, I_{s0} , and of the external voltage, V . The overall I - V characteristics is plotted in Fig. 4.4. In the absence of light, the dark characteristics is similar to the I - V curve of a pn junction. The presence of light (I_{ph}) has the effect of shifting the I - V curve down. From Fig. 4.4, it is possible to define a

Fig. 4.4 I - V characteristics of Si pn junction solar cell under dark conditions and under illumination with light of increasing intensity. Short circuit current and open circuit voltage both increase with increasing illumination

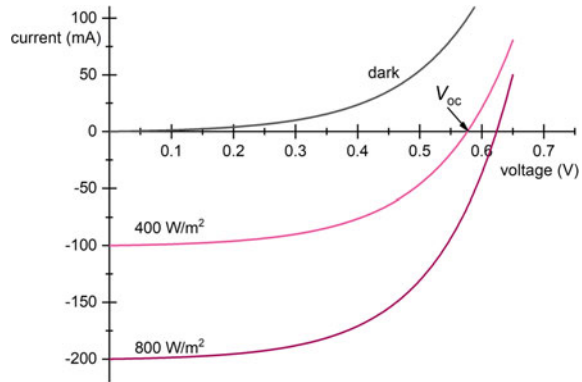


photo current I_{ph} , which is the current when the external voltage is zero and an open circuit voltage, V_{oc} , which is the voltage when the net current in the circuit is zero. Using (4.4), V_{oc} can be calculated as

$$I_{\text{ph}} = I_{\text{s0}} \left[\exp \left(\frac{eV_{\text{oc}}}{k_{\text{B}}T} \right) - 1 \right] \quad (4.5)$$

$$V_{\text{oc}} \approx \frac{k_{\text{B}}T}{e} \ln \left[\frac{I_{\text{ph}}}{I_{\text{s0}}} \right] \quad (4.6)$$

The higher the photon flux, the higher is the value of I_{ph} [by (4.1)], and the higher the value of V_{oc} . Similarly, lower reverse saturation current I_{s0} can also cause higher V_{oc} . In turn, I_{s0} can be lowered by choosing a material with a higher band gap, E_g , which will cause the intrinsic carrier density n_i to be lower. But this will also reduce the range of wavelengths that can be absorbed by the material, which will have the effect of lowering I_{ph} . The total power in the solar cell circuit is given by

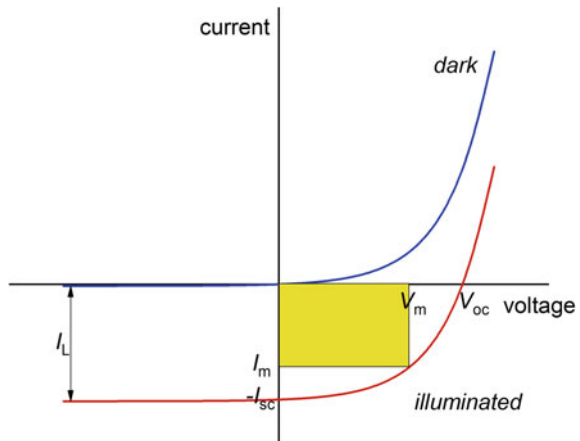
$$P = IV = I_{\text{s0}}V \left[\exp \left(\frac{eV}{k_{\text{B}}T} \right) - 1 \right] - I_{\text{ph}}V \quad (4.7)$$

For maximum power, its derivative with respect to the voltage should be zero. This gives a recursive relation between current and voltage:

$$\frac{dP}{dV} = 0 \quad (4.8)$$

$$I_m \approx I_{\text{ph}} \left(1 - \frac{k_{\text{B}}T}{eV_m} \right) \quad (4.9)$$

Fig. 4.5 *I-V* curve for a solar cell with maximum power indicated by the shaded area. The corresponding voltage and current are V_m and I_m . The value depends on the external load applied



$$V_m \approx V_{oc} - \frac{k_B T}{e} \ln \left(1 + \frac{e V_m}{k_B T} \right) \quad (4.10)$$

$$P_m \approx I_m V_m \approx I_{ph} \left[V_{oc} - \frac{k_B T}{e} \ln \left(1 + \frac{e V_m}{k_B T} \right) - \frac{k_B T}{e} \right] \quad (4.11)$$

The area under the curve in Fig. 4.5, corresponding to I_m and V_m , gives the maximum power. From (4.11), it can be seen that the maximum power is directly proportional to V_{oc} and can be increased by decreasing I_{sc} .

4.1.4 Solar Cell Efficiency

The total power per area (p_{in}) impinging on a cell for a given photon spectrum $\Phi^0(\lambda)$ is the integral of the incoming energy per time per area per bandwidth over the entire photon spectrum; i.e.,

$$p_{in} = \int_{\lambda} \frac{hc}{\lambda} \Phi_0(\lambda) d\lambda \quad (4.12)$$

A typical $\Phi_0(\lambda)$, expressed as photons/time/area/bandwidth, is plotted in Fig. 4.1b. In (4.12) the quantity h is the Planck constant and c is the speed of light.

Since the maximum electrical power per area p_m is the maximum power P_m divided by the cell area, device efficiency η is written as

$$\eta = \frac{p_m}{p_{in}} \quad (4.13)$$

For cells collecting light over a larger area than that generating the current (i.e. for concentrator solar cells), this expression is replaced by

$$\eta = \frac{A_s p_m}{A_c p_{in}} \quad (4.14)$$

where A_s is the solar cell area generating current and A_c is the area collecting the photons. The advantage of a concentrator configuration lies in its being able to harvest more incoming solar power with a given cell size.

The ideally shaped current density-voltage (J - V) characteristic would be rectangular and would deliver a constant current density J_{sc} until the open-circuit voltage V_{oc} . For such a characteristic, the maximum power point would have a current density of J_{sc} and a voltage of V_{oc} . A term called *fill factor* (FF) is introduced to measure how close a given characteristic is to conforming to the ideal rectangular J - V shape. The fill factor is given by

$$FF = \frac{p_m}{J_{sc} V_{oc}} \quad (4.15)$$

By definition, $FF \leq 1$.

A comprehensive state of current research in different solar cell technologies and their efficiency was reported in Fig. 1.2. It clearly shows the ongoing effort to increase the conversion efficiency of PV cells and modules, primarily for competitive advantage. It is well known [4–6] that to increase the efficiency of solar cells, it is important to choose a semiconductor material with an appropriate band gap that matches the solar spectrum. This will enhance the electrical and optical properties. Improving the method of charge collection is also useful for increasing the efficiency.

The most efficient type of solar cell to date is a multi-junction concentrator solar cell with an efficiency of 46.0% [7] produced by Fraunhofer ISE in December 2014. The highest efficiencies achieved without concentration include a material by Sharp Corporation at 35.8% using a proprietary triple-junction manufacturing technology in 2009 [8], and Boeing Spectrolab (40.7% also using a triple-layer design). The US company SunPower produces cells that have an efficiency of 21.5%, well above the market average of 12–18% [9]. Several companies have begun embedding power optimizers into PV modules called smart modules. These modules perform maximum power point tracking (MPPT) for each module individually, measure performance data for monitoring, and provide additional safety features.

4.1.5 Solar Cell Applications

Solar PV energy conversion is used today for both space and terrestrial energy generation. Solar arrays can be used to power orbiting satellites and other spacecraft, and in remote areas as a source of power for roadside emergency telephones, remote sensing, and cathodic protection of pipelines.

The International Space Station is a good example of solar cells being used in space. When finished, the station will have the most powerful solar array in space. Four sets of gold coloured wings (each one being 72 m long and larger than the space station itself) will contain 250,000 solar cells and the whole array will be able to power a small neighbourhood. Some of the energy will be used immediately, such as in life support machines, while some will be stored in batteries for when the station is not in use.

The need for much more extensive use of solar cells in terrestrial applications is becoming clearer with the growing understanding of the true cost of fossil fuels and with the widespread demand for renewable and environmentally acceptable terrestrial energy resources. Solar powered cars are cars which are powered by an array of PV cells. The electricity created by the solar cells either directly powers the vehicle through a motor, or goes into a storage battery.

To increase the use of solar photovoltaics, more effort is needed to enhance cell energy-conversion efficiency η , to increase module (a grouping of cells) lifetimes, to reduce manufacturing costs, installation costs, and the environmental impact of manufacturing and deploying solar cells.

4.2 Review of Photovoltaic Technologies: Types and Classifications

4.2.1 Overview

Solar cells are typically named after the semiconducting material they are made of. These materials must have certain characteristics in order to absorb sunlight. Some cells are designed to handle sunlight that reaches the Earth's surface, while others are optimized for use in space. Solar cells can be made of only one single layer of light-absorbing material (single-junction) or use multiple physical configurations (multi-junctions) to take advantage of various absorption and charge separation mechanisms. Based on either the active materials (i.e. the primary light-absorbing materials), solar cells can be classified into first, second and third generation cells (Fig. 4.6).

The first generation cells—also called conventional, traditional or wafer-based cells—are made of crystalline silicon, the commercially predominant PV technology, that includes materials such as polysilicon and monocrystalline silicon. Compared to other photovoltaic technologies, silicon solar cells have the advantage of using a photoactive absorber material that is stable, non-toxic, abundant and well understood. Second generation cells are thin film solar cells, that include amorphous silicon, CdTe and CIGS cells and are commercially significant in utility-scale PV power stations, building integrated photovoltaics or in small standalone power system. The third generation of solar cells includes a number of thin-film technologies often described as emerging photovoltaics. Most of them have not yet been commercially applied and are still in the research or development phase. Many use organic materials, often

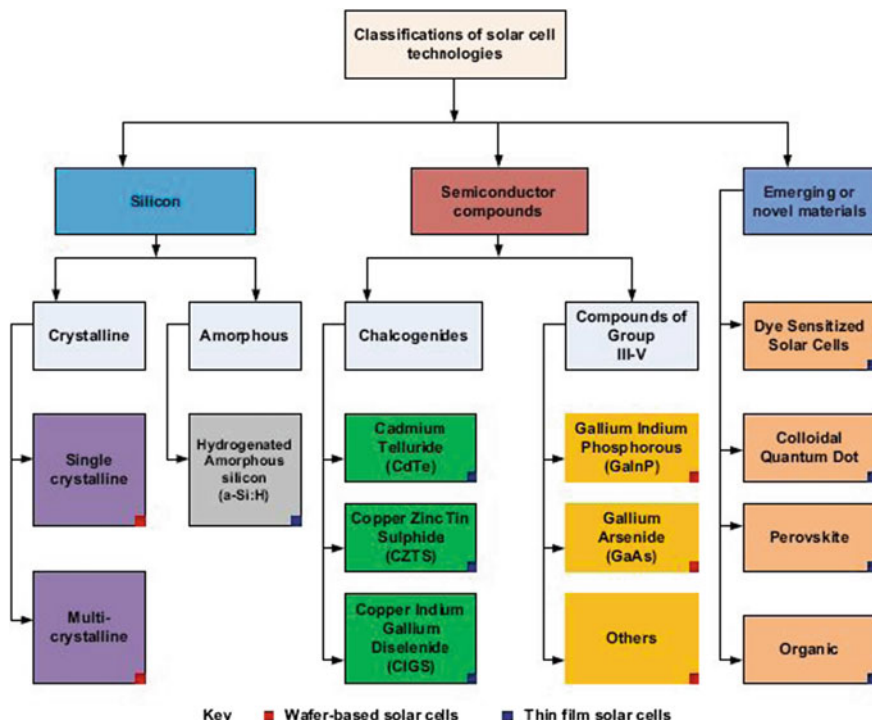


Fig. 4.6 Classification of solar cells based on the primary active material. Reprinted with permission from [10]. Copyright 2017 Elsevier

organometallic compounds as well as inorganic substances. Despite the fact that their efficiencies are low and the stability of the absorber material is often too short for commercial applications, there is a lot of research invested into these technologies as they promise to achieve the goal of producing low-cost, highly efficient solar cells.

4.2.2 The First-Generation Cells

As already mentioned, PV solar energy offers humankind a useful instrument to build a globally prosperous, sustainable, and environmentally friendly society. Its recent success as an economically viable source of electricity is founded on a simple optoelectronic device, the crystalline silicon solar cell. The year 2014 witnessed the breaking of the historic 25.0% power conversion efficiency record for crystalline silicon solar cells, which was set by the University of New South Wales (UNSW), Australia, in 1999 [11, 12].

4.2.2.1 Crystalline Silicon (c-Si) Solar Cells

Most PV technologies that have been deployed at a commercial level have been produced using silicon, with wafer-based crystalline silicon (c-Si) currently the most popular solar cell because it exhibits stable photo-conversion efficiency and can be processed into efficient, nontoxic and very reliable PV cells [13]. Wafer-based c-Si cells leverage over 50-year manufacturing experience; a vast technology base in terms of materials, established production processes and device designs; far-reaching track record based on performance, longevity and reliability as well as maximum performance of flat-plate technologies with a massive database [14].

A key disadvantage is that c-Si is a poor absorber of light due to its indirect energy bandgap of roughly 1.1 eV at room temperature [15], encouraging the use of fairly thick, rigid and brittle wafers to absorb most of the incident light in the absence of advanced light-trapping mechanisms [14–16]. This drawback culminates into huge capital outlay, especially as it relates to Balance of System (BOS), low power to-weight ratios and limitations in terms of flexibility and design of modules [16, 17].

Despite such drawbacks, c-Si cells still constitute roughly 90% of global module production and are the most developed of all solar cell technologies [18]. The main technological problems of c-Si include the high level requirements for material purification, the module form factor restrictions, batch-based cell production and module integration of processes with fairly low throughput [13, 15, 16]. Current research areas are targeted at manufacturing wafer-based solar cells at lower costs and reduced complexity [19]; increased modular conversion efficiencies; reduction in the quantity of silicon used per watt and reduction on the reliance on silver for contact metallization [16].

Emerging research areas for c-Si solar cells involve the use of thin membranes instead of wafers as starting material to produce thin-film c-Si PV [20]. Solar cells based on this technique have the potential to improve upon the limitations of conventional wafer-based c-Si cells, whilst retaining most of the advantages derived from the use of silicon [13]. They guarantee high quality performance with reduced manufacturing complexity and module cost. Thin-film c-Si PV can endure materials with lower quality in terms of smaller grains and higher impurity levels. They use lower cost materials, enabling flexible and lightweight modules which allows for high-throughput processing [14, 16]. The main disadvantage is that their performance efficiencies are low compared to wafer-based c-Si, and their manufacturing route in terms of scalability is unproven [13].

Wafer-based c-Si are produced from slices of either single-crystal silicon (sc-Si) or multicrystalline silicon (mc-Si), with each type boasting a market share of 35% and 55% respectively in 2014 [18]. Single-crystal silicon cells are typically made using the Czochralski (CZ) process, float-zone (FZ), or Bridgman techniques adopted for the production of wafers for integrated circuits [17]. They are endowed with higher crystal quality which increases charge extraction and power conversion efficiencies, increasing the need for more expensive wafers by 20–30% [16, 17]. On the other hand, mc-Si cells are fabricated using silicon feedstock through casting

technology [21]. They consist of several randomly oriented crystals or grains, which introduce boundaries that hinder electron flow or charge extraction and stimulate them to recombine with holes to decrease the power output of the solar cell [16, 17]. This makes mc-Si cells less efficient but less expensive to fabricate than sc-Si [17]. Efficiency at a lab scale for both sc-Si and mc-Si are 25.6% and 20.4% respectively [22]. For large-area modules, the efficiencies are 20.8% and 18.5% for sc-Si and mc-Si respectively [23].

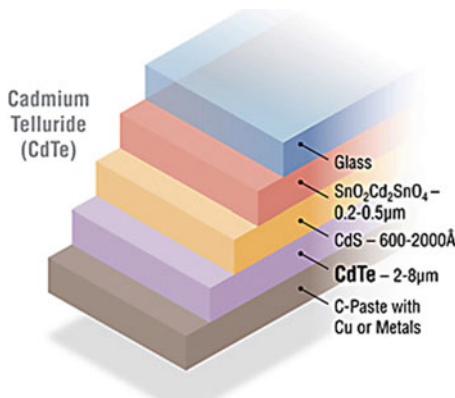
4.2.2.2 Amorphous Silicon (a-Si) Solar Cells

Amorphous silicon (a-Si) dominated the development of thin-film PV industry for some time because of its potential for low-cost production compared with c-Si. However, progress and development was hampered by the challenges relating to solar conversion efficiency and stability [14]. Amorphous silicon offers a stronger absorption coefficient than c-Si, enabling high absorption of solar radiation. They have a wider bandgap of about 1.7 eV compared to 1.12 eV for c-Si, yielding a high absorption characteristic. However, this large bandgap reduces the range of wavelengths that can be absorbed [16]. This is because the selection rules in indirect bandgap semiconductors that significantly limits absorption coefficient of c-Si does not apply to a-Si [17]. Amorphous solids are materials which lack long range crystalline order, containing large numbers of structural and bonding defects, known as dangling bonds [14, 17]. These bonds provide places for electrons to recombine with holes but they are passivated with hydrogen, yielding what is known as hydrogenated amorphous silicon (a-Si:H). The existence of dangling bonds and the mobility of hydrogen results in instability of a-Si:H cell under solar irradiation, leading to an initial decrease in efficiency [14]. This phenomenon is known as the Staebler–Wronski effect [24]. Although this phenomenon can be reversed through annealing at modest temperature over 150 °C, such an approach limits the maximum efficiency that can be attained and affects their long-term stability as well as manufacturing costs [25]. Hydrogenated amorphous silicon solar cells are well suited for small-scale applications with low-power requirements, but their reduced efficiency compared to other well-established thin-film PV technologies have limited their acceptance by the market [16]. The highest efficiency recorded is 13.4% for a triple-junction lab sample [23].

4.2.3 The Second Generation Cells

Although the cost of silicon-based solar cells have reduced considerably, stagnation in their performance conversion efficiencies prompted scientists and engineers to ponder over the use of alternative materials. This led to the development of solar cells based on semiconductor compounds.

Fig. 4.7 Graphics showing the five layers that comprise CdTe solar cells. Reprinted with permission from [30], Copyright 2015, Science Publishing Group



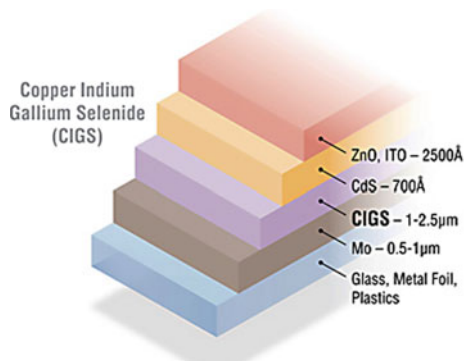
4.2.3.1 Cadmium Telluride (CdTe) Solar Cell

Cadmium telluride (CdTe) solar cell describes a PV technology that is based on the use of CdTe, a thin semiconductor layer designed to absorb and convert sunlight into electricity (Fig. 4.7). On a lifecycle basis, CdTe PV has the smallest carbon footprint, lowest water use and shortest energy payback time of all solar technologies [26, 27]. The toxicity of cadmium is an environmental concern mitigated by the recycling of CdTe modules at the end of their lifetime [28]. The usage of rare materials may also become a limiting factor to the industrial scalability of CdTe technology in the mid-term future. With a share of 5.1% of worldwide PV production, CdTe technology accounted for more than half of the thin film market in 2013 [29].

4.2.3.2 Copper Indium Gallium Selenide (CIGS) Solar Cells

The bandgap of Copper Indium Gallium Selenide ($\text{CuIn}_x\text{Ga}_{(1-x)}\text{Se}_2$, or CIGS) is 1.7 eV, which is high enough to cover the optimum region of bandgaps for solar cells based on single-junction, but the best devices are fabricated at a bandgap of 1.2 eV [14]. Figure 4.8 displays the five layers that comprise CIGS solar cells. The record efficiency for laboratory-based CIGS devices is around 20% with a world record efficiency of 20.3% [31]. CIGS solar cells exhibit high radiation resistance, making them suitable for space applications [16]. Major technical challenges include difficulty in controlling film stoichiometry and properties, low V_{oc} (roughly 0.64 eV) due to defects in materials, narrow understanding of the effects of grain boundaries and the processing of higher-bandgap alloys to allow for the fabrication of multi-junction devices [13, 14, 16]. Solar cells based on CIGS thin-film and related PV materials (e.g. CGS and CIS) have great potentials, provided expensive and scarce elements such as gallium and indium could be replaced or at least partially replaced by other elements.

Fig. 4.8 Graphics showing the five layers that comprise CIGS solar cells. Reprinted with permission from [30], Copyright 2015, Science Publishing Group



4.2.3.3 Gallium Arsenide (GaAs) Solar Cell

Gallium Arsenide (GaAs) has the well known advantages over silicon in that its electron mobility largely exceeds that of Si [14]. Furthermore, it enables single-junction III-V PV cells with high optical absorption coefficients, very low non-radiative energy loss, a near optimum direct bandgap, and good values of minority carrier lifetimes and mobility [15, 16]. These features make GaAs an excellent candidate material for fabrication of solar cells (Fig. 4.9) with efficiencies twice those of silicon [13]. Of any material system, GaAs-based solar cells hold the record regarding the efficiency at which they convert sunlight into electricity, with power conversion efficiencies of 28.8% and 24.1% for lab cells and modules respectively [22, 23]. A key disadvantage is the high cost of the material in terms of producing epitaxial layers or device quality substrates as compared to the crushing commercial edge associated with silicon [15]. This is largely due to factors such as imperfections of its crystal and undesirable impurities which reduce device efficiencies, rendering low cost deposition routes impossible [15]. This limits the large-scale deployment of GaAs solar cells, restricting their use to niche applications (e.g. space communications where higher efficiencies, better radiation resistance and improved power/weight ratios are required), in which their distinct capabilities justify their exorbitant cost. Cost-effective production processes for GaAs solar cells which involve the reuse of GaAs wafers have been reported [15, 32, 33], but have not been demonstrated in high-volume production [16].

4.2.3.4 Multi-junction (MJ) Solar Cell

Multi-junction (MJ) solar cells are solar cells with multiple p-n junctions made of different semiconductor materials (Fig. 4.10). The p-n junction of each material will produce electric current in response to different wavelengths of light. The use of multiple semiconducting materials allows the absorbance of a broader range of wavelengths, improving the efficiency with which the cell converts the sunlight into

Fig. 4.9 Cross-sectional diagram of GaAs solar cell

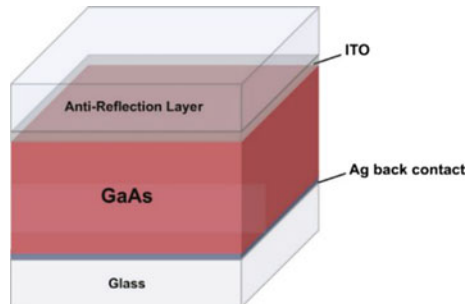
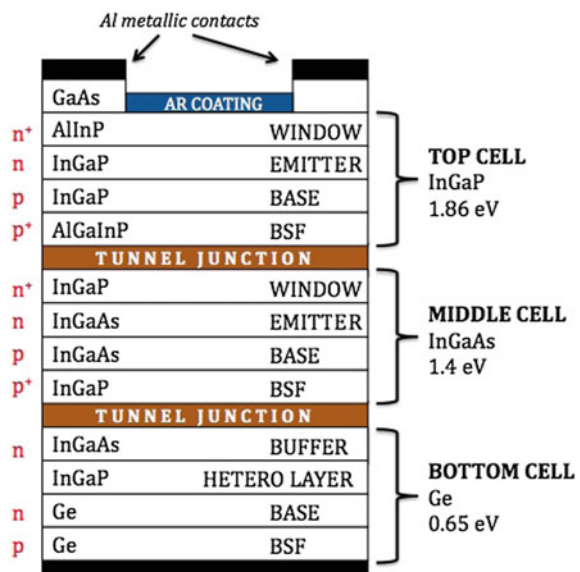


Fig. 4.10 Multi-junction solar cell (courtesy of Fraunhofer Institute for Solar Energy Systems)



electrical energy. Traditional single junction cells have a maximum theoretical efficiency of 34%. Theoretically, an infinite number of junctions would have a limiting efficiency of 86.8% under highly concentrated sunlight [34].

4.2.3.5 Concentrated PV Cell

Contrary to conventional photovoltaic systems, a concentrating photovoltaic (CPV) system uses an advanced optical system to focuses a large area of sunlight onto small, but highly efficient, multi-junction (MJ) solar cells for maximum efficiency (Fig. 4.11). Especially high concentrating photovoltaic (HCPV) systems have the potential to become competitive in the near future. They possess the highest efficiency of all existing PV technologies, and a smaller photovoltaic array also reduces the balance of system costs.

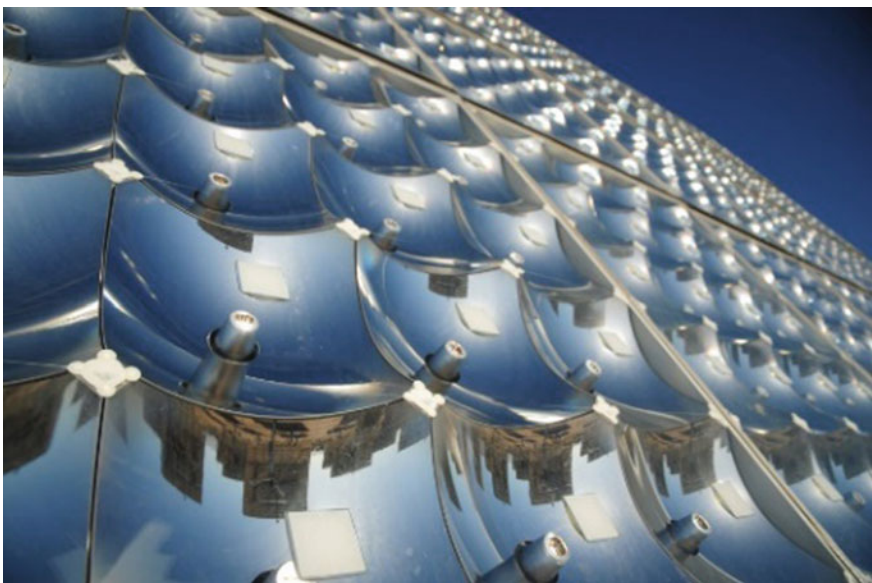


Fig. 4.11 Concentrated solar Cell. Reprinted with permission from [30], Copyright 2015, Science Publishing Group

4.2.4 *The Third Generation Cells*

4.2.4.1 Dye-Sensitized Solar Cell (DSSC)

Dye Sensitized solar cells (DSSC), also sometimes referred to as dye sensitised cells (DSC), were invented in 1991 by Professor Michael Grätzel and Dr Brian O'Regan at École Polytechnique Fédérale de Lausanne (EPFL), Switzerland and is often referred to as the Grätzel cell. To some extent, this new class of solar cells can be seen as artificial photosynthetic devices due to the way in which they copy natural conversion of light energy. DSSC is a technology that can be used to produce electricity in a wide range of light conditions, indoors and outdoors, enabling the user to convert both artificial and natural light into energy to power a broad range of electronic devices. A DSSC is a low-cost solar cell belonging to the group of thin film solar cells. It is based on a semiconductor formed between a photo-sensitized anode and an electrolyte, a photoelectrochemical system, as illustrated in Fig. 4.12. Dye Sensitized solar cells have a number of attractive features: they are simple to make by using conventional roll-printing techniques, are semi-flexible and semitransparent, and most of the materials used are low-cost. Although its conversion efficiency is less than the best thin-film cells, in theory its price/performance ratio should be good enough to allow them to compete with fossil fuel electrical generation by achieving grid parity.

4.2.4.2 Quantum Dot Sensitized Solar Cells (QDSSCs)

Similar to DSSCs, Quantum Dot Sensitized Solar Cells (QDSSCs) consist of a QD sensitized photoelectrode and a counter electrode separated by a liquid electrolyte, as presented in Fig. 4.13. In general, wide bandgap metal oxide (TiO_2 , ZnO , and SnO_2 ; in the following TiO_2 is used as an example) nanostructures (e.g. nanoparticulate, nanorods, nanowires, nanotubes, and inverse opal) are used as the photoelectrodes in QDSSCs. QDs can be deposited on the photoelectrodes by two kinds of in-situ growth methods, i.e. chemical bath deposition and successive ionic layer absorption and reaction, and by adsorption of pre-synthesized QDs through direct adsorption or linker-assisted QD deposition method [35–37]. A number of QDs, such as CdS , CdSe , CdTe , PbS , Sb_2S_3 , CuInS_2 , CdSeTe , $\text{CuInSe}_{1-x}\text{S}_x$ and core-shell structure or double layered QDs, such as CdSe/CdTe , ZnTe/CdSe , CdS/CdSe , PbS/CdS , have been applied as sensitizers in QDSSCs [35]. Aqueous polysulfide solution is most

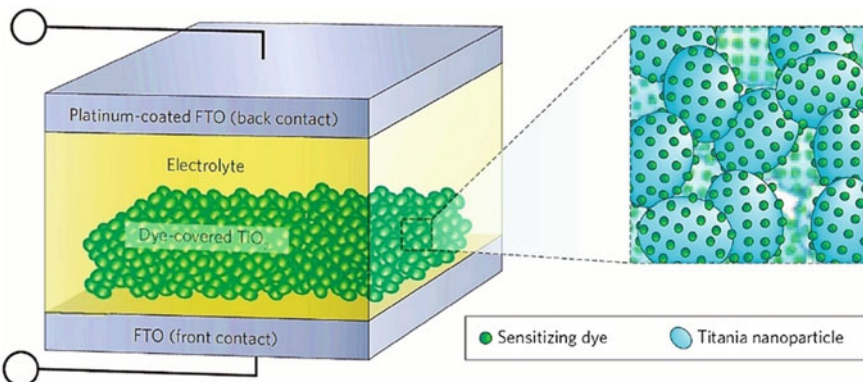
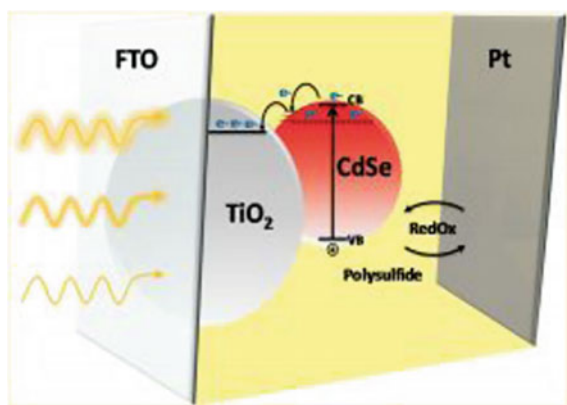


Fig. 4.12 Schematics of DSSC. Reprinted with permission from [30], Copyright 2015, Science Publishing Group

Fig. 4.13 Schematics of QDSSC based on CsSe QDs. Reprinted with permission from [40], Copyright 2011, American Chemical Society



widely used as the electrolyte for QDSSCs. Some solid-state hole transport materials (HTMs), such as P3HT, Spiro-OMeTAD, and CuSCN, are also used as hole scavenging and transport layers in QDSSCs [38, 39]. For the polysulfide electrolyte, copper sulfide (Cu_2S) is the most used counter electrode. For the solid-state HTMs, gold and silver are commonly used as electrodes.

4.2.4.3 Polymer Solar Cell

As displayed in Fig. 4.14, the material used to absorb the solar light in polymer solar cell, is an organic material such as a conjugated polymer. The basic principle behind both the polymer solar cell and other forms of solar cells, however, is the

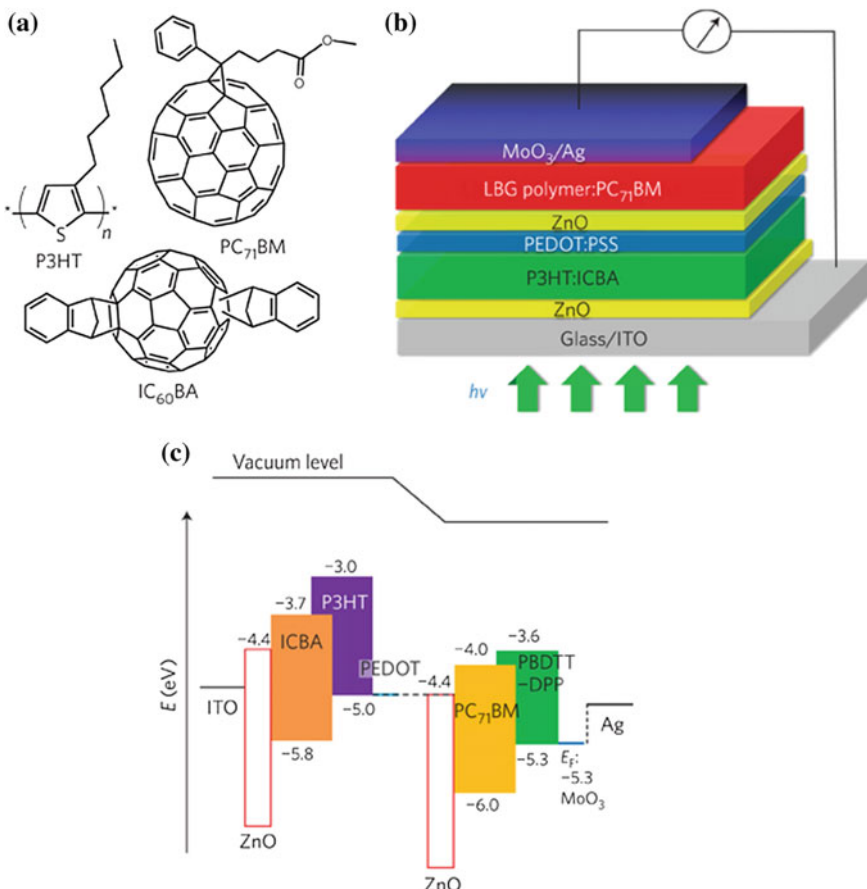


Fig. 4.14 Tandem polymer solar cells: **a** Chemical structures of P3HT, IC₆₀BA and PC₇₁BM, **b** Device structure of the inverted tandem solar cell, **c** Energy diagram of the inverted tandem devices. Reprinted with permission from [41], Copyright 2012, Nature Publishing Group

same. This discovery of conjugated polymers being able to transfer electrons upon doping with iodine made it possible to prepare polymer solar cells and thereby a new research area was born. Polymer solar cells have a potential advantage: that is their ability to be produced from solution. This means that they can be printed or coated, instead of using expensive vacuum deposition as for the first generation silicon solar cells. Polymer solar cells include organic solar cells (also called *plastic solar cells*). Compared to silicon-based devices, polymer solar cells are lightweight (which is important for small autonomous sensors), potentially disposable and inexpensive to fabricate (sometimes using printed electronics), flexible, customizable on the molecular level and potentially have less adverse environmental impact. Polymer solar cells also have the potential to exhibit transparency, suggesting applications in windows, walls, flexible electronics, etc.

4.2.4.4 Perovskite Solar Cell

A new arrival in the family of solar cells technologies is the organic-inorganic halide perovskite solar cells, which have advanced rapidly in only a few years after their invention, due to their low cost, high efficiency and straightforward architecture [42]. The power conversion efficiency of perovskite cells has been increased from 9.7 [43] to 22.1% [44] with the usage of solid-state organic HTMs, leading to be the best candidate for the third-generation solar cells. To date, organometallic trihalide perovskites $\text{CH}_3\text{NH}_3\text{PbX}_3$ (X is iodine or a mixture of iodine, chlorine and bromine) have been regarded as the most promising light absorption materials for solar energy conversion due to their wide absorption range [45], high extinction coefficient [46],

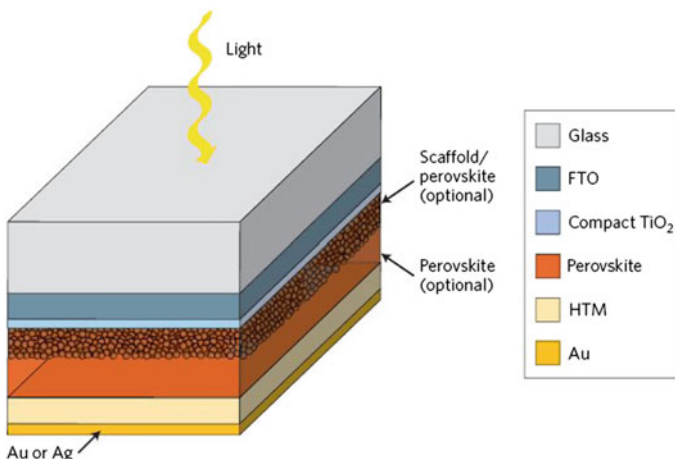


Fig. 4.15 Structure schematics of perovskite solar cells. Reprinted with permission from [49], Copyright 2012, Nature Publishing Group

ambipolar charge transport [47], and long electron-hole diffusion length [48]. Following light absorption, the generation and separation of photogenerated electron hole pairs occur within the bulk of the perovskite absorber, which then need to be in contact with charge-selective n type and p type transport layers for efficient extraction and transportation with minimal recombination losses, as shown in Fig. 4.15.

4.3 Solar Cell Device Physics

4.3.1 *The Prevalent Photovoltaic Physical Process*

The basic four steps needed for photovoltaic energy conversion are:

1. a light absorption process which causes a transition in a material (the absorber) from a ground state to an excited state,
2. the conversion of the excited state into (at least) a free negative and a free positive-charge carrier pair, and
3. a discriminating transport mechanism, which causes the resulting free negative-charge carriers to move in one direction (to a contact that we will call the cathode) and the resulting free positive charge carriers to move in another direction (to a contact that we will call the anode). The energetic, photogenerated negative-charge carriers arriving at the cathode result in electrons which travel through an external path (an electric circuit). While traveling this path, they lose their energy doing something useful at an electrical load, and finally they return to the anode of the cell. At the anode, every one of the returning electrons completes the fourth step of photovoltaic energy conversion, which is closing the circle by
4. combining with an arriving positive-charge carrier, thereby returning the absorber to the ground state.

In some materials, the excited state may be a photogenerated free electron-free hole pair. In such a situation, step 1 and step 2 coalesce. In some materials, the excited state may be an exciton, in which case steps 1 and 2 are distinct.

These four steps mainly contribute to the photovoltaic improvement of the various man-made photovoltaic devices. The following give the brief introduction to their own unique working principles for several representative solar cells.

4.3.2 *Silicon Solar Cells*

There are several different ways in which electron- and hole-selective contacts can be implemented on a silicon wafer. Classically, they have been formed by introducing a high concentration of dopants near the two surfaces of the wafer. Figure 4.16 shows the schematic structure of such a solar cell, based on a p-type crystalline silicon

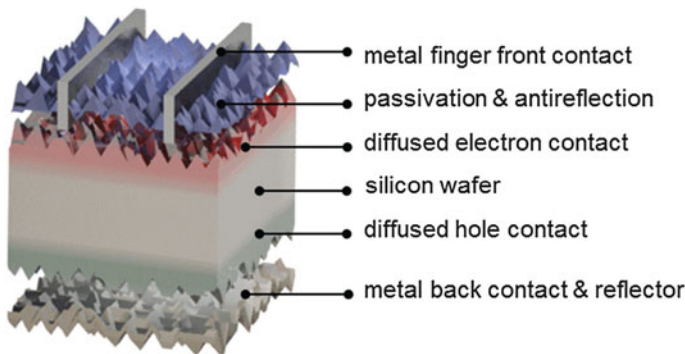
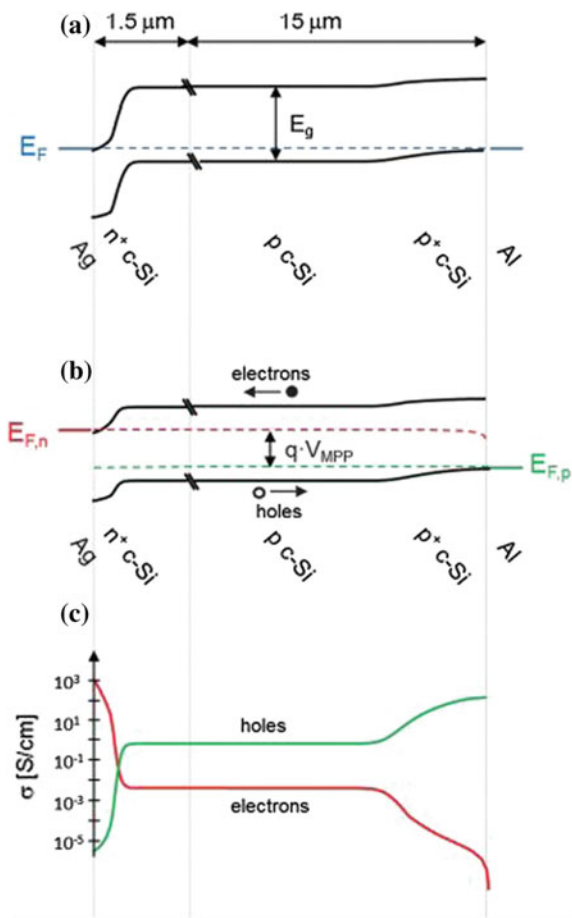


Fig. 4.16 Schematic of the components of a classic dopant-diffused silicon homojunction solar cell. Electrons and holes generated in the textured p-type silicon wafer are extracted via phosphorus-doped (front, red) and aluminum-doped (back, green) regions. The front surface is passivated with hydrogenated amorphous silicon nitride, which acts simultaneously as antireflection coating. Aluminum is employed as the back contact and serves as a dopant source during firing. Reprinted with permission from [52], Copyright 2016, Royal Society of Chemistry

wafer, a front phosphorus diffusion, and a back aluminum-doped region. For the classic dopant-diffused homojunction silicon solar cell, the choice of p-type material stems from both historical and technological reasons. The first applications of silicon solar cells in the 1950s were to power satellites, where p-type cells featured improved space-radiation hardness, compared to their n-type counterparts [50, 51].

Figure 4.17a shows the energy band diagram in equilibrium for such a silicon solar cell. The bending of the bands in the vicinity of both diffused regions indicates (i) that the concentrations of electrons and holes vary strongly with position (which can be described as a gradient of their chemical potentials), and (ii) that an electric field (evidenced by the gradient of the bands) is present. These two forces, the gradients of the chemical and electrical potentials, are identical in magnitude and opposite in direction, meaning that there is no net force acting on the carriers and no net movement, as indicated by the constant Fermi energy E_F . The energy band diagram in Fig. 4.17b shows that, at the maximum power point, the Fermi energy splits into two quasi-Fermi energies, as a consequence of the excess concentration of carriers generated by the one-sun illumination. Although indistinguishable in the graph, a very small gradient of the quasi-Fermi energies drives electrons to the left and holes to the right. The reason for such directional flow of the two charge carriers can be seen in Fig. 4.17c, which shows that the electron conductivity is orders of magnitude higher than the hole conductivity on the left (the n^+ region), and the hole conductivity much higher than the electron conductivity on the right (in the p^+ region). The output power is limited by recombination at the rear metal contact and in the absorber region, with the front phosphorus diffusion, and its surface also causing significant losses.

Fig. 4.17 Energy band diagrams of a standard n⁺pp⁺ silicon solar cell **(a)** in equilibrium and **(b)** at the maximum power point. Representative values were used to model the curves with the program PC1D (p-type wafer doped with $1 \times 10^{16} \text{ cm}^{-3}$ boron atoms, front n⁺ phosphorus diffusion with a surface concentration of $1 \times 10^{20} \text{ cm}^{-3}$ and depth of 0.36 μm, and back p⁺ aluminum-doped region with a surface concentration of $1 \times 10^{19} \text{ cm}^{-3}$ and a depth of 5 μm). **c** The electron and hole conductivities at the maximum power point, indicating that the n⁺ and p⁺ regions preferentially transport electrons or holes, respectively. Reprinted with permission from [52], Copyright 2016, The Royal Society of Chemistry



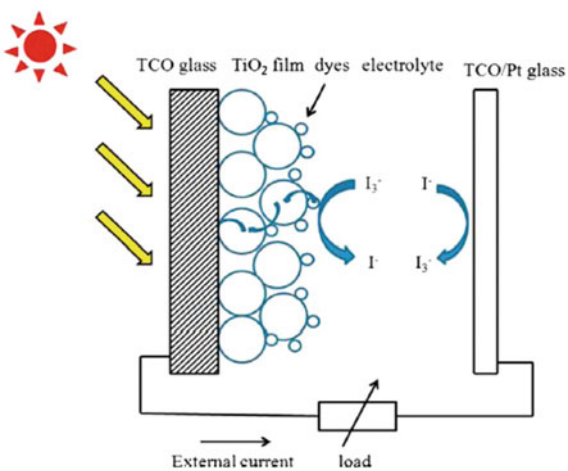
4.3.3 Dye Sensitized Solar Cells

A schematic representation of DSSCs is illustrated in Fig. 4.18. The system is composed of four main components:

1. a photoanode made up of a mesoporous oxide layer (typically, TiO₂) deposited on a transparent conductive glass substrate;
2. a monolayer of dye sensitizers covalently bonded to the surface of the TiO₂ layer to harvest light and generate photon-excited electrons;
3. an electrolyte containing redox couple (typically, I/I₃) in an organic solvent to collect electrons at the counter electrode and effecting dye-regenerating; and
4. a counter electrode made of a platinum coated conductive glass substrate.

When the sunlight strikes the solar cell, dye sensitizers on the surface of TiO₂ film get excited and the electrons in turn get injected into the conduction band of

Fig. 4.18 Schematic diagram of a dye-sensitized solar cell. Reprinted with permission from [53], Copyright 2012, Elsevier



TiO_2 . Within the TiO_2 film, the injected electrons diffuse all the way through the mesoporous film to the anode and are utilized to do useful work at the external load. Finally, to complete the cycle, these electrons are collected by the electrolyte at counter electrode, which in turn are absorbed to regenerate the dye sensitizer.

4.3.4 Quantum Dot Sensitized Solar Cells

As shown in Fig. 4.19a, once electron-hole pairs are generated in the QD sensitizer after optical absorption, photoexcited electrons are injected into the metal oxide electrode and then transported to collection electrode (transparent conducting electrode), while the oxidized QDs are regenerated by electrolyte (hole scavenging medium) and then the oxidized species of redox couple are regenerated at the counter electrode. Figure 4.19b shows the main possible charge transfer processes occurring at $\text{TiO}_2/\text{QD}/\text{electrolyte}$ interfaces, including injection (Inj), trapping (Trp), and recombination (Rec) of both photoexcited electrons and holes [54]. The possible injection paths include electron injection to TiO_2 from LUMO (Inj1) and from electron trapping levels (Inj2) and hole injection to electrolytes from the highest occupied molecular orbital (HOMO) (Inj3) and from hole trapping levels (Inj4). The possible recombination paths are internal recombination of photoexcited electrons and holes in QDs directly (Rec1) and through trapping levels (Rec2), injected electrons in TiO_2 back transfer to QDs (Rec3, at QDTiO_2 interface) and to electrolyte (Rec4, at $\text{TiO}_2/\text{electrolyte}$ interface), recombination of photoexcited electrons in QDs with oxidized species in electrolyte (Rec5, at $\text{QD}/\text{electrolyte}$ interface) [54]. All of the charge transfer processes play important roles for energy conversion efficiency of QDSSCs. In particular, charge recombination at each interface will reduce the charge separation efficiency and charge collection efficiency, which results in poor

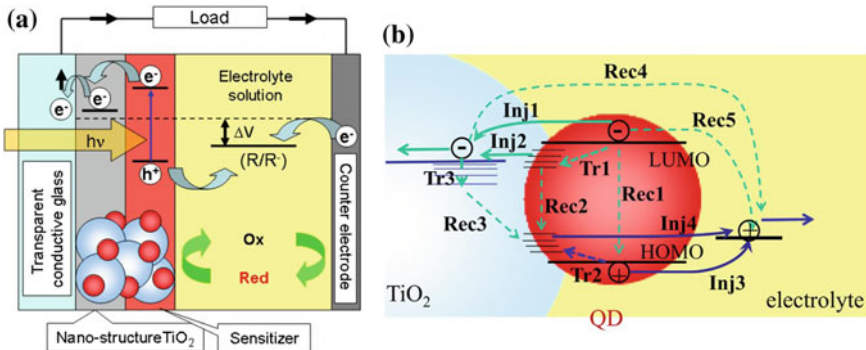


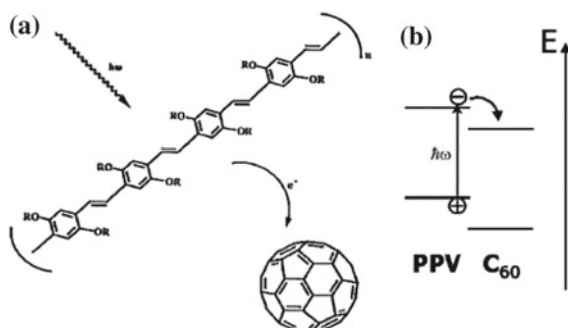
Fig. 4.19 Schematic illustrations of (a) the working principle and configuration of QD sensitized solar cells and b possible charge transfer processes occurring at TiO_2 /QD/electrolyte interfaces, including injection (Inj), trapping (Trp), and recombination (Rec) of photoexcited carriers. Reprinted with permission from [56], Copyright 2016, SPIE

photovoltaic performance, i.e. low J_{sc} , low V_{oc} , and low FF. Here, surface trap states in QDs, which do not exist in molecular dyes of DSCs, are crucial factors for larger recombination and poorer photovoltaic performance in QDSSCs [55]. In the last few years, many strategies, such as (1) surface/interface passivation of QDs and photoelectrodes and (2) use of core-shell QDs or double layered QDs as sensitizers, have been carried out for suppressing the recombination, reducing trapping and improving the injection of electron and holes in the QDSSCs.

4.3.5 Conjugated Polymer-Based Solar Cells

The primary photoexcitations in organic materials do not directly and quantitatively lead to free charge carriers but to coulombically bound EHPs, called excitons. It is estimated that only 10% of the photoexcitations lead to free charge carriers in conjugated polymers [32–58]. For efficient dissociation of excitons, strong electric fields are necessary. Such local fields can be supplied via externally applied electrical fields as well as via interfaces. At an interface, where abrupt changes of the potential energy occur, strong local electrical fields are possible ($E = -\text{grad } U$). Photoinduced charge transfer can occur when the exciton has reached such an interface within its lifetime. Therefore, exciton diffusion length limits the thicknesses of the bilayers [33–59]. Exciton diffusion length should be at the same order of magnitude as the donor acceptor phase separation length. Otherwise, excitons decay via radiative or nonradiative path ways before reaching the interface, and their energy is lost for the power conversion. Donor-acceptor-type bilayer devices can thus work like classical p-n junctions (Fig. 4.20). Exciton diffusion lengths in polymers and in organic semiconductors are usually around 10–20 nm [31–60]. Blending conju-

Fig. 4.20 Illustration of the photoinduced charge transfer (a) with a sketch of the energy level (b). After excitation in the PPV polymer, the electron is transferred to the C₆₀. Reprinted with permission from [61], Copyright 2007, American Chemical Society



gated polymers with electron acceptors, such as fullerenes, is a very efficient way to break apart photoexcited excitons into free charge carriers. Ultrafast photophysical studies show that the photoinduced charge transfer in such blends happens on a time scale of 45 fs. This is much faster than other competing relaxation processes [34–61]. Furthermore, the separated charges in such blends are metastable at low temperatures.

For efficient PV devices, the charge carriers need a driving force to reach the electrodes. A gradient in the chemical potentials of electrons and holes (quasi Fermi levels of the doped phases) is built up in a donor-acceptor junction. This gradient is determined by the difference between the HOMO level of the donor (quasi Fermi level of the holes) and the lowest unoccupied molecular orbital (LUMO) level of the acceptor (quasi Fermi level of the electrons). This internal electrical field determines the maximum open circuit voltage (V_{oc}) and contributes to a field-induced drift of charge carriers. Another driving force can be the concentration gradients of the respective charges, which lead to a diffusion current. The transport of charges is affected by recombination during the journey to the electrodes, particularly if the same material serves as transport medium for both electrons and holes [33–59]. As a last step, charge carriers are extracted from the device through two selective contacts. A transparent indium tin oxide (ITO) matches the HOMO levels of most of the conjugated polymers (hole contact). An evaporated aluminum metal contact with a work function of around 4.3 eV matches the LUMO of acceptor PCBM (electron contact) on the other side.

4.3.6 Perovskite Solar Cells

The primary charge separation in Perovskite Solar Cells (PSCs) occurs at perovskite junctions with TiO₂ and HTM, simultaneously. The ultrafast electron and hole injection from the photoexcited perovskite occurs over similar timescales [62]. The EHPs in perovskites are generated almost instantaneously after photoexcitation and dissociate rapidly in ≈ 2 ps to form electrons and holes with lifetimes up to a microsecond.

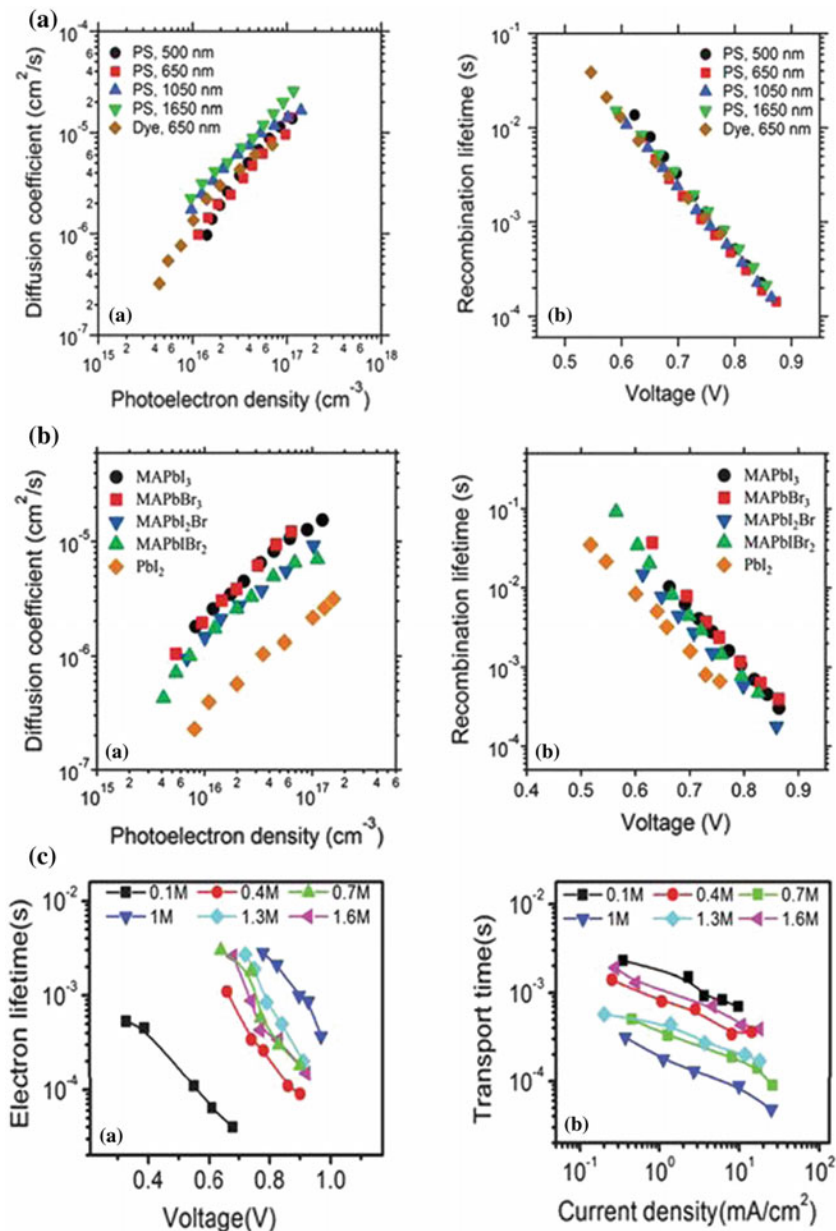


Fig. 4.21 **a** Electron-diffusion coefficient as a function of photoelectron density and recombination lifetime as a function of open-circuit voltage. PS: perovskite MAPbI_3 ; dye: Z907 dye. Reprinted with permission from [66]. **b** Comparison of electron-diffusion coefficient and recombination lifetime of mesoporous solar cells based on various perovskite absorbers with PbI_2 based cells. Reprinted with permission from [67]. **c** Electron lifetime and charge-transport time of PSCs based on MAPbI_3 prepared with different concentration PbI_2 precursor films. Reprinted with permission from [68]

For the perovskite/mesoporous TiO_2 blend, it is found that electron injection from perovskite to TiO_2 occurs in the subpicosecond range, but the lower intrinsic electron mobility in TiO_2 leads to an unbalanced charge transport [63, 64]. The charge-carrier mobility of perovskite deposited on mesoporous TiO_2 was attributed predominantly to holes. In contrast, perovskite deposited on mesoporous Al_2O_3 exhibited a 50%-lower mobility, but with the balanced mobility of holes and electrons. All these reports confirmed the superiority of the perovskite charge transfer/separation coupled with the suppressed charge recombination, and an extremely shallow trap depth (10 meV) with a low trap-state concentration [65].

Using intensity-modulated photocurrent/photovoltage spectroscopies, it is found that the transport and recombination in solid-state mesostructured PSCs are similar to those in solid-state DSSCs [52–66]. In these mesoporous PSCs with low perovskite pore filling in the TiO_3 network, the charge transport in perovskite cells is dominated by electron conduction within the mesoporous TiO_2 network, as shown in Fig. 4.21a. The charge diffusion length in mesostructured PSCs is found to be longer than $1 \mu\text{m}$ [66]. In the similar TiO_2 -based mesoporous solar cells using various perovskite compositions with similar perovskite pore filling via one-step solution deposition of perovskite, the electron-diffusion coefficient and recombination lifetime are all governed by the underlying mesoporous TiO_2 film, as shown in Fig. 4.21b [67]. However, when coated with PbI_2 instead of perovskite, the device exhibited a factor of 5 slower diffusion coefficient than perovskite-based devices [67]. Interestingly, when the MAPbI_3 perovskite was deposited via the two-step method with different concentrations of PbI_2 precursor solutions, the electron-transfer properties showed an obvious PbI_2 concentration dependence in Fig. 4.21c, suggesting that the transport is no longer dominated by the underlying mesoporous TiO_2 network [68]. The reason for this apparent PbI_2 concentration dependence of transport property may be associated with the different interfacial contacts between perovskite and TiO_2 with different amounts of pore filling. Snaith and his co-workers have discovered that the perovskite layer itself can block the primary recombination pathway between the TiO_2 and the HTM [69].

4.4 Summary

In this Chapter we reviewed the mechanisms ruling photovoltaic conversion. The physical principles were elaborated, and their implementation in real devices (cells and modules) were commented upon with reference to the three solar cell generations, namely bulk cells (mostly based upon single-crystalline and polycrystalline silicon), thin film cells (including CdTe , amorphous silicon, and CZTS), and cells based on dye sensitization, from fully organic to perovskite.

The reader interested in additional details on the physics of photovoltaics and on PV materials may further refer to classical books on PV physics [4–6].

References

1. ASTM Standard, <http://standards.globalspec.com/std/971343/astm-e490>. E490. Accessed 27 Dec 1973
2. ASTM Standard, <https://www.astm.org/Standards/G173.htm>. G173-03. Accessed 2012
3. S.J. Fonash, *Homojunction Solar Cells* (Elsevier, 2010)
4. J. Nelson, The Physics of Solar Cells, in Series on Properties of Semiconductor Materials (Imperial College Press, 2003)
5. A. Luque, S. Hegedus, *Handbook of Photovoltaic Science and Engineering* (Wiley, 2011)
6. P. Würfel, U. Würfel, *Physics of Solar Cells: From Basic Principles to Advanced Concepts* (Wiley, 2016)
7. D. Frank, New world record for solar cell efficiency at 46% french-german cooperation confirms competitive advantage of european photovoltaic industry. Technical Report 14 March 2016
8. Sharp Develops Solar Cell With World's Highest Conversion Efficiency of 35.8%, <https://phys.org/>. Accessed 3 June 2012
9. SunPower, Sunpower tm x-series data sheet. Technical Report (2013)
10. T. Ibn-Mohammed, S. Koh, I. Reaney, A. Acquaye, G. Schileo, K. Mustapha, R. Greenough, Renew. Sustain. Energy Rev. **80**, 1321 (2017)
11. J. Zhao, A. Wang, M.A. Green, Prog. Photovolt. Res. Appl. **7**(6), 471 (1999)
12. M.A. Green, Prog. Photovolt. Res. Appl. **17**(3), 183 (2009)
13. Energy Initiative Massachusetts Institute of Technology, *The future of solar energy- an interdisciplinary mit study*. Technical Report. Accessed 2015
14. J. Kilner, S. Skinner, S. Irvine, P. Edwards, *Functional materials for sustainable energy applications* (Woodhead Publishing Limited, 2012)
15. R. Miles, K. Hynes, I. Forbes, Prog. Cryst. Growth Charact. Mater **51**(1–3), 1 (2005)
16. J. Jean, P.R. Brown, R.L. Jaffe, T. Buonassisi, V. Bulović, Energy Environ. Sci. **8**(4), 1200 (2015)
17. Y. Zhou (ed.), *Eco- and Renewable Energy Materials* (Springer, 2013)
18. A. Metz, M. Fischer, G. Xing, L. Yong, S. Julsrud, *International technology roadmap for photovoltaic (itrpv)*. Technical Report. Accessed Mar 2013
19. A. Goodrich, P. Hacke, Q. Wang, B. Sopori, R. Margolis, T.L. James, M. Woodhouse, Sol. Energy Mater. Sol. Cells **114**, 110 (2013)
20. M.A. Green, Sol. Energy **74**(3), 181 (2003)
21. M.A. Green, *Solar cells: operating principles, technology, and system applications* (Prentice-Hall Inc, Englewood Cliffs, 1982)
22. L. Kazmerski, *Best research cell efficiencies*. Technical Report. Accessed 2010
23. M.A. Green, K. Emery, Y. Hishikawa, W. Warta, E.D. Dunlop, Prog. Photovolt. Res. Appl. **23**(1), 1 (2014)
24. D.L. Staebler, C.R. Wronski, Appl. Phys. Lett. **31**(4), 292 (1977)
25. C.A. Wolden, J. Kurtin, J.B. Baxter, I. Repins, S.E. Shaheen, J.T. Torvik, A.A. Rockett, V.M. Fthenakis, E.S. Aydil, J. Vac. Sci. Technol. A Vac. Surf. Films **29**(3), 030801 (2011)
26. J. Peng, L. Lu, H. Yang, Renew. Sustain. Energy Rev. **19**, 255 (2013)
27. M.M. de Wild-Scholten, Sol. Energy Mater. Sol Cells **119**, 296 (2013)
28. V.M. Fthenakis, Renew. Sustain. Energy Rev. **8**, 303 (2004)
29. Fraunhofer ISE, Photovoltaics report. Technical Report (2014)
30. A.M. Bagher, M.M.A. Vahid, M. Mohsen, Am. J. Opt. Photonics **3**, 94 (2015)
31. I. Repins, M.A. Contreras, B. Egaas, C. DeHart, J. Scharf, C.L. Perkins, B. To, R. Noufi, Prog. Photovolt. Res Appl. **16**(3), 235 (2008)
32. E. Yablonovitch, T. Gmitter, J.P. Harbison, R. Bhat, Appl. Phys. Lett. **51**(26), 2222 (1987)
33. F. Cucchiella, I. D'Adamo, P. Rosa, Renew. Sustain. Energy Rev. **47**, 552 (2015)
34. M. Green, *The Physics of Solar Cells: Third Generation Photovoltaics* (Imperial College Press, New York, 2003)
35. K. Zhao, Z. Pan, X. Zhong, J. Phys. Chem. Lett. **7**(3), 406 (2016)

36. C.H. Chang, Y.L. Lee, *Appl. Phys. Lett.* **91**(5), 053503 (2007)
37. H. Lee, M. Wang, P. Chen, D.R. Gamelin, S.M. Zakeeruddin, M. Gratzel, M.K. Nazeeruddin, *Nano Lett.* **9**(12), 4221 (2009)
38. H.S. Kim, J.W. Lee, N. Yantara, P.P. Boix, S.A. Kulkarni, S. Mhaisalkar, M. Gratzel, N.G. Park, *Nano Lett.* **13**(6), 2412 (2013)
39. P.P. Boix, G. Laramona, A. Jacob, B. Delatouche, I. Mora-Seró, J. Bisquert, *J. Phys. Chem. C* **116**(1), 1579 (2012)
40. M. Shalom, Z. Tachan, Y. Bouhadana, H.N. Barad, A. Zaban, *J. Phys. Chem. Lett.* **2**(16), 1998 (2011)
41. L. Dou, J. You, J. Yang, C.C. Chen, Y. He, S. Murase, T. Moriarty, K. Emery, G. Li, Y. Yang, *Nat. Photonics* **6**(3), 180 (2012)
42. J. Berry, T. Buonassisi, D.A. Egger, G. Hodes, L. Kronik, Y.L. Loo, I. Lubomirsky, S.R. Marder, Y. Mastai, J.S. Miller, D.B. Mitzi, Y. Paz, A.M. Rappe, I. Riess, B. Rybtchinski, O. Stafsudd, V. Stevanovic, M.F. Toney, D. Zitoun, A. Kahn, D. Cahen, *Adv. Mater.* **27**(35), 5102 (2015)
43. H.S. Kim, C.R. Lee, J.H. Im, K.B. Lee, T. Moehl, A. Marchioro, S.J. Moon, R. Humphry-Baker, J.H. Yum, J.E. Moser, M. Gratzel, N.G. Park, *Sci. Rep.* **2**(1) (2012)
44. NREL, Research cell efficiency records. Technical Report. Accessed April 2016
45. Y. Ogomi, A. Morita, S. Tsukamoto, T. Saitho, N. Fujikawa, Q. Shen, T. Toyoda, K. Yoshino, S.S. Pandey, T. Ma, S. Hayase, *J. Phys. Chem. Lett.* **5**, 1004 (2014)
46. S. Kazim, M.K. Nazeeruddin, M. Grätzel, S. Ahmad, *Angew. Chemie Int. Ed.* **53**(11), 2812 (2014)
47. J.M. Ball, M.M. Lee, A. Hey, H.J. Snaith, *Energy Environ. Sci.* **6**(6), 1739 (2013)
48. Q. Dong, Y. Fang, Y. Shao, P. Mulligan, J. Qiu, L. Cao, J. Huang, *Science* **347**(6225), 967 (2015)
49. M.A. Green, A. Ho-Baillie, H.J. Snaith, *Nat. Photonics* **8**(7), 506 (2014)
50. J. Mandelkorn, C. McAfee, J. Kespere, L. Schwartz, W. Pharo, *J. Electrochem. Soc.* **109**(4), 313 (1962)
51. H. Flicker, J.J. Loferski, J. Scott-Monck, *Phys. Rev.* **128**(6), 2557 (1962)
52. C. Battaglia, A. Cuevas, S.D. Wolf, *Energy Environ. Sci.* **9**(5), 1552 (2016)
53. J. Gong, J. Liang, K. Sumathy, *Renew. Sustain. Energy Rev.* **16**(8), 5848 (2012)
54. I. Mora-Sero, J. Bisquert, *J. Phys. Chem. Lett.* **1**(20), 3046 (2010)
55. G. Hodes, *J. Phys. Chem. C* **112**(46), 17778 (2008)
56. T. Sogabe, Q. Shen, K. Yamaguchi, *J. Photonics Energy* **6**(4), 040901 (2016)
57. P.B. Miranda, D. Moses, A.J. Heeger, *Phys. Rev. B* **64**(8) (2001)
58. A.J. Mozer, N.S. Sariciftci, C. R. Chimie **9**(5–6), 568 (2006)
59. J.M. Nunzi, C. R. Phys. **3**(4), 523 (2002)
60. C.J. Brabec, G. Zerza, G. Cerullo, S.D. Silvestri, S. Luzzati, J.C. Hummelen, S. Sariciftci, *Chem. Phys. Lett.* **340**(3–4), 232 (2001)
61. S. Gnes, H. Neugebauer, N.S. Sariciftci, *Chem. Rev.* **107**(4), 1324 (2007)
62. A. Marchioro, J. Teuscher, D. Friedrich, M. Kunst, R. van de Krol, T. Moehl, M. Gratzel, J.E. Moser, *Nat. Photonics* **8**(3), 250 (2014)
63. L. Wang, C. McCleese, A. Kovalsky, Y. Zhao, C. Burda, *J. Am. Chem. Soc.* **136**(35), 12205 (2014)
64. C.S. Poncea, T.J. Savenije, M. Abdellah, K. Zheng, A. Yartsev, T. Pascher, T. Harlang, P. Chabera, T. Pullerits, A. Stepanov, J.P. Wolf, V. Sundström, *J. Am. Chem. Soc.* **136**(14), 5189 (2014)
65. H. Oga, A. Saeki, Y. Ogomi, S. Hayase, S. Seki, *J. Am. Chem. Soc.* **136**(39), 13818 (2014)
66. Y. Zhao, A.M. Nardes, K. Zhu, *J. Phys. Chem. Lett.* **5**(3), 490 (2014)
67. Y. Zhao, A.M. Nardes, K. Zhu, *Faraday Discuss.* **176**, 301 (2014)
68. D. Bi, A.M. El-Zohry, A. Hagfeldt, G. Boschloo, *ACS Photonics* **2**(5), 589 (2015)
69. T. Leijtens, B. Lauber, G.E. Eperon, S.D. Stranks, H.J. Snaith, *J. Phys. Chem. Lett.* **5**(7), 1096 (2014)

Chapter 5

Hybrid Photovoltaic–Thermoelectric Generators: Theory of Operation



Abstract This chapter is devoted to provide the general theory describing the hybridization of solar cells with thermoelectric generators. Moving from a description of the system, its main components will be introduced and analysed. Their characteristics and their impact on the final system efficiency will be scrutinised. Specifically, the heat generation within solar cells will be detailed considering the main losses occurring in a PV cell. This will bring to an evaluation of the temperature sensitivity of solar cells, which is one of the most important parameter to be considered when pairing PV cells and TEGs. In addition, we will introduce the concept of fully hybridized systems, where the thermoelectric and PV devices are both thermally and electrically connected to each other.

5.1 System Description

The concept of the solar spectrum energy utilization by a HTEPV module is displayed in Fig. 5.1. Using a beam splitter (optical coupling) and a silicon solar cell under AM1.5G spectrum, 69.32% of the solar radiation is absorbed by the solar cell. The short-wavelength region of the power spectrum that can be used for TEG only accounts for 1.35% of the total incident radiation power. The main contribution of the TEG input power comes instead from the conversion of the long-wavelength fraction of the spectrum (28.55%). This argument provides the clue for an efficient combination of PV and TEG modules [1].

In principle, a Hybrid Thermoelectric Photovoltaic Generator (HTEPVG) can be described following the same scheme used in Chap. 3 for STEGs. Also in this case five main components can be identified, namely an optical collector, an opto-thermal convert, a thermal collector, a thermoelectric converter, and a heat dissipation system. The only difference with respect to STEGs is that in the case of HTEPV systems the opto-thermal converter is a solar cell. Thus, the main advantage of HTEPV generators relays in the fact that the opto-thermal converter is producing an electrical power (P_{pv}) that contributes to the overall output power. Therefore, the overall efficiency η_{htep} may be written as the sum of the TEG (η_{teg}) and the PV (η_{pv}) contributions:

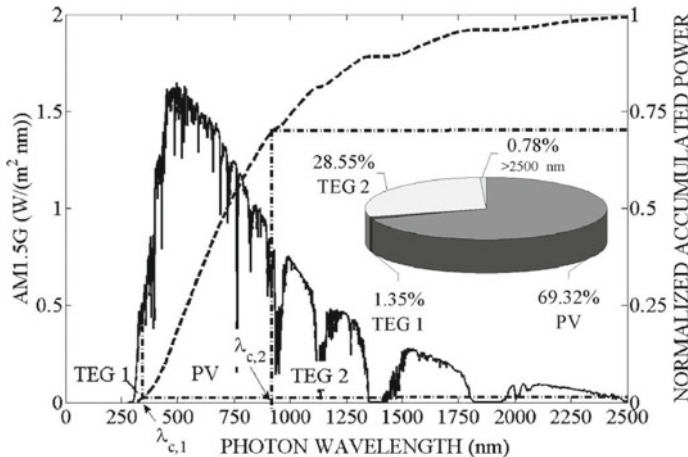


Fig. 5.1 Segmentation of AM1.5G spectrum in three regions for a solar cell and solar TEG with 4% efficiency. Normalized accumulated radiation power. Pie chart: converted power fraction of each module. From [1]

$$\eta_{\text{htepv}} = \eta_{\text{pv}} + \eta_{\text{steg}} = \frac{P_{\text{pv}}}{P_{\text{in}} A_{\text{pv}}} + \frac{P_{\text{steg}}}{P_{\text{in}} A_{\text{pv}}} \quad (5.1)$$

where A_{pv} is the solar cell area, P_{in} is the input (solar) power, while P_{pv} and P_{steg} are respectively the solar cell and TEG output power. It should be pointed out that (5.1) refers to the simplest case in which the PV and TEG sections are thermally coupled but electrically separated. The case of full pairing (full hybridization), i.e. of devices where the two stages are also electrically hybridized, will be discussed later (Sect. 5.5).

Apart from the opto-thermal converter and from the fact that for not electrically hybridized systems an electrically insulating layer is needed, the solutions reported in Chap. 3 for the other components of the STEG systems also apply to HTEPV generators. Therefore, the optical collector can be any optical concentration system implementing lenses and mirrors. Also, the thermal collector may be a flat plane or a cavity, and eventually it may have the same footprint area of the solar cell. Finally heat dissipation can be either passive or active.

5.2 Solar Cells as Efficient Opto-Thermal Converters

For strange that it may appear, solar cells are very efficient in converting solar power into *thermal* power. As a matter of fact, most of the power not converted into electrical power (namely, much more than half of the input power) becomes heat in a solar cell. To quantify such a conversion fraction one may write that

$$\xi_{\text{pv}} = 1 - (\eta_{\text{pv}} + R_{\text{pv}} + T_{\text{pv}}) \quad (5.2)$$

where ξ_{pv} is the heat fraction, while R_{pv} and T_{pv} are respectively the fractions of the solar power which are reflected by the solar cell or transmitted through it. As reported by many authors [2–7], the heat fraction is generated within solar devices by the following mechanisms (Table 5.1):

- spurious photon absorptions (e.g. due to contact grid shadows and radiation reflection) (L_1)
- source-absorber mismatch losses (L_2) due to the under-gap portion of the solar spectrum (L_{2a}), carrier thermalisation (L_{2b})
- electron-hole recombination current losses (L_3)
- electron-hole recombination voltage losses (L_4)

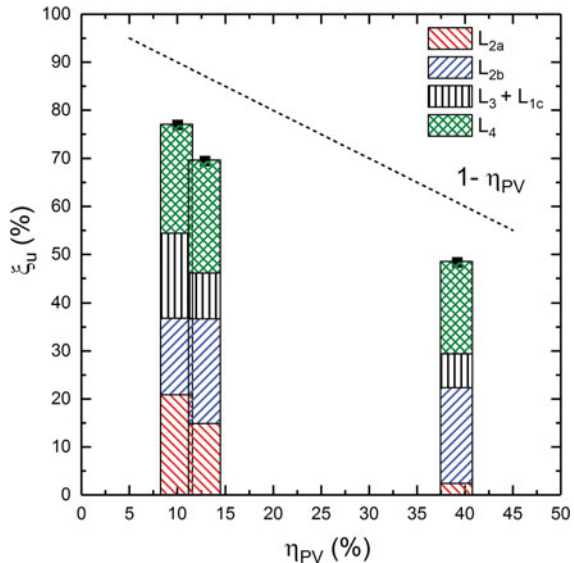
A model and an experimental method to measure the contributions of various heat losses in solar cells was recently reported by Lorenzi et al. [8]. Applying the method to three kinds of inorganic solar cells they concluded that up to 85% of the losses in PV generates heat. Also, the model proved that in single junction solar cells the energy gap modulates the balance between L_{2a} and L_{2b} , and that multi-junction cells are very effective at minimizing the L_{2a} term, although they cannot significantly reduce L_{2b} and L_4 terms. The amount of thermal losses for the three cells are reported in Fig. 5.2 versus their solar cell efficiency.

Therefore, in principle solar cells are very good opto-thermal converters. However, since their emittance is between 0.7 and 0.9 [9–12], high radiative heat exchanges significantly reduces their opto-thermal conversion efficiency η_{otconv} [cf. (3.1)].

Table 5.1 Energy loss in a HTEPV device powered by solar energy [7]

1. Optical Losses (L_1)	(a) contact grid shadow (L_{1a})
	(b) radiation reflection (L_{1b})
	(c) spurious absorption (L_{1c})
2. Source-absorber mismatch losses (L_2)	(a) non-absorbed photons with $E < E_g$
	(b) thermalisation of hot carriers (photons with $E > E_g$)
3. Electron-hole recombination current losses (L_3)	a) radiative recombination
	(b) non-radiative recombination
	(c) electrical shunts
4. Electron-hole recombination voltage losses (L_4)	Voltage drops associated to L_3 recombination mechanisms

Fig. 5.2 Histograms of thermal losses for three different inorganic solar cells (bulk silicon, thin film CIGS, and triple-junction). Reproduced with permission from [8]



To minimize radiative emittances, use of the so-called heat mirrors (HMs) may be considered. A HM is a layer or a multi-layer of materials ideally exhibiting high optical transparency in the spectral region where the PV absorber operates, showing at the same time high reflectance in the infrared range. In semiconductors, the switch between high transparency and high reflectance occurs at the material plasma frequency. Suitable materials for HMs are the so-called transparent conductive oxides (TCOs). Popular candidates are In:SnO₂ (ITO) [13] and Al:ZnO (AZO) [14], which are widely studied for their application as transparent conductive front contacts in solar cells [15], or as spectrum splitters in hybrid PV—thermal devices [16–18].

When HMs are used, the emittance of the solar cell ε_{pv} is replaced by an effective emissivity calculated as

$$\varepsilon'_{\text{pv}} = \varepsilon_{\text{pv}}(1 - \eta_{\text{hm}}^{\text{r}}) \quad (5.3)$$

where $\eta_{\text{hm}}^{\text{r}}$ is the back-reflecting efficiency for heat coming from the solar cell:

$$\eta_{\text{hm}}^{\text{r}} = \left[\left(\frac{\int R_{\text{hm}}(\lambda) d\lambda}{\int d\lambda} \right)_{\text{ir}} \right] \quad (5.4)$$

where $R_{\text{hm}}(\lambda)$ is the HM reflectance, and the subscript ‘ir’ means that the integral is evaluated over a range of wavelengths from 2,500 to 30,000 nm.

Since real HMs have transmittances smaller than one, their use also affects the incoming solar power—reducing it. Then, one defines the overall HM efficiency in transmitting the solar spectrum as

$$\tau_{\text{hm}} = \left[\left(\frac{\int T_{\text{hm}}(\lambda) d\lambda}{\int d\lambda} \right)_{\text{sun}} \right] \quad (5.5)$$

where T_{hm} is the HM transmittance, and the subscript ‘sun’ means that the integral is evaluated over a range of wavelengths from 250 to 2,500 nm.

5.3 Efficiency of HTEPV

Since the logical scheme of a HTEPVG is exactly that of a STEG, the efficiency of the TEG stage can be obtained as for a STEG by combining (5.1) and (3.12):

$$\eta_{\text{htepv}} = \eta_{\text{pv}} + \eta_{\text{steg}} = \eta_{\text{pv}} + \eta_{\text{opt}} \eta_{\text{ot}} \eta_{\text{teg}} \eta_{\text{diss}} \quad (5.6)$$

The second term in the RHS of (5.6) can be calculated as in the STEG case but for the η_{ot} term [cf. (3.5)]. To evaluate it in a HTEPVG, the HM transmittance τ_{hm} (5.5) has to be accounted for. In addition, ϵ_{otconv} has to be replaced by ϵ'_{pv} which encompasses the heat reflection properties of the HM. Finally, considering that some of the solar power is converted into electric power by the solar cell itself [cf. (5.2)], the opto-thermal efficiency for the HTEPVG case reads

$$\begin{aligned} \eta_{\text{ot}} = & \alpha_{\text{otconv}} \tau_{\text{enc}} \tau_{\text{hm}} \left[1 - (\eta_{\text{pv}} + R_{\text{pv}} + T_{\text{pv}}) \right] \\ & - \frac{\sigma A_{\text{abs}} \left[\epsilon'_{\text{pv}} (T_{\text{h}}^4 - T_{\text{a}}^4) + \epsilon_{\text{thcol'}} (T_{\text{h}}^4 - T_{\text{c}}^4) \right]}{C P_{\text{in}} \tau_{\text{opt}} A_{\text{opt}}} \end{aligned} \quad (5.7)$$

where we assume that the solar cell is at the same temperature of the TEG hot side, i.e. $T_{\text{pv}} = T_{\text{h}}$, and where, as in the STEG case, also for HTEPVG $\epsilon_{\text{thcol'}}$ is calculated by using (3.4).

Comparing (5.7) and (3.5) it is evident that in the HTEPVG case the input power is reduced. Therefore, HTEPV systems can be more convenient than STEGs as long as the PV contribution overcomes the reduction of the input power.

Considering the first term of (5.6), it is well known that η_{pv} depends on the optical concentration C and on the temperature $T_{\text{pv}} = T_{\text{h}}$. Solar cell efficiency dependency on these parameters is reported to be positive and logarithmic for C [19], and negative and linear for T_{h} [6, 20, 21]. Thus [22]

$$\eta_{\text{pv}} = \eta_{\text{pv}}^0 + \eta_{\text{pv-cond}} \quad (5.8)$$

where η_{pv}^0 is the PV efficiency for $C = 1$ and $T_{\text{h}} = 300$ K, and

$$\eta_{\text{pv-cond}} = \eta_{\text{pv}}^0 [\beta_{\text{op}} \log C - \beta_{\text{th}} (T_{\text{h}} - T_{\text{a}})] \quad (5.9)$$

where β_{op} and β_{th} are the optical concentration coefficient and the temperature coefficient, respectively. The latter depends in turn on the concentration ratio as

$$\beta_{\text{th}} = \beta_{\text{th}}^0(1 - \zeta \log C) \quad (5.10)$$

with β_{th}^0 the temperature coefficient at $C = 1$, and ζ the concentration coefficient of β_{th} .

Since solar cell temperature sensitivity is due to carrier recombination rates while optical concentration increases carrier injection, it follows that solar cell temperature sensitivity is *smaller* in the case of optically concentrated systems [23].

From (5.9) it is straightforward to conclude that the smaller is the value of β_{th} , the higher is the PV efficiency, and thus the HTEPG efficiency. Further discussions on the dependence of β_{th} on the PV material properties will be reported in Sect. 5.4.

As in the case of STEGs, also for HTEPGs some of the η_{htepv} components [η_{pv} , η_{teg} , and η_{ot} in (5.6)] are temperature dependent (Fig. 5.3). It can be easily concluded that a maximum HTEPG efficiency exists that is higher than that of the sole PV cell. As for STEGs, such a maximum occurs at an optimal working temperature T_h . However, enhanced efficiency cannot be always achieved since, as will be seen in Sect. 6.3, in most PV cells the value of β_{th} is too large, thus disabling it de facto. If this is the case, no benefit comes from thermoelectric hybridization, and alternate solutions (such as cooling, or co-generation of hot water) has to be considered.

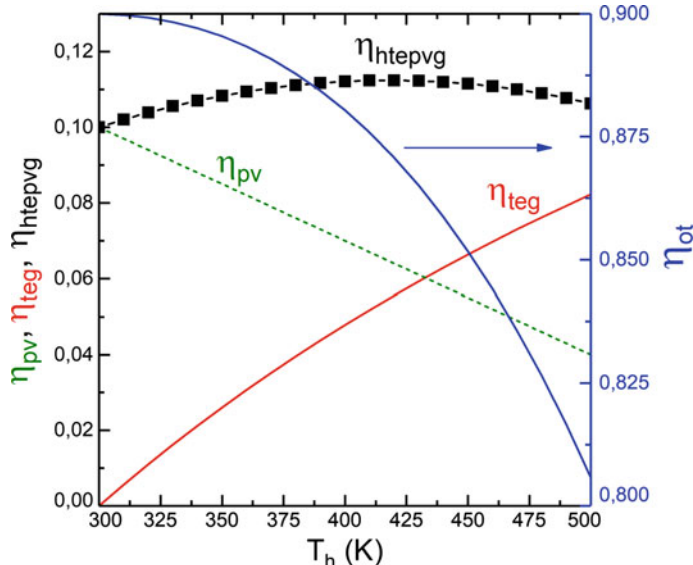


Fig. 5.3 Typical behaviour of η_{htepv} and its main components $\eta_{\text{pv}}, \eta_{\text{teg}}$, and η_{ot} as functions of T_h

5.4 PV Temperature Sensitivity

The temperature sensitivity of solar cell can be modeled by using the temperature linear coefficient β_{th} . Considering the case of no optical concentration (thus $C=1$, and β_{th}^0), Virtuani et al. [21] reported a detailed experimental determination of β_{th} for several materials. It shows how solar cells based on absorbers with high energy gaps (E_g) are less sensitive to temperature. This is quite intuitive, since temperature sensitivity of PV devices is dominated by carrier recombination.

Carrier recombination is either radiative or non-radiative. Radiative recombination consists in the annihilation of the electron-hole pairs created by the absorption of a photon, and the consequent emission of a photon with energy equal or smaller of the absorbed one. Non-radiative recombination also deals with electron-hole pair annihilation but without photon emission. Energy is here transferred to another carrier (Auger recombination) or converted into heat by recombination due to trap or impurity levels within the energy gap (Shockley-Read-Hall (SHR) recombination). It follows that carrier recombination (and therefore temperature sensitivity of the PV cell) is dominated by the value of E_g , and by the material quality.

In principle, since also E_g is temperature dependent (through lattice dilation), changes of the solar cell temperature also cause E_g to change, leading in turn to a

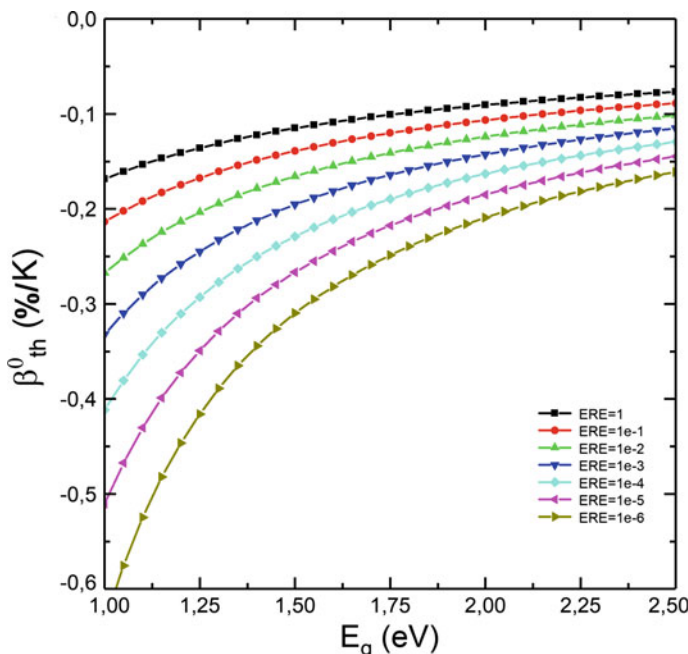


Fig. 5.4 Dependency of β_{th}^0 as a function of E_g , and of the External Radiative Efficiency

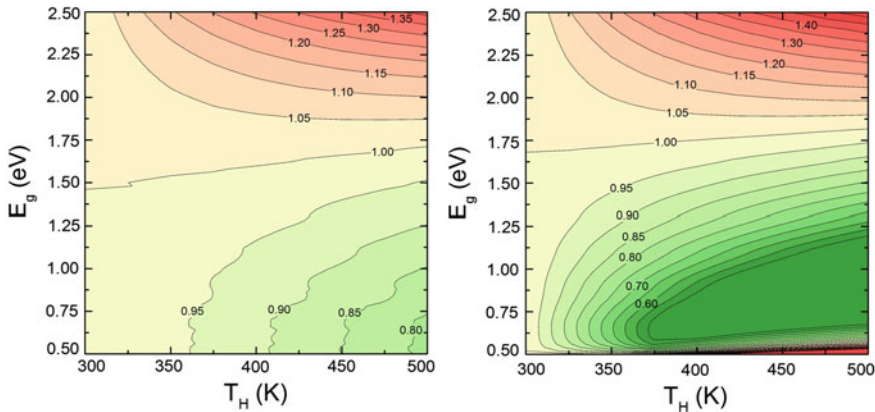


Fig. 5.5 Efficiency of HTEPV normalized on the sole PV efficiency at 300 K for ERE = 1 (left), and ERE = 0.001 (right). Adapted with permission from [7]

variation of β_{th}^0 . However, such changes of β_{th}^0 due to the temperature dependence of E_g is expected to be a second-order, negligible effect.

Material quality matters more, instead. A way to model non-radiative recombination is provided by the so-called External Radiative Efficiency (ERE) introduced by Green [24]. The ERE is an index defined as the ratio between the recombination current due to radiative recombination and that due to non-radiative recombination. Thus, a solar cells having ERE = 1 shows only radiative recombination, while a very small ERE values is dominated by non-radiative recombination.

The dependency of β_{th}^0 upon E_g and ERE was well discussed and reported in recent papers by Dupré et al. [6, 25] who conceived and described a thermal model for solar cells. Figure 5.4 reports such dependencies. They suggest that the convenience of thermoelectric hybridization is larger for solar cells having high energy gaps and being based on non-defective materials, as reported by Lorenzi et al. [7]. Figure 5.5 displays calculations of the HTEPGV efficiency normalized to the sole PV efficiency at 300 K, supporting such conclusions.

5.5 Fully Hybridized Solar Cells

As mentioned, further to using independently the electric power generated by the PV and the TEG stages, one may also connect electrically the PV and TEG stages. This can be done by placing the TEG either in series or in parallel to the PV cell. In both schemes (Fig. 5.6) the solar cell acts as a current generator in parallel to a (shunt) resistance and connected in series with a resistance. Instead, the TEG is represented as a resistance in series with a voltage generator. In both cases the hybrid device supplies power to the same electric load. Electrical hybridization of PV and TEG

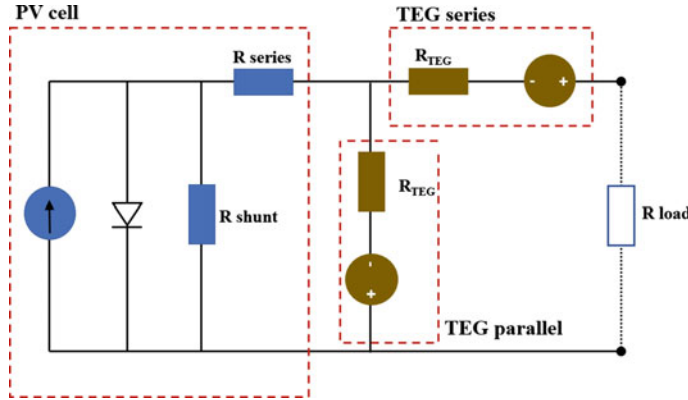


Fig. 5.6 Equivalent circuit of a fully hybridized HTEPVG with the two possible configuration, TEG in series with PV cell, and TEG in parallel

stages is motivated by the concern that the TEG power output is expected to be too low to independently power any active electric component.

When the two stages are also electrically paired, the total efficiency cannot be obtained simply by summing the PV and TEG contributions. Instead, the hybrid efficiency computes to

$$\eta_{\text{htepv}} = \eta_{\text{pv}} + \eta_{\text{steg}} - (1 - \eta_{\text{el}}) = \frac{P_{\text{pv}} + P_{\text{steg}} - P_{\text{el-loss}}}{P_{\text{in}} A_{\text{pv}}} \quad (5.11)$$

where η_{el} is the electrical hybridization efficiency, accounting also for the eventual power loss $P_{\text{el-loss}}$ caused by the presence of the TEG in the same electrical circuit of the solar cell. This loss originates from the change of the current-voltage ($I - V$) characteristics of the solar cell (Fig. 5.6). Actually, if the TEG is connected in series (Fig. 5.6, left), the PV cell senses the TEG as an additional series resistance. Then, the slope of the $I - V$ curve at high voltages decreases accordingly, then decreasing the solar cell filling factor. If the thermoelectric internal resistance R_{teg} is very large compared to the PV series resistance, then the $I - V$ curve becomes more similar to a straight line, and the short circuit current I_{sc} decreases. As for the voltage, the temperature difference across the TEG generates a thermoelectric voltage that sums up to the solar cell open circuit voltage V_{oc} , without changing the $I - V$ slope.

If instead the TEG is connected in parallel to the solar cell, the thermoelectric internal resistance becomes an additional shunt changing the $I - V$ slope at small voltages. In this case, if R_{teg} is comparable to the PV shunt resistance, the slope change is small and the solar cell V_{oc} does not change. Instead, if R_{teg} is small, V_{oc} significantly decreases, and the change in the $I - V$ slope becomes important. Finally the effect of the thermoelectric voltage leads to an increase of the PV I_{sc} (Fig. 5.7, right).

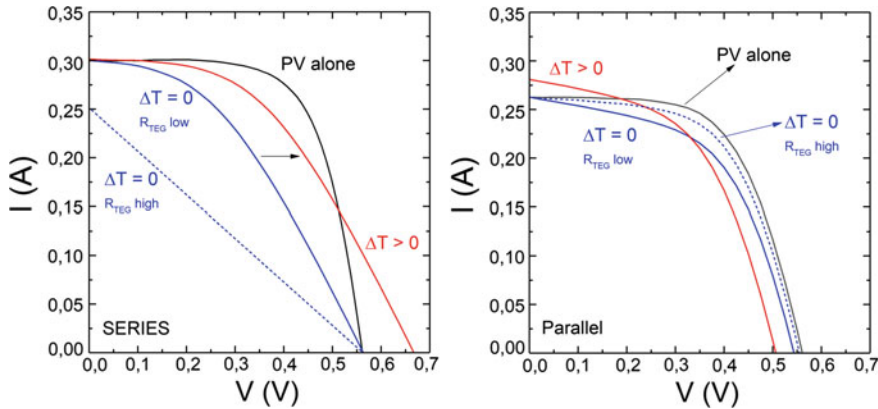


Fig. 5.7 Example of the solar cell IV characteristic modification in fully hybridized HTEPVGs. TEG connected in series (left) and in parallel (right) with the solar cell

Park et al. [26] showed that in a series connection and for a small silicon solar cell a lossless condition exists for which the full hybridized HTEPVG efficiency is equal to the sum of the TEG and PV contribution. They showed that the power loss $P_{el-loss}$ can be minimized for a given and sufficiently large temperature difference ΔT_{TEG} across the TEG, with the optimal ΔT_{TEG} depending on R_{teg} . It is to be remarked that further increasing ΔT_{TEG} leads however to an increase of $P_{el-loss}$. Thus, only one optimal working temperature exists for a lossless operation mode. However, it should be remarked that it is neither obvious or granted at all that the optimal temperature needed for maximum hybrid efficiency is the same as that needed for electrical lossless pairing.

For the parallel hybridization case, no evidence is available in the literature so far concerning the possibility of electrical lossless full hybridization.

5.6 Summary and Conclusions

The general theory of photovoltaic-thermoelectric hybrid solar cells has been introduced. It has been shown that HTEPV cells are special implementations of STEGs wherein the optical absorber is replaced by a (power-active) PV cell. The main components of a HTEPV generator have been analysed, discussing their characteristics and their impact on the final system efficiency. Mechanisms of heat generation within solar cells have been considered, and it has been shown how PV material selection affects the main losses occurring in a PV cell. Specifically, factors ruling the temperature sensitivity of solar cells, which is one of the most important parameter to be considered when pairing PV cells and TEGs, has been examined.

Furthermore, fully hybridized systems, where the thermoelectric and PV stages are both thermally and electrically connected to each other, has been evaluated, and pros and cons of such a layout have been scrutinized.

Actual implementations of HTEPV generators, with specific emphasis to material issues, will be addressed in Chap. 6.

References

1. D. Kraemer, L. Hu, A. Muto, X. Chen, G. Chen, M. Chiesa, *Appl. Phys. Lett.* **92**(24), 243503 (2008)
2. C.H. Henry, *J. Appl. Phys.* **51**(8), 4494 (1980). <https://doi.org/10.1063/1.328272>
3. P.F. Baldasaro, J.E. Raynolds, G.W. Charache, D.M. DePoy, C.T. Ballinger, T. Donovan, J.M. Borrego, *J. Appl. Phys.* **89**(6), 3319 (2001). <https://doi.org/10.1063/1.1344580>
4. T. Markvart, *Appl. Phys. Lett.* **91**(6), 2005 (2007). <https://doi.org/10.1063/1.2766857>
5. L.C. Hirst, N.J. Ekins-Daukes, *Prog. Photovolt. Res. Appl.* **19**(3), 286 (2011), <http://doi.wiley.com/10.1002/pip.1024>
6. O. Dupré, R. Vaillon, M.A. Green, *Sol. Energy Mater. Sol. Cells* **140**, 92 (2015). <https://doi.org/10.1016/j.solmat.2015.03.025>, <http://www.sciencedirect.com/science/article/pii/S0927024815001403>
7. B. Lorenzi, M. Acciarri, D. Narducci, *J. Mater. Res.* **30**(17), 2663 (2015)
8. B. Lorenzi, M. Acciarri, D. Narducci, *ArXiv e-prints* (2018)
9. A.a. Hegazy, *Energy Convers. Manag.* **41**, 861 (2000)
10. S. Armstrong, W.G. Hurley, *Appl. Therm. Eng.* **30**(11–12), 1488 (2010). <https://doi.org/10.1016/j.applthermaleng.2010.03.012>
11. L. Zhu, A. Raman, K.X. Wang, M.A. Anoma, S. Fan, *Optica* **1**, 32 (2014). <https://doi.org/10.1364/OPTICA.1.000032>
12. J. Zhang, Y. Xuan, *Energy Convers. Manag.* **129**, 1 (2016)
13. J.C. Fan, F.J. Bachner, *Appl. Opt.* **15**(4), 1012 (1976). <https://doi.org/10.1364/AO.15.001012>
14. Z.C. Jin, I. Hamberg, C.G. Granqvist, *Appl. Phys. Lett.* **51**(3), 149 (1987), <http://scitation.aip.org/content/aip/journal/apl/51/3/10.1063/1.99008>
15. K. Ellmer, *Nat. Photonics* **6**(12), 809 (2012), <http://www.nature.com/doifinder/10.1038/nphoton.2012.282>
16. A.G. Imenes, D.R. Mills, *Sol. Energy Mater. Sol. Cells* **84**, 19 (2004). <https://doi.org/10.1016/j.solmat.2004.01.038>
17. C. Shou, Z. Luo, T. Wang, W. Shen, G. Rosengarten, W. Wei, C. Wang, M. Ni, K. Cen, *Appl. Energy* **92**, 298 (2012). <https://doi.org/10.1016/j.apenergy.2011.09.028>
18. K. Sibin, N. Selvakumar, A. Kumar, A. Dey, N. Sridhara, H. Shashikala, A.K. Sharma, H.C. Barshilia, *Sol. Energy* **141**, 118 (2017). <https://doi.org/10.1016/j.solener.2016.11.027>
19. J.L. Gray, in *Handbook of Photovoltaic Science and Engineering*, ed. by L. Antonio, H. Steven (Wiley, 2003), pp. 106–107
20. P. Singh, N. Ravindra, *Sol. Energy Mater. Sol. Cells* **101**, 36 (2012). <https://doi.org/10.1016/j.solmat.2012.02.019>
21. A. Virtuani, D. Pavanello, G. Friesen, in *Proceedings of 25th EUPVSEC* (2010), pp. 4248–4252
22. G. Contento, B. Lorenzi, A. Rizzo, D. Narducci, *Energy* **131**(Supplement C), 230 (2017). <https://doi.org/10.1016/j.energy.2017.05.028>, <http://www.sciencedirect.com/science/article/pii/S0360544217307843>
23. G. Siefer, A.W. Bett, *Prog. Photovolt. Res. Appl.* **22**(5), 515 (2014), <http://doi.wiley.com/10.1002/pip.2285>

24. M.A. Green, *Prog. Photovolt. Res. Appl.* **20**(4), 472 (2012), <http://doi.wiley.com/10.1002/pip.1147>
25. O. Dupré, R. Vaillon, M.A. Green, *Sol. Energy* **140**, 73 (2016). <https://doi.org/10.1016/j.solener.2016.10.033>
26. K.T. Park, S.M. Shin, A.S. Tazebay, H.D. Um, J.Y. Jung, S.W. Jee, M.W. Oh, S.D. Park, B. Yoo, C. Yu, J.H. Lee, *Sci. Rep.* **3**, 2123 (2013). <https://doi.org/10.1038/srep02123>, <http://www.nature.com/srep/2013/130703/srep02123/full/srep02123.html>

Chapter 6

Hybrid Photovoltaic–Thermoelectric Generators: Materials Issues



Abstract This chapter is dedicated to present the state of the art of hybrid photovoltaic–thermoelectric generators based on either organic or inorganic photovoltaic cells. Present challenges and future perspectives of this approach to energy harvesting will be discussed with a special emphasis on materials issues. It will be seen that both classes of PV materials deserve attention in view of applications in hybridized converters, although absorber stability and degradation of its PV efficiency with increasing temperatures sets limitations to currently achievable efficiencies, also in view of the still low efficiency of thermoelectric stages.

6.1 Introduction

In the previous Chapter the physics of hybridization, both partial (thermal only) and full (thermal and electric) was outlined and discussed. It was shown how the convenience of hybridization to increase the solar conversion efficiency strictly depend upon the material. More exactly, since most of the power of any hybrid solar generator is originated by its PV stage, special care is needed to select PV materials with efficiencies only marginally degrading with the PC temperature. Furthermore, a suitable layout should also treasure the most typical characteristics of a thermoelectric generator, namely its very long lifetime. Therefore, PV stages of the hybrid cell must be selected to endure operative conditions, which should not lead to either degradation or failure of the PV components.

This Chapter will be focused on current attempts to fabricate and test hybrid solar cells using a variety of materials in their PV stage. Materials issues are sufficiently different for inorganic and organic PV stages to suggest separate discussions for each class of materials.

6.2 Organic Photovoltaic Materials

The advantages of using organic photovoltaics (OPV) cells for hybrid organic thermoelectric–photovoltaic (OTEPV) generators are mainly related to the reduced cost of OPV cells, admitting roll-to-roll mass production [1–6], as well as the mature technology for thermoelectric generators (TEGs) used near room temperature [7–10]. Unlike inorganic solar cells, OPV cells are usually partly transparent in the visible light range [11]. Therefore, it is important for the TE part to capture the unused portion of the solar spectrum using solar absorber layers [12, 13].

In organic thermoelectric–photovoltaic generators, the OPV cathode and the anode are electrically connected in series with the TE p-n junctions in series, (full hybridization—cf. Sect. 5.5 [14]). Such a flat device is capable of improving the overall solar to electrical conversion efficiency [15–19]. Figure 6.1 shows a schematic setup of a typical OTEPV device. The hot side of the TEG is thermally connected to the counter electrode of the OPV cell, harvesting transmitted sunlight and waste heat using a solar absorber layer. When a temperature gradient builds up vertically through the TEG, the TEG power output adds to the OPV power output due to the series electrical connection of both stages. The operational temperature for the OTEPV generator is limited by the OPV, and is normally less than 400 K for the sake of polymer durability [20–23]. However, OPV cells have better stability than other conventional PV cells regarding the conversion efficiency.

Since the efficiency of a generic OPV system is simply the ratio of output power P_{out} to input power P_{in} , in view of (4.12)–(4.13)

$$\eta_{\text{pv}} = \frac{P_{\text{out}}}{P_{\text{in}}} = \frac{V_{\text{oc}} I_{\text{sc}} FF}{\phi_{\text{sun}} S} \quad (6.1)$$

where V_{oc} , I_{sc} , FF , ϕ_{sun} and S are the open circuit voltage, the short-circuit current, the filling factor, the solar radiation intensity, and the device area, respectively. By definition the fill factor FF is given by $FF = (V_{\text{max}} \times I_{\text{max}})/(V_{\text{oc}} \times I_{\text{sc}})$, where V_{max}

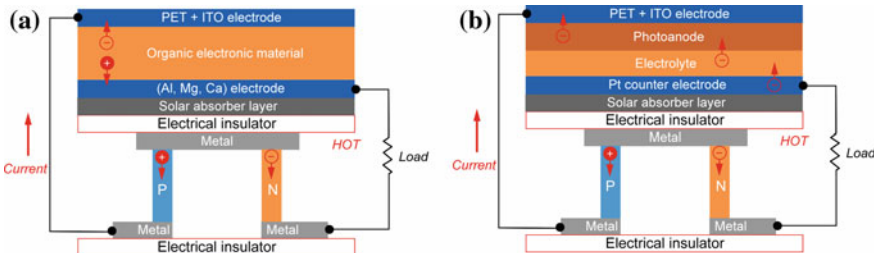


Fig. 6.1 Typical schematic diagrams of **a** the single layer OPV cell hybridized with a TEG device, and **b** the Dye-sensitized solar cell hybridized with a TEG device. In both cases the TEG device is connected thermally and electrically in series with the PV cell

Table 6.1 An overview of the state-of-the art OPV cells with their conversion efficiencies

Cell type	Conversion efficiency (%)	Reference
Small molecule OPVs	6.7–8.94	[24–27]
Polymer OPVs	8.4–10.6	[28, 29]
Perovskite OPVs	7–15	[30–32]
Dye-sensitized OPVs	11–13	[11, 33–35]

and I_{max} are the maximum voltage and maximum current achievable. The state-of-the art OPV cell efficiency is reported in Table 6.1.

6.2.1 Dye-Sensitized Solar Cells

Wang et al. were the first to propose a PVTE hybrid system based on dye-sensitized solar cells (DSSCs) and a microTEG based on bismuth telluride [15]. Figure 6.2 shows a schematics and a photograph of the PVTE hybrid device. A DSSC and a TE generator sit on top of each other, while a SSA is placed in between. The electric connection of the DSSC and TE generator are in series, the cathode and anode of the hybrid device are the cathode of the DSSC and the anode of the TE generator, respectively. According to the transmittance spectrum of the glass sheet coated with fluorine-doped tin oxide (FTO) and the DSSC cell shown in Fig. 6.2a, the DSSC absorbs part of the sunlight, which is converted into electricity.

A relatively large fraction of the radiation in the range from 600 to 1600 nm is transmitted by the PV stage, which suggests that this part of the radiative energy is not utilized by the DSSC cell. On the other hand, it is shown in Fig. 6.3b that the SSA has a markedly low reflectance in the wavelength range from 600 to 1600 nm. This means that the sunlight transmitted through the DSSC can be well absorbed by the SSA. Then the SSA converts the sunlight transmitted through the DSSC into heat. This heat is then further converted into electricity by the TE generator using the Seebeck effect. The hybrid device as a whole can absorb a wide wavelength range of the incident sunlight, and hence it leads to a larger energy conversion efficiency compared to the sole DSSC. An overall conversion efficiency of 13.8% could be actually achieved, and the power density generated by the PVTE system was about 12.8 mW/cm² when the temperature difference across the TEG was around 6 K. However, it may be expected that the device performance might increase with further optimization [15].

Chang et al. investigated a solar–thermoelectric module for power generation from solar energy [36]. The proposed method uses recycled external exhaust heat to generate electric power, further enhancing the thermoelectric conversion efficiency of the TEG. Using electrophoretic deposition, self-prepared CuO nanofluid is deposited onto a Cu plate and then let adhere to the surface of a TEG (Fig. 6.4). Experimental results show that the CuO thin film coating on the TEG surface can enhance the

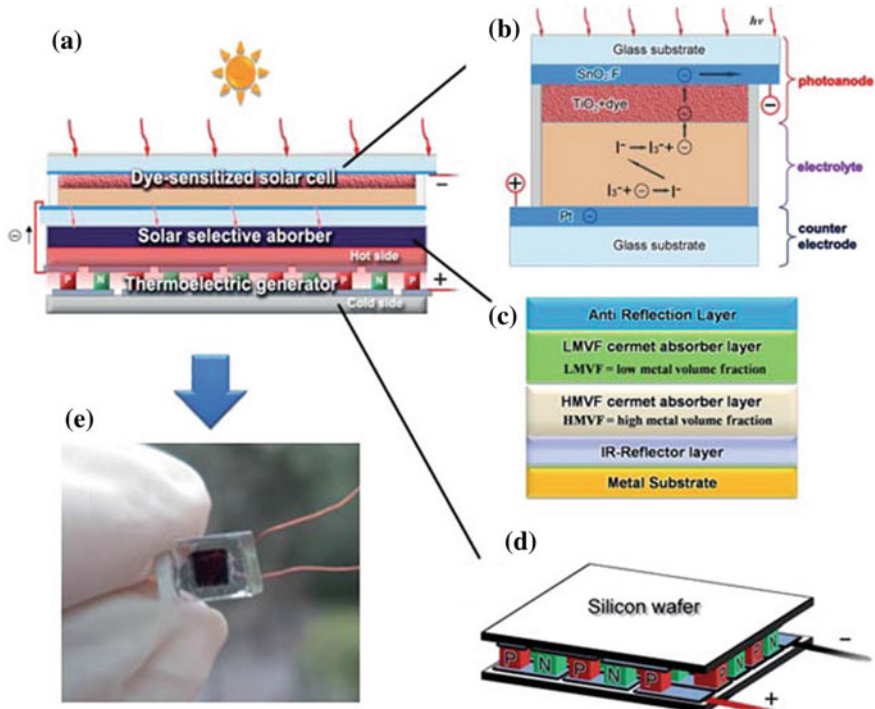


Fig. 6.2 Schematic illustration and photograph of a novel PVTE hybrid device using DSSC and SSA-pasted TE generator as the top and bottom cells: **a** hybrid device; **b** DSSC; **c** SSA; **d** TE; and **e** photograph of hybrid device. From [15]

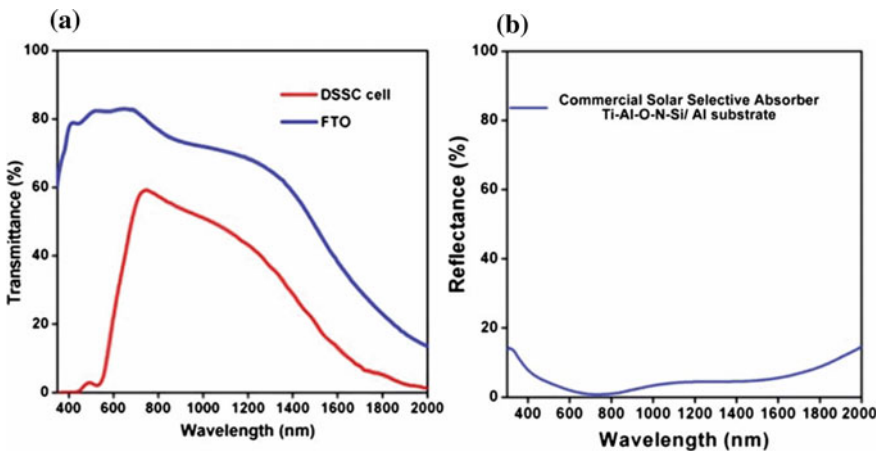


Fig. 6.3 **a** Transmittance spectra of the FTO and DSSC; **b** reflectance spectrum of the commercial SSA. From [15]

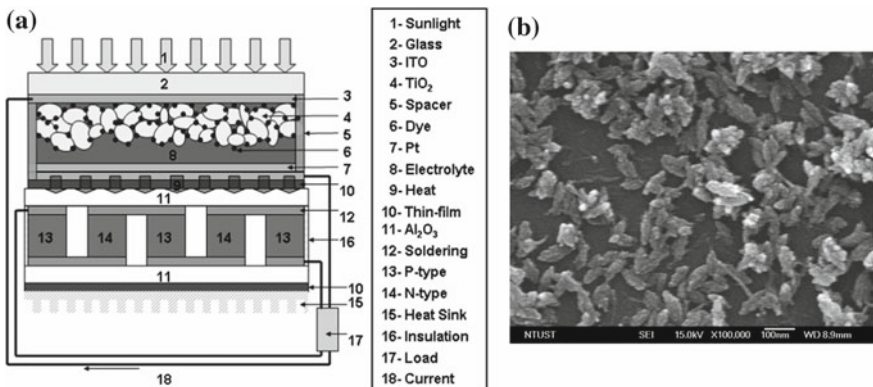


Fig. 6.4 **a** Schematic diagram of a solar-thermoelectric module. **b** SEM image of the CuO nanoparticles produced by the proposed process. From [36]

overall heat conduction, increasing the temperature by around 2 K. This leads to a voltage of around 14.8%, thus enhancing the thermoelectric conversion efficiency of the thermoelectric generator by 10% and increasing the overall power output by 2.35%. It was found that this solar-thermoelectric module can generate about 4.95 mW/cm² under a solar radiation intensity of about 100 mW/cm².

6.2.2 Polymer-Based Solar Cells

Suzuki et al. proposed an OTEPV hybrid device selectively working in two operation modes, either PV or TE [37]. The device was successfully fabricated using organic materials, regioregular poly(3-hexylthiophene-2, 5-diyl) (P3HT):FeCl₃ and [6, 6]-phenyl-C61-butric acid methyl ester (PCBM)/P3HT. When parallel circuit is connected, PV power generator operates under light irradiation. TE power is generated by connecting p-type layers in series with thermal gradient between T_{cold} and T_{hot}. Due to the limitation of the materials used, the PV output of the module can only reach 2.1×10^{-2} mW/cm² with the efficiency of $2.1 \times 10^{-2}\%$. In TE mode, the module can produce the power output of 0.015 nW over a temperature difference of 52 K. However, the work proposed an alternative and cost effective method to hybridized the two energy harvesting technologies. An example of the fabricated flexible OTEPV hybrid module was also demonstrated [37].

Zhang et al. fabricated a polymer solar cell-thermoelectric (PSCTE) hybrid system which utilized a P3HT/indene-C60 bisadduct (IC60BA) polymer solar cell [38]. The TE module used the TGP-715 chip from Micropelt, Germany. The spectrum absorption of the polymer solar cell is limited to the region from near-UV to visible, as shown in Fig. 6.5c. Therefore the TE module can collect the solar energy wasted by the PSC unit. Their results showed that the PSCTE system improved the total

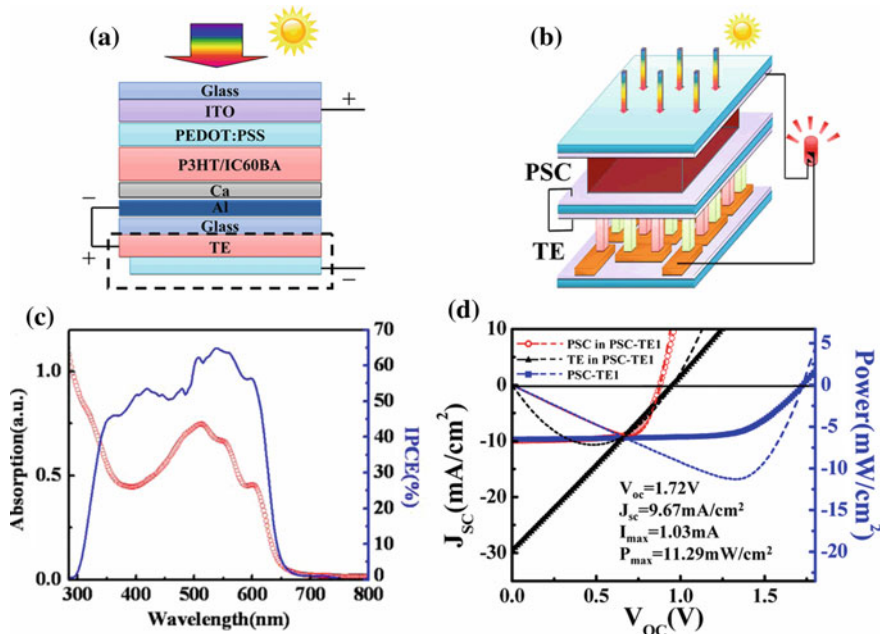


Fig. 6.5 **a** Schematic illustration of the PSCTE hybrid device using PSC as the top cell and TE as bottom cell. **b** Schematic illustration of the circuit when the LED is driven by PSCTE series-connected device **c** IPCE and absorption spectra of the PSC. **d** Photocurrentvoltage (the hollow circle is PSC, the solid triangle is TE, and the solid square is PSCTE) and power output (dotted line with corresponding color) curves of PSCTE and its subcells under AM 1.5 (100 mW/cm² radiative power). From [38]

power output compared to sole PSCs when a temperature gradient across TE module was introduced. The V_{oc} and the power output were improved dramatically, as shown in Fig. 6.5d, moving from 0.87 V for PSC alone to 1.72 V for PSC-TE hybrid system. Likewise, the P_{max} improved from 6.02 mW/cm² for PSC alone to 11.29 mW/cm² for the PSC-TE hybrid system, given a temperature difference of 9.5 K across the TE unit. The physical process that determines the overall power generation of the PSCTE hybrid system was also studied and analyzed in their work. They remarked how, while the hybrid system could drive a commercial light-emitting diode, the same was not possible by each separate stage of the solar converter (Fig. 6.5b).

Lee et al. fabricated an all-organic-based hybrid generator using an organic solar cell (OSC) paired with a polymer-based organic thermoelectric generator (OTG). For the latter, a single highly conductive PEDOT:PSS [poly(3, 4-ethylenedioxythiophene):polystyrene sulfonate] film was used, as shown in the schematics of Fig. 6.6a [39]. The PEDOT:PSS films as OTEG were fabricated by drop-casting a PEDOT:PSS solution on glass. Their results showed that the Seebeck coefficient of the single PEDOT:PSS film was $19.8 \mu\text{V/K}$. When the two devices were hybridized, hybridization loss (i.e. reduction in FF) caused by the internal resistance decreased by decreas-

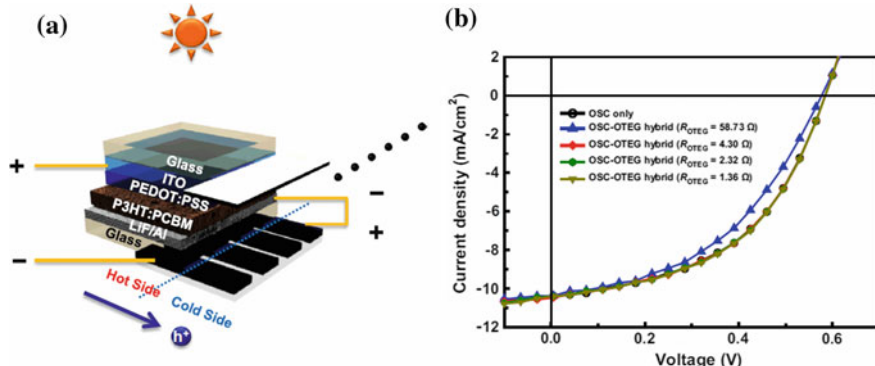


Fig. 6.6 **a** Schematic illustration of the OSC-OTEG hybrid device using a highly conductive PEDOT:PSS film as the OTEG with sunshade for the temperature gradient of the OTEG. **b** Photocurrent density-voltage ($J - V$) curves of the OSC-OTEG hybrid device depending on the resistance of each PEDOT:PSS film as the OTEG. From [39]

ing the resistance of the PEDOT:PSS film. They found that the hybridization loss of FF could be neglected when the resistance of the PEDOT:PSS film dropped below 1.36Ω (Fig. 6.6b). During their measurements, the temperature difference across the PEDOT:PSS film was 5 K. As the resistance of the PEDOT:PSS film was 1.36Ω , after hybridization, the power conversion efficiency (PCE) of the hybrid device was enhanced by the increased open circuit voltage generated by the PEDOT:PSS film. Though they had limited improvement of the overall OTEPV generator performance, their results suggested an alternative method to make use of cost-effective and flexible OTEG materials in all-organic-based hybrid solar generators.

6.2.3 Photothermally Activated Pyroelectrics

Park et al. provided a dynamic and static hybrid energy cell to harvest solar energy in full spectral range and thermal energy, using photothermal effects in PEDOT for pyroelectric conversion [40]. They used a poled ferroelectric film coated on both sides with PEDOT via solution casting polymerization of EDOT, and inserted it between the PV unit and TE unit in an OTEPV system (Fig. 6.7a). According to their results, the photothermal-pyro-thermoelectric device showed more than 6 times higher thermoelectric output with the additional pyroelectric output compared to a bare thermoelectric system under near-infrared irradiation. The photothermally driven pyroelectric harvesting film provided a very fast electric output with a high voltage output of 15 V. The pyroelectric effect was significant due to the transparent and highly photothermal PEDOT film, which could also work as an electrode. A hybrid energy harvester was assembled to enhance photoconversion efficiency of a solar cell with a thermoelectric device operated by the photothermally generated

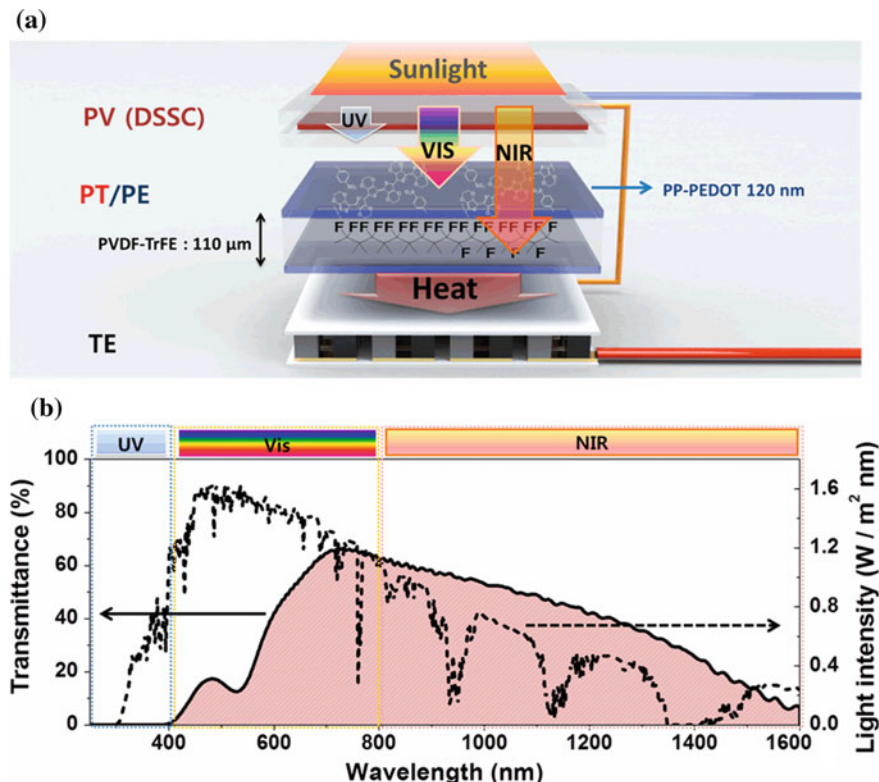


Fig. 6.7 **a** Illustration of photovoltaic and photothermal pyro-thermoelectric device. **b** UVvis-NIR transmittance spectra of DSSC and sunlight intensity (AM 1.5G, 100 mW/cm²). From [40]

heat. The PCE was increased more than 20% under sunlight irradiation (AM 1.5G) utilizing the light transmitted through the photovoltaic cell as a heat source that was converted into pyroelectric and thermoelectric output simultaneously from the photothermal PEDOT electrodes.

6.2.4 Perovskite Solar Cells

Zhang et al. estimated the feasibility of using the emerging perovskite solar cells and thermoelectric modules for a hybrid OTEPV system [41]. The results in their paper showed that because of the very low temperature coefficient of the perovskite solar cell, the efficiency of the perovskite solar cell-TEG hybrid system can amount to 18.6%, while the efficiency of the single perovskite solar cell is 17.8%. They also suggested that the selection of the SSA was vital for the performance of the whole hybrid system (Fig. 6.8). A three-dimensional numerical model of the hybrid system

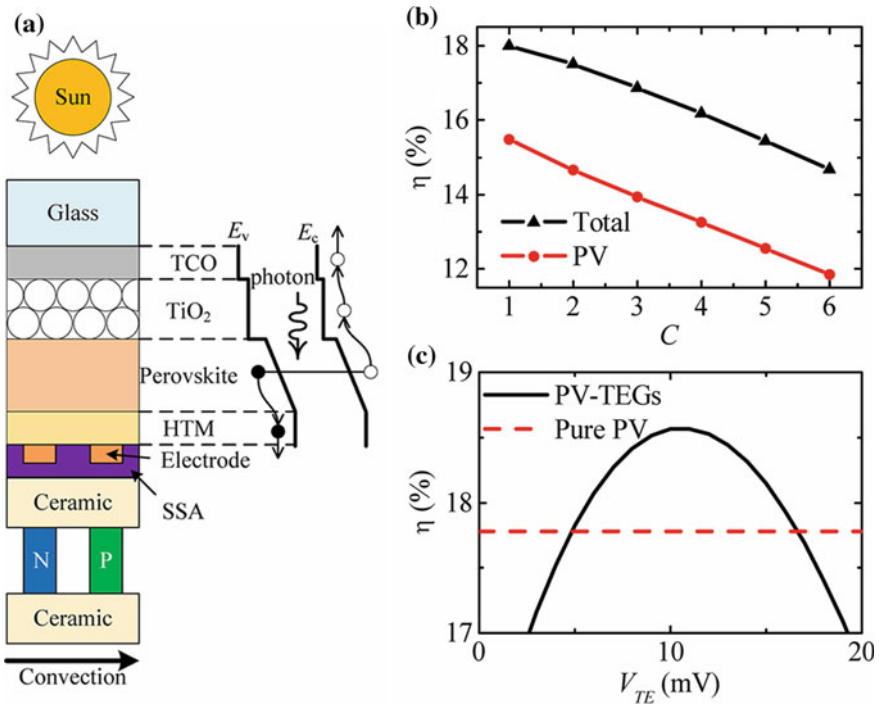


Fig. 6.8 **a** Schematic diagram of the perovskite solar cell-thermoelectric hybrid system. **b** Influence of the solar concentrating ratio on the efficiency of the hybrid system. **c** Total efficiency of the hybrid system with the perovskite solar cell and the efficiency of the pure perovskite solar cell. From [41]

was developed in Zhang's work [41]. They found that in their OTEPV hybrid system the decline in the conversion efficiency caused by the thermal concentration can be neglected up to thermal concentration ratios of 100. Their initial study suggests that perovskite solar cells are very interesting candidates for OTEPV hybrid systems. However, stability of solar cells based on perovskites is a widely known issue which could jeopardize thermoelectric hybridization, if not properly and duly addressed.

6.3 Inorganic Photovoltaic Materials

6.3.1 First Investigations: Polysilicon Solar Cells

Recently, quite a bit of interest has also arisen around the possibility to enhance the efficiency of inorganic solar cells by hybridization with TEGs, as shown by the increasing number of papers reporting on inorganic TE–PV (ITEPV) hybrid generators. Two approaches are mostly followed. The first one considers solar splitting

solutions in which a beam splitter directs the ultraviolet–visible part of the solar spectrum on the solar cell, and the infrared part of it on the TEG [17, 42–47]. The second approach is instead focused on the PV and TEG coupling as reported in Chap. 5. Since only the latter kind of strategy embeds a real photovoltaic–thermoelectric hybridization, we will limit the forthcoming analysis to this class of devices only.

Due to the fact that thermoelectric hybridization of inorganic solar cells is a very young field of research, most of the available literature evaluates the hybridization feasibility, in different contests and scenarios, through theory or numerical models. The first evaluation of this kind was published in 2006 by Vorobiev et al. [48] who modeled both spectrum–splitting and direct coupling strategies in HTEPVGs. In the latter approach they considered a multi–junction solar cell with efficiency as high as 30%, showing that thermoelectric hybridization can only mitigate the decrease of PV efficiency η_{pv} with temperature. Thus, no advantage in terms of final efficiency was reported.

Five years later Sark published a more general work in which he evaluated the amount of energy per year that would be possibly gained by thermoelectric hybridization of state-of-the-art polycrystalline silicon PV modules [18]. This evaluation showed a possible enhancement of $\approx 15\%$ on annual basis in the case of thermoelectrics with ZT values of 1.2, values which were considered easily achievable already at that time. However, also in this case the thermoelectric contribution was reported to act only as a mitigation of the PV temperature sensitivity, not being large enough to motivate any industrial implementation.

In spite of such a conclusion, Sark’s results along with the huge market potential of hybridized solutions involving silicon cells (covering nearly 90% of the total PV market) stimulated the publication of several works on this subject. As a matter of fact, papers dealing with the hybridization of silicon solar cells is the subject of most of the papers published in the field of ITEPV generators, including studies of optical concentrated systems [49, 50], evaluation of optimal electrical load conditions [51], and thermal management [52]. Also the effect of cooling with nanofluids [53] and solution implementing heat pipe were investigated [54]. Experimental works include instead studies on poly– and mono–crystalline silicon submodules [55, 56], thin film solar cells [57], and on the effect of TEG design on the system efficiency [58]. In addition, also electrical hybridization [59], and optical concentration by parabolic trough [60] were experimentally studied.

Regardless of the great variety of the papers reporting on silicon PV hybridization, all of them confirmed, either explicitly or implicitly, that at present thermoelectric hybridization can only mitigate the efficiency decrease of solar cells when PV temperature increases. This is a consequence of the already mentioned remarkable temperature sensitivity of silicon solar cells, that cannot be overcome by the still small efficiency of TEGs. In this context claims of improved efficiencies sometime appeared in literature (e.g. in [59]) have to be carefully evaluated.

6.3.2 Multi-junction Concentrated Solar Cells

Beyond silicon, one of the most studied solution is the hybridization of multi-junction solar cells. The reason for this interest stands on the fact that this kind of solar systems normally work at very high levels of optical concentration—and thus they exploit great potentials for heat recovery.

Theoretical works on this subject are focused mainly on the investigation of the opportunities and on the feasibility of thermoelectric hybridization, with a special attention paid to various optimization parameters such as optical concentration, TEG thermal resistance, encapsulation, and the cooling method [61–65].

Although these investigations reported a better feasibility compared to the case of silicon, also in these cases for current thermoelectric ZT s thermoelectric hybridization is found only to mitigate the strong temperature sensitivity of the PV efficiency, with basically no advantage compared to cooling. This result is well confirmed by the only experimental paper available in literature on this subject by Beeri et al. [66], who showed no efficiency gain compared to the sole PV at room temperature. Therefore also for multi-junction solar cells higher ZT values are needed to make possible the effective implementation of TEGs in hybrid solar converters.

6.3.3 Non-silicon-Based Solar Cells

Other solutions investigated by research groups around the world involved hybridization of CIGS (copper indium gallium selenide), GaAs, CdTe, amorphous silicon, perovskites, and CZTS (copper zinc tin sulfide) solar cells, mostly through theoretical studies. Actually, only CIGS and GaAs solar cells were experimentally hybridized.

The first experimental report was a paper by Hsueh et al. [67] who developed a hybrid system made of a state-of-the-art CIGS solar cell with efficiency of 16%, a commercial TEG, and an anti-reflective coating made of ZnO nanowires. Even if the authors report a huge efficiency increase (from 16 to $\sim 21\%$) due to the thermoelectric hybridization with only 11 K of temperature difference at the TEG sides, a normalization of the TEG footprint area on the solar cell dimensions reduce this increase to a much smaller $\sim 0.45\%$. This normalized result is in line with what reported by theoretical works which investigated hybridization of CIGS solar cells [49, 68–70]. All of them works basically reported that, as for silicon, also for CIGS solar cells at room temperature no advantage in terms of efficiency enhancement compared with the PV case alone can be achieved with current TEGs. Actually, the CIGS η_{PV} temperature sensitivity is very close to that of silicon, since the two materials exhibit a very similar energy gap.

However, theoretical predictions [49, 70] showed the possibility of achieving an efficiency gain using optical concentration. It is actually known how optical concentration reduces carrier recombination and thus temperature sensitivity especially

in CIGS solar cells, which are dominated by non-radiative recombination. Despite this theoretical evidence, no experimental work have been published to verify this thesis yet.

Concerning instead GaAs, Da et al. [71] reported experiments evaluating the thermoelectric hybridization of GaAs solar cells in both terrestrial and space environments. Also in this case, they showed an increase of PV conversion performances capable only to maintain the efficiency of the solar cell close to its room temperature value—without any efficiency gain. A highly detailed theoretical analysis on the optimization parameters for this type of ITEPV converters was provided by Zhang et al. [64].

Other PV materials have been the subject of theoretical works only. The most interesting results are reported for amorphous silicon (aSi) and CZTS, which seem so far the best candidates for thermoelectric hybridization with current TEG technologies. These results show the possibility of an efficiency increase ranging between 30 and 50% of the sole PV value for amorphous silicon [69, 72] and up to 57% for CZTS [72, 73]. However, these figures require working temperatures up to 200–250°C, which could induce irreversible degradation of the PV stage of the HTEPG system. Therefore, the testing of the solar cell feasibility at such high temperatures, and the development of proper encapsulations and heat mirrors have to be pursued in the near future to validate model predictions.

6.4 Summary and Conclusions

It has been shown that both organic and inorganic PV materials may play a role in the development of hybridized solar converters. Organic PV materials reports prospective advantages in terms of low costs and easy preparation even of large-area devices. However, PV efficiencies are still far lower than those achievable in inorganic PV materials, and the contribution from the TEG stage, albeit relatively large, cannot fill the efficiency gap yet.

Use of inorganic PV materials is in principle a more natural choice, also in view of their predominant role in the PV market. However, it is nowadays well accessed that at least for silicon (and, likewise, in other inorganic semiconductors with comparable energy gaps), decay of PV efficiency due to the increasing temperature of the PV stage can be at most mitigated by the TEG stage—while the overall efficiency cannot be significantly boosted in comparison to pure PV solar generators.

Room for HTEPVs remains open in large-gap, low-cost PV materials, whose performances are less sensitive to the higher temperatures needed to pair them with TEGs. Therefore, concentrated solar cells based on aSi and CZTS are expected to be suitable playgrounds to experiment PV-TE hybridization, along with stabilized perovskite solar cells.

Finally, it surely deserves to be mentioned that further disruptive opportunities might arise by a more intimate hybridization of the PV and TE stages, as shown for instance in a recent paper by Luo et al. [74] who reported on a synergistic

photovoltaic/thermoelectric effect in a thin-film nanostructured CdTe/Bi₂Te₃ junction. In this system the Bi₂Te₃ layer acts simultaneously as the solar cell *n* type material, and as a thermoelectric material subjected to a temperature gradient spontaneously generated across the junction. The thermoelectric potential of the Bi₂Te₃ layer facilitates the charge separation, and converts the waste heat into electricity, increasing the solar cell performance. Even though the efficiencies reported for this novel class of HTEPV generators are very limited ($\sim 2.7\%$, with a thermoelectric contribution around 35%), the approach might be of notable relevance to enhance power conversion efficiency over the whole solar spectrum.

References

1. J.E. Carlé, F.C. Krebs, Sol. Energy Mater. Sol. Cells **119**(Supplement C), 309 (2013)
2. F.C. Krebs, N. Espinosa, M. Hösel, R.R. Søndergaard, M. Jørgensen, Adv. Mater. **26**(1), 29 (2013)
3. A. Gambhir, P. Sandwell, J. Nelson, Sol. Energy Mater. Sol. Cells **156**, 49 (2016)
4. L. Chang, I.E. Jacobs, M.P. Augustine, A.J. Moulé, Org. Electron. **14**(10), 2431 (2013)
5. F.C. Krebs, J. Fyenbo, D.M. Tanenbaum, S.A. Gevorgyan, R. Andriessen, B. van Remoortere, Y. Galagan, M. Jørgensen, Energy Environ. Sci. **4**(10), 4116 (2011)
6. F.C. Krebs, M. Jørgensen, Adv. Opt. Mater. **2**(5), 465 (2014)
7. H. Goldsmid, Materials **7**(4), 2577 (2014)
8. B. Poudel, Q. Hao, Y. Ma, Y. Lan, A. Minnich, B. Yu, X. Yan, D. Wang, A. Muto, D. Vashaei, X. Chen, J. Liu, M.S. Dresselhaus, G. Chen, Z. Ren, Science **320**(5876), 634 (2008)
9. L. Han, S.H. Spangsdorf, N.V. Nong, L.T. Hung, Y.B. Zhang, H.N. Pham, Y.Z. Chen, A. Roch, L. Stepien, N. Pryds, RSC Adv. **6**(64), 59565 (2016)
10. K. Kusagaya, M. Takashiri, J. Alloys Compd. **653**, 480 (2015)
11. A. Hagfeldt, G. Boschloo, L. Sun, L. Kloo, H. Pettersson, Chem. Rev. **110**(11), 6595 (2010)
12. S. Oh, P. Rai, M. Ramasamy, V.K. Varadan, Microelectron. Eng. **148**, 117 (2015)
13. Y. Zhang, Y. Xuan, Sol. Energy Mater. Sol. Cells **144**(Supplement C), 68 (2016)
14. G.J. Snyder, E.S. Toberer, Nat. Mater. **7**(2), 105 (2008)
15. N. Wang, L. Han, H. He, N.H. Park, K. Koumoto, Energy Environ. Sci. **4**(9), 3676 (2011)
16. D. Yang, H. Yin, IEEE Trans. Energy Convers. **26**(2), 662 (2011)
17. D. Kraemer, L. Hu, A. Muto, X. Chen, G. Chen, M. Chiesa, Appl. Phys. Lett. **92**(24), 243503 (2008)
18. W.G.J.H.M. van Sark, Appl. Energy **88**(8), 2785 (2011)
19. B.S. Dallan, J. Schumann, F.J. Lesage, Sol. Energy **118**, 276 (2015)
20. M. Jørgensen, F.C. Krebs, in *Stability and Degradation of Organic and Polymer Solar Cells* (Wiley, 2012), pp. 143–162
21. M. Hermenau, M. Riede, K. Leo, in *Stability and Degradation of Organic and Polymer Solar Cells* (Wiley, 2012), pp. 109–142
22. K. Tvingstedt, C. Deibel, Adv. Energy Mater. **6**(9), 1502230 (2016)
23. E.A. Katz, D. Faiman, S.M. Tuladhar, J.M. Kroon, M.M. Wienk, T. Fromherz, F. Padinger, C.J. Brabec, N.S. Sariciftci, J. Appl. Phys. **90**(10), 5343 (2001)
24. Y. Sun, G.C. Welch, W.L. Leong, C.J. Takacs, G.C. Bazan, A.J. Heeger, Nat. Mater. **11**(1), 44 (2011)
25. M. Riede, T. Mueller, W. Tress, R. Schueppel, K. Leo, Nanotechnology **19**(42), 424001 (2008)
26. A. Mishra, P. Buerle, Angew. Chem. Int. Ed. **51**(9), 2020 (2012)
27. A.K.K. Kyaw, D.H. Wang, D. Wynands, J. Zhang, T.Q. Nguyen, G.C. Bazan, A.J. Heeger, Nano Lett. **13**(8), 3796 (2013)

28. L. Ye, S. Zhang, W. Zhao, H. Yao, J. Hou, *Chem. Mater.* **26**(12), 3603 (2014)
29. C. Cui, W.Y. Wong, Y. Li, *Energy Environ. Sci.* **7**(7), 2276 (2014)
30. M.M. Lee, J. Teuscher, T. Miyasaka, T.N. Murakami, H.J. Snaith, *Science* **338**(6107), 643 (2012)
31. M. Liu, M.B. Johnston, H.J. Snaith, *Nature* **501**(7467), 395 (2013)
32. N.G. Park, *Mater. Today* **18**(2), 65 (2015)
33. F.D. Lewis, X. Zuo, *Photochem. Photobiol. Sci.* **2**(11), 1059 (2003)
34. M.K. Nazeeruddin, E. Baranoff, M. Grätzel, *Sol. Energy* **85**(6), 1172 (2011)
35. S. Mathew, A. Yella, P. Gao, R. Humphry-Baker, B.F.E. Curchod, N. Ashari-Astani, I. Tavernelli, U. Rothlisberger, M.K. Nazeeruddin, M. Grätzel, *Nat. Chem.* **6**(3), 242 (2014)
36. H. Chang, M.J. Kao, K.C. Cho, S.L. Chen, K.H. Chu, C.C. Chen, *Curr. Appl. Phys.* **11**(4), S19 (2011)
37. T. Suzuki, K. Yoshikawa, S. Momose, in *2010 International Electron Devices Meeting* (IEEE, 2010)
38. Y. Zhang, J. Fang, C. He, H. Yan, Z. Wei, Y. Li, *J. Phys. Chem. C* **117**(47), 24685 (2013)
39. J.J. Lee, D. Yoo, C. Park, H.H. Choi, J.H. Kim, *Sol. Energy* **134**(Supplement C), 479 (2016)
40. T. Park, J. Na, B. Kim, Y. Kim, H. Shin, E. Kim, *ACS Nano* **9**(12), 11830 (2015)
41. J. Zhang, Y. Xuan, L. Yang, *Int. J. Energy Res.* **40**(10), 1400 (2016)
42. M. Mizoshiri, M. Mikami, K. Ozaki, *Jpn. J. Appl. Phys.* **51**(6 PART 2) (2012)
43. X. Ju, Z. Wang, G. Flamant, P. Li, W. Zhao, *Sol. Energy* **86**(6), 1941 (2012)
44. Y. Li, S. Witharana, H. Cao, M. Lasfargues, Y. Huang, Y. Ding, *Particuology* **15**, 39 (2014)
45. E. Elsarrag, H. Pernau, J. Heuer, N. Roshan, Y. Alhorr, K. Bartholomé, *Renew. Wind Water Sol.* **2**(1), 16 (2015)
46. E.J. Skjølstrup, T. Søndergaard, *Sol. Energy* **139**, 149 (2016)
47. M. Hajji, H. Labrim, M. Benissa, A. Laazizi, H. Ez-Zahraouy, E. Ntsoenzok, J. Meot, A. Benyoussef, *Energy Convers. Manag.* **136**, 184 (2017)
48. Y. Vorobiev, J. González-Hernández, P. Vorobiev, L. Bulat, *Sol. Energy* **80**, 170 (2006)
49. J. Zhang, Y. Xuan, L. Yang, *Energy* **78**, 895 (2014)
50. R. Lamba, S.C. Kaushik, *Energy Convers. Manag.* **115**, 288 (2016)
51. W. Lin, T.M. Shih, J.C. Zheng, Y. Zhang, J. Chen, *Int. J. Heat Mass Transf.* **74**, 121 (2014)
52. W. Zhu, Y. Deng, Y. Wang, S. Shen, R. Gulfram, *Energy* **100**, 91 (2016)
53. S. Soltani, A. Kasaeian, H. Sarrafha, D. Wen, *Sol. Energy* **155**, 1033 (2017)
54. G. Li, X. Zhao, J. Ji, *Energy Convers. Manag.* **126**, 935 (2016)
55. M. Fisac, F.X. Villasevil, A.M. López, *J. Power Sources* **252**, 264 (2014)
56. H. Karami-Lakeh, R. Hosseini-Abardeh, H. Kaatuzian, *Int. J. Thermophys.* **38**(5), 1 (2017)
57. Y. Deng, W. Zhu, Y. Wang, Y. Shi, *Sol. Energy* **88**, 182 (2013)
58. D. Kossyvakis, G. Voutsinas, E. Hristoforou, *Energy Convers. Manag.* **117**, 490 (2016)
59. K.T. Park, S.M. Shin, A.S. Tazebay, H.D. Um, J.Y. Jung, S.W. Jee, M.W. Oh, S.D. Park, B. Yoo, C. Yu, J.H. Lee, *Sci. Rep.* **3**, 2123 (2013)
60. M. Mohsenzadeh, M. Shafii, H.J. Mosleh, *Renew. Energy* **113**(Supplement C), 822 (2017)
61. E.A. Chavez-Urbiola, Y.V. Vorobiev, L.P. Bulat, *Sol. Energy* **86**, 369 (2012)
62. T. Cui, Y. Xuan, Q. Li, *Energy Convers. Manag.* **112**, 49 (2016)
63. O.Z. Sharaf, M.F. Orhan, *Energy Convers. Manag.* **121**, 113 (2016)
64. J. Zhang, Y. Xuan, *Energy Convers. Manag.* **129**, 1 (2016)
65. A. Rezania, L. Rosendahl, *Appl. Energy* **187**, 380 (2017)
66. O. Beeri, O. Rotem, E. Hazan, E.A. Katz, A. Braun, Y. Gelbstein, *J. Appl. Phys.* **118**(11) (2015)
67. T.J. Hsueh, J.M. Shieh, Y.M. Yeh, *Prog. Photovolt. Res. Appl.* **23**(4), 507 (2015)
68. B. Lorenzi, M. Acciarri, D. Narducci, *J. Mater. Res.* **30**(17), 2663 (2015)
69. R. Björk, K.K. Nielsen, *Sol. Energy* **120**, 187 (2015)
70. D. Li, Y. Xuan, Q. Li, H. Hong, *Energy* **126**, 343 (2017)
71. Y. Da, Y. Xuan, Q. Li, *Energy* **95**, 200 (2016)
72. G. Contento, B. Lorenzi, A. Rizzo, D. Narducci, *Energy* **131**, 230 (2017)
73. B. Lorenzi, G. Contento, V. Sabatelli, A. Rizzo, D. Narducci, *J. Nanosci. Nanotechnol.* **17**(3), 1608 (2017)
74. B. Luo, Y. Deng, Y. Wang, M. Gao, W. Zhu, H.T. Hashim, J. García-Cañadas, *RSC Adv.* **6**(115), 114046 (2016)

Chapter 7

Photovoltaic–Thermoelectric–Thermodynamic Co-Generation



Abstract In this chapter, we will describe triple cogeneration technologies for solar conversion. The costs of solar conversion technologies are determined by the efficiency of power conversion, the lifetime and reliability of its components, the cost of the raw materials, potentially including storage, and any fabrication or construction required. Recently, photovoltaics and solar thermal have emerged as viable candidates for low cost power production; they each have losses that vary across the solar spectrum, with realized and theoretical efficiencies that are well below fundamental thermodynamic limits. Thus, it is desirable to split the solar spectrum to utilize both technologies in parallel over their respective optimal wavelength ranges. This chapter will present promising triple co-generation solutions that have been developed and implemented to provide electric power generation by a combination of photovoltaic and thermal generation. In particular, we show that splitting the solar spectrum, and then using high-energy solar photons for photovoltaics and medium-energy solar photons for thermoelectrics with a bottoming Rankine cycle has potential to achieve 50% solar-to-electricity conversion using existing materials. Also, over 50% of the harvested energy goes to thermal storage for generation after sunset, which could enable highly efficient baseload solar electricity and heat generation at all hours of the day.

7.1 Photovoltaic–Thermoelectric–Thermodynamic Co-Generation

7.1.1 Introduction to Triple Cogeneration

Utilization of direct solar energy harvesting represents a major trend in the energy sector, which has been enabled by over 50 years of continual improvements in efficiency and costs. As a result, the solar industry has been grown quickly in the past 8 years, at a rate of approximately 15% per year compounded annual growth in generating capacity deployed per year [1]. However, the solar energy fraction of total United States power generation is still only 0.6% as of 2015 [2], which is 1.7×10^{11} kWh per year. The fundamental limit of solar energy density on the earth is known

to be 1 kW/m^2 at most; given partial cloud and aerosol cover; the annual average in North America is only around $600\text{--}700 \text{ W/m}^2$ during day time on average. Photovoltaic cells can generate electricity directly from solar photons, but their operating principles limit their conversion efficiencies [3]. Optical concentration of 500 suns can push up the energy conversion efficiency up to 46% using a stack of four materials in a multi-junction solar cell [4]; nonetheless, this is still far below the thermodynamic limit of 84.5% [5]. In addition, these multi-junction cells are generally much more expensive than their single junction counterparts, although this disadvantage can be partially mitigated by inexpensive optical concentration. Still, this approach also does not work at night, and is not dispatchable without relatively expensive electrical storage (i.e., batteries). Thermoelectric materials can convert heat directly into electricity, but also have limited efficiency due to the fundamental link between the transport of heat and electricity. Thus, there are three major, fundamental challenges for current direct solar energy harvesting technologies:

1. Limited power densities
2. Efficiencies well below the thermodynamic limit
3. Limited time of production (i.e., when the sun is out)

In this chapter, we explore the concept of triple co-generation. Here, we aim to fully extract the energy of solar spectrum by using a total of three different technologies, each applied to a range of photon energies, to get the overall system efficiency much closer to the theoretical (Carnot) limit. The first two items above are improved by this approach. Using a thermal storage allows consumption to be shifted from time of collection, which significantly benefits the third item.

The question, then becomes, ‘what should triple co-generation look like?’ Two essential mechanisms are utilized by splitting the solar spectrum into two usable photon energy ranges. The technology for separating solar photons into distinct energy ranges has been referred to as a selective solar absorber and reflector (SSAR) [6]. The SSAR must reflect higher energy photons, absorb medium energy photons, and reflect low energy photons to prevent radiative heat loss via low-energy photons. The higher energy photons (UV and visible) for (#1) can directly generate electricity in photovoltaic (PV) cells; medium-energy photons can be collected as high temperature heat for (#2), which can be used directly, or converted into electric power using thermoelectric energy harvesting. The final dispensable generation component of the triple is (#3) a mechanical thermodynamic energy conversion (heat engine) in conjunction with a high temperature thermal storage. The heat engine typically considers a Rankine cycle, which is used for coal-fired power plants in scale of $10^7 \sim 10^9$ Watts per unit with a superheated steam ($\approx 600^\circ \text{C}$). The efficiency of heat engines a reasonably high in rate to the thermodynamic limit. Recent development of organic Rankine cycles (ORCs) provides a smaller scale power delivery from few 10^5 Watts with lower source temperature ($\approx 200^\circ \text{C}$). This third generator is capable of quasi-steady state operation, which can be shifted in time via low-cost thermal storage. With enough capacity, such a system can continue generating electricity throughout the evening. The system can be made highly flexible by adjusting the division of incoming solar power between photovoltaics and solar thermal generation. The size

and operating temperature of the components can be selected to help minimize the overall system leveledized cost of energy (LCOE), including a favorable weighting for the dispatchable power component. The capital cost (USD/W) can serve as an important secondary consideration.

Before proceeding any further, it should be noted that the choice of fully neglecting here the possibility of a direct thermal pairing between PV and thermoelectric stages (which was instead the favorite choice in HTEPV generators—cf. Chaps. 5 and 6) originates from the fact that such a layout would be unavoidably inefficient. Actually, the TEG stage would be cramped between the requirement of keeping its hot-side temperature low enough to prevent a degradation of the PV efficiency, and that of maintaining its cold-side temperature sufficiently high to warm the fluid flowing through the thermal stage enough to be usable. This would inescapably make the power output from the thermoelectric stage too marginal to justify its deployment (and cost).

The net power output of triple co-generation, when combining photovoltaics, thermoelectrics, and a Rankine cycle (RC) is given by:

$$W_{NET} = W_{PV} + W_{TE} + W_{RC} - (W_{pump1} + W_{pump2}) \quad (7.1)$$

While splitting and transferring energy between sub-systems creates a penalty, this can be minimized with proper design. The overall system efficiency is predicted to reach up to 50% with 50% of dispatchability, without requiring any breakthroughs in existing materials for thermoelectric (TE), spectral splitting, or photovoltaics. A potential implementation is shown in Fig. 7.1. This section will discuss the physics behind this potential performance.

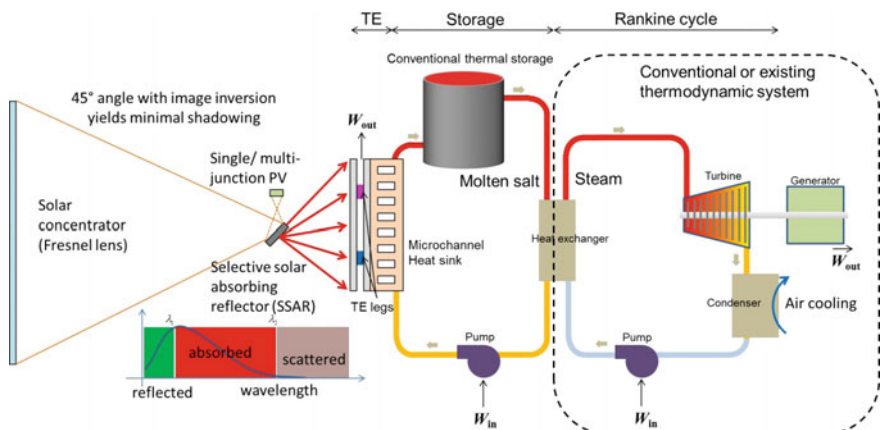


Fig. 7.1 Block diagram illustrating the key components of triple co-generation, along with a proposed experimental implementation. Adapted with permission from [7]

7.1.2 Component Technologies

Triple cogeneration has one necessary functionality, spectral splitting, achieved using a spectrally selective device, which creates two usable spectral ranges. The first, higher energy range, can be used for high-efficiency photovoltaics. The second, medium energy range, can be used for thermal conversion. The latter path can use a range of different thermal conversion technologies, including thermoelectrics, heat engines, and thermophotovoltaics. It may or may not involve low-cost thermal storage. In the following subsections, we discuss the operation of each of these component technologies in detail.

7.1.2.1 Spectrally-Selective Solar Filter

A spectrally-selective solar filter is the foundation of triple cogeneration. While this component can be designed in many different ways, the key functionality is to divide the solar spectrum into at least two usable energy ranges. Ideally, this will send each part of the solar spectrum to where it can be used most effectively. From a thermodynamic perspective, it turns out that the best conversion strategy for high-energy photons is photovoltaic direct conversion to electricity. For medium-energy photons, particularly below 1 eV, it can in fact be more effective to use thermal conversion, especially if one is confined to a single photovoltaic bandgap. However, for low-energy photons, it is best not to absorb them at all, to help suppress infrared radiation, as is described below in more detail.

One potential implementation of this concept is a selective solar absorber and reflector (SSAR). Such a selective solar surface allows one to cleanly discriminate between these three wavelength ranges, and only absorb the middle range. This can be constructed as follows. First, one starts with a highly selective solar absorber as a baseline. While Kirchoff's law of thermal radiation requires that the absorptivity equals the emissivity at each wavelength in thermal equilibrium, we can make use of the temperature difference between the surface of the sun (approximately 5500 °C) and the terrestrial absorber. Since according to Wien's law, the peak emission wavelength scales inversely with temperature, the emission spectrum of the absorber typically peaks at a much longer wavelength. This creates an opportunity to distinguish between short wavelengths, at which most solar emission can be absorbed, and longer wavelengths, at which most thermal re-radiation can be suppressed. The overall performance can be quantified using the thermal transfer efficiency η_t , at a temperature T and solar concentration factor C using the following equation [6, 8]:

$$\eta_t = B\bar{\alpha} - \frac{\bar{\varepsilon}\sigma T^4}{CI_s} \quad (7.2)$$

where B is the window transmissivity, $\bar{\alpha}$ is the spectrally averaged absorptivity, $\bar{\varepsilon}$ is the spectrally averaged emissivity, σ is the Stefan-Boltzmann constant, and I_s is the

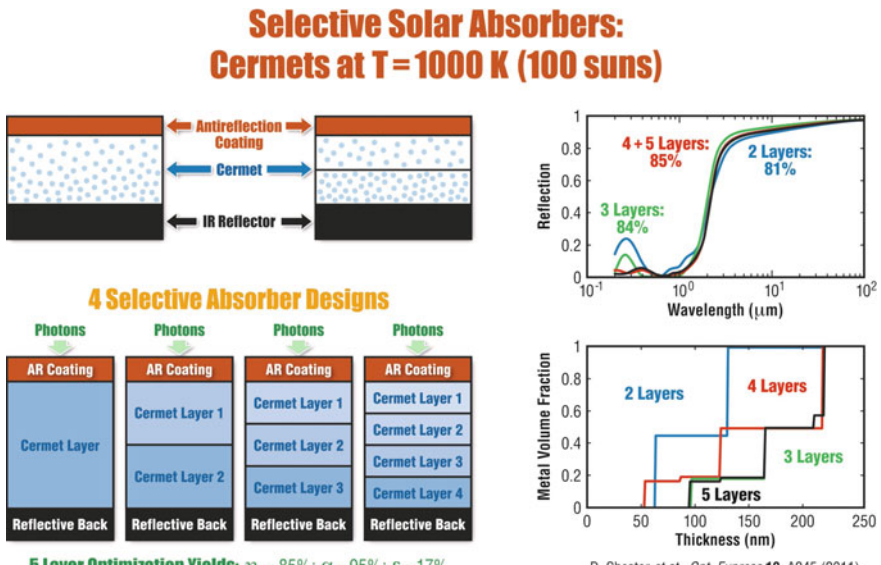
solar constant, generally taken as 1 kW/m^2 . Since the absorptivity and emissivity are required to match at each wavelength in equilibrium, the spectrally-averaged emissivity will gradually increase with absorber temperature, ultimately approaching the value of the spectrally-averaged absorptivity.

Ceramic-metal composites, known as cermets, are capable of providing high levels of spectral selectivity, which in some cases can approach theoretical limits. For low-temperature operation, they are already available commercially, and can absorb up to 95% of sunlight, while only re-emitting a small fraction of the energy of a blackbody—as low as 5% at 100°C [9]. To achieve similar functionality at higher temperatures, new designs are needed. Good candidates for the cermet constituents are metals with high melting points such as Cu, Au, Ni, Mo, Cr, Co, Pt, and W, and dielectrics such as oxides of the preceding compounds, along with SiO_2 , Al_2O_3 , and MgO . Among these, the most widely used selective coatings, due to their low cost, are black chrome, a graded $\text{Cr}-\text{Cr}_2\text{O}_3$ cermet [10–12], and nickel-pigmented anodic Al_2O_3 [13, 14]. There has been a great deal of work in fabricating cermets. They are generally characterized by measured absorptivity $\bar{\alpha} > 0.9$ and emissivities which vary significantly with temperature [6, 15]. Some of the best performance in recent work is captured in Table 7.1, where double-layer cermet structures feature prominently. For example, Zhang et al. found some of the best results by optimizing a $\text{Mo}:\text{Al}_2\text{O}_3$ double cermet on a Cu substrate at 350°C [16]. It has also been shown that W:AlN double cermet designs, display performance only slightly worse at the same temperature [17]. Furthermore, Al:AlON cermet coatings are arguably just as good at lower temperatures of 80°C [8, 18]. In recent work, illustrated in Fig. 7.2, one can use a cermet made from new materials with even higher melting points, such as tungsten and aluminum oxide (the basic starting point for sapphires). These structures were optimized under two operating conditions, as a proof of concept. For unconcentrated sunlight ($C = 1$) at an absorber temperature of 400 K , 4 layers of $\text{W}:\text{SiO}_2$ with increasing metal volume fraction showed $\bar{\alpha} = 0.979$ and $\bar{\varepsilon} = 0.042$ at 400 K , for a thermal transfer efficiency of 0.843 [19]. For concentrated sunlight ($C = 100$) at an absorber temperature $T = 1000 \text{ K}$, the optimized design showed $\bar{\alpha} = 0.945$ and $\bar{\varepsilon} = 0.172$ at 1000 K , for a thermal transfer efficiency of 0.7559 [19]. Calculations have shown that this design can capture up to 85% of sunlight as heat under 100 suns concentration, and 91% under 500 suns concentration, even when operating at 1000 K . The overall performance of this optimized 4-layer structure exceeds that of any other cermet-based selective solar absorber found in the literature under 100 suns concentration, which operates at 1000 K [7, 19].

Another option is to use semiconductors as filters. Intrinsic or lightly-doped semiconductors with direct bandgaps generally will absorb strongly above their bandgap energy, followed by an Urbach tail right near the band edge, with very little absorption below the bandgap energy. Depending on the operating conditions, such as temperature, and desired cutoff wavelength, different materials may be more or less suitable for this design. It has recently been shown theoretically that the efficiency of these materials can theoretically approach that of cermets [21]. While fabricated structures to date have not fully realized this potential yet, thinner structures provide hope for success at higher temperatures (up to at least 600°C) [22].

Table 7.1 Comparison of experimental cermet material systems in recent publications

Experimental cermet material system	Absorptivity $\bar{\alpha}$	Emissivity $\bar{\epsilon}$ (temperature)	Reference
$\text{Al}_2\text{O}_3/\text{Mo}:\text{Al}_2\text{O}_3(f = 0.34)/\text{Mo}:\text{Al}_2\text{O}_3(f = 0.53)/\text{Mo}$	0.955	0.08 (350 °C)	[20]
$\text{AlN}/\text{W}:\text{AlN}/\text{W}:\text{AlN}/\text{Al}$	0.94 ± 0.02	0.09 (350 °C)	[17]
$\text{AlN}/\text{Al}:\text{AlON}(f = 0.143)/\text{Al}:\text{AlON}(f = 0.275)/\text{Al}$	0.96	0.08 (80 °C)	[18]
$\text{Al}_2\text{O}_3/\text{Al}:\text{AlON}(f = 0.093)/\text{Al}:\text{AlON}(f = 0.255)/\text{Al}$	0.974	0.033 (80 °C)	[8]
Almeco-TiNOX	0.95	0.05 (20 °C)	[19]



D. Chester et al., Opt. Express 19, A245 (2011).

Fig. 7.2 Proposed selective solar surface at 1000 K, based on cermets (tungsten and alumina nanocomposites). Adapted with permission from [7]

Finally, it becomes necessary to design these selective solar absorbers to efficiently reflect high-energy photons. The most straightforward way to achieve this is to use a multilayer Bragg reflector stack on top of the emitter. Recent experiments have shown that even if the absorber is extraordinarily hot, the reflector can be thermally decoupled from this system [23].

7.1.3 Tandem Solar Cells with Optical Concentration

Solar optical concentration C is a key engineering component of this concept. Depending on the scale of solar correction, there are several ways to design the concentrator, such as a tower corrector with flat panel mirrors [24], a parabolic 3D curved dish reflector [25], a parabolic trough reflector [26], or a Fresnel lens [27]. Considering the smallest integration of the system, array of squared Fresnel lens with auto tracking mechanism suits to the concept. For example, the best solar intensity from the map in the United States [28] shows $7.5 \text{ kWh/m}^2/\text{day}$, which can be translated to approximately 1 kW per 1 m^2 in time average effectively for 8 hours per day. Let's consider a conceptual unit, which includes a square Fresnel lens, a PV cell, and a thermoelectric generator in 1 m^2 foot print. Mechanical tracking system support the entire unit and rotate the angle three dimensionally to align to the orientation of solar. Concentrations of 100 suns (or more) allow the lateral area of the PV cells and thermoelectric generators to be much smaller than the collection area, e.g. $10 \times 10 \text{ cm}^2$ for every square meter. Therefore, the mechanical fixture should focus on supporting the lens.

The system physical integration is discussed later. Here, one thermodynamic generator with thermal storage covers entire array of solar concentrator units and locates just next to them to minimize the working flow distance. An array of 20 units corrects 20 kW of solar power and generates 10 kW of electricity with total efficiency of 50%. This amounts to operation at 5 kW for 8 daytime hours and 8 nighttime hours.

7.1.4 High Temperature Thermoelectrics

In this section, the modeling of thermoelectric generators is discussed. We begin by presenting the theoretical energy conversion of thermoelectrics, which is given by:

$$\eta_{\text{TE}} = \left(1 - \frac{T_c}{T_h}\right) \left(\frac{m - 1}{m + \frac{T_c}{T_h}}\right) \quad (7.3)$$

This equation is well-known to be the maximum efficiency for given temperatures for the hot and cold side of the thermoelectric leg (T_h and T_c). Here, T_h and T_c are not given, however, since these values must be determined by energy balance. Recursive calculation is needed to find the true value of these in practice. The value 'm' comes from the ratio of internal and external electrical resistance and is known to be $\sqrt{1 + Z\bar{T}}$ [30] at the optimum, where \bar{T} is mean temperature across the thermoelectric leg (Fig. 7.3).

Obviously, extracting the maximum power out of applied heat is the best solution to obtain the maximum efficiency as a part of an integrated system. In comparison, in a single thermoelectric generator system, irreversible thermal contacts exist for both hot and cold side. Thus, the thermoelectric temperatures T_h and T_c should never be

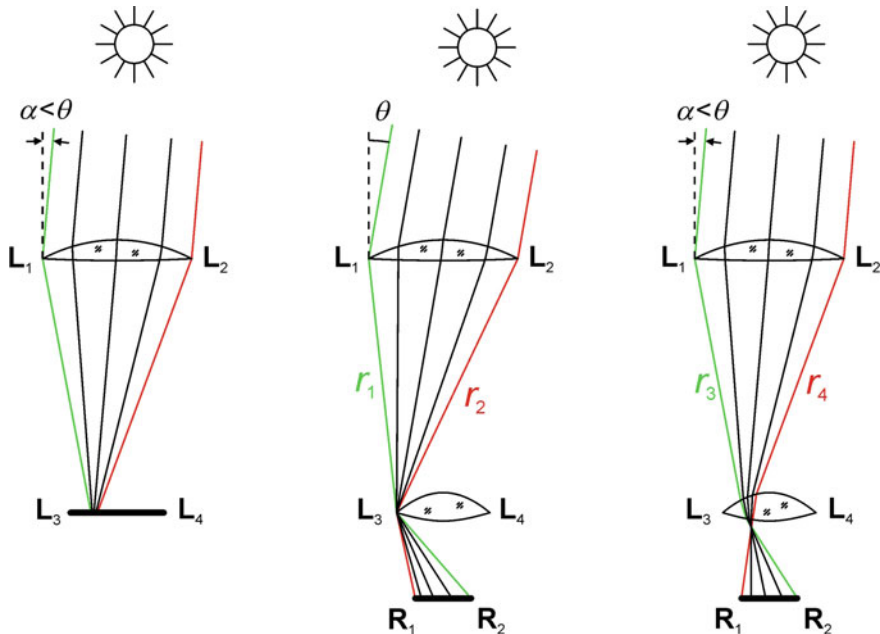


Fig. 7.3 Schematic of a Fresnel lens combined with a Kohler integrator for solar tracking. Adapted with permission from [29]

the same as given temperatures of heat reservoirs (heat source T_s and thermal ground T_a). At the extreme to achieving the reservoir temperatures, the system efficiency for the single system achieve the maximum but reach the power output goes to zero (Fig. 7.4). This relation was derived by Curzon-Ahlborn [31] and the efficiency of this heat engine is found to be $\eta = 1 - \sqrt{\frac{T_a}{T_s}}$, which corresponds to the efficiency at the maximum power output instead of Carnot efficiency $\eta = 1 - \left(\frac{T_a}{T_s}\right)$, which corresponds to the maximum efficiency.

To obtain the maximum possible power output, it is critical that the thermoelectric generator be designed to match the external thermal contacts (rest of the thermal resistance in a unique heat flow). Alternatively, the external thermal contacts can be selected to match the thermoelectric generator. At the design point, the optimum condition for T_h and T_c is determined.

Aforementioned analytic model for the electro-thermal co-optimum design is generic for any temperature range, which is determined by the external reservoirs. In real case, however, the material properties are temperature dependent by nature. Hence the materials must be carefully selected match to the operational temperature range. Obviously, Seebeck coefficient S , electrical conductivity σ , and thermal conductivity β are all temperature dependent properties and then the dimensionless figure-of-merit ZT is temperature dependent accordingly. The following figure

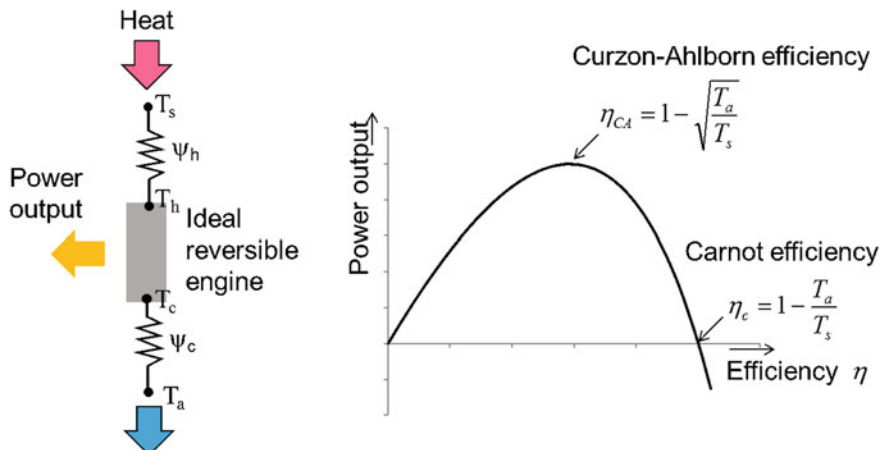


Fig. 7.4 Power versus efficiency relation for ideal heat engine ($ZT \rightarrow \infty$) with irreversible thermal contacts (ψ_h and ψ_c)

shows the ZT value as function of temperature for typical materials. As the characterization is properly conducted, any thermoelectric material shows a peak in ZT value at a certain temperature point. This is important in particular for this higher temperature application. The mechanism of holding a peak as a function of temperature can be explained by the large change in Seebeck coefficient (thermopower), which is squared in computing the ZT value, just like voltage is squared in computing the power through a resistor (since the voltage generated from a given temperature difference is proportional to the Seebeck coefficient). A method to construct the thermoelectric legs with multi heterogenous materials, so called segmented legs is considered for an application with large temperature difference [32]. Otherwise, the mean ZT across the resulting temperature span ($T_h - T_c$) of the thermoelectric legs to be considered as the real performance.

Beside the thermoelectric properties, there are several other significant considerations on other material properties are necessary. Due to the heterogeneous packaging of the thermoelectric modules, thermal expansion mismatch of the materials with substrate, contacts, and coating materials. A combination of ceramics and metals typically exhibits a large mismatch. Linear thermal expansion coefficient for Nitrides are relatively smaller $2\text{--}5 \times 10^{-6}/\text{K}$, while the oxides fit generally in $5\text{--}10 \times 10^{-6}/\text{K}$ range. Metals are typically in range of $10\text{--}20 \times 10^{-6}/\text{K}$. The thermal expansion coefficient more varies for semiconductors but is typically in $2\text{--}7 \times 10^{-6}/\text{K}$. Stress control at the contacts is rather important compared to the near room temperature applications due to the large temperature change in on/off of heat and the large temperature difference between the hot and cold side. Analytical and numerical stress analysis studies are found in [34, 35] (Fig. 7.5).

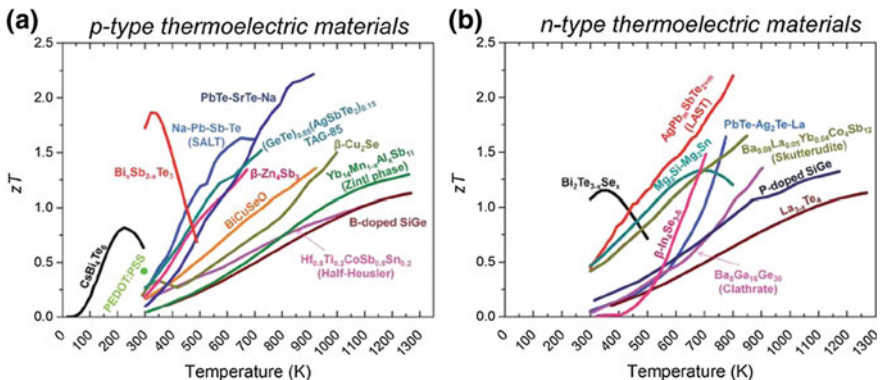


Fig. 7.5 Temperature dependent ZT of the best **a** p-type and **b** n-type thermoelectric materials discovered to date. Adapted with permission from [33]

7.1.5 High Temperature Thermal Storage

Dispatchability is an ability to distribute the power when power source is completely off or shutdown. Due to the nature of solar, there is a significant gap between demand and supply. Rechargeable batteries are of course a popular and simple solution. Unfortunately, commercial batteries are not as affordable as solar cells today. Let us consider a dispatchability of 50% as if the demand and supply balanced. Power consumption of day time is 50% and another for after dark. Reasonable market pricing of solar PV cells cost about 2200 USD for 1 kW power output (2.2 USD/W) [36], while a rechargeable battery, i.e. lithium ion (Li-ion) battery, costs for 4 h x 1 kW (anticipating 50% of total electricity consumption per day) likely be 4,000 USD (1000 USD/kWh) [37].

Another strategy is applicable for this tri-generation concept. Waste heat out from the thermoelectric power generator can be buffered in a thermal storage and later consumed for generating power. The downstream mechanical thermodynamic generator operates with a time shift so that rechargeable electrochemical battery will not be necessary.

In theory, the waste heat from the thermoelectric can be as high as the temperature where a Rankine cycle (steam turbine) work, which is up to 540 °C [38]. At such high temperature, molten salts, e.g. a combination of 60% sodium nitrate and 40% potassium nitrate, are practically used in a solar tower power plant, e.g. Solar Two built in the Mojave desert of California was adapted from its predecessor in 1995 [39]. The operating temperature of the Solar Two system seemed to be in the 350–380 °C range. At the melting temperature, these materials represent a viscosity are fairly close to that of water at room temperature and slightly higher in range of 0.5–1 mPa [40]. Hence the fluid dynamic handling can be quite similar to water.

The storage tank and pump system could be designed much like a hot water storage system, except with a potentially much larger heat loss per unit time. Clearly, thermal

insulation of the tank and pipes are critical. This topic has been investigated for solar thermal systems for many years, resulting in practical material candidates [41].

To briefly compare battery and thermal storage, consider that the power density is 2–3 times greater for Li-ion compared to the Rankine cycle, but the energy density of a Li-ion battery is less than that of thermal storage. A direct apples-to-apples comparison is difficult, but as the system becomes larger, the net benefits of using thermal storage with Rankine cycle will be greater. The large Rankine cycle system has an efficiency of 40–43%. More details will follow in the next section.

7.1.6 *Thermodynamic Mechanical Heat Engines*

The thermodynamic cycle, in particular, a Rankine cycle, takes the bottoming part in this tri-generation concept. Because of that, the heat source temperature for the component is relatively moderate. Applicable technology is an open cycle (external combustion cycle) and Rankine cycle is the most popular in the category. Steam turbines have been utilized for many of power plants in wide range of capacity (100 kW to 500 MW) and recently ORCs for relatively lower temperature heat sources (typically 500 W to 1 MW). ORC system is typically utilized for waste heat recovery or geothermal power generation. ORCs use some variation of carbon based high molecular mass fluids and the name comes from the working fluid. The largest single ORC with 16 MW capacity developed for geothermal application [42]. The efficiency depends on the inlet temperature of working fluid and condensation temperature. The performance is lower than steam turbines not only by the thermodynamic nature in low grade heat, but also due to the smaller enthalpy of the organic working fluid. Net energy efficiency of typical ORC system is in range of 5–15% [43] while primary energy efficiency of a coal fired steam turbines show a range of 40% [44] but it is reduced by 5% in reducing natural water consumption for cooling the condenser [45].

7.2 Efficiency of Triple Co-Generation System

The overall performance of a triple co-generation system will depend on a number of factors. It will always be limited by the quality of the spectral splitting—below a certain threshold, depending on the exact choice of technologies, it would never make sense to utilize such an approach. However, if the spectral splitting approach, such as an SSAR, could be made sufficiently good, then it would make sense to calculate the overall system performance. Although theoretically solar thermal has a higher efficiency limit than solar photovoltaics, in practice, solar photovoltaics generally have higher efficiencies, since they use fewer steps to generate electricity. Thus, we can use the world-record efficiency for tandem cells of 31% as a threshold for examining triple co-generation technology as a potential improvement over simpler

approaches. In the following sections, we focus on the specific case of photovoltaic-thermoelectric-Rankine cycle co-generation. We provide a detailed mathematical model for calculating the system efficiency as a function of the underlying components, and then look at the effects of changing concentrations, and the prospects for scaling these systems to different sizes.

7.2.1 Modeling of Spectrum Integrated System and Trade-Off

The maximum conversion efficiency possible for any system converting thermal energy into electricity is the so-called Carnot efficiency η_C . For the temperatures characteristic of solar power conversion, this thermodynamic limit is typically estimated to be between 85 and 95%, depending on whether any additional loss mechanisms are included [46].

The overall performance of a triple co-generation system can be represented as follows:

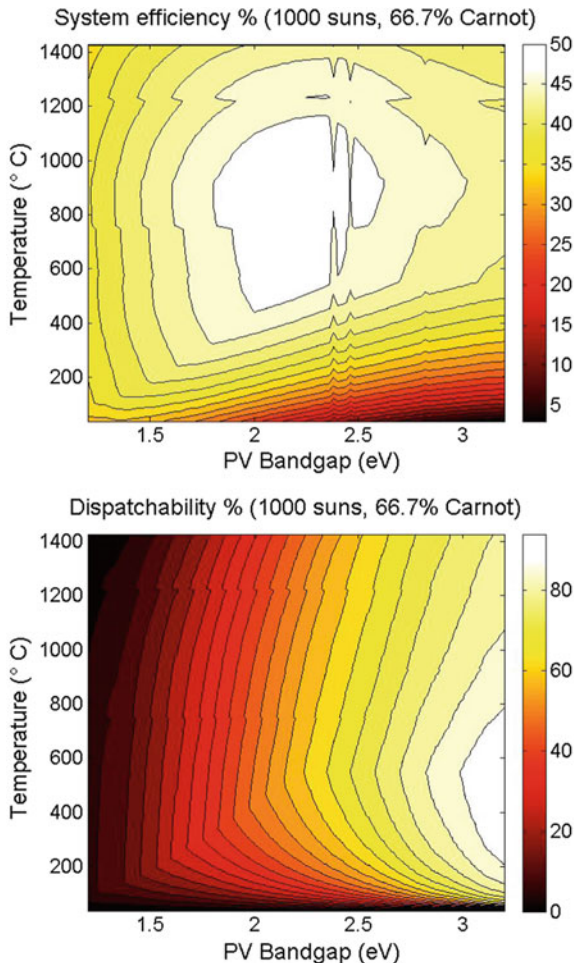
$$\eta = \eta_{\text{pv}} + \eta_{\text{SSS}}[\eta_{\text{te}} + (1 - \eta_{\text{te}})\eta_{\text{me}}] \quad (7.4)$$

where η_{SSS} is the fraction of total incident solar radiation absorbed as heat by the selective solar surface (SSS); η_{te} is the thermoelectric component efficiency; η_{pv} is the photovoltaic component efficiency using the reflected light, which cannot exceed $1 - \eta_{\text{SSS}}$; and η_{me} is the mechanical engine conversion efficiency.

We can now calculate the overall system performance for a specific test case, in which we use a spectrally selective absorbing reflecting under 500 suns illumination, and split the spectrum at a variable bandgap E_g . Figure 7.6 shows that the system efficiency (left) and dispatchability (right) as a function of the bandgap (x-axis), and hot-side SSAR temperature T_{SSS} (y-axis). The thermal components consist of a thermoelectric and a Rankine cycle that goes from 37 °C (cold side) to the minimum of SSAR temperature T_{SSS} or 550 °C. For simplicity, we assume that the efficiency of the Rankine cycle is 2/3 that of the Carnot efficiency. If we assume that $T_{\text{SSS}} = 1000$ °C, the thermoelectric consists of a silicon-germanium alloy, the tandem PV bandgaps are 1.7 and 2.2 eV (using, e.g., InGaAlP/GaInP), which operates at 72 °C, we find that the maximum system efficiency will be 50%. Thus, the resulting improvement in efficiency from using our system is immense, even compared to the best case of a record tandem cell operating at 31% efficiency [4]. Furthermore, if we incorporate a sufficient amount of thermal energy storage (TES), up to 63% of the energy harvested can be stored for hours, which would be sufficient to maintain power generation throughout the day with only 1.5% energy loss on average [7]. The levelized cost of energy could be as low as 5.8 cents per kWh (assuming 7% discount rate, 30 years lifetime) [7].

Potential applications include baseload utility-scale power generation to replace fuel-burning power plants; self-contained dispatchable power generation isolated (off-grid) households and individuals; and emergency relief via local micro-grid formation, such as when existing infrastructure is damaged for extended time periods.

Fig. 7.6 (Left) System efficiency limits and (right) dispatchable energy fraction as a function of PV bandgap and selective solar absorbing reflector operating temperature, using tandem-junction PV, TE with $ZT=1$, and a mechanical engine operating at $2/3$ of the Carnot limit. Adapted with permission from [7]



Manufacturing these systems at scale even has the potential to create new, strategically important domestic jobs in the energy sector.

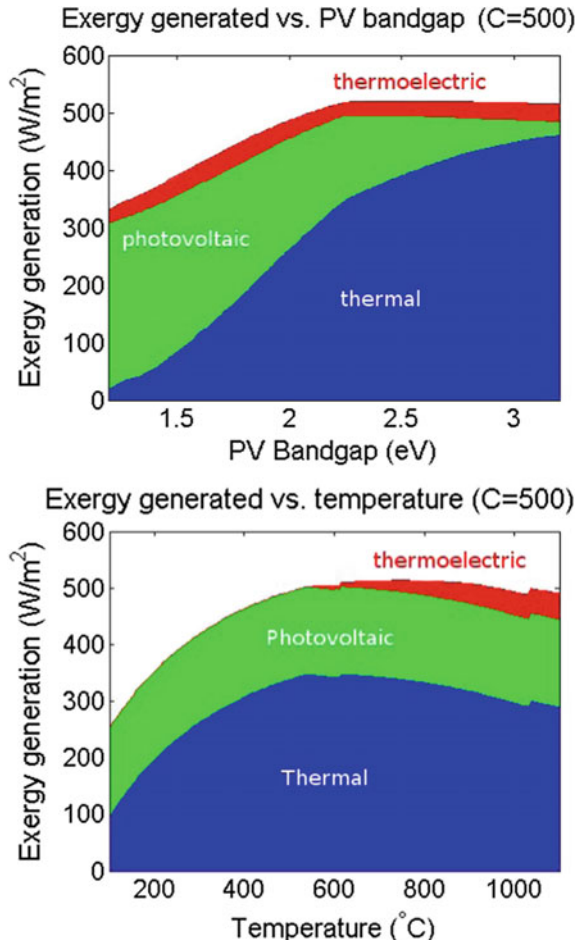
7.2.2 Efficiency and Concentration

Here, we will consider concentrating photovoltaic modules compatible with $500\times$ solar concentration, with an integrated copper backplane for rapid cooling and electronics for efficient power extraction (Fig. 7.7).

In general, tandem cell efficiencies under 1 sun are over 31%, while record 5-junction cells under hundreds of suns concentration can reach over 46% efficiencies

Fig. 7.7 (Left)

Contributions to exergy generation as a function of PV bandgap at a constant solar absorber temperature (800°C). (right)
 Contributions to exergy generation as a function of solar absorber temperature at a fixed PV bandgap (2.2 eV). Adapted with permission from [7]

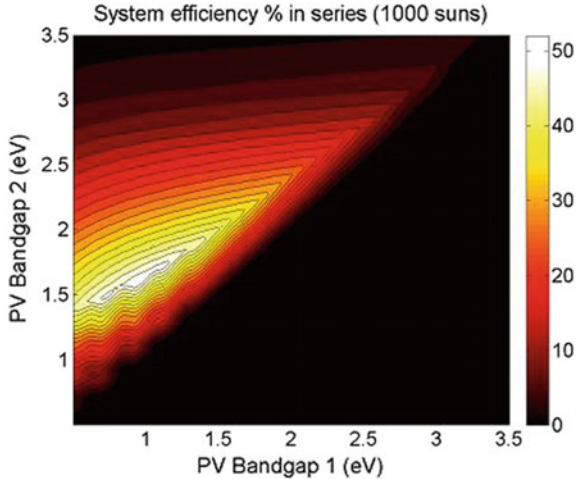


[4]. Nonetheless, given sufficient levels of solar concentration, only two PV materials with different bandgaps, connected in series, are required to reach efficiencies well over 40% [46]. In Fig. 7.8, we show the maximum efficiency of a two-terminal tandem cell connected in series, as a function of the lower PV bandgap on the x-axis, and the larger PV bandgap on the y-axis. The highest overall efficiency of 42.2% is observed for bandgaps of 1.1 and 1.7 eV. Still, relatively little loss in absolute efficiency is associated with going up to higher bandgaps. Thus, lower bandgaps can approach 1.7 eV and still preserve tandem efficiencies over 40%.

To justify the figure and results present, the calculation can be performed as follows. We begin with the energy conversion efficiency of the PV diode, which is given by [21]:

$$\eta = \frac{J_{\text{sc}} V_{\text{oc}} FF}{CI_s} \quad (7.5)$$

Fig. 7.8 PV conversion efficiency for 2-terminal tandem cells versus lower PV bandgap 1 (x-axis) and higher PV bandgap 2 (y-axis) under 1000 suns concentration. The best efficiency of 42.2% is observed for bandgaps of 1.1 and 1.7 eV



where V_{oc} is the open-circuit voltage, J_{sc} is the short-circuit current, FF is the fill-factor, C is the solar concentration, and I_s is the solar constant, generally taken to be 1 kW/m².

The short-circuit current density depends directly on the degree of absorption of incoming light, which is given by:

$$J_{sc} = \int d\lambda \left[\frac{e\lambda}{hc} \frac{dI}{d\lambda} A(\lambda) IQE(\lambda) \right] = \int d\lambda w(\lambda) A(\lambda) IQE(\lambda) \quad (7.6)$$

where $A(\lambda)$ is the absorption, $IQE(\lambda)$ is the Internal Quantum Efficiency, $\frac{dI}{d\lambda}$ is the light intensity exposed by the solar cell per unit wavelength (given by the ASTM AM1.5G solar spectrum [47]), e is the elementary charge of an electron, h is Planck constant, and c is the speed of light. In our calculations, we assume that $IQE(\lambda) = 1$ for $\lambda \leq \lambda_g$, and 0 otherwise. The open-circuit voltage is then calculated using the following expression:

$$qV_{oc} = E_g - nk_B T \ln \left(\frac{A}{en_{ph}} \right) \quad (7.7)$$

where n is the diode ideality factor.

The fill factor FF is computed using a reduced V_{oc} ($z_{oc} = qV_{oc}/nk_B T$):

$$FF = \frac{z_{oc} - \ln(z_{oc} + 0.72)}{z_{oc} + 1} \quad (7.8)$$

7.2.3 System Scaling Impact

Scaling of the system does not behave linearly. Since the thermodynamic cycle fundamentally works more efficiently as its scale increases. The minimum scale this tri-generation supposed to work properly in range of 10 kW or larger in power output, which would likely support a smaller community, occupying from several to dozens of households. This system would fit into the design of a so-called micro-grid, and provide tremendous value to any location where no power grid access exists.

7.3 Solar Photovoltaic/Thermophotovoltaic/Thermal Triple Cogeneration

In this section, we consider the potential advantage of using thermophotovoltaics as an alternative to thermoelectrics. The overall theoretical efficiency is even higher than in the previous case, since solar thermophotovoltaics have theoretical efficiencies on their own that approach 85% [48]. However, in practice, the realized efficiencies of thermophotovoltaics approach 24% heat-to-electricity [49]. As a result, while thermophotovoltaics by themselves are not yet viable as a replacement for the best photovoltaic diodes, they have potential to replace thermoelectrics as part of a topping cycle.

7.3.1 TPV Integrated System

For medium-energy photons, thermophotovoltaic (TPV) represents a straightforward alternative to thermoelectrics. Here, let us call conventional solar photovoltaics “optical PV” to differentiate them more explicitly from TPV. TPV essentially uses a photodiode to generate electricity much like in optical PV, but optimized for significantly longer average optical wavelengths. This means that the semiconductor needs to be lower band gap materials, e.g. indium gallium arsenide (InGaAs) or gallium antimonide (GaSb), etc., rather than standard optical photovoltaic materials with larger bandgaps, such as crystalline silicon, cadmium telluride, copper indium gallium selenide (CIGS), or gallium arsenide.

A TPV system generally consists of a thermal emitter which absorbs near infra-red (NIR) and infra-red (IR) wavelength to selectively emit to the low-bandgap photodiode. It has previously been shown that the selective absorber already works as the thermal emitter, hence there is a great benefit to exploring this combination. The energy conversion efficiency of the TPV alone is power conversion efficiency of the TPV diode is given by (7.4). The open circuit voltage (7.6) depends on the

recombination term A , typically consisting of at least radiative recombination and Shockley-Read-Hall recombination mechanisms, given by [21]:

$$A = \frac{q(\varepsilon + 1) E_g^2 k_B T}{4\pi^2 \hbar^3 c^2} + \frac{4qD}{L_D N_D} \left(\frac{k_B T \sqrt{m_e^* m_h^*}}{2\pi \hbar^2} \right)^3 \quad (7.9)$$

where ε is the dielectric permittivity, \hbar is the reduced Planck constant, c is the speed of light, D is the diffusion coefficient, L_D is the diffusion length, N_D is the defect density, and m_e^* and m_h^* are the effective masses for electrons and holes, respectively. In general, additional terms such as Auger recombination can be added in the presence of high injection currents. The dark current is then given by $J_s = A e^{-E_g/nk_B T}$.

The fill factor FF can be estimated as FF_{sh} , which can be calculated using (7.7) along with

$$FF_s = FF_o [1 - 1.1r_s] + 0.185r_s^2 \quad (7.10)$$

and

$$FF_{sh} = FF_s \left[1 - \left(\frac{V_{oc} + 0.7}{V_{oc}} \right) \frac{FF_s}{r_{sh}} \right] \quad (7.11)$$

where $r_s = I_{sc}R_s/V_{oc}$ is the reduced series resistance, and $r_{sh} = I_{sc}R_{sh}/V_{oc}$ is the reduced shunt resistance. The short circuit current J_{sc} (7.5) may be rewritten as

$$J_{sc} = \int_0^\infty d\lambda \frac{2qc}{\lambda^4} \frac{\varepsilon(\lambda)EQE(\lambda)}{\exp(hc/\lambda k_B T) - 1} \quad (7.12)$$

where q is the electron charge, c is the speed of light in vacuum, λ is the wavelength, $\varepsilon(\lambda)$ is the spectral emittance of the emitter, $EQE(\lambda)$ is the external quantum efficiency of the device, V is the voltage, T_d is the device temperature. Clearly, predicting the precise values of all these quantities is non-trivial, and requires a powerful simulation framework.

Our detailed electro-optically coupled simulation framework is given in Fig. 7.9, which combines our drift-diffusion model for electronic transport with our finite-difference time domain simulation for optical and thermal transport. This framework is adapted from a previous study of nanowire solar cells [50].

7.3.2 Practical Considerations

The conversion efficiency means that the rest of fractional energy conversion all goes to generating heat. That comes from electron-hole recombination process, which is common for the photovoltaics. Some of the higher energy carriers excited by photons in valence band creates the potential to drive the current into the load. Also, the excited carriers more scatter to phonons and the negative carrier. First one directly creates the

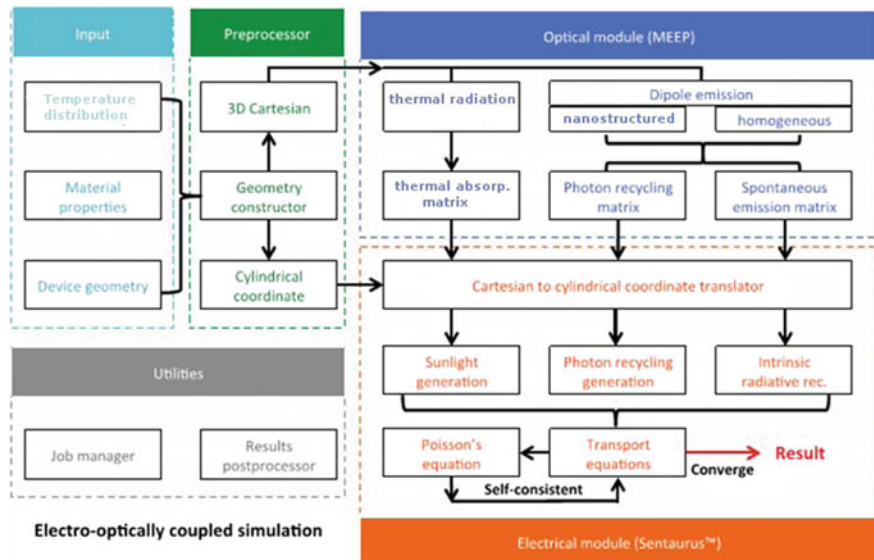


Fig. 7.9 Electro-optically coupled simulation framework for thermophotovoltaic system power generation. It allows one to precisely design both selective emitters and photovoltaic cells based on novel semiconductors, with performance tuned to match TPV selective emitter spectra (adapted from [50])

heat and the latter creates the photon, resulting in heat generation as well. Due to the smaller band gap material, the thermal losses associated can exceed those observed in the best solar PV devices [51].

Due to the involvement of heat generation, temperature dependency of the I-V characteristic needs to be carefully investigated. As an example, a GaAs based material works at the temperature range up to 345 K [52], which clearly requires a good heat sink to dump the excess heat to ambient. This also clarifies a less opportunity of recovering waste heat out of the TPV. In this case, the efficiency of waste heat recovery should be much less than 6.7% (Curzon-Ahlborn efficiency) at the maximum power output condition. This efficiency is the theoretical upper limit as the heat engine is perfectly reversible.

Integrating across the entire solar spectrum, the overall efficiency can be estimated to exceed 50%, using currently available selective emitters and absorbers, when operating at 900 °C.

A significant challenge associated with using TPV in this tri-generation concept originates from its unwanted thermal generation out of the thermodynamic loss of the photo-electro direct conversion. This problem is derived from a common challenge of photovoltaics and it is more severe for TPV devices due to its lower band gap nature of the photo diode cells.

Another possibility would be to combine TPV with selective PV generation. That is with a high-performance liquid cooled base frame (cold plate) both for optical PV

and TPV with the selective solar absorber and reflector. The trade-off of driving liquid pump to circulate the refrigerant may compensate for adding TPV over a standalone optical concentrated PV system.

7.4 Summary

In conclusion, we developed the concept of triple co-generation as an approach for efficient conversion of sunlight to electricity. The two foundations of this approach are to split the solar spectrum into photovoltaic and thermal wavelength ranges, and to optimize the overall system design to maximize the net power output, as in (7.1). The photovoltaic aspect can be implemented using existing technology, with emphasis on higher bandgap materials like III-phosphides (III-Ps). We find that with proper design, existing materials are sufficient to provide up to 50% efficient conversion of sunlight into electricity, with 50% or more potentially stored using low-cost thermal storage, in lieu of batteries. This approach thus has potential to provide continuous baseload power throughout the day and night.

References

1. Solar Energy Industry Association, Solar industry data, yearly U.S. solar installation by 2016 (2016), <http://www.seia.org/research-resources/solar-industry-data>
2. Lawrence Livermore National Laboratory, Estimated U.S. energy consumption in 2015 (2016), https://upload.wikimedia.org/wikipedia/commons/e/ec/Energy_US_2015.png
3. W. Shockley, H.J. Queisser, *J. Appl. Phys.* **32**(3), 510 (1961)
4. M.A. Green, K. Emery, Y. Hishikawa, W. Warta, E.D. Dunlop, *Prog. Photovoltaics Res. Appl.* **23**(1), 1 (2015)
5. P. Wuerfel, *Sol. Energy Mater. Sol. Cells* **46**(1), 43 (1997)
6. P. Bermel, J. Lee, J.D. Joannopoulos, I. Celanovic, M. Soljacic, *Ann. Rev. Heat Transfer* **15**(15), 231 (2012)
7. P. Bermel, K. Yazawa, J.L. Gray, X. Xu, A. Shakouri, *Energy Environ. Sci.* **9**(9), 2776 (2016)
8. Q.C. Zhang, *J. Phys. D Appl. Phys.* **32**(15), 1938 (1999)
9. T. Sathiaraj, R. Thangaraj, H.A. Sharbaty, M. Bhatnagar, O. Agnihotri, *Thin Solid Films* **190**(2), 241 (1990)
10. G.E. McDonald, *Sol. Energy* **17**(2), 119 (1975)
11. J.C.C. Fan, S.A. Spura, *Appl. Phys. Lett.* **30**(10), 511 (1977)
12. C.M. Lampert, J. Washburn, *Sol. Energy Mater.* **1**(1–2), 81 (1979)
13. Å. Andersson, O. Hunderi, C.G. Granqvist, *J. Appl. Phys.* **51**(1), 754 (1980)
14. A. Scherer, O.T. Inal, R.B. Pettit, *J. Mater. Sci.* **23**(6), 1934 (1988)
15. C.E. Kennedy, Review of mid- to high-temperature solar selective absorber materials. Technical Report No. TP-520-31267 (2002)
16. Q.C. Zhang, *Sol. Energy Mater. Sol. Cells* **62**(1–2), 63 (2000)
17. Q.C. Zhang, *J. Phys. D Appl. Phys.* **31**(4), 355 (1998)
18. Q.C. Zhang, K. Zhao, B.C. Zhang, L.F. Wang, Z.L. Shen, D.Q. Lu, D.L. Xie, B.F. Li, *J. Vac. Sci. Technol. A Vac. Surf. Films* **17**(5), 2885 (1999)
19. D. Chester, P. Bermel, J.D. Joannopoulos, M. Soljacic, I. Celanovic, *Opt. Express* **19**(S3), A245 (2011)

20. Q.C. Zhang, Y. Yin, D.R. Mills, Sol. Energy Mater. Sol. Cells **40**(1), 43 (1996)
21. P. Bermel, W. Chan, Y.X. Yeng, J.D. Joannopoulos, M. Soljacic, I. Celanovic, in *Thermophotovoltaic World Conference*, vol. 9 (2010)
22. H. Tian, Z. Zhou, T. Liu, C. Karina, U. Guler, V. Shalaev, P. Bermel, Appl. Phys. Lett. **110**(14), 141101 (2017)
23. O. Ilic, P. Bermel, G. Chen, J.D. Joannopoulos, I. Celanovic, M. Soljačić, Nat. Nanotechnol. **11**(4), 320 (2016)
24. US Department of Energy, Office of Energy Efficiency and Renewable Energy, Power tower system concentrating solar power basics (2013), <https://energy.gov/eere/energybasics/articles/power-tower-system-concentrating-solar-power-basics>
25. N.S. Kumar, K. Reddy, Energy Convers. Manag. **49**(4), 812 (2008)
26. M. Giuffrida, G.P. Tornielli, S. Pidatella, A. Repetto, E. Bellafronte, P.E. Zani, in *Photovoltaic Solar Energy Conference* (Springer, Netherlands, 1981), pp. 391–395
27. S.A. Kalogirou, Prog. Energy Combust. Sci. **30**(3), 231 (2004)
28. NREL, Concentrating solar resource of the united states (2012), http://www.nrel.gov/gis/images/eere_csp/national_concentrating_solar_2012-01.jpg
29. J. Chaves, *Introduction to Nonimaging Optics*, 2nd edn. (CRC Press, 2015)
30. K. Yazawa, A. Shakouri, J. Appl. Phys. **111**(2), 024509 (2012)
31. F.L. Curzon, B. Ahlborn, Am. J. Phys. **43**(1), 22 (1975)
32. T. Caillat, J.P. Fleurial, G. Snyder, A. Zoltan, D. Zoltan, A. Borshchevsky, in *Proceedings of the 18th International Conference on Thermoelectrics* (Cat. No.99TH8407) (IEEE, 1999)
33. M. Rull-Bravo, A. Moure, J.F. Fernández, M. Martín-González, RSC Adv. **5**(52), 41653 (2015)
34. E. Suhir, A. Shakouri, J. Appl. Mech. **80**(2), 021012 (2013)
35. A. Ziabari, E. Suhir, A. Shakouri, Microelectron. J. **45**(5), 547 (2014)
36. <http://news.ennergysage.com/how-much-does-the-average-solar-panel-installation-cost-in-the-u-s/>
37. <https://electrek.co/2017/01/30/electric-vehicle-battery-cost-dropped-80-6-years-227kwh-tesla-190kwh/>
38. S. Imano, E. Saito, J. Iwasaki, M. Kitamura, High-temperature steam turbine power plant, U.S. Patent No. US 8201410 B2 (2012)
39. H.E. Reilly, G.J. Kolb, An evaluation of molten-salt power towers including results of the solar two project. Technical Report (2001)
40. S. Mahiuddin, K. Ismail, Fluid Phase Equilib. **123**(1–2), 231 (1996)
41. S.W. Moore, in *Solar Collectors, Energy Storages, and Materials*, ed. by F. de Winter (MIT Press, 1990), pp. 831–880
42. <https://www.turbomachinerymag.com/the-high-16-mw-turbine-for-a-geothermal-plant-in-croatia/>
43. R. Rowshanzadeh, Performance and cost evaluation of organic rankine cycle at different technologies. Master thesis, KTH Royal Institute of Technology, Sweden, 2010
44. K. Yazawa, M. Hao, B. Wu, A.K. Silaen, C.Q. Zhou, T.S. Fisher, A. Shakouri, Energy Convers. Manag. **84**, 244 (2014)
45. Electric Power Research Institute, Program on technology innovation: New concepts of water conservation cooling and water treatment technologies. Technical Report 1025642 (2012)
46. C.H. Henry, J. Appl. Phys. **51**(8), 4494 (1980)
47. ASTM G173-03, Standard tables for reference solar spectral irradiances: Direct normal and hemispherical on 37 degree tilted surface (2005)
48. N.P. Harder, P. Wuerfel, Semicond. Sci. Technol. **18**(5), S151 (2003)
49. B. Wernsman, R. Siergiej, S. Link, R. Mahorter, M. Palmisiano, R. Wehrer, R. Schultz, G. Schmuck, R. Messham, S. Murray, C. Murray, F. Newman, D. Taylor, D. DePoy, T. Rahmlow, IEEE Trans. Electron Devices **51**(3), 512 (2004)
50. X. Wang, M.R. Khan, M. Lundstrom, P. Bermel, Opt. Express **22**(S2), A344 (2014)
51. M.G. Mauk, in *Mid-infrared Semiconductor Optoelectronics* (Springer, London, 2006), pp. 673–738
52. B. Kucur, M. Ahmetoglu, I. Andreev, E. Kunitsyna, M. Mikhailova, Y. Yakovlev, Acta Phys. Pol. A **129**(4), 767 (2016)

Chapter 8

Hybrid Solar Harvesters: Technological Challenges, Economic Issues, and Perspectives



Abstract A summary of the main issues covered in the previous chapters will serve a comparative analysis of the current and perspective possibilities that the hybridization of thermoelectric and photovoltaic generators provides. Materials demand, technological open questions, and market-related issues will be discussed. Also concerning the competition with alternate hybridization strategies, an analysis of HTEPV cost-effectiveness will be outlined. It will be shown that HTEPV may have a key role in the development of renewable energy sources, provided that a careful selection of photovoltaic materials is made. The importance of rethinking the layout of thermoelectric generators will be stressed, along with the merits of hybridization in concentrated solar generators. As an overall conclusion, pairing thermoelectric generators to photovoltaic cells will be proved to be profitable for third-generation PV materials, where hybridization might support the differentiation of the solar module market, currently pinned to silicon-based technology.

8.1 Introduction

The final chapter of this book aims at summarizing the main issues covered in a volume that was thought and written as a primer for newcomers considering to enter the field of hybrid solar harvesting, and specifically the field of thermoelectric–photovoltaic generators.

Materials and technological challenges will be summarized, recalling the main conclusions reached in the previous chapters. The second part of this chapter will be then focused on economic issues that hybrid harvesters have to face in their path to market. It has been already remarked (Sect. 1.1.2) how today the market of solar converters is dominated by one technology. Silicon-based cells and modules (first and second generations) set the reference cost-of-ownership and the power and energy costs that any alternate technology have to defeat. Therefore, HTEPV generators, although yet in their infancy, must also be thought as competitive approaches to solar conversion—at present and in the near future. This point will be covered, although sketchily, in this chapter, before drawing some final remarks on the future of HTEPV devices.

8.2 Photovoltaic and Thermoelectric Materials

The making of an efficient and profitable HTEPV generator was shown to require a number of carefully planned moves. Starting with *active* materials, namely the PV absorber and the thermoelectric elements, it was shown how the PV material governs the effectiveness of any hybridization, ruling it out for some common PV system (e.g. non-concentrated polycrystalline silicon); and how instead low-cost, non-toxic materials with acceptable *ZTs* at moderate-to-low temperatures are still needed for the thermoelectric legs.

PV technology is currently dominated by silicon. Wafer-based crystalline silicon (c-Si) is still currently the most widespread technology due to its stable photo-conversion efficiency and its ease of processing—along with its efficiency, non-toxicity, and high reliability [1]. Wafer-based c-Si cells profits of more than 50-year manufacturing experience and of a vast technology.

Despite Si dominance, alternate PV materials have received attention over the last decade. Amorphous silicon played a significant role in the development of thin-film PV cells because of its low-cost production. Progress was hampered however by its conversion efficiency and stability [2].

Cadmium telluride solar cells have been considered for thin-film PV cells. Life-cycle analyses show that CdTe PV has the smallest carbon footprint, requires the lowest water use and has the shortest energy payback time of all PV technologies [3, 4]. Further deployment of CdTe PV cells was slowed down by Cd toxicity concerns. Furthermore, limited geo-availability of tellurium along with the increasing demand has become a limiting factor to the industrial scalability of CdTe technology. This notwithstanding, CdTe solar cells cover 5.1% of worldwide PV production [5].

Copper Indium Gallium Selenide ($\text{CuIn}_x\text{Ga}_{(1-x)}\text{Se}_2$ —CIGS) has attracted attention for PV applications due to its optimal bandgap for solar cells based on single-junctions [2]. Its further development for commercial thin-film PV devices has been hampered by the difficulty of controlling film stoichiometry and defects in materials, and by still immature process technology [1, 2, 6]. Solar cells based on CIGS thin-film and related PV materials (e.g. CGS and CIS) are however still considered promising, especially were relatively expensive elements (Ga and In) be (partially) replaced by more common elements.

Of any PV material, GaAs holds the record solar conversion efficiency (28.8 and 24.1% for lab cells and modules, respectively [7, 8]). Its wider industrial use was instead limited by the high materials cost, especially when epitaxial layers are required [9]. Furthermore, crystal imperfections and impurities still reduce device efficiencies when low cost deposition routes are considered [9].

Dye-sensitized solar cells are low-cost solar cells with a number of attractive features, including their simple manufacture, their semi-flexibility and semi-transparency. However, their conversion efficiency is still much lower than second-generation thin-film cells, not yet exceeding the threshold (at module level) for profitable deployment in commercial solar harvesters. Organic-inorganic halide perovskites, which have advanced rapidly in recent years, are promising candidates

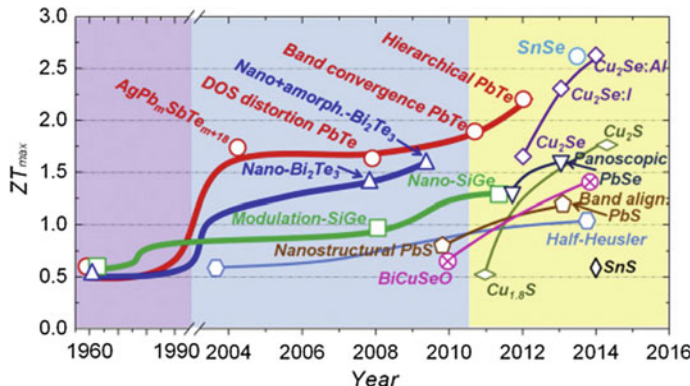


Fig. 8.1 Increase of the maximal thermoelectric figures of merit by materials classes. Reprinted with permission from [12]

as prospective third-generation PV materials due to their low cost, high efficiency and straightforward architecture [10]. Stability issues still prevent their progress, at present.

On the thermoelectric side, few areas of materials science have witnessed over the last ten years more progress and advances. The nanotechnologic toolbox has imparted a tremendous momentum to the increase of the achievable figure of merit, more than doubling the efficiencies of thermoelectric devices [11], with a remarkable range of optimal operational temperatures (Fig. 8.1). Although off-the-shelf TEGs are still mostly based upon tellurides, skutterudites [13] and tetrahedrites [14] are hitting the market, extending the temperature range over which TEGs will be capable of converting heat into electricity. Also for thermoelectric materials, new candidate materials are selected not only upon their efficiency but also in view of their geo-abundance, costs, and non-toxicity.

8.3 Technological Challenges

Materials issues are not limited to *active* parts of the two solar stages, since not less relevant is the role of materials (and materials technology) in the making of the harvester. As an example, suppressing thermal cross-talk among thermoelectric legs is of paramount relevance in STEGs, and very low emittances from leg lateral surfaces is not less important in HTEPV generators. Also on the PV side, effective heat mirrors limiting the upward dissipation of heat were shown to remarkably enhance the overall efficiency of TEGs. Furthermore, heat dissipation at the TEG cold side, playing a key role in any TEG, is a formidable challenge still nowadays, calling for innovative materials and advanced surface finishing.

Even when ideal materials were available and unlimited technological possibilities were open, still the pairing of a PV stage, the efficiency of which is commonly larger at lower temperatures, with a thermoelectric stage, requiring higher temperature at its hot side and large temperature differences across its leg, generates a scenario leading either to a compromise between opposite temperature requirements or to innovative pairing layouts.

It has been shown in Chap. 6 that, in principle, both organic and inorganic PV materials may be paired to TEG stages for the development of hybridized solar converters.

Organic PV materials, although prospecting advantages for their low cost and easy preparation for large-area devices, have currently PV efficiencies still too low to become competitive even when paired to TEGs.

Inorganic PV materials may disclose more realistic opportunities of successful hybridization. With the major exception of silicon, where the decrease of PV efficiency due to the increasing temperature of the PV stage can be at most mitigated by the TEG stage, large-gap, low-cost PV materials have performances less sensitive to the higher temperatures needed to pair them with TEGs. Therefore, concentrated solar cells based on a-Si and CZTS may be sensibly expected to be suitable for hybridization, possibly along with stabilized perovskite solar cells.

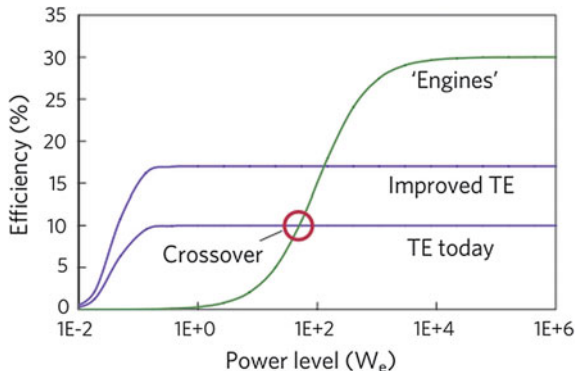
Technological challenges, even when related to materials, may be expected to find solutions upon initial industrialization. Although laboratory prototypes of HTEPV generators have been already fabricated and tested, hybrid solar harvesters have not yet moved to manufacturing. To this aim, an evaluation of the economic sustainability of HTEPV converters is needed, eventually pointing out the range and type of plant powers where hybridization may be profitable.

8.4 Economical Sustainability

8.4.1 Thermoelectric Generators

Analyses of the economic sustainability of TEGs compared to other thermal engines have quite a long tradition. While in the first part of the 20th century, also due to the low ZT achievable before nanotechnology, TEGs found civilian applications only as electric sources when no other source of power could have been available [15], the remarkable improvement of efficiencies occurred after 1990 set a competition among strategies to convert heat into electricity. In a rather famous paper appeared in *Nature Materials* in 2009, Vining [16] showed how TEGs would have had no chance to compete on the market with more traditional generators such as Rankine, Stirling, and Otto engines for *any* sensible ZT , save for the capability of TEGs to convert small amounts of heat at relatively low temperatures (Fig. 8.2). Miniaturization appeared to provide a natural niche of development for TEGs, which was actually pursued over the subsequent decades by the application of TEGs to recover power in the

Fig. 8.2 Comparison among efficiencies of several heat engines (including TEGs) versus electric power output. Reprinted with permission from [16]



automotive segment [17]—and, more recently, by foreseeing use of miniaturized or integrated TEGs [18] in the Internet of Things [19]. This notwithstanding, TEGs have also found deployment as relatively large power supplies, recovering heat in industrial plants [20], where lack of moving parts and reliability have made TEGs a favorite technological choice.

Economical sustainability of TEGs was more thoroughly investigated in more recent years. The importance of a full optimization of both electrical and thermal circuits was discussed by Yazawa and Shakouri [21] who remarked how the use of small fill factors F (namely smaller ratios between the cross-sectional areas of TE legs and the overall TEG footprint) would have been beneficial to the installment costs (per watt), as small fill factors (in the order of 0.03) would enable the use of thin film power generators, with a further reduction of materials costs. Assuming a TE materials cost leveled to that of state-of-the-art Bi_2Te_3 (approx. 500 USD/kg), it was estimated that TEG materials costs would scale down from more than 10,000 USD/m² for $F = 1$ down to 1.34 USD/m² for $F = 0.01$, when an optimal leg length of $\approx 30 \mu\text{m}$ was computed. Costs per watt are estimated in the order of 0.1 USD/W. Although the whole analysis admittedly relies upon the assumption of excellent (lossless) electric contacts and neglects parasitic thermal effects (i.e. thermal crosstalk among legs), it finally shows how most of the competitiveness of TEGs relies on such side technological issues more than on the TE material itself.

A somewhat different approach was pursued by Yee et al. [22], who focused their optimization on the power cost instead than on the efficiency. They observed that optimizing on ZT and *then* looking for the lowest possible system cost forces the analysis to obtain the smaller possible cost at the highest peak power, while neglecting scenarios where lower peak powers might lead to lower power costs. In addition, using the cost per power as a metric for optimization enables a simpler comparison of TEGs with other heat conversion strategies. Operating TEGs at maximum power, efficiency is set by (2.43). Neglecting once again parasitic thermal effects and matching thermal impedance, overnight capital costs is evaluated not considering operating, maintenance, and hermetic seal costs. Volumetric module

costs C''' (USD/m³) combines with areal module costs C'' (USD/m²) and with heat exchangers costs C_{HX} (USD/(W K⁻¹)). Thus total TEG cost C_{TEG} accounts to

$$C_{\text{TEG}} = (C'''L + C'')SF + C_{\text{HX}}US \quad (8.1)$$

where S is the exchange area, L is the leg length, and U is the heat transfer coefficient. Since the power output P_{TEG} reads

$$P_{\text{TEG}} = \frac{\alpha_{pn}^2 \sigma \Delta T^2}{16} \frac{L}{(2(\kappa F/U) + L)^2} \quad (8.2)$$

the cost per unit power reads

$$\chi_{\text{TEG}}(L, F) = \frac{16}{\alpha_{pn}^2 \sigma \Delta T^2} \left(2 \frac{\kappa F}{LU} + 1 \right)^2 \left(C'''L^2 + C''L + \frac{C_{\text{HX}}UL}{F} \right) \quad (8.3)$$

where κ and σ are the thermal and electric conductivity of the leg elements (assumed to be the same for the p and n elements), $\alpha_{pn} \equiv \alpha_p - \alpha_n$, and ΔT is the temperature difference between the two heat reservoirs.

Equation (8.3) admits no global minimum on F and UL/κ . Nonetheless, χ_{TEG} displays a minimum for $F = UL/(2\kappa)$, resulting from a competition between costs and thermoelectric performances. For smaller L (at constant F) materials costs decrease along with the temperature drop across the device, so that also power output decreases. Furthermore, one note that a characteristic point exists

$$\begin{cases} L = \sqrt{\frac{C_{\text{HX}}\kappa}{C'''}} \\ F = \frac{U}{2} \sqrt{\frac{C_{\text{HX}}}{C'''\kappa}} \end{cases}$$

below which any further decrease of L and F has only marginal benefits on χ_{TEG} . Using exemplar values for C'' , C''' , and C_{HX} one obtains optimal χ_{TEG} around 60 USD/W, including the large contribution arising from the heat exchanger (approx. 1,800 USD/m²).

Of special relevance to hybrid solar generators is the scenario wherein no heat exchanger cost adds up. Thus (8.3) simplifies to

$$\chi_{\text{TEG}}^*(L, F) = \frac{16}{\alpha_{pn}^2 \sigma \Delta T^2} \left(2 \frac{\kappa F}{LU} + 1 \right)^2 (C'''L^2 + C''L) \quad (8.4)$$

and neither characteristic points or lines of minimal costs exist any longer. It may be shown, however, that lower χ_{TEG}^* may be achieved for leg lengths L shorter than the thermal-impedance-matching value $2F\kappa/U$. Stated differently, *more favorable*

power costs are obtained for TEGs operating under non-optimized conditions, as the lower materials costs overcompensate the reduced power output.

8.4.2 Photovoltaic Cells and Modules

Affordability and sustainability of PV cells and modules are set by standard economic parameters including the total capital costs, electricity costs, and the payback period (PBP).

Currently, module costs are typically only 40–60% of total PV system cost. It has remarkably changed over the last decade. In 2013, for a system having a power of 10 kW it was about 1,900 USD/kW_p, scaling down to 1,650 USD/kW_p for a 100-kW system. In 2009, typical figures were instead between 4,150 and 6,000 USD/kW_p for a 1-kW system. The remaining half of the capital costs cover instead the inverter, PV array support structures, electrical cabling, equipment (collectively referred to as Balance-of-System (BOS))—and system installation. Manifestly enough, BOS and installation costs are subject to a rather wide variability depending on costs for site preparation [23].

A breakdown of capital costs and its trend from 2010 is displayed in Fig. 8.3. As noted in Sect. 1.1.2, PV cost structure sets a threshold to the minimal efficiency of a PV material, independently of the materials cost, that is estimated to be 10% at module level (12% at cell level).

An additional index of affordability for PV cells is the PBP, namely the period of time needed to pay back the capital cost. PBP should not be confused with the energy payback period (EPBP), which counts instead the period of time needed to generate the amount of energy spent to build the PV system [25]. At a capital cost of 5,000 USD/kW_p and at an initial electricity rate of 0.10 USD/kWh, a home system capable of 23 kW_p pays back in 20 years, with minor changes for larger plants. This still acceptably compares with an anticipated PV module lifetime of 25 years and an inverter lifetime of 5 years. PBPs drop down significantly due to rebates, tax deductions and reductions, or Solar Renewable Energy Certificates, often becoming close to just one year [26].

8.4.3 Hybrid Solar Harvesters

A full economic analysis of HTEPV generators is a very complex task for at least four reasons. First, the number of solutions to pair PV and TE stages are extremely diversified, encompassing direct thermal contact, thermal concentration, solar-split strategies, and many intermediate solutions. Second, as shown in Chaps. 5 and 6, power output from HTEPV critically depends on several subtle constructive details. This was experimentally proved in the case of STEGs, where improvements of power outputs of a factor three was achieved by a very accurate minimization of thermal

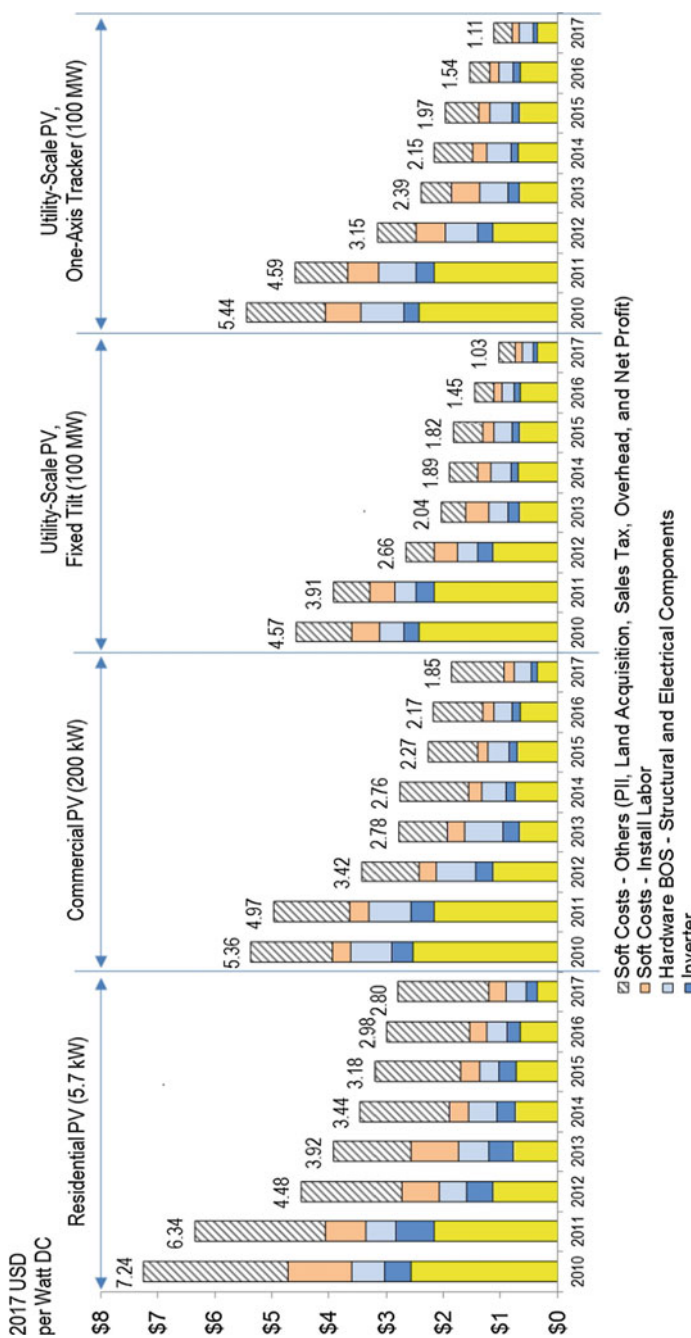


Fig. 8.3 Trends of total costs and cost structure of PV systems by classes of users (power capacity). Reprinted from [24]

shunts in the generator [27]. This implies that any economic evaluation based on computational models might easily turn out to be overoptimistic, especially in view of the low technological maturity of the HTEPV technology. Third, also on the PV side it is very challenging to compare costs of existing PV technology with those of radically different technologies based on new materials [28], adding to any estimate the incertitude of the cost of PV modules based on yet-to-deploy PV materials. This is even more true for TEGs, the market of which is extremely limited and, with very few exceptions, still limited to Bi_2Te_3 -based systems—the layout of which was shown [29] not to be necessarily adequate for solar harvesting. Finally, a cost analysis should not be limited to consider the capital costs and the pay-back period but should also fully analyze its cost over the whole lifetime cycle of the harvester, also considering the additional costs of disposal—an additional component really difficult to quantify in view of the constructive complexity of *any* HTEPV generators, whichever pairing geometry be considered.

All this said, considering HTEPV technologies as convenient only based upon their larger solar conversion efficiency would be anyway unacceptable. This has motivated over the last few years a very preliminary effort to estimate HTEPV harvester costs per unit power output.

Possibly the very first attempt to assess the economic sustainability of HTEPV generators was reported by van Sark in 2011 [30]. Referring to a very simple (direct) pairing scheme, van Sark computed that the fraction of the PV cell area to be covered by TEG generators, based on the total heat flux to be dissipated by the PV cell and the dissipating capacity of commercial thermoelectric modules, should have been between 1/3 and 1/5. Setting the maximum acceptable increase of price for the hybrid module equal to the extra power output from the thermoelectric stage ($\approx 10\%$), for a PV module delivering electric power with an efficiency of 15% at a base price of 3 USD/W (450 USD/m²) the largest affordable cost of the thermoelectric stage should be 45 USD per m² of the PV module, namely from 135 to 225 USD per m² of the thermoelectric module—that is more than one order of magnitude less than the current TEG prices (1–2 USD/cm²). Van Sark concluded that not only are more efficient TEGs needed but also that a major reduction of selling prices is required to make hybrid harvesters profitable.

Van Sark analysis is exceptionable in many respects. Among them, it systematically mixes prices and costs, mostly using the formers. Prices are subjected to market fluctuations, and are driven by demand and by production volumes. Historical series of Si-based PV prices clearly displays such a volatility [31].

More recently, Zhu et al. [32] proposed an alternate approach to economic feasibility of hybrid harvesters. Limiting to power costs χ_{HTEPV} (USD/W), it is

$$\chi_{\text{HTEPV}} = \frac{\chi_{\text{PV}}\eta_{\text{PV}}G S_{\text{PV}} + C''_{\text{TEG}}S_{\text{TEG}} + C''_{\text{SSA}}S_{\text{SSA}}}{\eta_{\text{PV}}G S_{\text{PV}} + \eta_{\text{TE}}(G S_{\text{SSA}} + (1 - \eta_{\text{PV}})G S_{\text{PV}})} \quad (8.5)$$

where S_{PV} , S_{TEG} , and S_{SSA} are the PV, TEG, and the solar selective absorber (SSA) areas, χ_{PV} is the power cost of the PV cell (USD/W), C''_{SSA} and C''_{TEG} are the costs per unit area of the SSA and of the TEG, G is the solar input power density, and η_{PV} and η_{TE} are the efficiencies of the PV and TEG stages.

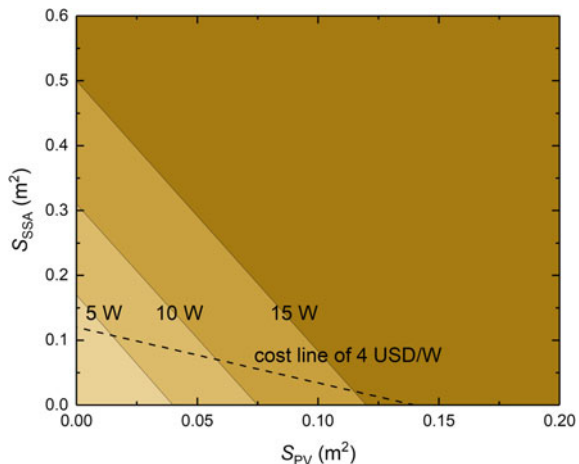
Profitability occurs when $\chi_{\text{HTEPV}} \leq \chi_{\text{PV}}$ under the additional requirement that the total power output also exceeds a minimum output power, set by user-application needs. Quite unfortunately, the analysis by Zhu et al. assumed unrealistically low PV and TEG efficiency (10 and 3%, respectively) and fully neglected the areal cost of installation, which is known (Chap. 1) to set the threshold efficiency of any PV material. In addition, PV efficiency is taken as a constant, not depending on (decreasing with) the hybridization—an assumption limiting the validity of the economic model to ideal solar-split solutions. With all these limitations in mind, the model led to the conclusion that, depending on minimum output power, HTEPV harvesters are economically feasible for large S_{PV} and S_{SSA} (Fig. 8.4), with an extended region of profitability (area above the cost line in Fig. 8.4).

A possibly more realistic approach to a preliminary estimate of power costs might proceed by splitting HTEPV generator costs as

1. fixed costs (the BOS), C_{BOS} , taken as grossly independent of the system size
2. the costs of the PV cell, scaling with the sole PV power output: $C_{\text{PV}} = \chi_{\text{PV}} \eta_{\text{PV}} (c_{\text{conc}} G) S$, where c_{conc} is the optical concentration in concentrated solar cells
3. the cost of the TEG stage, C_{TEG} , to be computed following either (8.3) or (8.4)
4. the SSA cost $C''_{\text{SSA}} = c_{\text{SSA}} S_{\text{SSA}}$

Instead, the output power may be conveniently written as $P_{\text{HTEPV}} = \eta_{\text{HTEPV}} (C_{\text{conc}} G) S$ (cf. Fig. 5.5), where η_{HTEPV} captures both PV efficiency degradation with temperature

Fig. 8.4 Profitability region of HTEPV according to Zhu et al. [32]. TEG and PV efficiencies are taken equal to 3 and 10%, respectively, while solar power density is set to 1000 W/m². Adapted with permission from [32]



and the additional power output due to the electric power generated by the TEG stage. Therefore the power cost (USD/W) reads

$$\chi_{\text{HTEPV}} = \frac{C_{\text{BOS}} + \chi_{\text{PV}} \eta_{\text{PV}} c_{\text{conc}} G S + C_{\text{TEG}} + C''_{\text{SSA}} S_{\text{SSA}}}{\eta_{\text{HTEPV}} C_{\text{conc}} G S} \quad (8.6)$$

The corresponding power cost for the sole PV cell is instead

$$\chi_{\text{PV}} = \frac{C_{\text{BOS}} + \chi_{\text{PV}} \eta_{\text{PV}} c_{\text{conc}} G S}{\eta_{\text{PV}} c_{\text{conc}} G S} \quad (8.7)$$

so that a hybridization figure of merit h is defined:

$$h \equiv \frac{\chi_{\text{HTEPV}}}{\chi_{\text{PV}}} = \left(1 + \frac{C_{\text{TEG}} + C''_{\text{SSA}} S_{\text{SSA}}}{C_{\text{BOS}} + \chi_{\text{PV}} \eta_{\text{PV}} c_{\text{conc}} G S} \right) \times \frac{1}{\eta_{\text{HTEPV}} / \eta_{\text{PV}}} \quad (8.8)$$

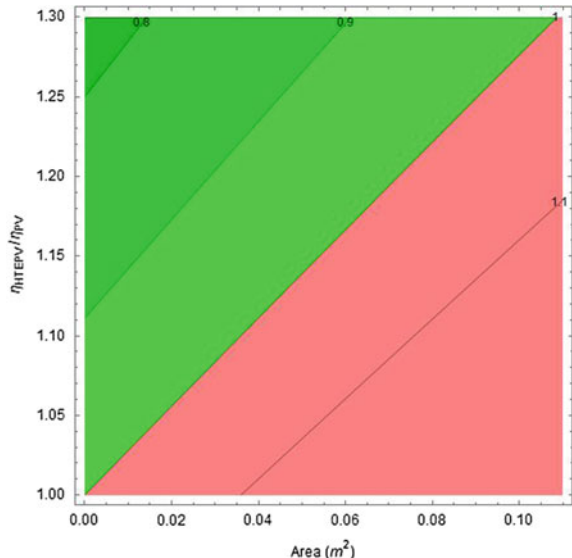
Profitability clearly requires $h < 1$.

For non-concentrated modules ($c_{\text{conc}} = 1$), C_{TEG} must account for the heat exchanger cost following (8.3), as heat dissipaters are not normally required in standard PV modules. Thus, taking $S_{\text{SSA}} = S_{\text{TEG}} = S$, one obtains

$$h_{\text{non-conc}} = \left(1 + \frac{(C''' L + C'') F + C_{\text{HX}} U + C''_{\text{SSA}}}{C_{\text{BOS}} / S + \chi_{\text{PV}} \eta_{\text{PV}} G} \right) \times \frac{1}{\eta_{\text{HTEPV}} / \eta_{\text{PV}}} \quad (8.9)$$

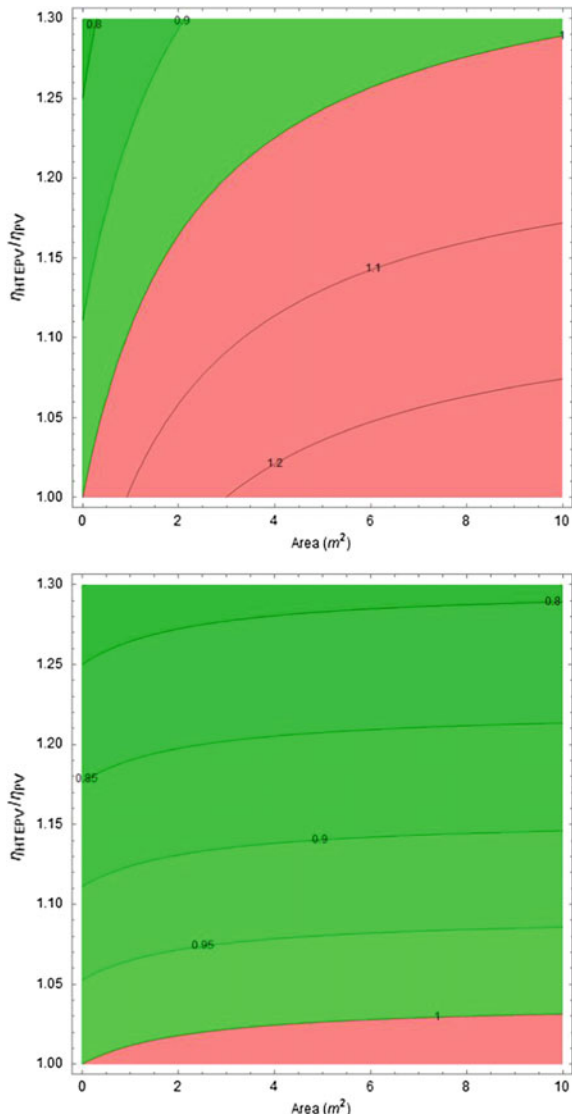
Fig. 8.5 Hybridization figures of merit h of HTEPV according to (8.9).

Profitability occurs for $h < 1$. Cost parameters are taken from [22, 32]:
 $C''' = 0.89 \text{ USD/cm}^3$,
 $C'' = 0.017 \text{ USD/cm}^2$,
 $C_{\text{HX}} = 18.48 \text{ USD/(W/K)}$,
 $U = 100 \text{ W m}^{-2} \text{ K}^{-1}$,
 $C_{\text{BOS}} = 7000 \text{ USD}$,
 $C''_{\text{SSA}} = 0.001 \text{ USD/cm}^2$,
 $\chi_{\text{PV}} = 5 \text{ USD/W}$, $\eta_{\text{PV}} = 15\%$, $G = 1000 \text{ W/m}^2$,
 $L = 0.1 \text{ cm}$



As expected, heat exchanger costs are found to dominate the figure of merit. Hybridization is found to be convenient only for small areas, with h being truly insensitive to the filling factor (Fig. 8.5). Power outputs are therefore very limited, not exceeding 20 W_p.

Fig. 8.6 Hybridization figures of merit h of HTEPV according to (8.10) for concentration of 10 suns and fill factors of 1 (top) and 0.1 (bottom). Profitability occurs for $h < 1$. Cost parameters are taken from [22, 32]: $C''' = 0.89 \text{ USD/cm}^3$, $C'' = 0.017 \text{ USD/cm}^2$, $C_{\text{HX}} = 18.48 \text{ USD/(W/K)}$, $U = 100 \text{ W m}^{-2} \text{ K}^{-1}$, $C_{\text{BOS}} = 7000 \text{ USD}$, $C''_{\text{SSA}} = 0.001 \text{ USD/cm}^2$, $\chi_{\text{PV}} = 2 \text{ USD/W}$, $\eta_{\text{PV}} = 15\%$, $G = 1000 \text{ W/m}^2$, $L = 0.1 \text{ cm}$



In concentrated modules, instead, hybridization does not require the addition of heat exchangers, which are already part of the PV module. Therefore, replacement of C_{TEG} by (8.4) leads to

$$h_{\text{conc}} = \left(1 + \frac{(C'''L + C'')F + C_{\text{HX}}U + C''_{\text{SSA}}}{C_{\text{BOS}}/S + \chi_{\text{PV}}\eta_{\text{PV}}c_{\text{conc}}G} \right) \times \frac{1}{\eta_{\text{HTEPV}}/\eta_{\text{PV}}} \quad (8.10)$$

As a result, profitability is here much more extended, enabling module areas of several m^2 already at modest concentrations ($c_{\text{conc}} = 10$) (Fig. 8.6). Hybridization figures of merit lower than 1 are obtained for any module area when concentration further increases, with filling factors farther extending hybridization profitability.

8.4.4 Pay-Back Period

As already remarked, PBPs are currently cut down by taxation and other supporting benefits. True PBPs are easily computed to be around 20 years for both domestic and industrial solar power plants. In hybrid solar harvesters, PBPs scale with h and with the ratio of HTEPV to PV capital costs. In the case of concentrated solar cells, this leads to an increase of PBP of less than 5% in the worst case. Since TEGs are known to have a very extended lifetime, larger than solar cells, hybridization retains acceptable PBPs even in the absence of a favorable taxation.

8.5 Conclusive Remarks

The comparative analysis of the current and perspective possibilities provided by the hybridization of thermoelectric and photovoltaic generators has shown positive also from the economical viewpoint. This landscape further motivates the ongoing research effort, both at the device and at the materials level, toward the development of hybrid solar harvesters. On one side, higher-efficiency, lower-cost thermoelectric materials would extend profitability also to non-concentrated solar cells, at the same time promoting the introduction of novel high-band-gap PV materials (or rejuvenating age-old materials such as a-Si or Cu_2O). Materials research is further needed also to enable effective implementation of the hybrid technology. Such research partially meets demands already well expressed in the standard PV technology (e.g. for more efficient heat mirrors) while partially covers issues of relevance to general-purpose TEGs (e.g. low emittance to minimize leg thermal cross-talking). In addition, smart and creative pairing strategies between PV and TEG stages (eventually extended to the thermal stage for tri-generation) are to be encouraged. As an example, the importance of rethinking the layout of thermoelectric generators has been underlined as a simple key element to enhance HTEPV efficiency.

However, even at the current state of the art HTEPV generators may play a remarkable role in the development of more efficient renewable energy sources, provided that a careful selection of photovoltaic materials is made. Possibly, the last open question remains that of where and how hybrid solar harvesters will enter their phase of industrialization. The segment of concentrator photovoltaics is a sensible context, and might provide the momentum that research and development urgently needs to move a wealth of innovative approaches aiming at a better use of solar power out of research laboratories, taking the ultimate challenge of facing market competition by advancing scientific ideas toward production.

References

1. Energy Initiative Massachusetts Institute of Technology, *The future of solar energy- an interdisciplinary mit study*. Technical Report. Accessed 2015
2. J. Kilner, S. Skinner, S. Irvine, P. Edwards, *Functional Materials For Sustainable Energy Applications* (Woodhead Publishing Limited, 2012)
3. J. Peng, L. Lu, H. Yang, Renew. Sustain. Energy Rev. **19**, 255 (2013)
4. M.M. de Wild-Scholten, Sol. Energy Mater. Sol. Cells **119**, 296 (2013)
5. Fraunhofer ISE, Photovoltaics report. Technical Report (2014)
6. J. Jean, P.R. Brown, R.L. Jaffe, T. Buonassisi, V. Bulović, Energy Environ. Sci. **8**(4), 1200 (2015)
7. L. Kazmerski, *Best research cell efficiencies*. Technical Report. Accessed 2010
8. M.A. Green, K. Emery, Y. Hishikawa, W. Warta, E.D. Dunlop, Prog. Photovoltaics Res. Appl. **23**(1), 1 (2014)
9. R. Miles, K. Hynes, I. Forbes, Prog. Cryst. Growth Charact. Mater. **51**(1–3), 1 (2005)
10. J. Berry, T. Buonassisi, D.A. Egger, G. Hodges, L. Kronik, Y.L. Loo, I. Lubomirsky, S.R. Marder, Y. Mastai, J.S. Miller, D.B. Mitzi, Y. Paz, A.M. Rappe, I. Riess, B. Rybtchinski, O. Stafudd, V. Stevanovic, M.F. Toney, D. Zitoun, A. Kahn, D. Ginley, D. Cahen, Adv. Mater. **27**(35), 5102 (2015)
11. J. He, T.M. Tritt, Science **357**(6358) (2017)
12. X. Zhang, L.D. Zhao, J. Materomics **1**(2), 92 (2015). <https://doi.org/10.1016/j.jmat.2015.01.001>, <http://www.sciencedirect.com/science/article/pii/S2352847815000258>
13. G. Rogl, P. Rogl, Curr. Opin. Green Sustain. Chem. (2017)
14. X. Lu, D.T. Morelli, in *Materials Aspect of Thermoelectricity*, ed. by C. Uher (CRC Press, 2016), p. 473
15. M. Rubinstein, Energy Convers. **9**(4), 123IN1127 (1969)
16. C.B. Vining, Nat. Mater. **8**(2), 83 (2009)
17. J. Yang, F.R. Stabler, J. Electron. Mater. **38**(7), 1245 (2009)
18. M. Strasser, R. Aigner, C. Lauterbach, T. Sturm, M. Franosch, G. Wachutka, Sens. Actuators A Phys. **114**(2), 362 (2004)
19. H. Jayakumar, K. Lee, W.S. Lee, A. Raha, Y. Kim, V. Raghunathan, in *Proceedings of the 2014 International Symposium on Low Power Electronics and Design* (ACM, 2014), pp. 375–380
20. Alphabet Energy. Alphabet energy's thermoelectric advances. <http://www.alphabetenergy.com/thermoelectric-advances/>
21. K. Yazawa, A. Shakouri, Environ. Sci. Technol. **45**(17), 7548 (2011)
22. S.K. Yee, S. LeBlanc, K.E. Goodson, C. Dames, Energy Environ. Sci. **6**, 2561 (2013)
23. <https://www.solarwirtschaft.de>
24. R. Fu, D.J. Feldman, R.M. Margolis, M.A. Woodhouse, K.B. Ardani, US solar photovoltaic system cost benchmark: Q1 2017 Technical Report. National Renewable Energy Laboratory (NREL), Golden, CO (United States) (2017)

25. V. Fthenakis, E. Alsema, Prog. Photovoltaics Res. Appl. **14**(3), 275 (2006)
26. <http://pvwatts.nrel.gov/>
27. D. Kraemer, Q. Jie, K. McEnaney, F. Cao, W. Liu, L.A. Weinstein, J. Loomis, Z. Ren, G. Chen, Nat. Energy **1**, 16153 (2016)
28. P.A. Basore, IEEE J. Photovoltaics **4**(6), 1477 (2014)
29. D. Narducci, B. Lorenzi, in *2015 IEEE 15th International Conference on Nanotechnology (IEEE-NANO)* (IEEE, 2015), pp. 196–199
30. W. Van Sark, Appl. Energy **88**(8), 2785 (2011)
31. D. Feldman, *Photovoltaic (PV) pricing trends: historical, recent, and near-term projections.* Technical Report (2014). <https://escholarship.org/uc/item/06b4h95q>
32. W. Zhu, Y. Deng, Y. Wang, S. Shen, R. Gulfam, Energy **100**(Supplement C), 91 (2016)

Index

A

Amorphous silicon, 4, 70, 73, 82, 88, 113, 114, 138

B

Balance-of-System (BOS), 72, 143, 146

C

Copper Indium Gallium Selenide (CIGS), 4, 70, 74, 75, 94, 113, 132, 138

Copper Zinc Tin Sulde (CZTS), 4, 88, 113, 114, 140

Cost structure

- hybrid photovoltaic-thermoelectric generators, 146, 149
- photovoltaic cells, 143, 144
- thermoelectric generators, 143

D

Domenicali equation, 23

Dye Sensitized Solar Cells (DSSC), 7, 77, 83, 84, 104, 105, 138

E

Economic issues

 system scaling, 132

Economic sustainability, 140, 145

Endoreversible heat engine, 11, 12, 37, 38

 Curzon–Ahlborn efficiency of, 37, 38

 Van den Broeck efficiency of, 38

Exoreversible heat engine

 Schmiedl-Seiffert efficiency of, 38

F

Fixed costs, 6, 146

H

Heat dissipater, 52, 54, 147

Heat Mirrors (HMs), 93, 114, 139, 149

Hybrid photovoltaic-thermoelectric generators

- dye-sensitized, 104, 105
- efficiency, 11, 17, 18, 27, 30, 40, 41, 113, 139, 146
- fully hybridized, 91, 99–101
- materials, 103
- multi-junction concentrated, 113
- non-silicon-based, 113
- perovskite-based, 110
- polymer-based, 107
- polysilicon-based, 111
- technological challenges, 137, 140
- thermally hybridized, 104

Hybridization figure of merit, 147

I

Investment costs, 2

O

Onsager relations, 15

Optical collector, 45, 50, 52, 91, 92

Optical concentration, 46, 50, 52, 55, 56, 92, 95–97, 112, 113, 118, 123, 146

Opto-thermal converters, 92

P

Pay-back period, 145, 149

Peltier effect, 12
 Perovskites, 80, 86, 111, 113, 138
 Photon management, 94, 111, 112, 118, 119, 143, 146
 Photothermally activated pyroelectrics, 109
 Photovoltaic cells
 conjugated polymer-based, 85
 current-voltage characteristics, 65
 first-generation, 71
 multiple-junction, 70, 75
 perovskite-based, 88
 second-generation, 70, 73, 137
 silicon-based, 73, 137
 single-junction, 70, 74
 Photovoltaic efficiency, 6, 95, 96, 98, 103, 112–114, 119, 140, 146
 temperature dependence, 98
 Photovoltaic filling factor, 99, 104
 Power cost, 1, 141, 143, 145
 Power factor, 21, 34, 57
 Profitability, 146–149

Q

Quantum Dot Sensitized Solar Cells (QDSS-Cs), 78, 84

S

Seebeck effect, 105

Solar spectrum, 64, 69, 91, 93, 94, 104, 112, 115, 117, 118, 120, 131, 134, 135
 Solar thermoelectric generators, 7, 45
 efficiency of, 52, 57, 58

T

Tandem solar cells, 123
 Thermal collector, 45, 50, 53, 91, 92
 Thermal storage, 117, 118, 123, 126, 127, 135
 Thermoelectric compatibility, 30, 31, 41
 Thermoelectric efficiency, 30, 41, 47
 constant-Property Limit, 17
 Dirichlet boundary conditions, 17
 finite-rate, 36
 Neumann boundary conditions, 17
 non-steady state conditions, 40
 Thermoelectric figure of merit, 12, 17, 34, 57
 engineering, 34, 35, 41
 Thermoelectric filling factor, 56
 Thermoelectric potential, 32, 115
 Thermophotovoltaic generation, 132, 134
 Thermophotovoltaic integrated systems, 132
 Thomson effect, 17, 35, 40
 Triple co-generation, 7, 117–119
 efficiency, 127